

Delft University of Technology

Quantitative Characterization of Joint Properties in a
Dolomite Deposit Using Virtual Outcrop Models, Rock
Core Analysis, and Field Data for Geotechnical
Applications

Master Thesis project: MSC Applied Earth Sciences track
geo-engineering

Authors:

Harold Jolly (4867823)

Supervisors:

Pierre-Olivier Bruna
Dominique Ngann-Tillard
Julien Vanneste
Aleksandr Nikulshin

May 27, 2024



1 Acknowledgments

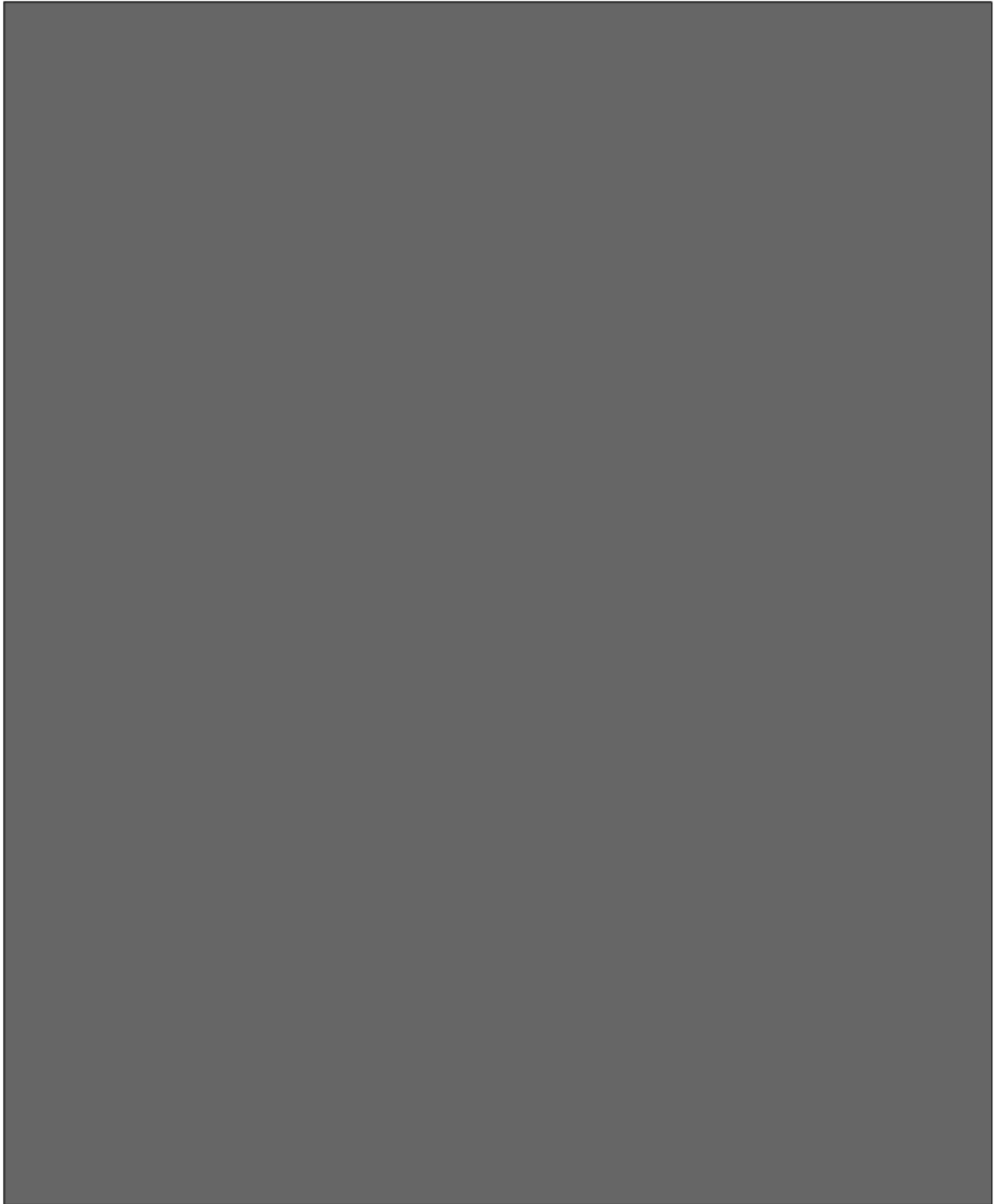
My deepest gratitude goes to my thesis committee, particularly the chair, Dr. Pierre-Olivier Bruna, for his invaluable patience and feedback. Sincere thanks are also extended to the Geology and Mining Department of Lhoist Western Europe, specifically Julien Vanneste and Aleksandr Nikulshin, for their trust, time, and the valuable resources they provided, which significantly contributed to my work. The software from Petroleum Experts, MOVE, also played a role in the completion of this thesis, and their contribution is greatly appreciated.

Contents

1 Acknowledgments	1
2 Introduction	4
2.1 Problem Statement	4
2.2 Objectives	4
3 Initial site assessment	6
3.1 Location and background	6
3.2 Geological Context	7
3.2.1 Main formations of the MLD deposit	7
3.2.2 Hercynian orogeny	8
3.2.3 Extensional Domains of the Jurassic and Cretaceous	9
3.2.4 Current stress regime	9
3.3 Geological features	9
3.3.1 Joint sets	9
3.3.2 Bedding planes	10
3.3.3 Small karstic voids	11
3.3.4 Dissolution joints	11
3.3.5 Fracture corridors	12
3.3.6 Epikarst- Pinnacle zone	13
3.3.7 Faults	13
3.3.8 Iron- fault related karst	14
4 Background information and methodology data collection	16
4.1 Background definitions	16
4.1.1 Structural and background joints	16
4.1.2 Weakness zones and joints	17
4.2 Joint condition ratings from the rock mass classification systems	17
4.3 Photogrammetry model data collection	19
4.3.1 Joint orientation	20
4.3.2 Joint Intensity	20
4.3.3 Joint intensity - VB-P10	21
4.3.4 Joint intensity- SL-P10	21
4.4 Borehole core descriptions	22
4.4.1 Induced fractures	22
4.4.2 Joint intensity (RQD and BH-P10)	22
4.4.3 Joint condition	23
4.5 Field Investigation	23
4.5.1 Orientation data	24
4.5.2 Joint condition	24
5 Results	25
5.1 Joint Orientation	25
5.2 Joint intensity	27
5.2.1 SW-P21	27
5.2.2 VB-P10	28
5.2.3 SL-P10	28
5.2.4 BH-P10	29
5.2.5 Bed thickness	31
5.2.6 Joint spacing	33
5.3 Joint Shape	34
5.3.1 Maximum joint height and length	35
5.3.2 Aspect ratio	38
5.3.3 Joint geometry distributions for DFN modelling applications	39
5.4 Joint condition	40
5.4.1 Joint condition ratings Ja, Jr for structural joints	40
5.4.2 Joint condition ratings Ja, Jr for background joints	42
5.4.3 Estimates of the joint friction angle	42
5.5 Geotechnical domains	44

5.5.1	F1 domain	45
5.5.2	F2 and F3 domains	47
5.5.3	S0 domain	47
5.5.4	S1 domain	48
5.5.5	S2a and S2b domains	48
5.6	Interpretation of joint intensity datasets	48
5.6.1	Interpretation BH-P10 dataset	48
5.6.2	relationship between P32, P21 and P10	50
5.6.3	DFN P32 dataset	51
6	Model building (Quarry wide DFN)	51
6.1	Integrated dataset	51
6.2	Spatially modelling the P32 fracture intensity	52
6.2.1	Kriging interpolation	52
6.2.2	Block model	53
6.3	DFN model	54
6.4	Block size analysis	55
6.4.1	sensitivity analysis	55
6.4.2	Empirical solution	58
6.5	Geotechnical model displaying blockiness of rock mass..	59
7	Leveraging quantitative joint characterization for rock mass classification and	62
7.1	Rock mass classification	62
7.1.1	Field Q values	62
7.1.2	Field RMR	64
7.1.3	Borehole Q values	66
7.1.4	Influence bed thickness RMR and Q values	66
7.1.5	Joint condition influence on RMR and Q values	67
8	Discussion	79
8.1	Dataset validity	79
8.2	DFN modelling for geotechnical application	79
9	Conclusion	82
10	References	83
11	Appendix	87
A	Scan-Windows	89
B	Methodology photogrammetry model Scan-Windows	94
C	Integrated P32 dataset	105
D	Joint Condition	108
E	RMR and Q values	110

2 Introduction



2.2 Objectives

Utilizing a diverse array of data sources, including photogrammetry, field surveys, and borehole core analyses, this thesis aims to collect data on the joint properties within the study area. From these data, a geotechnical map will be developed to delineate various geotechnical domains, and comprehensive Discrete Fracture Network (DFN) models will be constructed to predict in-situ joint intensities. The thesis is structured around three main objectives:

- 1. Quantitative joint characterization of the study area**

This involves detailed data collection on the joint properties of the study area. The data is collected based on different datasets:

- **Rock core descriptions:**Detailed logging of unoriented rock cores. Parameters include joint condition, intensity, RQD.
 - **Data collection on virtual outcrops**
 - **Field Investigation:** Data collection on joint parameters such as joint condition. Investigation of geological features such as large karstic zones or faults.
2. **Quarry wide DFN generation- and DFN based geotechnical modelling:**
This section aims to produce a quarry- wide DFN. The aim of this DFN is to produce a block model displaying the fracture intensity variation across the quarry. The influence of joints on the block size potential will also be investigated during this thesis.
3. **Leveraging datasets for rock mass classification**
- **Rock mass classification systems:**Using the collected data on joint characteristics and mechanical properties of the rock material (collected in a previous study see Appendix G) to classify the rock mass. The RMR and Q system will be used as classification systems in this study.

3 Initial site assessment

3.1 Location and background



The quarry is 1.3 kilometers in length, 500 meters in width, and 100 meters in depth. It operates as an open-pit mine with eight levels or benches, on average 16 meters in height. The bottom three levels—8, 7, and part of 6—lie beneath the natural water table. The quarry spans from an elevation of 38 meters at its lowest level to 180 meters at the top, with a vertical extent of 120 meters being mined.

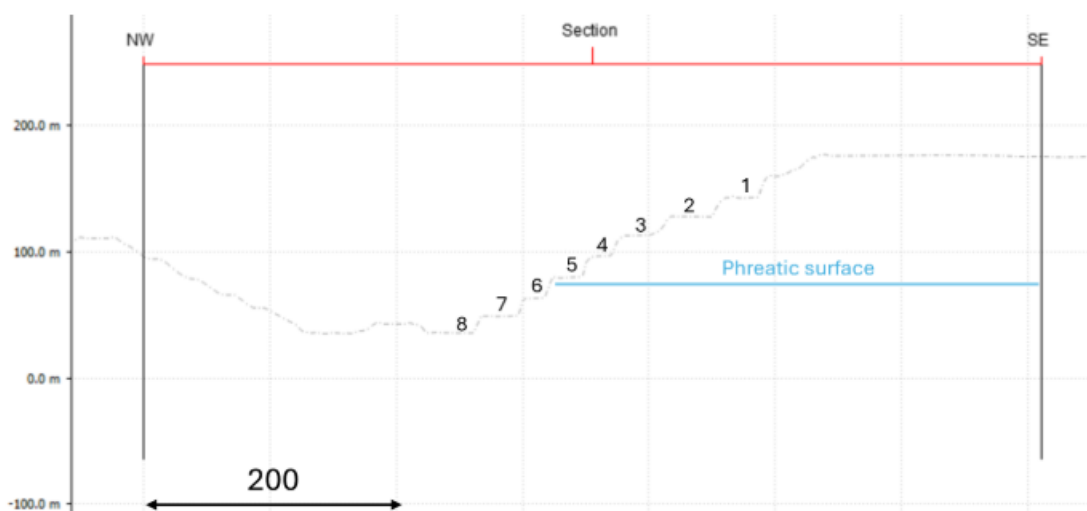


Figure 3.2: Cross section of the topography of the quarry intersection all bench heights (MOVE software reference)

3.2 Geological Context

3.2.1 Main formations of the MLD deposit

The quarry covers three main geological formations, the Terwagne, Longpré and Engihoul (Poty, 2001). These formations were deposited during the Carboniferous period in the Dinant Sedimentary Area (DSA), specifically during the Tournaisian and Visean stages of the Carboniferous period (Poty, 2001; Van der Voet, 2022). The three primary geological formations are further divided into distinct geological members (Poty, 2001). Lhoist has classified and subdivided the main geological formations using their own terminology, which is based on the chemical characteristics of the carbonate rocks (see Table 3.1). This report will only cover the main formations of the quarry which are Terwagne, Longpré and part of the Engihoul formation (up and until the Maurenne member). The formations will be referred to as formations E, D, and C respectively.

Stratigraphic bedding planes referred to as stratigraphic joints by Lhoist are represented in figure 3.3. The stratigraphic joints often delimit geological members or Lhoist's geological strata.

In the study area, geological formations D and C exhibit non-continuous bedding planes due to the dolomitization process affecting these layers (Lauwers, 2023). The dolomitization process of the Tournaisian limestones (D and C) occurred during an early Visean regression cycle (Van der Voet, 2022). A process known as replacement dolomitization, took place in sea-water environments (Lauwers, 2023; Van der Voet, 2022). The bedding planes of formation E (Visean) are continuous and clearly visible in contrast to bedding planes of formation D and C (see figure 3.8). The bed thickness are also larger in formation D compared to formation C in particular in the upper parts of formation D and the Avins member of this formation. The Avins member is 10-12m thick with almost no visible bedding planes.

Table 3.1: Geological formations found in the MLD area according to Poty (2001). The Lhoist terminology and the terminology used during this report are also given in this table.

Lhoist strata terminology	Geological layers (Poty, 2001)	Member	Era - Stages	Terminology for this study
SOB	//	//	Cenozoic Era	SOB
F	Neffe	//	Paleozoic- Visean	F
E2	Terwagne	//		E
E1		//		
D2	Longpré	Avins	Paleozoic- Tournaisian	D
D1		Fiémalle		
D0				
C2b	Engihoul	Ourthe		C
C2a				
C1b		Yvoir		
C1a				
B		Maurenne		
A2				
A1		Landelies		A1
A0	Pont d'Arcole	//	A0	
FAM	Evieux	//	Paleozoic- Famenian	FAM

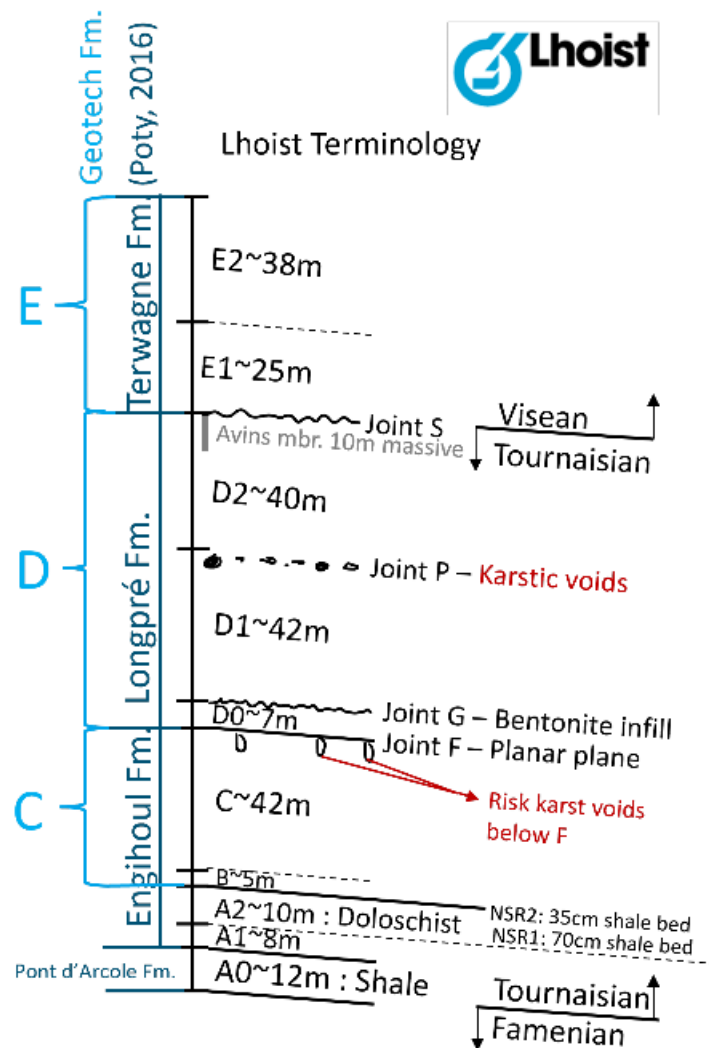


Figure 3.3: Stratigraphy of the area with stratigraphic joints delimiting formations.

3.2.2 Hercynian orogeny

The Hercynian orogeny, spanning from the late Devonian to the early Permian, was characterized by compressive stresses that led to the formation of multikilometer NE-SW folds and reverse faults (Bour, 2010; Sonnet, 2004). The study area is situated on the Southern edge of the Namur synclinorium, between two major reverse faults, the Midi-Eiffel fault and the Landenne fault (Van der Voet, 2022). The Midi-Eiffel fault delimits the structural units of the Brabant Parautochthon and the Ardennais Allochtone (Bour, 2010; Pingot, 2022). The study area is located on the Brabant Parautochthon, characterized by less deformation in the Devonian-Carboniferous sedimentary deposits than on the Ardennais Allochtone (Passagez, 2012; Van der Voet, 2022). Small reverse faults NE-SW associated with the compressive regime occurring during the Hercynian orogeny have been observed in the quarry (Mathieu, 1962; Passagez, 2012).

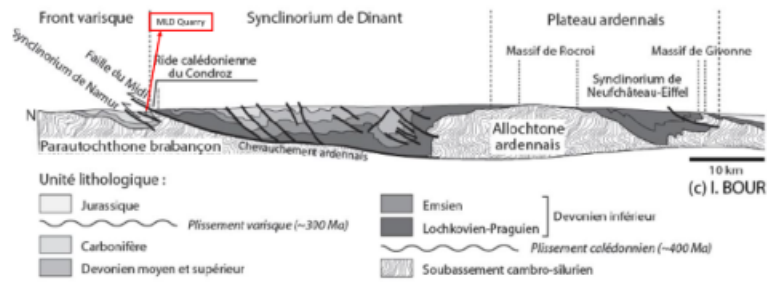


Figure 3.4: North-South cross-section of Wallonia study area is situated to the South of the 'Faille du midi' of the midi fault (Bour, 2010)

3.2.3 Extensional Domains of the Jurassic and Cretaceous

During the Jurassic and Cretaceous, the system was in extension. The extensional events formed strike-slip faults and is the origin of the two main joint sets measured of the study area Mathieu (1962); Van der Voet (2022); Vandycke (1997). The two main subvertical joint sets described in literature are oriented NNE-SSW (N25) and ESE-WNW (N295).

3.2.4 Current stress regime

The nearest stress regime measurements to the study area were taken in the Liège-Gulpen area, where the horizontal principal stress direction is oriented east-west (Delvaux, 1997). The current stress tensor observed in Liège closely resembles the paleo-stress tensor documented in the Engis-Flône quarries, which are situated approximately 30 km from the study area (Delvaux, 1997). Additionally, stress measurements taken in the Hainaut region, 60 km west of the quarry, indicate a horizontal principal stress direction of northwest-southeast, which is consistent with the prevailing stress regime across Western Europe (Delvaux, 1997). It is important to emphasize that the major principal stress in the area is expected to be the vertical stress related to the overburden.

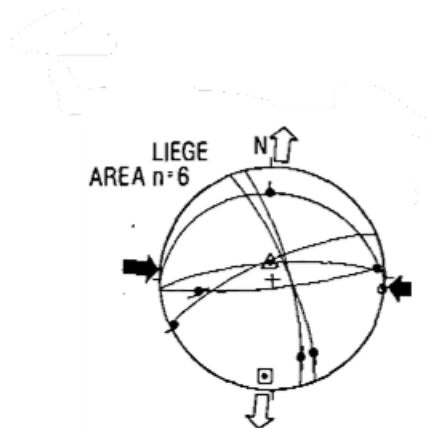


Figure 3.5: Current day Stress tensor measured in the Liège-Gulpen area from Delvaux (1997)

3.3 Geological features

3.3.1 Joint sets

The study area is dominated by two subvertical joint sets oriented NNE-SSW and ESE-WNW (Delvaux, 1997; Mathieu, 1962; Passagez, 2012). Both subvertical joint sets can be organized into fracture corridors (see section 3.3.5). In formations D and C, most joints are not bed-bounded (Van der Voet, 2022). The joints formed after the dolomitization process during the Paleozoic-Cretaceous extensional domain.

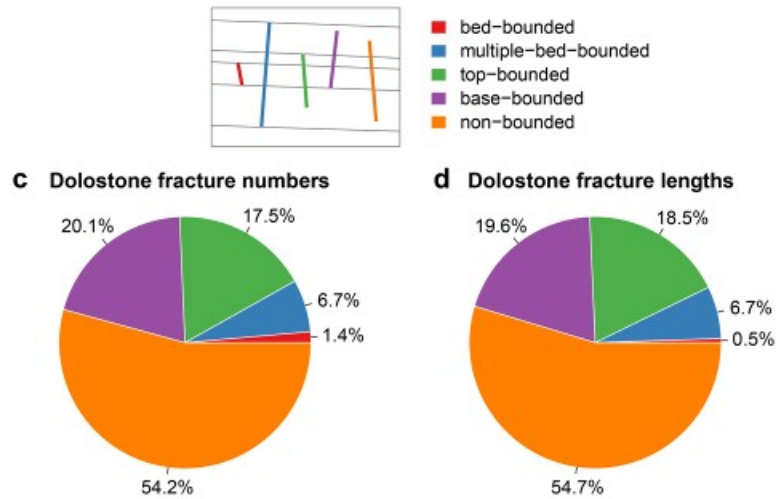


Figure 3.6: Figures (c) and (d) represent the percentage of fractures and the percentage of fracture length in each category, respectively (figure from Van der Voet (2022)).

3.3.2 Bedding planes

The bedding planes are not continuous due to dolomitization process, particularly in formations D and C (see figure 3.8). Based on descriptions and field observations from Mathieu (1962), formation D has larger bedding planes than formation C, and formation E has the smallest bed thickness. Formation D is particularly affected by dolomitization and has few continuous bedding planes across the entire formation. The top of formation D (Avins member) has no continuous bedding plane for over 10 meters. The bottom of formation D, Lhoist terminology D0, has no continuous bedding plane for 7-8 meters as seen on figure 3.8.

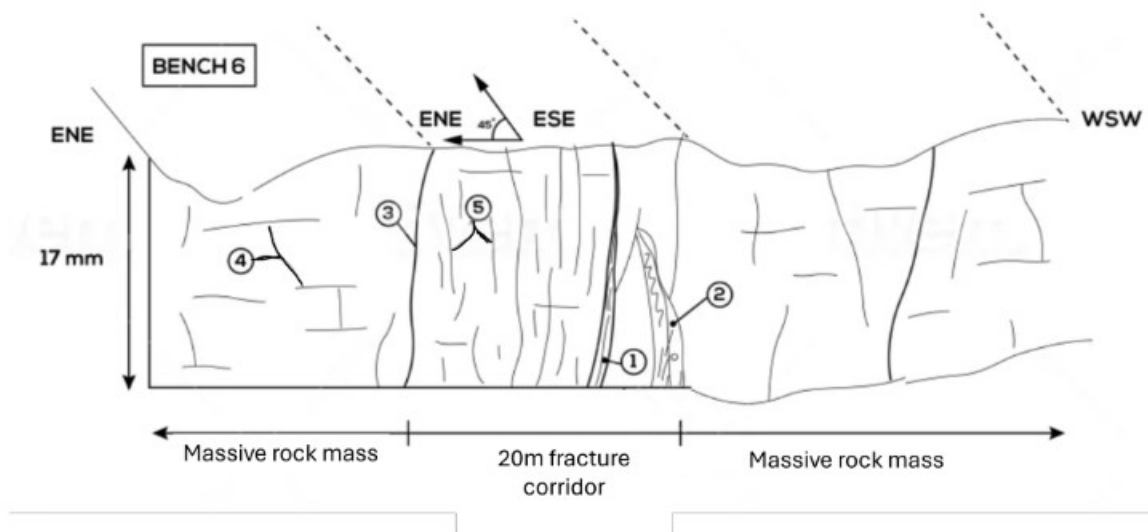


Figure 3.7: Sketch of a fracture corridor with geological features associated to fracture corridors in the MLD quarry.

Table 3.2: Geological features displayed on figure 3.7

Number	Geological feature
1	Dissolution joint filled with orange silty clay 10cm thick.
2	Karstic void 0.7-1m wide.
3	Dissolution joint across entire bench height. Rough undulating joint with gouge as infill.
4	Non-continuous bedding planes in formation D
5	Joints inside fracture corridor filled with a thin layer (1-5mm) of dolomitic sand.

3.3.3 Small karstic voids

Small karstic voids are occasionally encountered in the quarry and are often associated with other geological structures such as fracture corridors and faults related to karsts (see section 3.3.8). Moreover, two stratigraphic locations (Joint P and Joint F) are more susceptible to the development of karstic voids within the geological framework. The voids associated with stratigraphic joint P exhibit varying dimensions, with widths and heights both ranging from 0.5 to 2 meters, and are filled with silty clay. Small karstic voids are occasionally found at the top of the Engihoul formation, just below stratigraphic joint F (see figure 3.8) (Poty, n.d.).

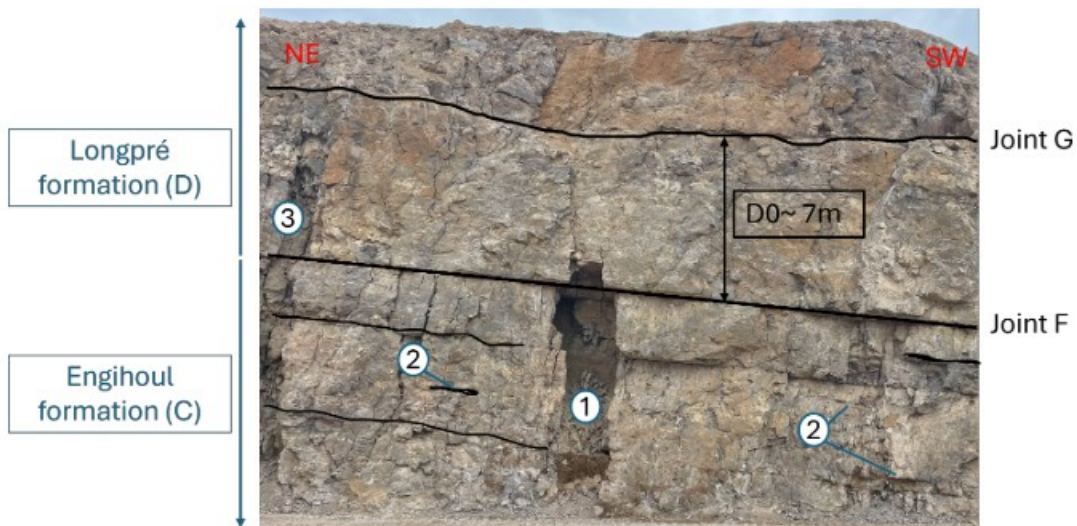


Figure 3.8: Bench 7, stratigraphic joint F delimiting formation C and D. 1) Typical Karstic void for the study area 6m by 1.5m. 2) Non-continuous bedding planes in formation C. 3) Small fracture corridor across formation D and C. D0, Lhoist terminology for bottom of Longpré formation.

3.3.4 Dissolution joints

Dissolution joints can be observed in the quarry and in the surrounding galleries. Most dissolution joints are observed above the water table ($z=75$). Quantification on the frequency of dissolution joints will be provided during this thesis. Most dissolution joints are smaller than 10cm wide, but some can be 2 meters wide or more. This can be the case for dissolution joints related to minor faults (see section 3.3.8).



Figure 3.9: Dissolution joints found in the iron shafts near the quarry. Both are found in formation D.

3.3.5 Fracture corridors

The two main subvertical joint sets in the area contain zones characterized by a high concentration of joints compared to the surrounding rock, the zones are referred to as fracture corridors. These corridors often coincide with rock mass alterations, and the joints within them are commonly filled with silty-clays or dolomitic sand (see figure 3.10). The corridors associated to the subvertical joints striking ENE have widths of 25 meters or less. Corridors striking ESE-WNW can be larger (up to 50m) and are often highly affected by rock alteration. Karstic voids and dissolution joints are often associated to the ESE-WNW striking fracture corridor along with iron deposition (see section 3.3.8).

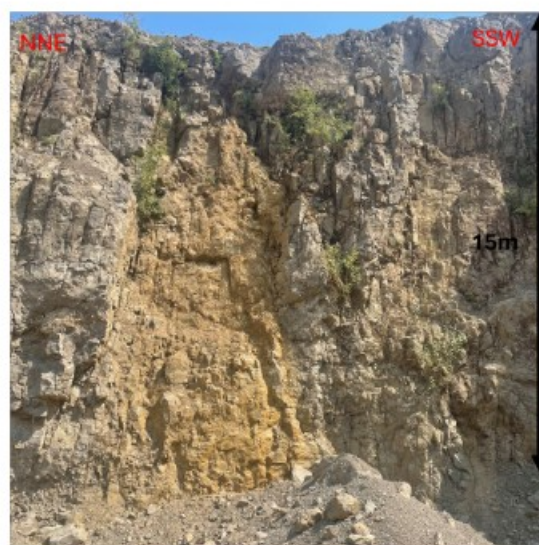


Figure 3.10: Fracture corridor with similar strike as the J2 set with background joints with dolomitic sand as infill



3.3.7 Faults

Minor faults with displacements of less than 2 meters have been identified during field investigations. The nature of the faults (reverse, normal or strike-slip) is difficult to determine due to noncontinuous bedding planes, alteration and the subvertical nature of the faults. Both Passagez (2012) and Mathieu (1962) have described observations of faults in the quarry. Some faults are also associated to Iron deposition (see section 3.3.8). Small ramp faults systems have also been occasionally found on the upper benches of the quarry (Bench 4 and above).

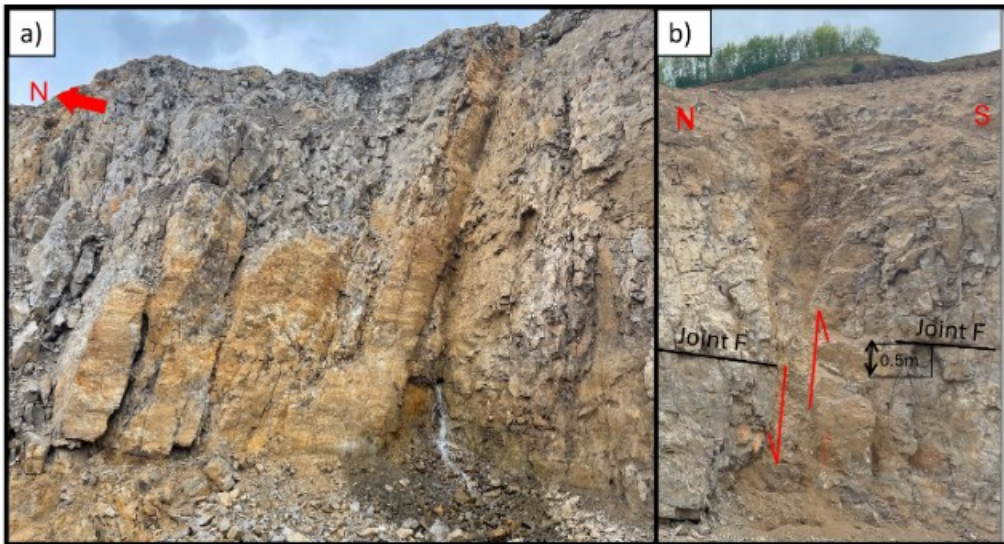


Figure 3.12: a) Slickensided surface with similar orientation as the J2 set on bench 8 acting as preferential water flow path. b) Fault on bench 7 oriented E-W probably dating to the Hercynian orogeny.

3.3.8 Iron- fault related karst

In the vicinity of the quarry, 4-5 ESE and SE (strike direction) subvertical veins have been exploited (Dejonghe, 2010a). Perpendicular to those veins, smaller karstic joints have also been exploited at the base of the Visean Dolomite (Dejonghe, 2010b). In the quarry and in former iron ore shafts belonging to Lhoist, similar-oriented karsts and iron veins have been found. The size of the iron veins ranges from centimeters to 3 meters in width, according to Dejonghe (2010b); this is consistent with our findings. It is possible to observe a 2 meter wide vein that has been exploited in the St-Barbe gallery on figure 3.13.



found in faults striking E-W, WNW-ESE and most likely date back from the Jurassic-Cretaceous extensional domains (Dejonghe, 2010a). Some geological cross-sections, similar subvertical zones have been described as "damaged terrain". Such a zone can be observed in figure 3.15.

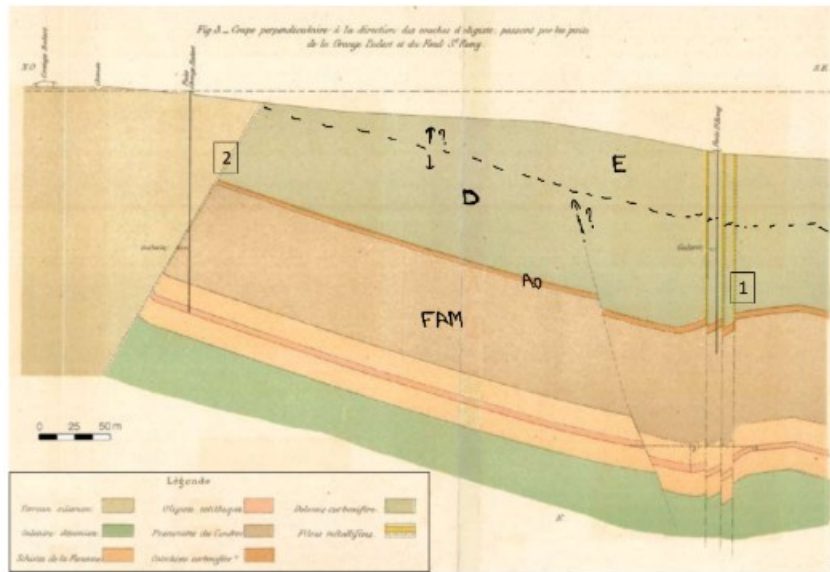


Figure 3.14: Iron ore concession of Landenne. 1) series of small, undetermined faults resulting in iron veins 2) Landenne Fault (Firket, 1878)

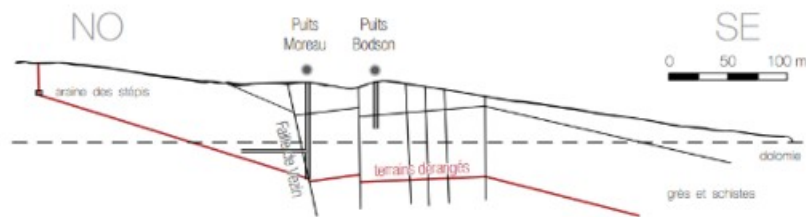


Figure 3.15: Cross-section of former Iron ore deposits mentioning "Damaged terrain" (Dejonghe, 2010b)

During the Jurassic and at the start of the Cretaceous, hydrothermal fluids that went through faults and open fractures mobilised dissolved iron from the Givetian-Frasnian formations to the Carboniferous carbonate rock deposit (Dejonghe, 2010b). Subsequently, iron, zinc, sulfur, and other minerals precipitated to form mineral ore veins. Iron sulfides were the most common minerals to precipitate, but galena and other minerals also formed in the region (Denayer et al., 2010). The iron ore veins date back to no later than the Cretaceous due to the lack of iron present in later sedimentary deposits from the Cenozoic (Dejonghe, 2010b; Denayer et al., 2010). Subsequently, meteoric water intrusion dissolved the iron sulphides to goethite when oxidized. This caused the water to be acidic, favoring chemical alteration (Denayer et al., 2010). This created so-called 'Iron-hats', the rocks exposed to oxygen have been altered over a wider area, and the width of the karstic zone decreases with depth. The karsts should decrease in width below the water table (Denayer et al., 2010).

4 Background information and methodology data collection

This section will elaborate on essential terminology pertinent to the study, including background-structural joints and weakness zones. Additionally, the section will detail the methodologies employed to collect quantitative datasets on the joint parameters, ensuring a thorough understanding of the technical approaches and procedures involved.

The data requirements for this study are classified into four main categories, as shown in table 4.1. Each category consists of different parameters or datasets that will be used for rock mass classification systems, geotechnical and DFN modelling. Data on joint characteristics were also collected from diverse sources, including rock core descriptions, field investigations, and photogrammetry models as seen on figure 4.1.

Table 4.1: Joint characteristics collected during field study

Category	Parameter	Unit	RMR	Q	DFN
A. Joint orientation	Dip angle- Dip direction	[-]	B	-	Yes
	Number of joint sets	[-]	-	Jn	-
B. Joint intensity	Joint spacing	m	A2	-	Yes
	RQD	%	A3	RQD	-
	P10	[joints/m]	-	-	Yes
	P21	[m/m ²]	-	-	Yes
C. Joint Shape	Joint size (Length and persistence)	rating — [m]	A4a	-	Yes
	Joint aperture	[mm]	A4b	-	Yes
D. Joint Condition	Joint roughness	rating	A4c	Jr	-
	Joint alteration (infill)	rating	A4e	Ja	-

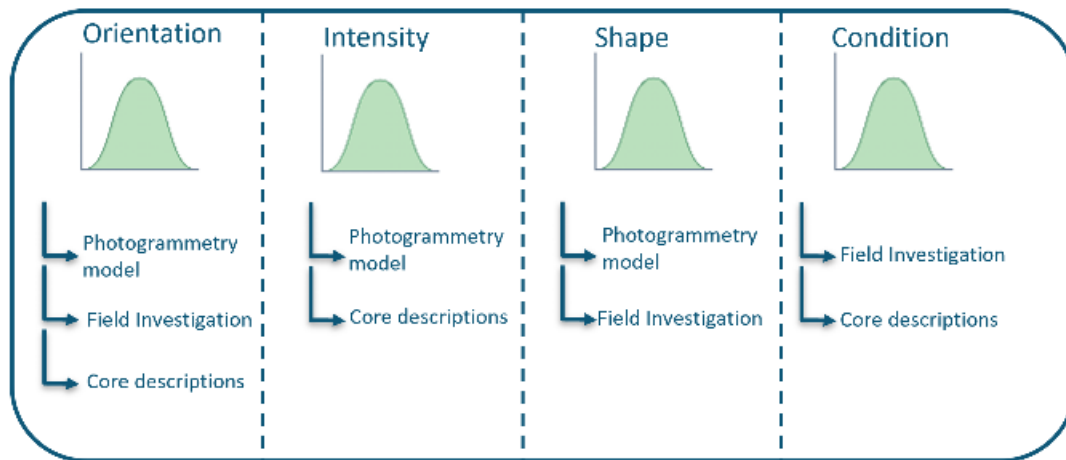


Figure 4.1: The datasets gathered for joint characterization originate from various sources.

4.1 Background definitions

4.1.1 Structural and background joints

In this study, joint sets are determined based on joint orientation data and joint shape to address censorship issues arising when some joint heights exceed the extents of the quarry benches, as illustrated in figure 4.2. This causes truncation problems where the true joint height distribution cannot be defined (Bisdorn, 2011). To solve this problem the concept of structural joint is introduced in this study. Structural joints are based on the definition of Esterhuizen et al. (2011),

bottom or the top of the bench, as illustrated in figure 4.2. In such instances, joints truncated by the bench but extending across at least 6 meters are considered structural joints. This classification approach is designed to prevent the overestimation of structural joints by not including every joint that is bound by either the bench's bottom or top.

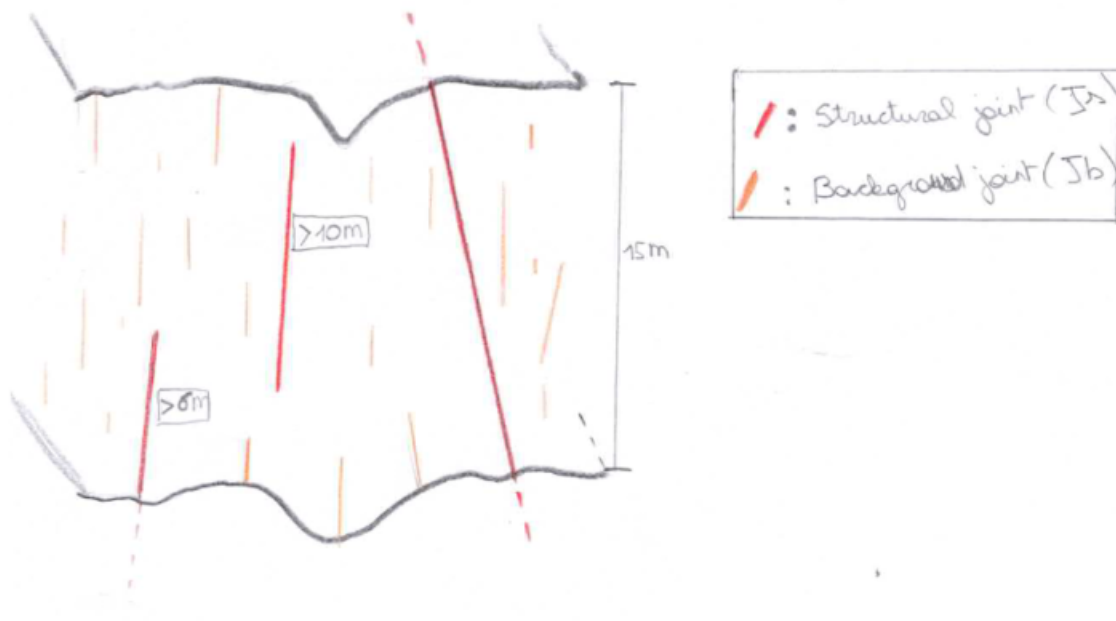


Figure 4.2: Structural joints and background joints definition during this case study

4.1.2 Weakness zones and joints

A differentiation is made between joints and weakness zones. All discontinuities in the rock mass that have an aperture smaller than 10cm will be considered as joints, apertures larger than 10cm will be considered weakness zones. This follows the guidelines from the NGI (2015).

4.2 Joint condition ratings from the rock mass classification systems

The joint condition is determined by two primary components, the joint roughness and joint alteration (Barton, 1978). The assessment of joint alteration and roughness ratings follows the rating systems outlined by Bieniawski (1989) and NGI (2015). The ratings for the joint condition for both classification methods are determined through the specified methodologies:

- Joint Roughness rating:
The joint roughness estimates are based on the descriptive term methodology in accordance with ISRM standards (Barton, 1978).
- Joint alteration (Weathering, infill, aperture):
Weathering grade and joint infill estimates using rough quantitative descriptions as per ISRM standards (Barton, 1978). The ISRM recommends conducting laboratory tests to examine the mineralogy and swelling of the joint infill. However, no samples of the joint infill material were obtained for testing. The granulometry and swelling of the joint infill have been estimated using stickiness, taste, and graininess tests, following the method described by ministry of environment (1998).

The ratings of the RMR and Q system related to the joint condition (alteration and roughness) is provided in the tables below. The complete ratings system for both rock mass classification systems is found in Appendix E.

Table 4.2: Joint roughness rating (Jr) for the Q system with the 7 categories of joint roughness

Joint Roughness Number		Jr
a) Rock wall contact, and		
b) Rock-wall contact before 10 cm of shear movement		
A	Discontinuous joints	4
B	Rough or irregular, planar	3
C	Smooth, undulating	2
D	Slickensided, undulating	1.5
E	Rough or irregular, planar	1.5
F	Smooth, planar	1
G	Slickensided, planar	0.5
c) No rock wall contact when sheared		
H	No wall contact after 10 cm of shear	1

Table 4.3: Qualitative descriptions for the Joint alteration ratings (Ja) included in the Q system (NGI, 2015)

Joint alteration Number (Ja)		ϕ_{approx} [degrees]	Ja
a) Rock-wall contact (no mineral fillings, only coatings)			
A	Tightly healed, hard, non-softening, impermeable filling, i.e., quartz or epidote		0.75
B	Unaltered joint walls, surface staining only.	25-35	1
C	Slightly altered joint walls. Non-softening mineral coatings; sandy particles, clay-free disintegrated rock, etc.	25-30	2
D	Silty or sandy clay coatings, small clay fraction (non-softening)	20-25	3
E	Softening or low friction clay mineral coatings, i.e., kaolinite or mica.	8-16	4
b) Rock-wall contact before 10 cm shear (thin mineral fillings)			
F	Sandy particles, clay-free disintegrated rock, etc	25-30	4
G	Strongly over-consolidated, non-softening, clay mineral fillings (continuous, but <5mm thickness).	16-24	6
H	Medium or low over-consolidation, softening, clay mineral fillings (continuous, but <5mm thickness).	12-16	8
J	Swelling-clay fillings, i.e., montmorillonite (continuous, but <5 mm thickness). Value of Ja depends on percent of swelling clay	6-12	8-12
c) No rock-wall contact when sheared (thick mineral fillings)			
K	Zones or bands of disintegrated or crushed rock. Strongly overconsolidated.	16-24	6
L	Zones or bands of clay, disintegrated or crushed rock. Medium to low over-consolidated or softening fillings	12-16	8
M	Zones or bands of clay, disintegrated or crushed rock. Swelling clay, Ja depends on percent swelling clay-size particle	6-12	8-12
N	Thick continuous zones or bands of clay. Strongly over-consolidated	12-16	10
O	Thick, continuous zones or bands of clay. Medium to low over-consolidation	12-16	13
P	Thick, continuous zones or bands with clay. Swelling clay. Ja depends on percent of swelling clay	6-12	13-30

Table 4.4: Joint condition rating for the RMR system (A4 rating). Ratings A4b, A4d, and A4e pertain to the joint alteration and rating A4c pertain to the roughness.

Condition of discontinuity	Very rough surfaces Not continuous No separation Unweathered wall rock	Slightly rough surfaces Separation <1mm Highly weathered walls	Slightly rough surfaces Separation <1mm Highly weathered walls	Slickensided surfaces or Gouge <5mm thick or Separation 1-5mm continuous	Soft gouge >5mm thick or Separation >5mm Continuous
Rating- A4	30	25	20	10	0
Guidelines for classification of discontinuity					
A4a -persistence rating	<1m 6	1 to 3m 4	3 to 10m 2	10 to20m 1	>20m 0
A4b- Separation rating	None 6	<0.1mm 5	0.1-1mm 4	1-5mm 1	>5mm 0
A4c- Roughness rating	Very rough 6	Rough 5	Slightly rough 3	Smooth 1	Slickensided 0
A4d- Infill rating	Non 6	Hard infilling <5mm 4	Hard filling >5mm 2	Soft infill <5mm 2	Soft infilling >5mm 0
A4e- Weathering rating	Unweathered 6	Slightly weathered 5	Moderately weathered 3	Highly weathered 1	Decomposed 0

4.3 Photogrammetry model data collection

An unmanned aerial vehicle (UAV), was utilized to capture aerial photographs of quarry benches. These images were then used to create a 3D photogrammetric model using Agisoft Metashape software (2022). According to ISRM standards, photogrammetry models are utilized to systematically collect quantitative data on joint properties (Barton, 1978). Fractures within the model are traced using the trace polyline tool in CloudCompare and are stored in separate folders organized by set. The joint sets are determined based on orientation data and joint geometry as discussed in section 4.1. The tracing of fractures is carried out on rectangular windows, referred to as scan-windows (SW), on relatively flat outcrops measuring 16 meters in height. An example of such a scan-window, SW13 (scan-window 13), is depicted in figure 4.3.

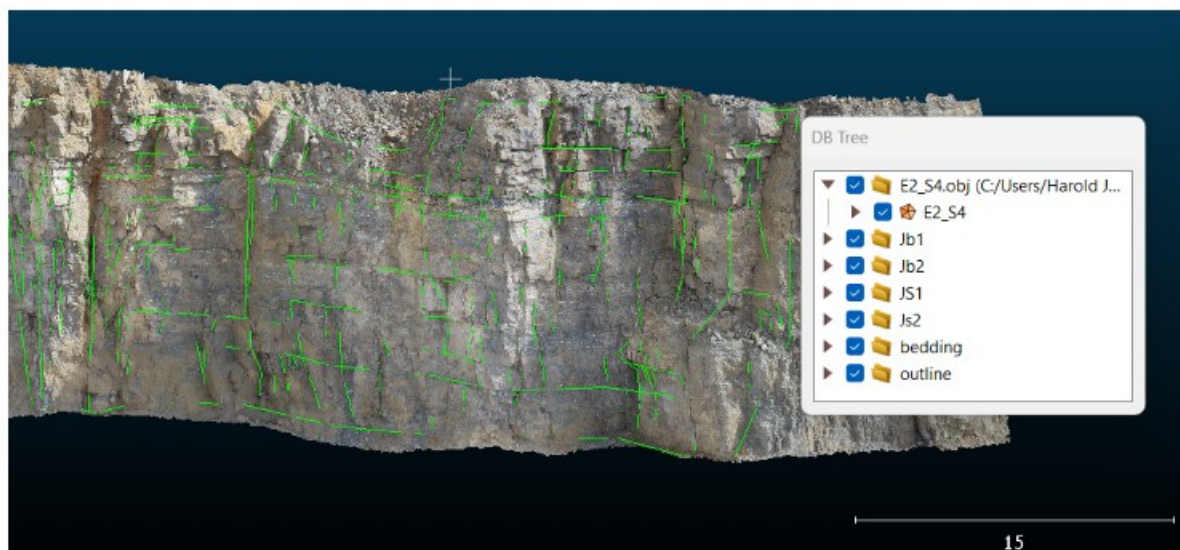


Figure 4.3: Example of scan-window SW13. Not all the joints appear to be traced; the polylines are sometimes hidden behind the photogrammetry surface.

The fracture traces are saved as .dxf file by set. A Python code developed for this study reads each .dxf file and orthogonally projects the fractures on a 2D plane parallel to the z-axis. An example of the projected fractures on the 2D plane can be observed in figure 4.4. Virtual boreholes (VB) are horizontally traced each 0.5 meters across the scan-windows (figure 4.4).

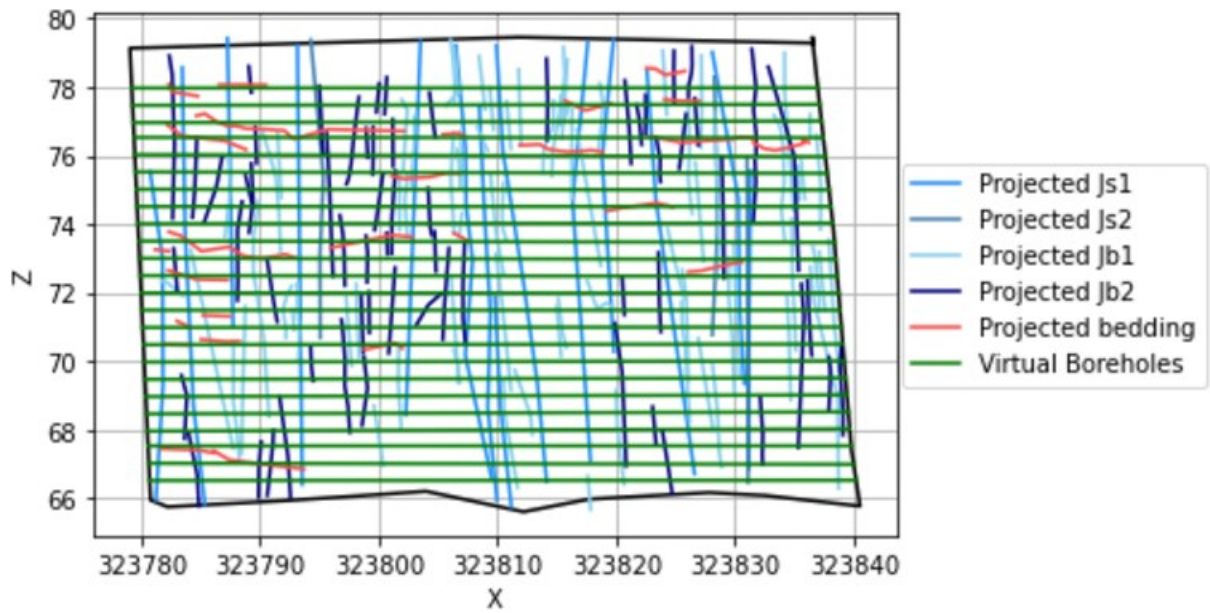


Figure 4.4: Example of 2D projected joints for scan-window 3 (SW3)

Data on joint shape and intensity were collected from fracture traces, scan-windows, and virtual boreholes within each scan-window. Appendix B includes a Python script and a comprehensive guide for tracing fractures in CloudCompare and executing the Python code. This script aids in analyzing and processing the collected data, allowing for a detailed examination of the joint properties across different sections of the quarry.

4.3.1 Joint orientation

Orientation data was collected from the photogrammetry model using Cloudcompare's Compass plugin. This plugin can be used on the failure surface of a joint to estimate the dip angle and direction by best-fitting a plane through the point cloud (Thiele et al., 2017). Appendix B provides a detailed description on how to use the Compass plugin in Cloudcompare.

4.3.2 Joint Intensity

A number of studies have collected joint datasets on outcrops or from borehole rock cores. Most studies focus on properties such as fracture density and intensity, but various authors apply different labels to these definitions. In this study we will refer to the generic term joint intensity to refer to the P10, P21 or P32 (Dershowitz, 1984; Nahli, Oryzavica, & Radityo, 2017). Only P10, P21 and P32 joint intensity datasets will be collected and used during this study.

		Dimension of Feature			
		0 number	1 length	2 area	3 volume
Dimension of Sampling Region	1 line	P ₁₀ 1-D frequency fracture intensity	P ₁₁ Dimensionless intensity		
	2 area	P ₂₀ 2-D frequency	P ₂₁ Fracture intensity	P ₂₂ Dimensionless intensity	
	3 Volume	P ₃₀ 3-D frequency		P ₃₂ Fracture intensity	P ₃₃ Dimensionless intensity

Figure 4.5: Joint intensity definitions used in this study (figure (Nahli et al., 2017))

4.3.3 Joint intensity - VB-P10

The virtual boreholes were used to measure the P10 joint intensity (VB-P10) for structural and background joints within each orientation set. The VB-P10 data is corrected for orientation bias using Terzaghi corrections. This method corrects for the sampling bias that occurs due to the orientation of joints relative to the virtual borehole orientation. Terzaghi's correction is outlined in the equation:

$$P_{10} = \frac{P_{10_0}}{\sin(\alpha)} \quad (1)$$

Where:

P_{10} : True joint intensity

P_{10_0} : Uncorrected

α : Angle between average joint strike and Scan Window strike.

Joint Spacing

The virtual boreholes are used to compute the fracture spacing by joint set. Orientation correction was also used to have the true fracture spacing per joint set using equation 2 as per ISRM standards (Barton, 1978).

$$S = d * \sin(\alpha) \quad (2)$$

Where:

S: True fracture spacing

d: Distance between fractures

α : Angle between average joint strike and scanline strike.

4.3.4 Joint intensity- SL-P10

Scan-Lines (SL), which traced only structural joints, encompassed larger sections of virtual outcrops compared to Scan-Windows. Based on the SL, joint intensity data of structural joints (SL-P10) can be determined for sections of outcrop exhibiting similar joint intensities. The SL-P10 is determined by joint set (only for structural joints). To address the orientation bias of the P10 joint intensity, Terzaghi correction are applied.

4.4 Borehole core descriptions

Borehole rock cores were available for this study. Additionally, an optic scan was available for 85m of one of the boreholes (borehole 172). The contractor, DMT, managed both the interpretation of the fractures and the optic scan (DMT, 2019). Core descriptions were performed using the data collection method of geotechnical consultant Geocos. This method, known as RMR geocos (Lhoist, personal communication), is used to estimate the Q system and RMR rating from borehole rock cores. In order to collect the data, geotechnical sections with similar joints, recovery, and rock strength are defined. In those geotechnical sections, the data collected consisted of:

1. Joint intensity: Rock Quality Designation (RQD), recovery rate, and counting the number of joints.
2. Joint condition ratings for RMR and Q system.

Data on joint condition and joint counts were collected only when the core recovery was good enough to allow for a geotechnical description. The joints were categorized into three categories based on their dip relative to the axis of the rock core. To prevent confusion with orientation-based joint sets, the term "joint category" is used instead of "joint sets."

Table 4.5: Joint categories used during geotechnical core logging

Joint class	Angle relative to core axis
1	60-90 degrees
2	30-60 degrees
3	0-30 degrees

4.4.1 Induced fractures

During borehole core descriptions, Lhoist geologists instructed to count every fracture that could not be defined with 100 % certainty as an induced fracture (Lhoist, personal communication). This is a conservative counting method and leads to a high number of induced fractures counted as natural fractures. Counting induced fractures gives erroneous RQD and P10 values due to overestimating the number of fractures in the rock material (NGI, 2015). To mitigate the oversampling of fractures, the joints observed from an optic scan will be compared to the joints counted on the same rock core interval. The comparative analysis will be utilized to calculate the percentage of overcounted joints per category.

4.4.2 Joint intensity (RQD and BH-P10)

The RQD and recovery were measured in accordance with ISRM standards (Barton, 1978). The joints were classified in their respective categories by characterizing their dip angle. The number of joints per category was also counted per geotechnical section. The geotechnical sections were defined based on rock core sections with similar joint conditions and RQD in accordance with the ISRM and the works of Bieniawski (1989) (Barton, 1978). Using the length measured from each section and the number of joints counted, borehole P10 (BH-P10) data can be computed. The BH-P10 are also corrected for orientation bias using Terzaghi corrections, as outlined in the equation:

$$BH-P10 = \frac{BH-P10'}{\cos(\alpha)} \quad (3)$$

Where:

BH-P10 : Joint intensity corrected for sampling bias.

BH-P10' : Joint intensity without Terzaghi correction

α : Angle between the borehole and the normal of the joint set.

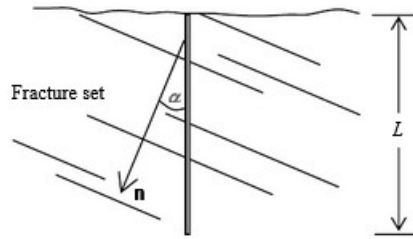


Figure 4.6: Sampling bias due to joint orientation angle between the normal of the joints and the borehole α (Figure from Wang and Mauldon (2006))

4.4.3 Joint condition

The datasets for joint alteration and roughness were collected using the methodology outlined in section 4.2. Joint condition ratings for the RMR and Q systems are only provided for the worst joint condition per geotechnical borehole section.

4.5 Field Investigation

Data was collected in a field investigation both in the quarry and in-situ. Two datasets were collected in the field: the joint orientations and the joint condition (joint alteration and roughness)



Figure 4.7: Dolomeuse Gallery, 1.5m wide. The shafts have been excavated at a pace of 1-3m a day (Pacyna & Denayer, 2010)

4.5.1 Orientation data

The joint orientation was measured in the field using a book and the FieldMOVE Clino app. The ISRM standards call for the use of a compass (Barton, 1978); the features of the FieldMOVE Clino app may be considered similar to those of a compass (Barton, 1978; Petex, n.d.).

4.5.2 Joint condition

The datasets for joint alteration and roughness were collected in the field using the methodology outlined in section 4.2. Field statistics on individual joint conditions were collected at locations where a photogrammetry model was available. The position of each joint was recorded. In the field, joint descriptions primarily focused on structural aspects due to their importance.

5 Results

This section focuses on analyzing and presenting quantitative data related to joint characteristics. It will establish statistical distributions for joint parameters by utilizing the collected quantitative datasets.

5.1 Joint Orientation

Joint sets will be defined based on the contouring of the orientation data (Takako, Elmo, & Rogers, 2018). The joint orientations are imported into the Stereonet software (Allmendinger, 2023). Kamb contour plots are generated in Stereonet to graphically display joint cluster.

In total, 591 joints have been measured using borehole optic scan data, a photogrammetry data, and field data. The stereoplots of each dataset can be observed on figure 5.1. Two subvertical joints with dip directions ed NNE-SSW and ESE-WNW and the subhorizontal bedding plane are the main orientation sets observed in the area. When measuring joints on the photogrammetry model, sub-horizontal joints could not be measured (fig 5.1 (a)). Joint orientations measurements on the photogrammetry model are only feasible along sub-vertical joints where blasting favored failure along sub-vertical discontinuities. The sub-vertical joints assessed in the field exhibit greater variability than the orientation dataset measured on the photogrammetry model (see fig. 5.1 (b)). The greater variability in the sub-vertical joint orientations might be due to measurement errors, joints were measured from a distance due to safety requirements. In total, three joints sets were measured from field data, two sub-vertical sets analogue to those measured on the photogrammetry model and a third sub-horizontal set (bedding planes).

The orientation of the 89 joint from the optic scan was also available. The same subvertical joint sets can be observed in figure 5.1 (c). The boreholes were drilled parallel to the subvertical joints. This causes sampling biases when plotting figure 5.1 (c) and explains the relative prominence of sub-horizontal joints on the figure.

Three joint sets can be determined: the bedding planes and two orthogonal sets of sub-vertical joints. Mathieu (1962); Van der Voet (2022) have also recognized the same two subvertical joint sets.

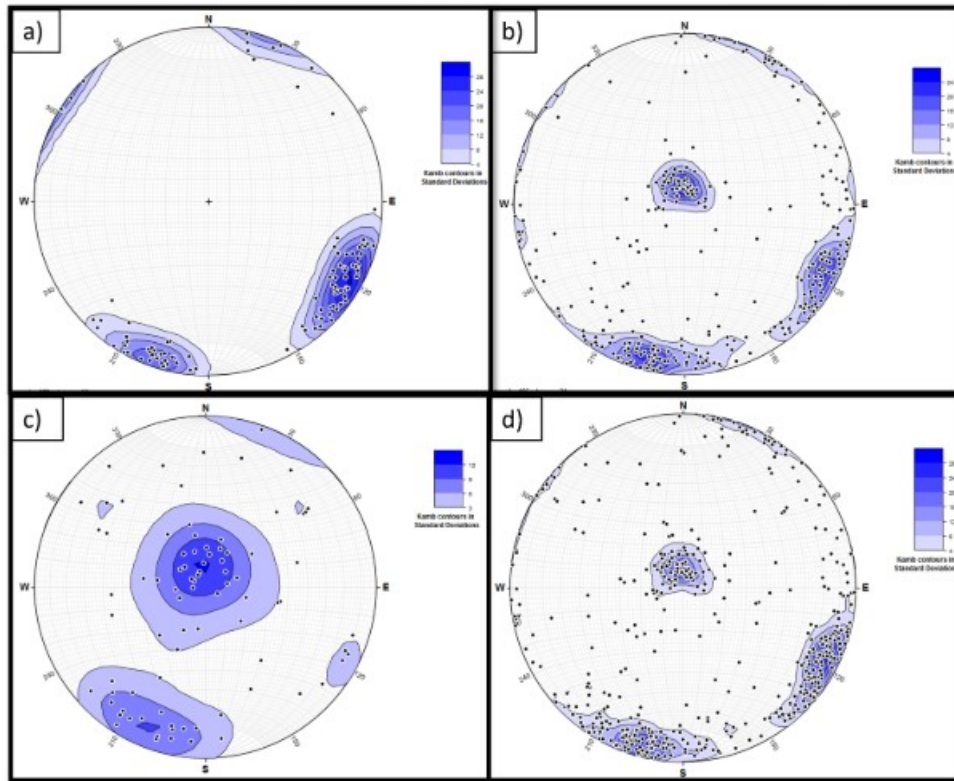


Figure 5.1: (a) Stereonet of the poles from the photogrammetry dataset. (b) Stereonet of the orientation poles from the field dataset. (c) Stereonet of the poles from borehole optic scan dataset. (d) Stereonet combining all datasets.

Two subvertical joint sets, named J1 and J2 are defined based on the orientation data of subvertical sets collected on the photogrammetry model. The range of dip directions was selected from the contour plot based on the photogrammetry orientation dataset (fig 5.1 (a)); because, this dataset was acquired with more consistency. The Fisher method is the statistical approach used to generate orientation data in Discrete Fracture Network (DFN) models in this study. The fisher K coefficient has been computed using a python script using the python library mpl.stereonet.

Table 5.1: Orientation parameters for Joint set 1 and Joint set 2

Parameter/ Joint	J1	J2
N	178	198
Min dip direction	280	355
Max dip direction	325	45
Mean dip direction	301	19
Mean dip angle	80	80
Fisher kappa	45	35

The J1 and J2 joint sets are further divided into sub-sets based on the joint shape (see section 4.1). A diagram shows the four possible joint set terminology used in this study (see figure 5.2).

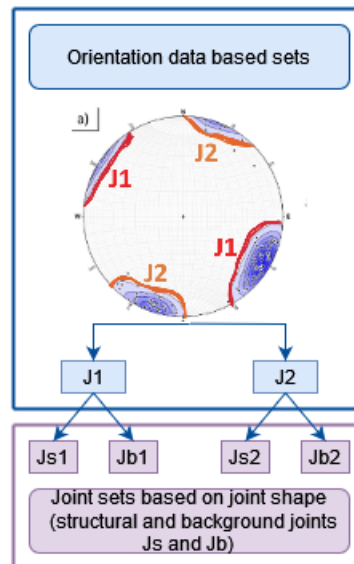


Figure 5.2: Two sub-vertical orientation sets (J1 and J2) subdivided in background and structural joints based on joint condition and shape

5.2 Joint intensity

The SW-P21, VB-P10 and fracture spacing have been measured independently per joint set. The BH-P10 dataset does not take into account the joint intensity by set because of unoriented rock cores. The subvertical joint sets can be recognized on the cores because of the dip angle relative to the core axis.

5.2.1 SW-P21

Fracture inside 13 scan-windows were traced on Cloudcompare, the fracture traces were used to obtain P21 data.

Table 5.2: P21 for the 13 scan-windows and SW from Van der Voet (2022). P21 have not been corrected for orientation

SW I.D.	Area [m ²]	P21- Js1	P21- Js2	P21- Jb1	P21- Jb2	P21- bedding	P21- Total
SW1	406	0.24	0.00	0.52	0.00	0.00	0.75
SW2	244	0.13	0.00	0.69	0.00	0.00	0.83
SW3	783	0.20	0.03	0.25	0.17	0.16	0.81
SW4	577	0.00	0.13	0.00	0.36	0.08	0.57
SW5	601	0.00	0.11	0.00	0.40	0.12	0.62
SW6	368	0.00	0.33	0.00	0.95	0.07	1.35
SW7*	522	0.09	0.06	0.00	0.00	0.48	0.63
SW8	339	0.19	0.15	0.38	0.30	0.41	1.43
SW9	121	0.00	0.18	0.00	0.47	0.34	0.99
SW10	185	0.00	0.15	0.00	0.31	0.17	0.64
SW11	196	0.35	0.00	0.47	0.00	0.13	0.94
SW12	302	0.09	0.11	0.37	0.32	0.07	0.97
SW13	381	0.30	0.00	0.31	0.00	0.00	0.60
SW_EV1	2199	Na	Na	Na	Na	Na	0.83
SW_EV2	919	Na	Na	Na	Na	Na	0.73
SW_EV3	820	Na	Na	Na	Na	Na	0.62
SW_EV4	709	Na	Na	Na	Na	Na	0.97

Table 5.3: Location and geometry of each SW

SW I.D.	Formation	Orientation	Length [m]	Area [m ²]	Bench	X	Y	Z
SW1	D	100	25	406	6	193925.05	130323.48	68
SW2	D	85	14	244	6	193946.93	130323.6	68
SW3	D	84	51	783	6	193936.34	130320.08	68
SW4	D	48	32	577	6	193974.54	130330.33	68
SW5	D	47	25	601	4	194232.31	130350.83	97
SW6	D	37	23	368	4	194168.793	130319.544	97
SW7	E	79	68	522	2	194179.721	130254.785	135.5
SW8	E	84	51	339	2	194353.861	130329.103	136
SW9	D/C	37	12	121	7	194178.9	130486.196	56
SW10	C	37	19	185	7	194152.34	130442.5	56
SW11	D	107	12	196	6	194051.27	130354.43	68
SW12	D	73	17	302	6	194111.85	130369.67	68
SW13	D	133	24	381	4	194518.81	130726.58	97
SW.EV1	D	80	210	2199	6	193915.55	130324.89	68
SW.EV2	D/C	35	100	919	7	194193.62	130518.19	56
SW.EV3	C	35	88	820	7	194267.86	130627.99	56
SW.EV4	C	35	80	709	8	194181.67	130580.2	45

5.2.2 VB-P10

Table 5.4: P10 fracture intensity per joint set corrected for orientation measured using virtual boreholes on the scan-windows (VB-P10)

Scan-window	VB-P10: Js1	VB-P10: Jb1	VB-P10: Js2	VB-P10: Jb2	VB-P10: Tot
SW1	0.27	0.34	0.00	0.00	0.61
SW2	0.17	0.81	0.00	0.00	0.98
SW3	0.24	0.30	0.10	0.48	1.12
SW4	0.00	0.00	0.16	0.43	0.59
SW5	0.00	0.00	0.15	0.48	0.63
SW6	0.00	0.00	0.33	0.95	1.28
SW7*	0.14	0.00	0.11	0.00	0.25
SW8	0.30	0.63	0.15	0.60	1.68
SW9	0.00	0.00	0.20	0.49	0.69
SW10	0.00	0.00	0.17	0.37	0.54
SW11	0.54	0.66	0.00	0.00	1.21
SW12	0.14	0.56	0.29	0.66	1.64
SW13	0.34	0.37	0.00	0.00	0.71

5.2.3 SL-P10

The SL-P10 only collected joint intensity data on the structural joints Js1 and Js2. Statistics on the Js joints have been collected on 1.2km of scanlines. The scanlines and the structural joints mapped in the quarry can be observed on figure 5.3. The large scanlines are broken down into sections with statistically similar joint condition. A single point data on each location is collected. The SL-P10 results are given in table 5.5.



Figure 5.3: Example of scanlines, the SL-P10 values are found in table 5.5

Table 5.5: results for the SL-P10 data

Scanline	P10-Js1	P10-Js2	X	Y	Z	Formation	Domain
SL_1	0.30	0.29	641100.06	5594140.11	64.5	D	S2a
SL_2		0.25	641059.86	5594124.35	64.5	D	S2a
SL_3	0.21	0.14	641022.81	5594114.52	64.5	D	S2a
SL_4	0.23	0.12	641001.26	5594114.45	64.5	D	S2a
SL_5	0.19	0.077	640864.53	5594090.71	64.5	D	S2a
SL_6		0.15	640775.9	5594078.6	64.5	D	S2a
SL_7	0.32	0.17	640679.5	5593983.1	82	D	S2a
SL_8		0.46	640606.99	5593881.77	100	D	S2a
SL_9	0.25		641338.6	5594480.7	39	C	S2b
SL_10	0.29	0.09	641069.29	5594081.83	97	D	S2a
SL_11	0.21	0.17	641005.58	5594065.63	97	D	S2a
SL_12	0.30	0.08	640914.4	5594066.73	82	D	S2a
SL_12.5	0.22	0.23	640849.91	5594060.98	82	D	S2a
SL_13		0.06	641271.7	5594374.01	39	C	S2b
SL_14		0.21	641217.96	5594311.44	39	C	F
SL_15		0.05	641194.3	5594283.67	39	C	S2b
SL_16		0.09	641607.25	5594457.6	97	D	S2a
SL_17		0.11	641582.09	5594415.17	97	D	S2a
SL_18		0.20	641523	5594339.1	97	D	S2a
SL_19		0.23	641368.55	5594190.41	97	D	F
SL_20		0.33	641348.11	5594163.54	97	D	F

5.2.4 BH-P10

Three fracture categories based on the dip angle relative to the core axis have been collected during rock core descriptions (see section 4.4). The number of induced fractures for each category was estimated by comparing the number of fractures interpreted on 80 meters of optic scan with the same 80 meters of rock cores available for BH172.

Table 5.6: Estimates of the % of induced fractures counted during fracture picking

Joint category	Angle to core axis	% of joints observed on optic scan and during core description.
1	60-90 deg	19%
2	30-60 deg	54%
3	0 - 30 deg	84%

The amount of category 2 and 3 joints was overestimated compared of to the interpreted joints on the borehole optic scan. In those categories, 54% and 84% of fractures counted during fracture picking are not observed on the borehole optic scan. Three reasons might explain the discrepancy between optic scan data and rock core description data:

1. The borehole optic scan may have been limited to interpreting only visible fractures; closed and incipient joints may not have been consistently detected due to resolution issues of the borehole optic scan. (Genter et al., 1997).
2. Fractures can develop during the drilling process due to various factors. Stress induced fractures originate from stresses related to the drilling activities, as discussed by Chatterjee and Mukherjee (2023). This can lead to the formation of petal or disc fractures. Petal fractures, which are easily recognizable, have been observed on the rock cores.
3. Human induced sub-horizontal fractures might occur as the drilling operator hammers the cores out of the drill casing or trims the core lengths to make sure they fit inside the core boxes. During the drilling of BH176, the operator was instructed to identify and mark all human induced fractures on several core boxes (Figure 5.4). Observations indicated that the majority of the sub-horizontal joints observed on the rock cores were of human induced origin.



Figure 5.4: Red boxes surround joints originating from hammer blows to retrieve cores from the casing or to fit the rock cores into core boxes. These human induced joints have been marked by the drilling operator.

The discrepancy between the category 1 joints observed on the rock cores and those detected by the optic scan is minimal compared to category 2 and 3 fractures (see table 5.6). 81% category 1 joints are both observable on the rock cores and on the optic scan.

Intensities of joints related to categories 2 and 3 were excluded from the analysis because they are difficult to estimate reliably from rock core descriptions. Most category 3 joints, which are sub-horizontal, are associated with bedding discontinuities and this will be addressed in section 5.2.5. Consequently, only BH-P10 of category 1 (subvertical joints) are considered, as they are more accurately estimated from core descriptions.

The mean dip angle (80 degrees) measured from the orientation data (section 5.1) was used for Terzaghi correction. The results of the P10 estimates from the rock core descriptions are provided in table 5.7



Figure 5.5: Fractures (red boxes) not interpreted on the borehole optic scan in formation E. Some display clear signs of surface staining. Black boxes are joints observed during core descriptions and observed on the optic scan.

Table 5.7: BH-P10 for each formation and BH, aggregate dataset (i.e. J1 and J2 combined in P10)

BH	Formation	Core recovery	P10 estimates
172	E	0.81	1.44
172	D	0.80	2.56
172	C	0.73	4.32
176	E	0.95	0.43
176	D	0.99	0.62
176	C	1.00	0.69
177	E	0.62	0.93
177	D	0.83	2.61
177	C	0.86	2.75
180	E	0.88	0.83
180	D	0.87	1.41
180	C	0.96	1.67
181	E	0.93	0.68
181	D	0.99	1.10
181	C	0.99	0.89

5.2.5 Bed thickness

The bed thickness was interpreted using measurement data from Mathieu (1962), core descriptions, and field observations. Mathieu (1962) defined the bed thickness of formations E, D, and C with detailed descriptions for each continuous bedding plane. Alongside these descriptions, non-continuous bedding planes are also mentioned. The bedding planes are least continuous in formation D. In the upper parts of formation D and the bottom part of formation D (referred to as D0 in Lhoist terminology), some stratigraphic sections lack continuous bedding planes for up to 5-10 meters (Lauwers, 2023; Mathieu, 1962).



Figure 5.6: Rock core samples indicate bedding thickness at least 1 meter thick for formation D.

Based on the descriptions of Mathieu (1962) and rock core descriptions, the average interpreted bed thickness is higher than the one estimated by Van der Voet (2022) for formations D and C, which was interpreted at 25cm. Van der Voet (2022) traced every bedding plane, including non-continuous bedding planes, across entire sections of outcrop (80 - 200 meter sections) to define the interpreted bed thickness. Using this methodology, she interpreted the average bed thickness to be 25 cm. It is possible that her findings reflect the average bed thickness of the initial bedding planes prior to dolomitization. However, this appears too conservative for design purposes, as the presence of incipient bedding planes every 25 cm is unlikely. Borehole cores longer than 25 cm were frequently retrieved, and even under drilling stresses, cores at least one meter in length were commonly obtained. The integrity of the dolomitized bedding planes as potential weak points for failure remains uncertain. However, the retrieval of large, over one-meter thick core samples may suggest that at least part of the dolomitized bedding planes may have significant cohesion.



Figure 5.7: Formation C in BH176, bed thickness including all sub-horizontal joints is around 70cm similar to Mathieu (1962) descriptions.

The continuous bed descriptions for formation C are smaller than for formation D. Based on rock core descriptions, the bed thickness interpreted including all sub-horizontal joints on figure 5.7 (11 in total) should be around 70cm. This disregards the induced sub-horizontal joints.

Formation E shows a significant difference in bed thickness compared to Formations D and C. Its bedding planes are less affected by dolomitization due to differing dolomitization processes between the Tournaisian and Visean formations (see Section 3.2.1).

Table 5.8: Table of the visual and interpreted bed thickness for formations D, C and E

Formation	Average continuous bedding plane (cm)	Average interpreted bed thickness with non-continuous bedding plane (cm)
E	20-35	20-35
D2 (above joint P)	400	150
D1 (below joint P)	250	100
C	70-100	50

5.2.6 Joint spacing

The joint spacing is calculated from the Virtual Boreholes. The true fracture spacing, i.e. fracture spacing corrected for orientation bias, is calculated according to ISRM standards (Barton, 1978). The average true joint spacing in fracture corridors is below 1m. Outcrops that did not include fracture corridors have higher joint spacing between 1.4 and 2.7 meter per joint set. Geological settings with fracture corridors typically exhibit exponential fracture spacing distributions (Olson, 2004). This is also the case for the study area, joint spacing exhibit a typical negative exponential distribution as seen on figure 5.8.

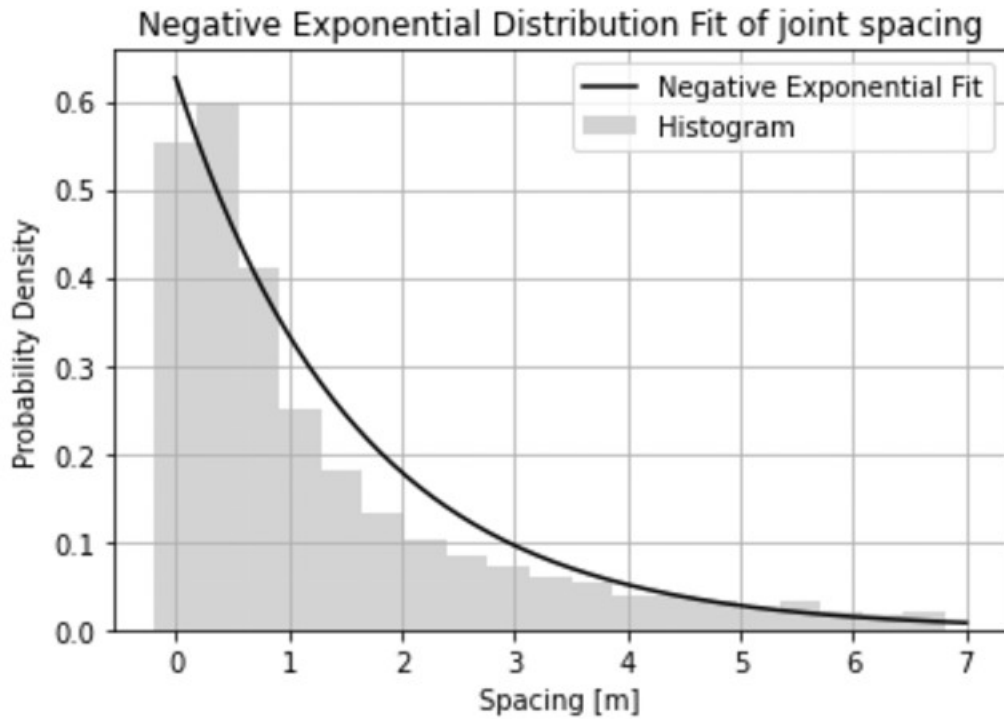


Figure 5.8: Joint spacing displaying negative exponential distribution.

Table 5.9: Mean fracture spacing for the joint sets 1 and 2 (Includes Js and Jb together)

	SW J1 - mean spacing [m]	J2 - mean spacing [m]	Fracture corridor
1	2.7	Nan	No
2	0.94	Nan	Yes
3	2.2	2.34	No
4	NaN	1.69	No
5	NaN	1.63	No
6	NaN	0.73	Yes
8	NaN	2.81	No
9	NaN	1.43	No
10	NaN	2.11	No
11	0.76	1.2	Yes
12	2.14	None	No
13	2.12	None	No

5.3 Joint Shape

The goal of this section is to determine the joint geometry in the study area. In sedimentary rocks, proportionality rules between joint spacing, height and mechanical layer thickness exist (Bai, Pollard, & Gao, 2000).

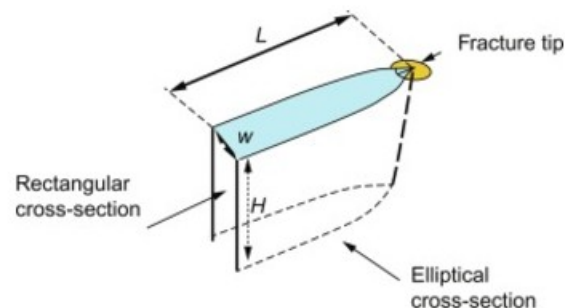


Figure 5.9: Hydraulic fracture geometry. L= length, w= aperture, H= height

Defining the mechanical layer thickness within the geological setting poses significant challenges. Additionally, the proportionality rules linking joint spacing, bed thickness, and fracture geometry cannot be applied in environments characterized by fracture corridors (Olson, 2004). Consequently, the modeling of joint geometry will rely primarily on field observations, complemented by statistical analyses of joint height measurements obtained from scan-windows.



Figure 5.10: Bedding plane F delimiting formation D and C. Most joints are bounded by this bedding surface. A fracture swarm, or corridors can also be observed on the left of the figure.

5.3.1 Maximum joint height and length

The maximum joint heights and lengths of structural joints were estimated using Cloudcompare, field observations and archives.

In the archives, a figure was found without scale, but based on the geological contacts, approximate location given by Mathieu (1962), surface topography and historical maps, the outcrop was geolocated on the current quarry and its height estimated at 70m. Figure 5.11 brings valuable information on the fracture height. The maximum joint height observed on figure 5.11 is between 25 to 30 meters high. In addition, one dissolution joint has been observed across two bench heights, this joint could not be traced further (figure 5.12). This joint may be extending further than 30 meters but joints extending further than two bench heights are rarely observed. It is reasonable to assume a maximum joint height of 30 meters.

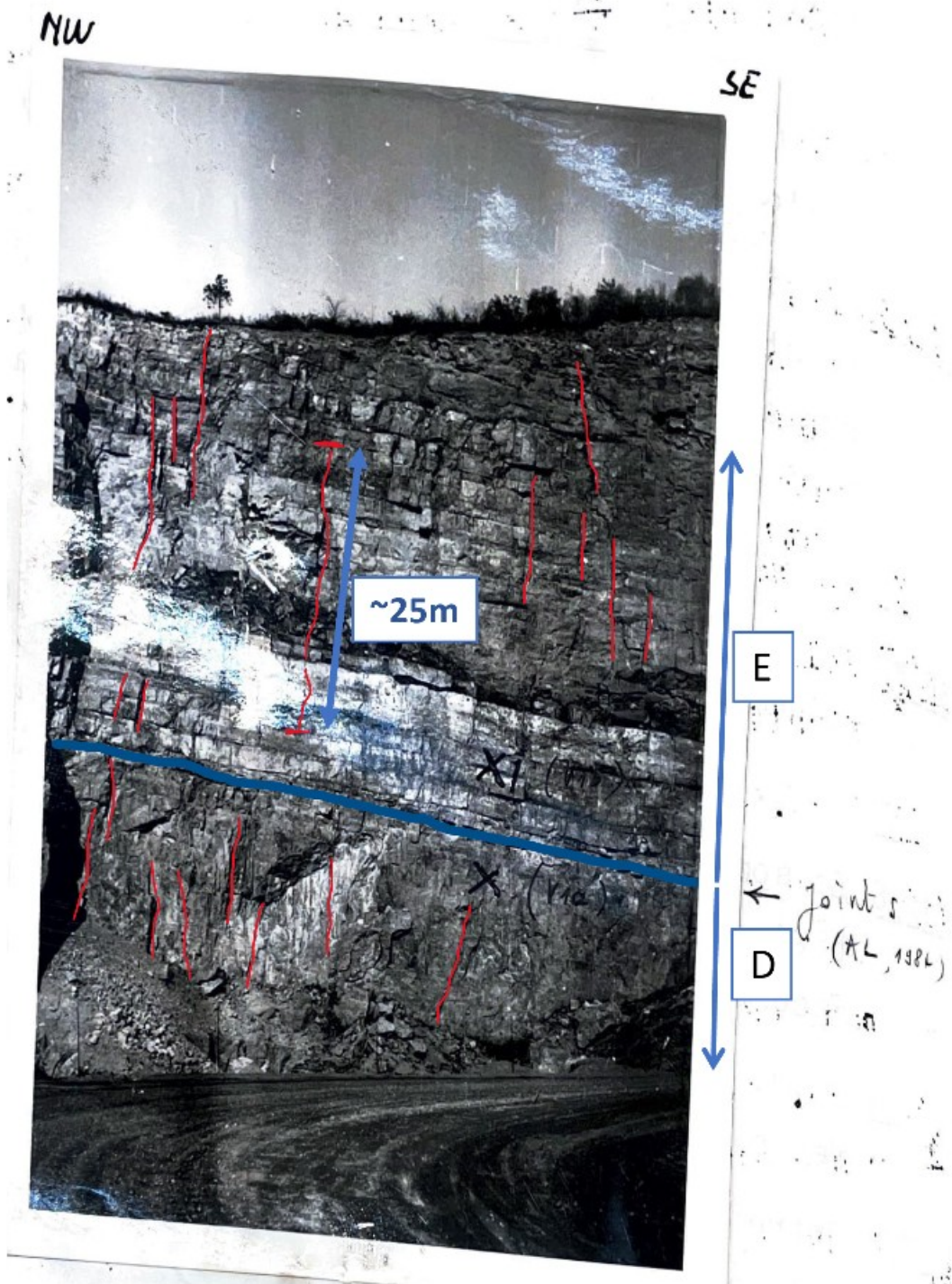


Figure 5.11: Figure from Mathieu (1962), located in an excavated part of the quarry. This figure was approximately taken near the Lambert72 coordinate (193297.3, 130068.2, 90.5).



Figure 5.12: Joint at least 30 meters in height on bench 1 and 2. The joint is not observed on bench 0 (bench with overburden removal)

Using the Compass plugin in Cloudcompare, nine structural joints have been traced across two bench heights when the orientation of the bench was sub-perpendicular to the strike of one of the joints sets.

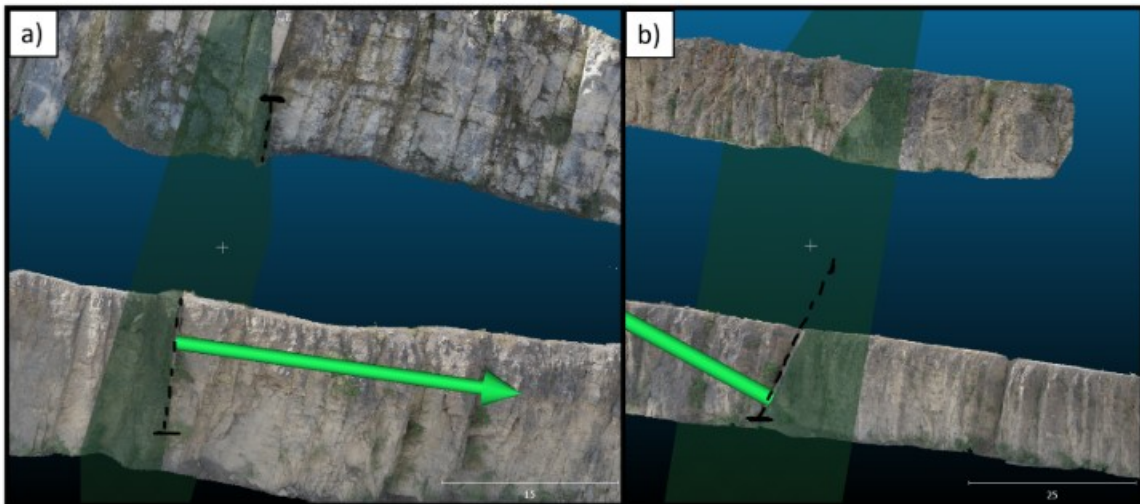


Figure 5.13: Structural joints traced across multiple bench heights by extending surfaces (green rectangles) with the measured dip direction and angle of structural joints. a) Js1 joints traced across 20m in height. b) Js2 joint at least 15m in joint height that could not be traced across 3 bench heights.

No joints have been traced across more than two benches. Furthermore, when a structural joint was traced across two consecutive benches the joints strike had to be sub-perpendicular to the bench orientation. If the angle between the joint strike and bench, referred to as beta (5.14 (b)), was too small, tracing joints across two bench heights proved challenging. Interpretation of joints traced across multiple benches indicate that most structural joints range between 10-20 meters.

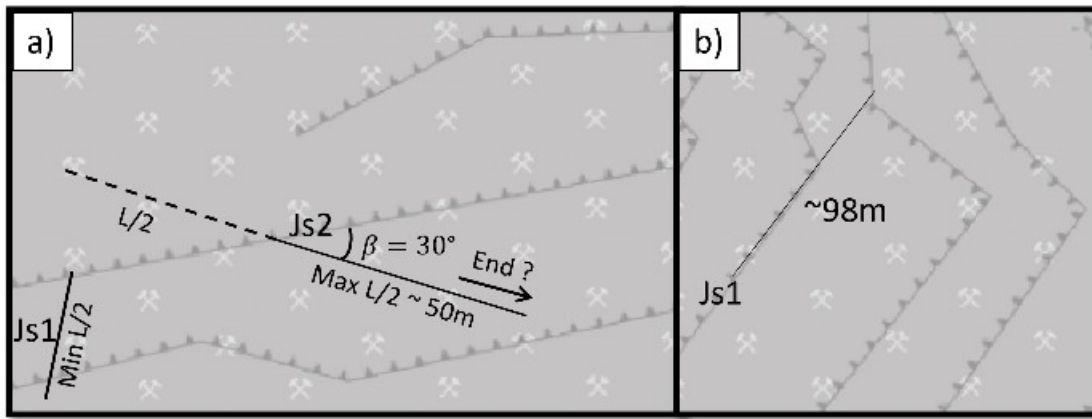


Figure 5.14: Example of three joints traced in the MLD quarry (Black lines). a) Js1 joint traced across two bench heights, Js2 with low β could not be traced across multiple benches b) Js1 joints traced along the length using surface staining and across its height with perpendicular benches to the joint's strike.

5.3.2 Aspect ratio

Surface staining on freshly blasted outcrops parallel to the strike of joint set 1 indicate the presence of a subvertical joint. The stained surfaces were used to interpret the height and length of 4 joints, the results are provided in table 5.10. One joint in a corner of the quarry could be followed across both height and length. This joint is estimated to have a height of 25 meters and a length of 100 meters and is schematically presented on figure 5.14 (b). Based on the four joint observations made, the range of aspect ratio's is estimated to be between 3 and 4.5.

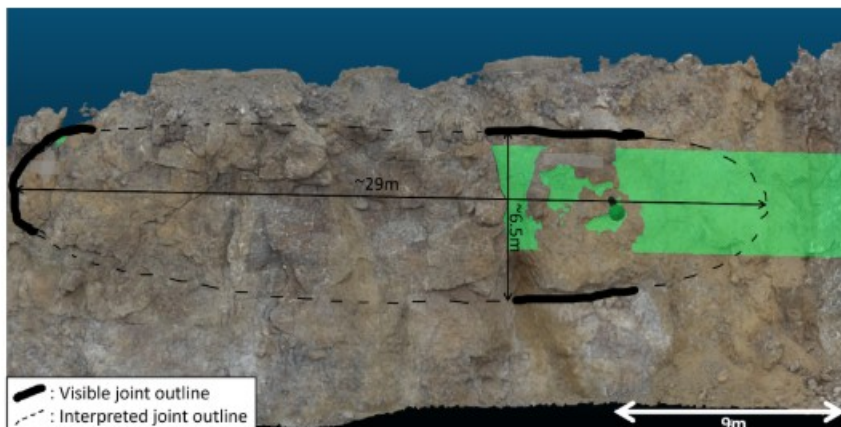


Figure 5.15: Joint traced along the surface staining

The results show that the fracture length is much longer than the fracture height, this is typical for materials with a high subcritical index (Olson, 2004). Odling et al. (1999) researched the aspect ratio on non-strata-bound joints in Norway and found an aspect ratio of 8. Such a value for the aspect ratio seems unrealistic for the study area as more fractures should have been able to be traced across multiple benches even with low sub-parallel joint strike to the bench orientation (see figure 5.14).

Table 5.10: Interpreted aspect ratio's of four joints based on surface staining from freshly blasted outcrops

i.d.	Interpreted length [m]	Interpreted height [m]	Aspect ratio [-]
1	75	25	3
2	98	26	3.8
3	5.5	1.8	3.1
4	29	6.5	4.5

5.3.3 Joint geometry distributions for DFN modelling applications

This study assumes that the joint length distribution matches the joint height distribution scaled by the aspect ratio, similar to assumptions made by Bisdom (2011); Odling et al. (1999) for generating DFNs. DFN models using three different combinations of length/height distributions could be generated:

DFN	Joint length-height distribution
1	Power-law with combined background and structural joints.
2	Power-law fitted separately for structural and background joints.
3	Power-law for background joints. Constant height for structural joints

Combined structural and background joints modelling approach

The empirical cumulative distribution function (CDF) for both the structural and background joints was compared to the theoretical CDF of a power law distribution. A minimum joint height of 1 meter was applied across all formations. The choice to use a power law distribution was influenced by the fact it is a very common distribution for the joint height (Bisdom, 2011; Odling et al., 1999).

Table 5.11: Power law exponents and minimum/maximum joint heights for aggregate height distribution

Formation - set	Minimum height [m]	Maximum height [m]	Power law exp
E - J1	1	30	1.5
E - J2	1	30	1.5
D and C - J1	1	30	1.1
D and C - J2	1	30	1.3

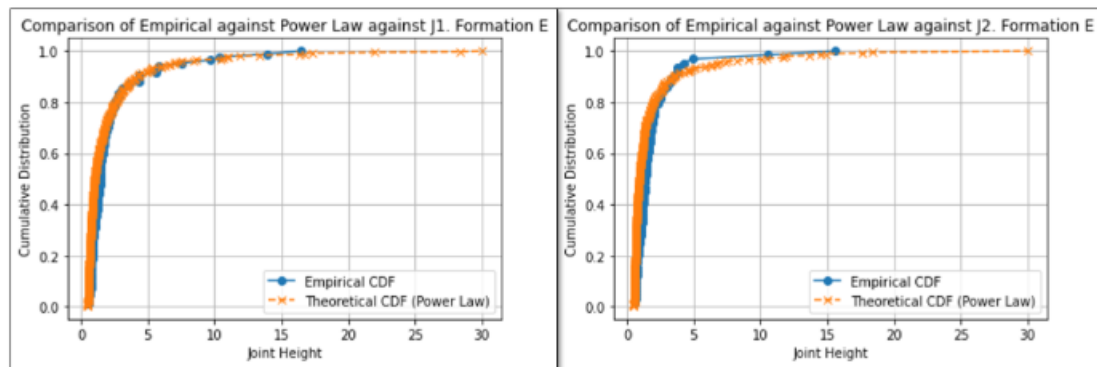


Figure 5.16: Best fit CDF for combined structural and background joint approach in formation E.

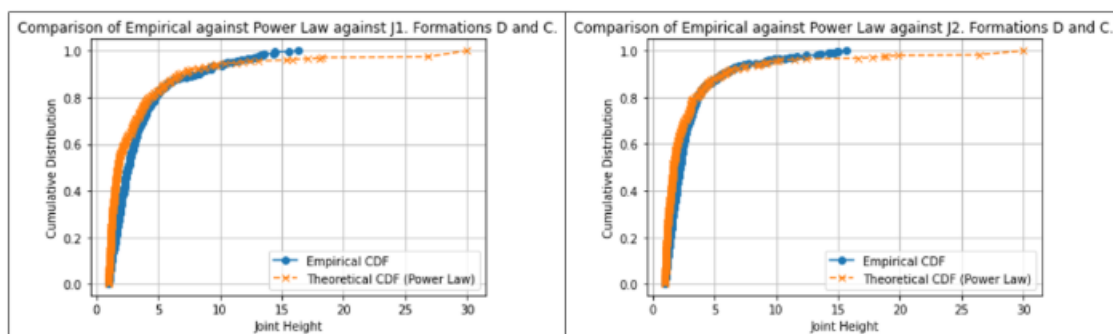


Figure 5.17: Best fit CDF for combined structural and background joint approach in formation D and C.

Separate structural and background joint height distribution

Separate joint height distributions were established for background and structural joints. The best fit power-law exponent was used for the background joint sets. Most structural joints are estimated to be between 9-20 meters in height, based on the difficulties in tracing these joints across different benches.

Table 5.12: Dissagregate power law deistribution for structural and background joints. Range of constant joint height can also be used to model the DFN for structural joints.

Formation - set	Minimum height [m]	Maximum height [m]	Constant joint height [m]	Power law exp
E - Jb1	1	10	//	1.6
E - Jb2	1	10	//	1.6
E - Js1	9-14	30	13-25	1-1.5
E - Js2	9-11	30	13-18	1-1.5
D and C - Jb1	1	10	//	1.25
D and C - Jb2	1	10	//	1.4
D and C - Js1	9-14	30	13-25	0.9-1.5
D and C - Js2	9-11	30	13-18	1.2 - 1.6

Most power law exponents for joint length distribution are between 1.5 to 3, the power law exponent found for the study area are lower than the typical range of power-law exponents expressing the joint length distributions (Bonnet et al., 2001). Bisdom (2011) studied the fracture height distribution for carbonate deposits in Southern France found power law exponents in a similar range as this study (between 0.6 to 1.3).

5.4 Joint condition

5.4.1 Joint condition ratings Ja, Jr for structural joints

The descriptions of joint infill, aperture, and roughness have been utilized to determine Jr and Ja ratings according to the Q system (see Appendix D).

Joint roughness

The joint roughness was evaluated using a photogrammetry model along with the roughness scale provided by the ISRM (Barton, 1978). Variations in the joint roughness ranged from rough undulating to rough planar. A significantly higher proportion of Js1 joints are classified as rough planar ($J_r = 1.5$), with 39% of Js1 joints falling into this category—nearly twice the percentage of Js2 joints at 19%.

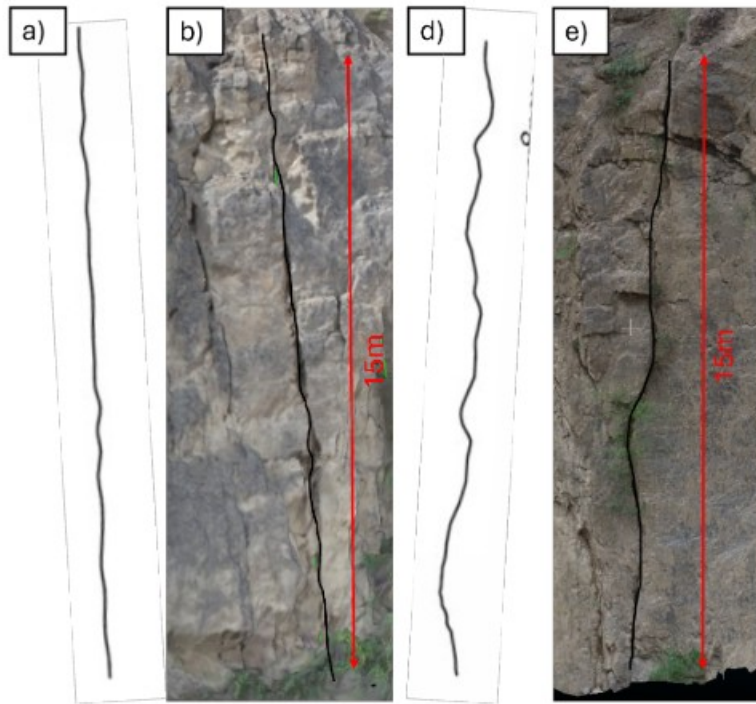


Figure 5.18: a) Roughness profile for a rough planar joint (Barton, 1978). b) Rough planar joint profile overlain on Js1 joint (Bench 6). d) Roughness profile for a rough undulating joint (Barton, 1978). e) Rough undulating Js2 joint (Bench 4)

Joint condition

A couple of observations can be made on the joint condition:

1. Joint condition improves below Bench 6, with no dissolution joints observed. The only dissolution 'joints' observed below bench 6 are faults.
2. A higher percentage of Js2 joints are more likely to be affected by dissolution phenomena leading to a higher percentage of Jr=1.

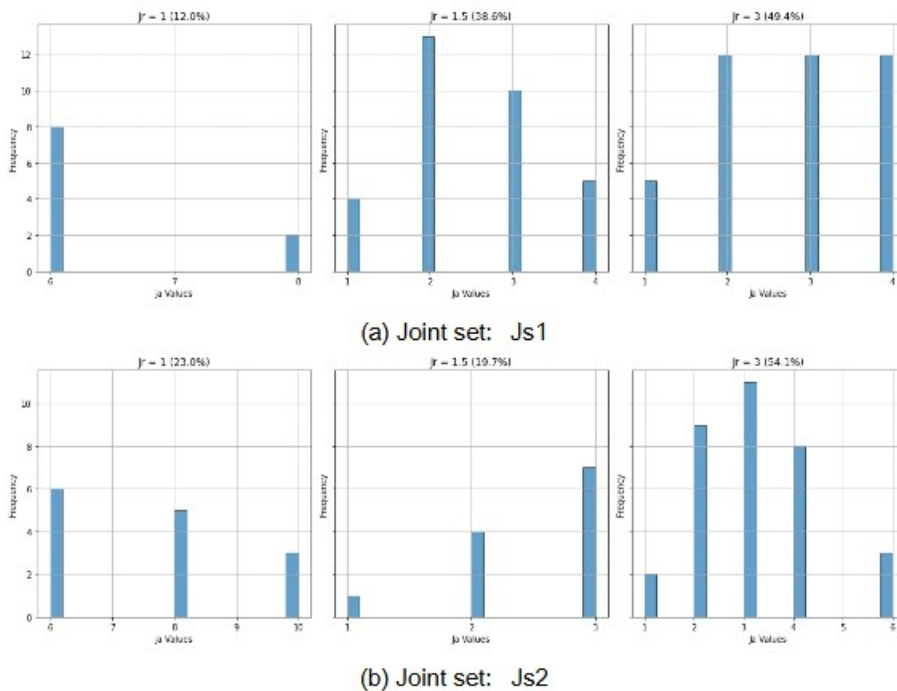


Figure 5.19: Jr and Ja measurements for structural joint sets Js1 and Js2

5.4.2 Joint condition ratings Ja, Jr for background joints

The Ja and Jr ratings for joints described in the borehole rock core were used to establish the distribution of these ratings among the background joints. No differentiation is made between Jb1 and Jb2 joints with regards to joint condition. Field observations suggest that all background joints exhibit rock wall contact during shearing; however, they can occasionally contain thin mineral fillings. Dolomitic sand from alteration is prevalent across background joints. The roughness ratings for the background joints range from rough undulating to rough planar.

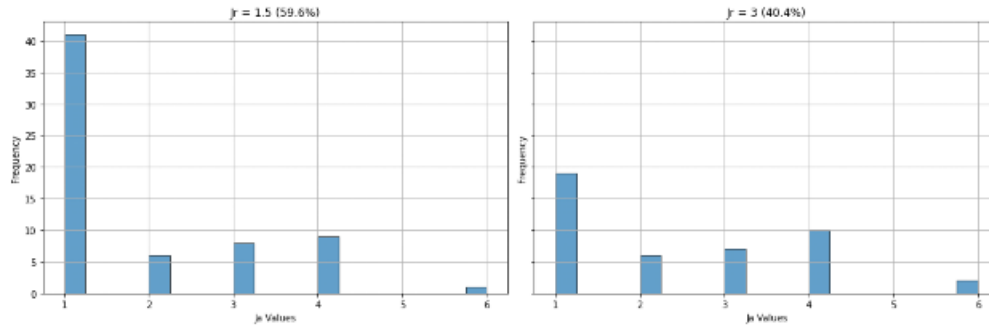


Figure 5.20: Jr and Ja measurements for background joints

5.4.3 Estimates of the joint friction angle

Using the rating parameters Jr and Ja, it is possible to estimate the joint friction through Equation 4. Equation 4 provides a fair estimate of the actual friction angle under different joint roughness and alteration conditions Barton, Lien, and Lunde (1974); NGI (2015).

$$\text{Joint friction} = \tan^{-1} (Jr/Ja) \quad (4)$$

Differences in joint frictions between joints with no wall contact during shear or with joint wall contact are significant. In the case of no wall contact after 10cm of shear (Jr=1), the joint friction will be dominated by the joint infill. Three cases of the joint infill have been observed at MLD.

1. Unconsolidated orange clay.
2. Fine grained dolomitic sand from alteration of the dolomite.
3. Thick gouge as infill (see figure 5.21).



Figure 5.21: Structural joint with thick gouge infill.

Using Equation 4, estimates for joints with thick clay infill yield friction angles of 6%. When the infill consists of gouge, the estimated joint friction is around 10%, both of which are slightly lower than literature reports. Joints with non-swelling clay infill 10-20 mm thick exhibit friction angles of 13-14% (Rocscience, n.d.). Joints with gouge shear zones typically have friction angles around 20% this is much higher than the 10% estimated (Wyllie & Norrish, n.d.). Barton et al. (1974) recognizes that friction angles for clays and gouge are lower than the residual peak strength of non swelling clays. Significant dissolution phenomena can adversely affect shear strength, making the values estimated by Equation 4 a conservative design criterion for low friction angles.



Figure 5.22: 1) joint with no wall contact when sheared, clay infill. 2) Rough planar and rough undulating joints with thin coating of dolomitic sand

Most joints in the area have rough, undulating surfaces in direct contact with rock walls, which Barton (1978) notes [REDACTED]. For unaltered, rough, undulating joints, the highest friction angle can reach up to 71 degrees, as calculated using equation 4. Friction angles for these joints can also be determined through other rock mass classification systems, such as the SSPC, which estimates a friction angle of 53 degrees (Hack, 1998). There is a 20-degree difference in friction angles between these two classification systems for rough, undulating joints without infill. The discrepancy in high friction angles remains a topic of ongoing discussion in rock mechanics (Ngan-Tillard, 2024). The friction angle variation between the SSPC and Q systems is minimal for lower friction angles. This study adopts a conservative maximum friction angle of 50 degrees, which aligns with the SSPC estimate for rough, undulating joints without infill (Hack, 1998).

Using Equation 4 along with the J_a and J_r values and assuming a maximum friction angle of 50 degrees, categorical statistics were created to describe the percentage of each joint friction angle.

Table 5.13: Categorical statistics for the friction angle of Js1 joints

Friction Angle [deg]	Percentage of joints [%]
7°	2%
10°	10%
21°	6%
27°	12%
37°	30%
45°	15%
50°	25%

Table 5.14: Categorical statistics for the friction angle of Js2 joints

Friction Angle [deg]	Percentage of joints [%]
7°	13%
10°	10%
27°	16%
37°	20%
45°	18%
50°	23%

Table 5.15: Categorical statistics for the friction angle of background joints (Jb1 and Jb2)

Friction Angle [deg]	Percentage of joints [%]
10°	10%
27°	9%
37°	15%
45°	6%
50°	60%

5.5 Geotechnical domains

Geotechnical domains are defined based on quantitative datasets and based on observations of geological features (Barton, 1978; Bieniawski, 1989). A geotechnical domain should have statistically similar geotechnical features, such as joint orientation, condition, or intensity.

The geotechnical domains are classified into two types of domains, subvertical fault domains (F domains) and stratigraphic domains (S domains). The stratigraphic domains (S domains) are based on two variables: the depth of cover and the geological formations. The S domains are situated between the subvertical F domains.

Table 5.16: Summary of the geotechnical and DFN domains

Geotechnical domain	Formations
F1	E-D-C
F2	E-D-C
F3	E-D-C
S0	E-D-C
S1	E
S2a	D-C
S2b	D-C

5.5.1 F1 domain

The F1 domain is one of the most prominent karstic features in the quarry. As observed in figure 5.23, this zone is striking E-W. The extent the domain decreases with depth, typical of an iron-hat structure (see section 3.3.8). Karstic voids filled with silty clay can be observed in this zone, (figure 5.24). To the West of the exposed karstic surface observed in figure 5.24, Mathieu (1962) mentions the presence of a normal faults with two meters of displacement. A. Lauwers also mentioned chemical anomalies when this area was exploited (personal communication).

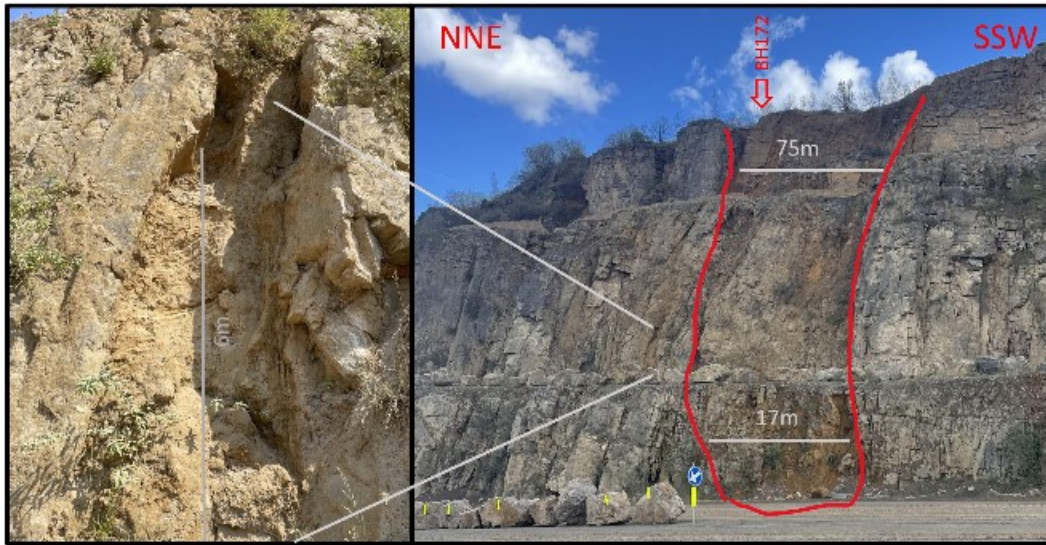


Figure 5.24: F1 subvertical domain, heavily altered dolomite, karstic voids and high fracture intensities dominate the domain. The alteration decreases with depth.

Borehole 172 was drilled 150 meters to the East of the outcrop seen in figure 5.24 along the strike of the F1 domain (see figure 5.23). The fracture frequency and joint condition in this borehole were three to four times higher than in other boreholes (see sections 5.2.4). The recovery was also bad, with 80% and 73% recovery in formations D and C respectively. It is likely that karstic voids similar to those in figure 5.24 (left) filled with clay and silt were encountered during drilling.



Figure 5.25: Borehole 172 drilled accros karstic voids, between 128.7 and 131.7 only 60cm of cores are recovered on a borehole section 3m long.

Collapse zones in the fields above the quarry have also been identified in the strike direction of the F1 domain. The collapse zones are two-to-three meters of elevation change and are probably buried dolines (see figure 5.26). Lastly, the geological map of Wallonia indicates the presence of underground iron mines. Iron ore and subvertical karsts are related to each other, as discussed in section 3.3.8. The F1 domain was mapped taking into account the literature review mentioning karst, field observations, and the borehole core descriptions.

5.5.2 F2 and F3 domains

Lhoist has mapped two subvertical zones based on high iron contamination of their deposit. Both high iron zones are displaying the typical geometry where the horizontal extent of the iron vein is decreasing towards the bottom of the quarry. This is likely associated with the phenomenon of iron hats described in section 3.3.8. The main vein in the F2-domain is 1.5 meters thick and consists of goethite. On both sides of the vein, there are numerous subvertical fractures and the rock material has been weathered reducing the UCS of the intact rock material. A fault aligning with high iron zones was mapped by Lhoist in a now backfilled area of the quarry. Those high iron domains will be used as structural domains and are referred to as F2 and F3 (see map in figure 5.23).

5.5.3 S0 domain

The S0 domain consists of the top superficial karst and sand pockets related to former river channels. This area is referred to by Lhoist as the pinnacle zone, more information can be found in section 3.3.

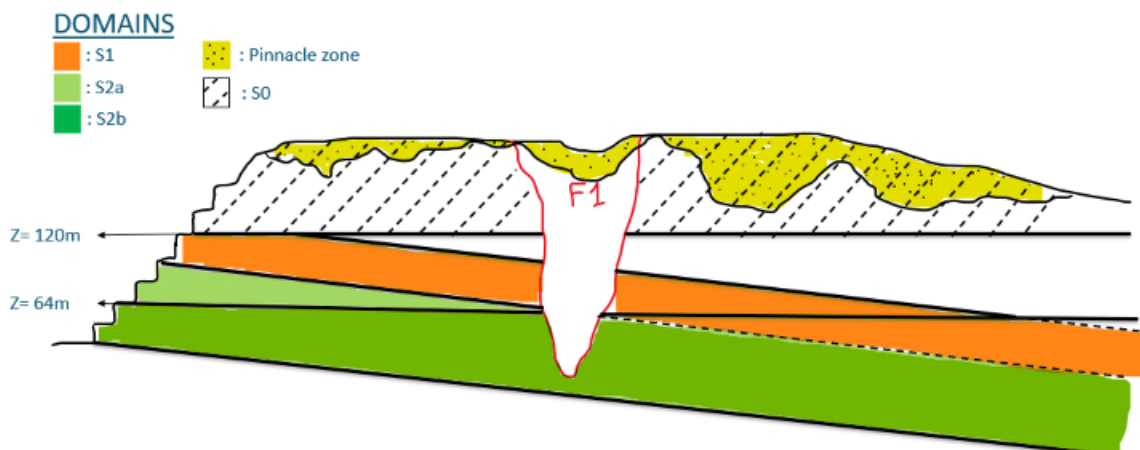


Figure 5.27: Schematic cross-section representing the geotechnical domains of the MLD quarry

5.5.4 S1 domain

The S1 domain encompasses formation E outside the fault domains and below the S0 domain (see fig 5.27). Formation E has different geotechnical features than formations D and C. The bed thickness of Formation E are smaller than those of Formations D and C. This is due to varying dolomitization process during diagenesis (see section 3.2.1). This also affected the joint height distribution compared to formations D and C (see 5.3).

5.5.5 S2a and S2b domains

The S2 domains consist of formations D and C outside the F domains and below the S0 domain. No significant statistical differences in fracture intensity were observed between formations D and C. However, field observations indicated an improvement in joint condition with increasing depth. As mentioned in section 4.2, no observations of joints without rock wall contact have been made below bench 6, except for faults in F2 and F3 domain. Joint condition plays a key role in block stability (NGI, 2015). Observations of improved joint condition with increasing depth have led to domain S2 being subdivided into sub-domains S2a and S2b. The sub-domains can be observed in figure 5.27.

5.6 Interpretation of joint intensity datasets

5.6.1 Interpretation BH-P10 dataset

The BH-P10 does not differentiate between the Js1, Jb1, Js2 and Jb2 joint sets. In contrast, the VB-P10 dataset does differentiate between the different joint sets. DFN modelling requires fracture intensities determined by set. Consequently, the percentage ratio of each joint set in the BH-P10 will be interpreted using the optic scan and the VB-P10 data.

Table 5.17: Percentage of P10 data corrected for orientation by joint set.

Location - Formation	% J1	% J2
S domains		
SW3 - E (S1)	49%	51%
SW8 - D (S2)	56%	44%
F domains		
SW12 - D	42%	58%
Optic Scan - E	22%	78%
Optic Scan - D	43%	57%

SW8 and SW3 are the only scan-windows that include all sets inside the S-domains. SW12 and the optic-scan were both situated inside F domains and included all joint sets. Inside the F domains, heavily weathered fracture corridors with similar orientation as J2 joints are observed (see section 3.3.5). The percentage of J2 set should be higher for boreholes situated inside F domains because of fracture corridors consisting of J2 joints found in those domains.

The percentage of background joints and structural joints for each set has been estimated using the average percentages of Jb and Js. On average, around 35% of J1 VB-P10 values consist of structural joints, and 20% of J2 VB-P10 values consist of structural joints.

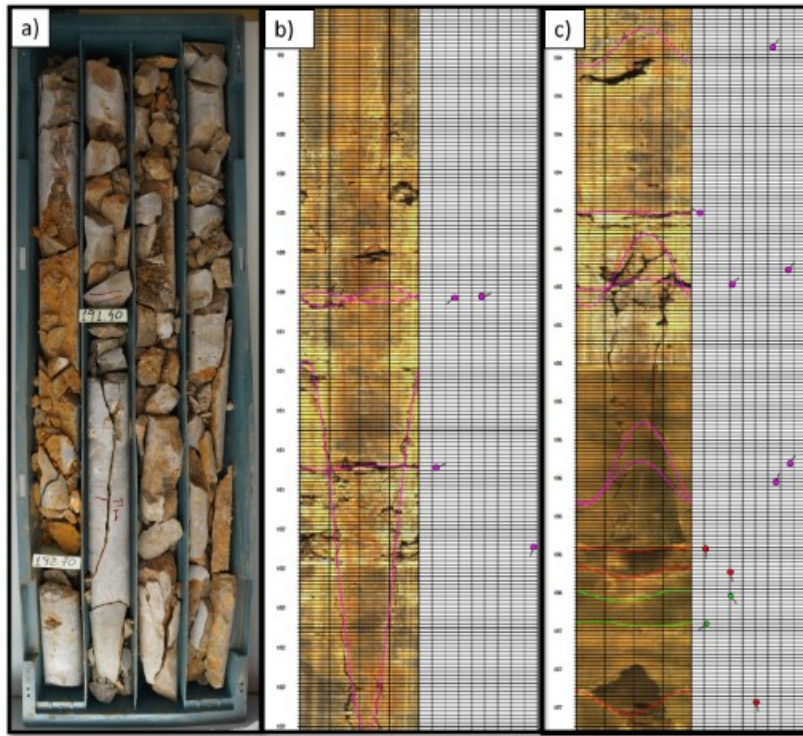
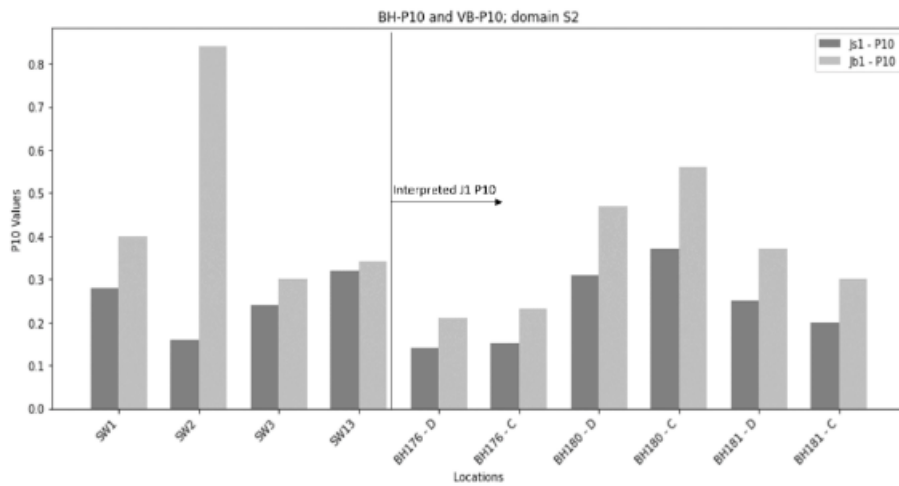


Figure 5.28: (a) High frequency of subvertical fractures in formation C, BH172. (b) and (c) optic scan from BH172.

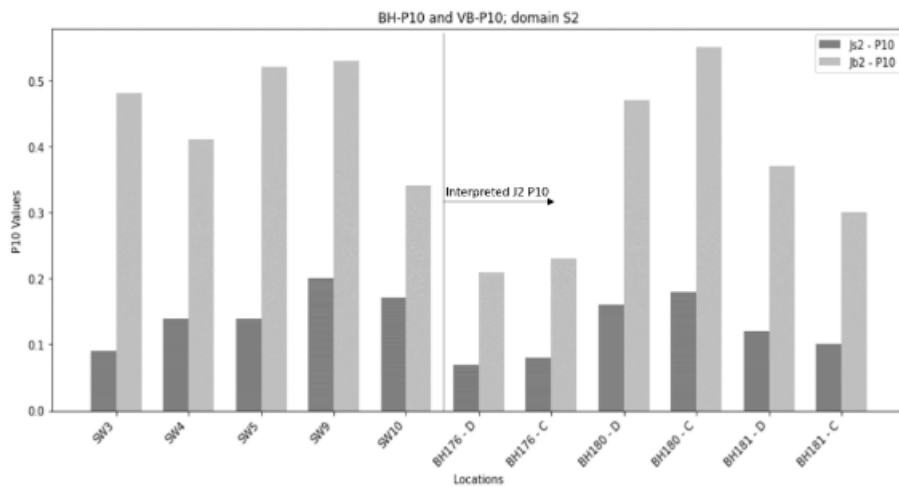
Table 5.18: Interpreted BH-P10 values defined by joint set.

BH	Formation	Domain	P10- Tot	Js1 - P10	Jb1 - P10	Js2 - P10	Jb2 - P10
172	E	F1	1.44	0.13	0.19	0.28	0.84
172	D	F1	2.56	0.44	0.66	0.36	1.09
172	C	F1	4.32	0.74	1.11	0.62	1.85
176	E	S1	0.43	0.08	0.13	0.06	0.17
176	D	S2	0.62	0.14	0.21	0.07	0.21
176	C	S2	0.69	0.15	0.23	0.08	0.23
177	E	F2	0.93	0.08	0.12	0.18	0.54
177	D	F2	2.61	0.45	0.67	0.37	1.11
177	C	F2	2.75	0.47	0.71	0.39	1.17
179	C	S2	1.69	0.29	0.44	0.24	0.72
180	E	S1	0.83	0.16	0.24	0.11	0.32
180	D	S2	1.41	0.31	0.47	0.16	0.47
180	C	S2	1.66	0.37	0.56	0.18	0.55
181	E	S1	0.68	0.13	0.20	0.09	0.26
181	D	S2	1.10	0.25	0.37	0.12	0.37
181	C	S2	0.89	0.20	0.30	0.10	0.30

To verify the interpreted BH-P10 values from table 5.18, the VB-P10 and interpreted BH-P10 are plotted against each other.



(a) Joint sets: Js1 and Jb1



(b) Joint sets: Js2 and Jb2

Figure 5.29: VB-P10 values and interpreted BH-P10 values per joint set.

5.6.2 relationship between P32, P21 and P10

MOVE software does not give the option to use P10 and P21 values as input; only P30 or P32 datasets can be used. The higher-order fracture frequency should be equal to or slightly higher than the lower-order fracture frequency ($P32 \geq P21 \geq P10$) (Bisdom, 2011; Wang & Mauldon, 2006). This holds true when joint frequency has been corrected for orientation. A numerical stereological rule introduced by Wang and Mauldon (2006) also exists. Bisdom (2011) used this stereological rule to relate P10, P21 and P32 and found that the differences between P10, P21 and P32 were small. In this study, it is assumed that $P32 = P21 = P10$ when fracture intensity has been corrected for orientation.

To verify that $P32 = P21 = P10$, the VB-P10 and SW-P21 datasets were plotted against each other as both datasets are derived from the same fracture traces. As observed in figure 5.31, there is almost no difference between the P10 and P21 values. The largest variation between P21 and P10 in figure 5.31 is 12%, seen in scan-window 8. VB-P10 values will be used as they are considered more reliable than P21 values. Variations between P21 and P10 can be attributed to fractures on the edges of the scan window not always being properly traced (see figure 5.30).

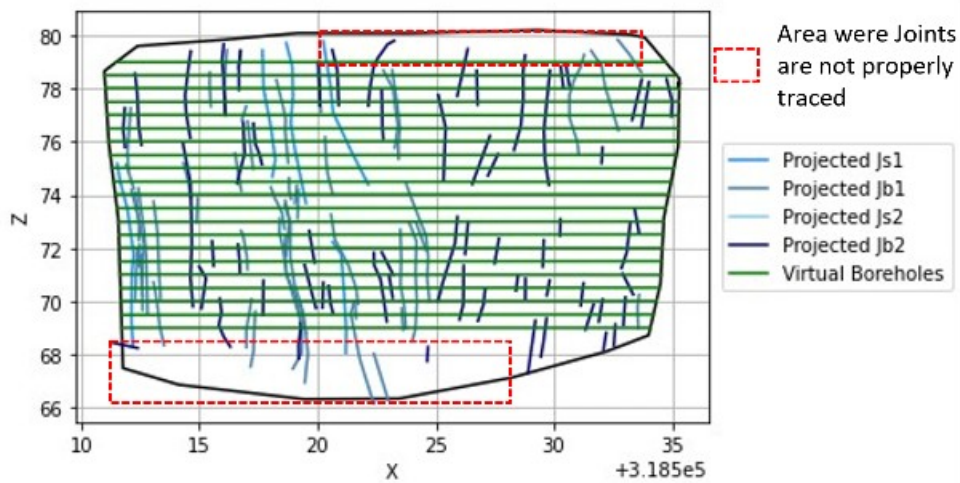


Figure 5.30: SW12, P21 include areas where joints are not properly traced.

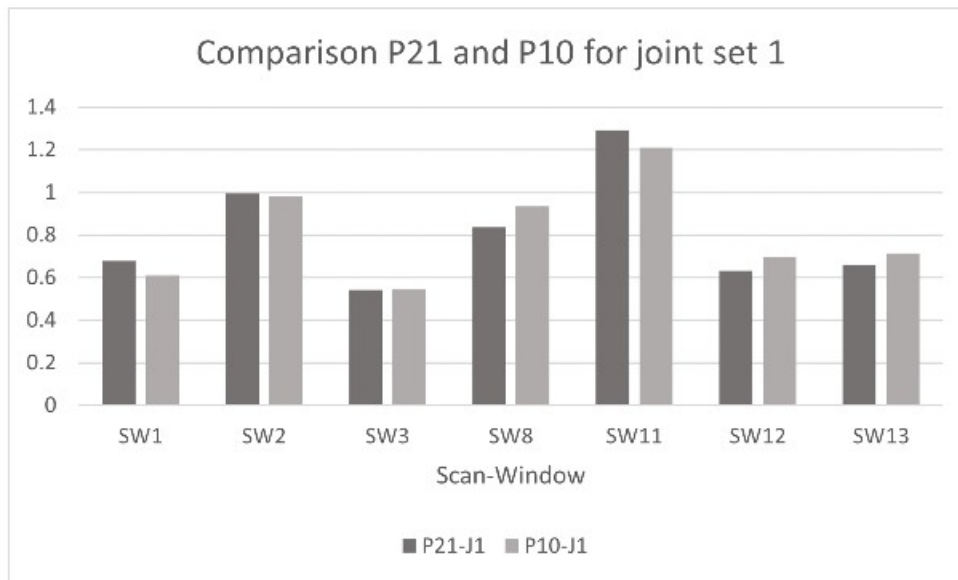


Figure 5.31: Comparison P21 and P10 for J1 joints (Js1, Jb1)

5.6.3 DFN P32 dataset

The complete dataset of interpreted P32 values is given in Appendix C.

6 Model building (Quarry wide DFN)

6.1 Integrated dataset

Based on the joint characterization in section 5, statistical datasets for joint orientation, intensity and shape have been determined (Table 6.1).

Table 6.1: Range of parameters and distributions used to generate a quarry wide DFN's

Set	Property	Distribution	Parameters
Js1	Orientation	Fisher	Dip α = 300 deg; dip ang = 80 deg; Fisher k = 45
	Intensity	-	P32 [m ² /m ³] interpolated; Range P32= 0.13- 0.74 a = 0.9-1.5;
	Shape	Power-Law Uniform	min h= 10m, max h= 30m; Aspect ratio= 3-4.5 h = 15-25m; Aspect ratio: 3-4.5
Jb1	Orientation	Fisher	Dip α = 300 deg; dip ang = 80 deg; Fisher k = 45
	Intensity	-	P32 [m ² /m ³] interpolated; Range of P32= 0.21-1.11 a = 1.4;
	Shape	Power-Law	min h= 1m, max h= 10m; Aspect ratio= 3-4.5
Js2	Orientation	Fisher	Dip α = 19 deg; dip ang = 80 deg; Fisher k =35
	Intensity	-	P32 [m ² /m ³] interpolated; Range of P32= 0.05-0.62 a = 1.2-1.6; min h= 10m, max h= 30m;
	Shape	Power-Law Uniform	Aspect ratio= 3-4.5 h = 15-20m; Aspect ratio= 3-4.5
Jb2	Orientation	Fisher	Dip α = 19 deg; dip ang= 80 deg; Fisher k = 35
	Intensity	-	P32 [m ² /m ³] interpolated; Range of P32= 0.21-1.85 a = 1.4; min h= 1m max h= 10m;
	Shape	Power-Law	Aspect ratio= 3-4.5

6.2 Spatially modelling the P32 fracture intensity

Geostatistical methods are used to interpolate the P32 values for each joint sets. The steps to model the P32 dataset on a block model are the following:

- Import and project the P32 dataset on 2D surfaces in MOVE.
- Perform variography to determine the model and parameters and perform Kriging interpolation on 2D horizons.
- Transfer the interpolated P32 values from the 2D horizons to their corresponding positions within the 3D block model

6.2.1 Kriging interpolation

The P32 point cloud on 2D horizons was interpolated using the Kriging algorithm. Kriging stands as a valid interpolation method, known for generating the best linear unbiased estimations (Rogers et al., 2014). However, limitations accompany Kriging interpolation, notably in parameter and model selection, which rely on variography and can introduce subjectivity, potentially impacting interpolations (Todini, Pelligrini, & Mazzetti, 2001). Another limitation of Kriging interpolation pertains to edge effects; interpolations at the dataset's boundaries are uncertain because of the lack of data beyond the point cloud Xu and Dowd (2012). The joint intensities interpolated between the boreholes and quarry walls will be most precise. Interpolations were carried out across three horizons by joint set. These horizons mark the top and bottom of the Tournaisian formations D and C, respectively, as well as an intermediate horizon.

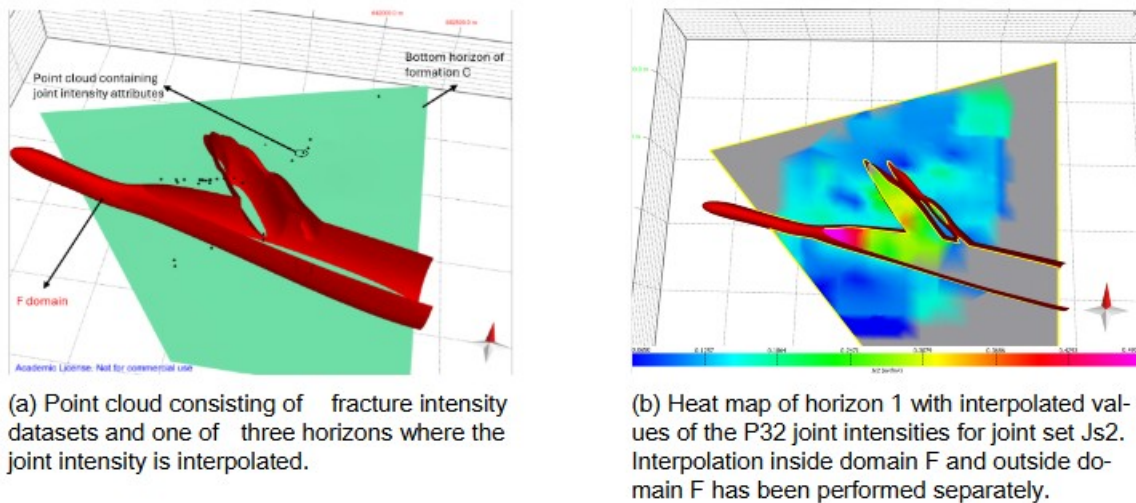


Figure 6.1: Figures of the P32 point cloud data and interpolation of P32 values on a 2D horizon.

The F domains were associated with fracture corridors consisting of J2 joints, independent interpolation of J2 P32 data within and outside the F domains were performed to force higher fracture frequencies within the F domains. The P32 data of the J1 joints were interpolated as a single dataset across the entire 2D horizons. No relationships between F domain and J1 joints were observed based on field observations. Kriging interpolation is capable of incorporating directional bias (anisotropy). 120 meters (equal to maximum joint length) of anisotropy along the strike of the sets was introduced to emphasise the directional trend of the high P32 data related to fracture corridors. Bisdom (2011) modelled each fracture corridor as a continuous features across his domain with high P32 values.

6.2.2 Block model

Between each of the three horizon surfaces, Geocellular volumes with blocks 25x25m wide were generated to create a block model of the joint intensities. The block height varied between 25-30m in height. The nearest interpolated P32 value on one of the three horizons is assigned to each block (Petroleum Expert, personal communication).

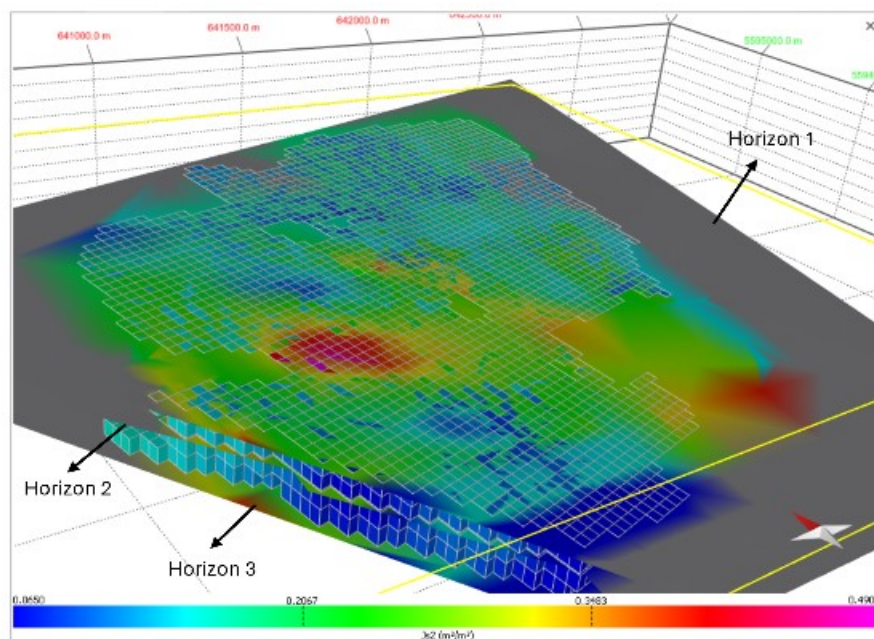


Figure 6.2: Block model of the P32 data per joint set. Example for joint set Js2.

6.3 DFN model

DFN model can be created by employing various combinations of distribution values listed in Table 6.1. Based on the quarry wide-DFN's, total P32 (excl. bedding) values can be calculated. The DFN was however generated using interpolated values of the P32 dataset. DFN has only a limited practical application when using MOVE and a P32 point cloud. Generating different DFN models using different combinations of values inside table 6.1 does not affect P32 data. DFN models using MOVE to predict joint intensity could have been useful when using Optic Scan logs where local DFN's could be generated and scaled to the entire quarry (Petex, 2022). Only blocks that had complete fracture intensity data for all joint sets were selected.

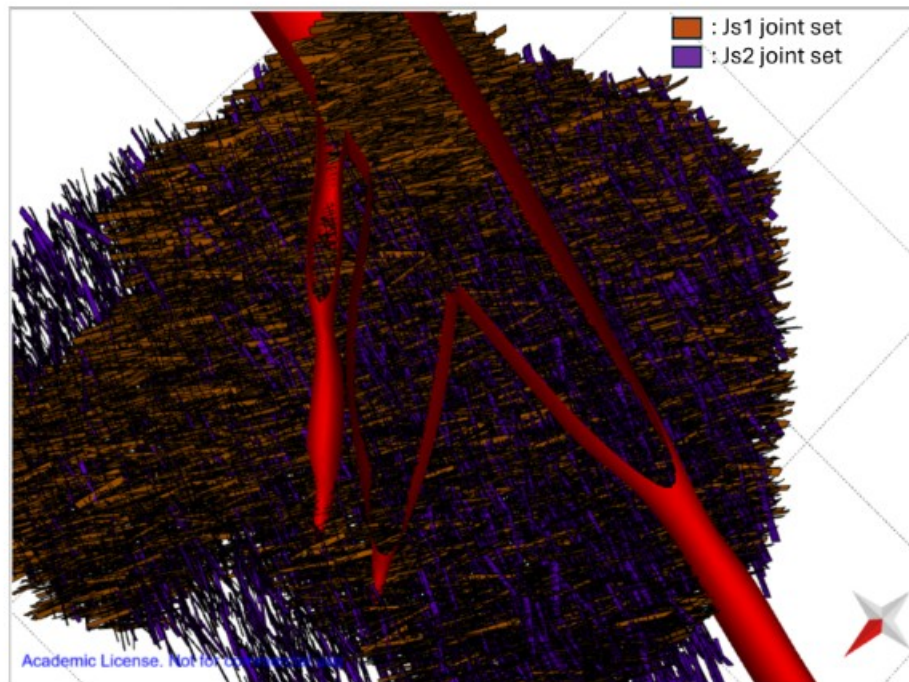


Figure 6.3: Example of a quarry wide DFN for the study area.

The P32 values corresponding to the centroids of selected blocks were employed to produce a heat map in QGIS, visualizing the total P32 fracture intensity (excl. bedding) across the quarry (see Figure 6.4). The heat map can give valuable information on:

- Subvertical joints sets influence the hydraulic networks of the area. This hydraulic network plays a pivotal role in the dissolution processes of the rock, as noted by Passagez (2012). In essence, a greater intensity of subvertical joints may indicate higher risks of karsts.
- The majority of the area has a total P32 (excl. bedding) between $1.1\text{m}^2/\text{m}^3$ and $1.6\text{m}^2/\text{m}^3$.
- Higher fracture frequencies may influence the RMR, Q values and block size potential.

6.4 Block size analysis

To develop a geotechnical model for the quarry, understanding the relationship between P32, bed thickness, and block size is essential. Using true joint spacing data from section 5.2.6, a sensitivity analysis and empirical solutions will explore:

1. How bed thickness influences block forming potential.
2. The impact of P32 (excl. bedding) on the block volume potential.

6.4.1 sensitivity analysis

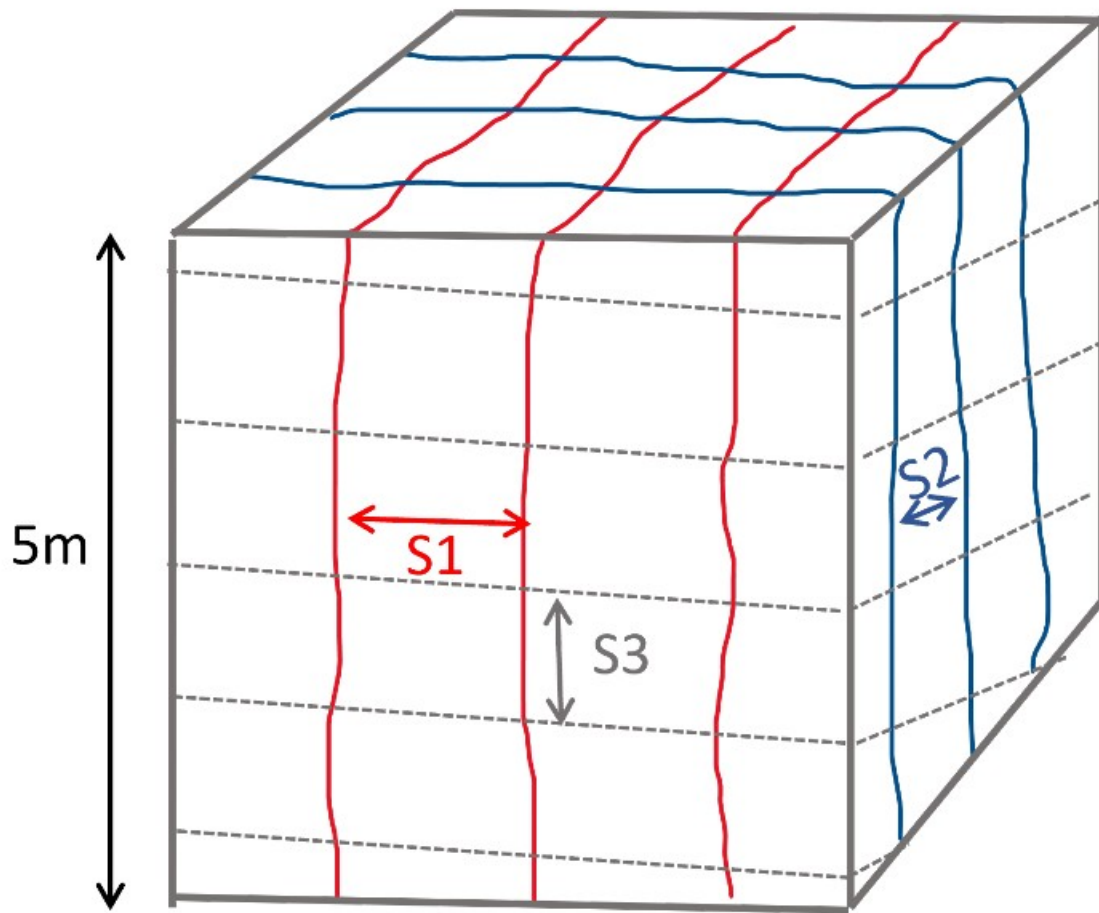
The sensitivity analysis of the the block volume distribution was estimated by using the following formula:

$$V_b = \frac{S_1 * S_2 * S_3}{\sin(\gamma_1) * \sin(\gamma_2) * \sin(\gamma_3)} \quad (5)$$

Where:

1. S: Spacing
2. γ : Angles between the joint sets

For this study, it's assumed that all joints intersect at right angles, leading to the block volume formula $V_b = S_1 \times S_2 \times S_3$, which yields the most conservative volume estimation (90 degree angle providing the largest possible denominator to the equation above).



S1: Spacing joint set 1

S2: Spacing joint set 2

S3: Spacing bedding planes

Figure 6.5: True joint spacing for the bedding, J1 and J2 joints.

Results: Influence bed thickness

The volume of the blocks is greatly affected by the assumptions on bed thickness. In cases where the bedding planes are widely spaced (with spacing exceeding 1.5 meters), it is expected that more than 50% of the blocks will have a volume larger than 1 cubic meter for P32 (excl. bedding) below 1.3m²/m².

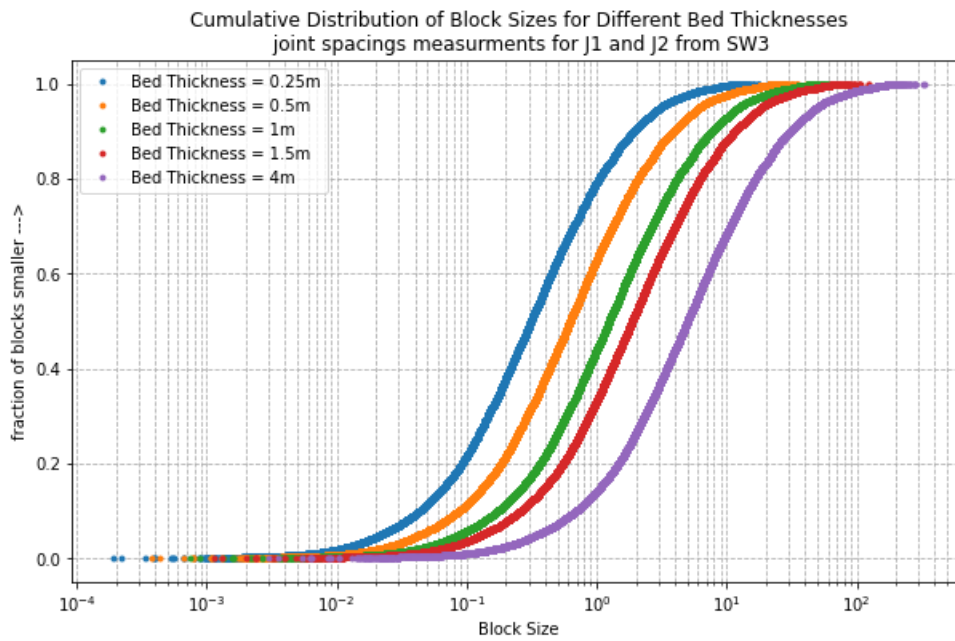


Figure 6.6: Influence of the bed thickness on the block size

Results: Influence P32 (excl. bedding)

Five different scenario's have been tested to examine the influence of the P32 joint intensity of subvertical joints on the block size. The five scenario's are provided in table 6.2. The P32 value listed in Table 6.2 is calculated as the sum of the P10 data from where the spacing data from the SW has been retrieved.

Table 6.2: Scenarios used to investigate block volumes for a 1.5m bedding plane

Scenario	Comment	S1 data	S2 data	P32 (excl. bedding)
1	Low fracture intensity.	SW3	SW3	1.05 m ² /m ³
2	Mean fracture intensity	SW13	SW4	1.29 m ² /m ³
3	High fracture intensity for 1 joint set, fracture corridor associated with J1	SW2	SW5	1.59 m ² /m ³
4	Fracture intensity equally high for both sets, based on a single outcrop in the F domain	SW12	SW12	1.56 m ² /m ³
5	Worst case scenario for joint intensity	SW11	SW6	2.44 m ² /m ³

The findings indicate that while fracture intensity affects block sizes, the spacing distribution of fractures also impacts the size of the blocks. Scenarios 3 and 4 exhibit similar fracture intensities. Nonetheless, the block distributions vary between these scenarios, due to two distinct factors. In the scenario with a high fracture intensity associated with a single joint set (scenario 3), the blocks tend to be more rectangular. In contrast when both joint intensities are high, equidimensional cubical blocks form. The influence of the block shape is taken into account in empirical solutions (Palmstrom, 2005). This difference in shape, along with variations in the joint spacing data, may account for the dissimilar block distributions observed between scenario 3 and 4.

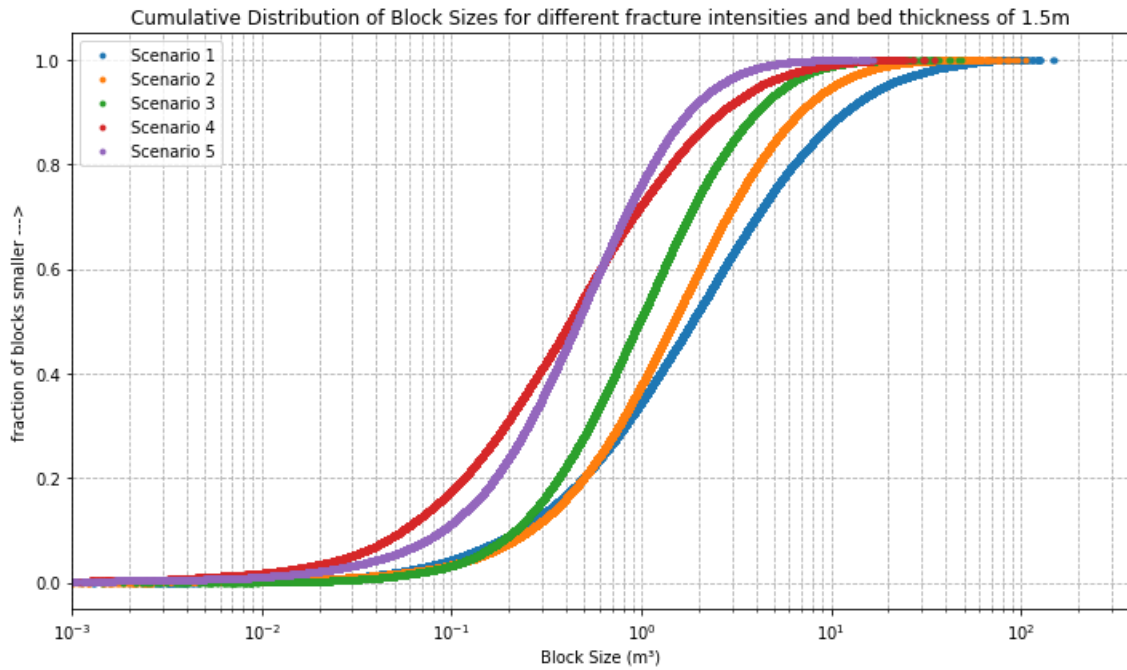


Figure 6.7: Influence of different scenario's of fracture intensity on the block size

6.4.2 Empirical solution

Empirical correlations relating the volumetric joint count ($J_v = P30$) and the average block volume have been established by (Palmstrom, 2005). The volumetric joint count (J_v or $P30$) is equal to the number of joints intersecting a m^3 of rock volume.

$$J_v = 1/S_1 + 1/S_2 + 1/S_3 \quad (6)$$

S_1 , S_2 and S_3 use the same terminology as the sensitivity analysis. A correlation between J_v and the block volume was determined to be:

$$V_b = \beta * J_v^{-3} \quad (7)$$

Where β is the block shape factor, for this study equidimensional cubical blocks are assumed which provides the safest estimates ($\beta = 27$).

Results:

The same five scenarios as in table 6.2 for the sensitivity analysis have been used for different combinations of bed thickness.

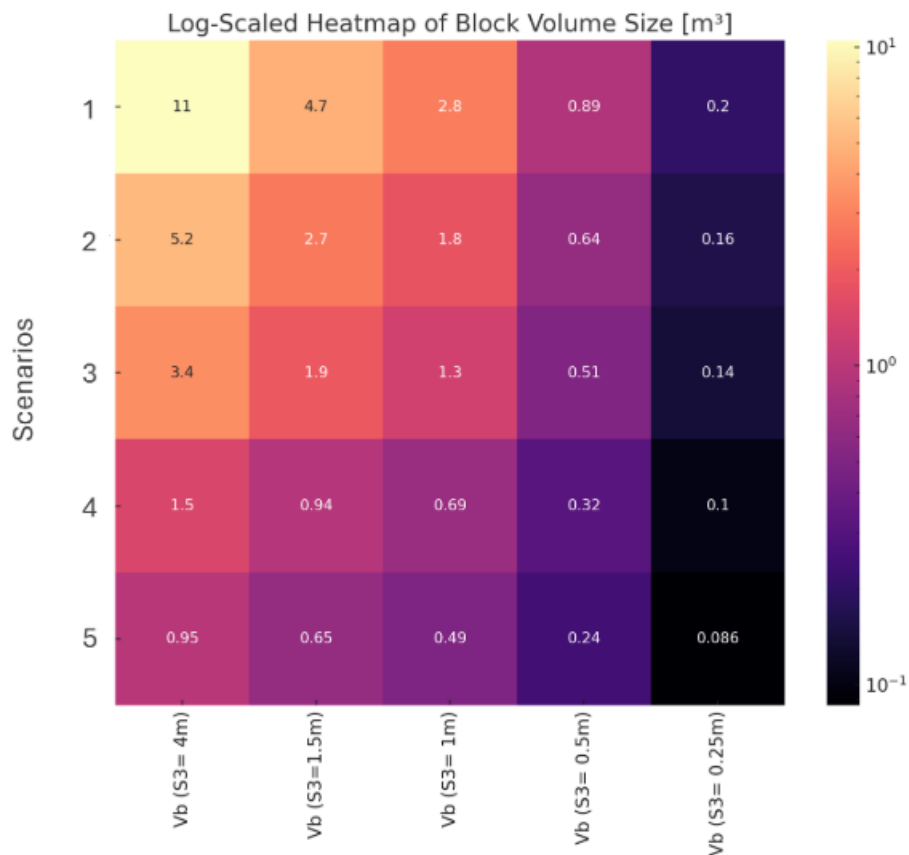


Figure 6.8: Heat map of the mean block volume using analytical solutions for different scenarios and bed thickness. (S3 = bed thickness). Block volume (vb) smaller than 1m³ is considered as blocky rock mass (Schlotfeldt & Carter, 2018).

Scenarios 3 and 4 both feature a P32 (excluding bedding) of 1.60 m²/m³. The average block volume approaching this threshold suggests a transition towards a rock mass characterized by smaller blocks (with volumes less than 1m³) as the bed thickness falls below 1m. The reduction in block volume is evident in Figure 6.6, where there is a significant shift in the distribution of block thickness towards smaller blocks between 1 and 0.5 meters. This contrast is more pronounced compared to the shift observed between blocks with bed thicknesses from 1.5 to 1 meter. For very massive bed thickness (4m), the average block volume is larger than 1m³ for 4 out of 5 scenarios. The estimates provided in figure 6.8 are conservative, as increases in bed thickness will also provide more favorable block shapes which should positively influence the block shape factor β (Elci & Turk, 2014; Palmstrom, 2005).

6.5 Geotechnical model displaying blockiness of rock mass.

(Schlotfeldt & Carter, 2018) identified that a P32 lower than 4m²/m³ leads to a massive rock mass with volumes greater than 1m³. Empirical solution for block volume estimates that a massive rock mass should have subvertical P32 joint intensity lower than 1.5m²/m³ for 1m bed thickness. This equates to a total P32 (P32 bedding + P32 subvertical joints) of 2.5m²/m³. Rogers et al. (2014) used DFN to investigate the block forming potential and found similar results.

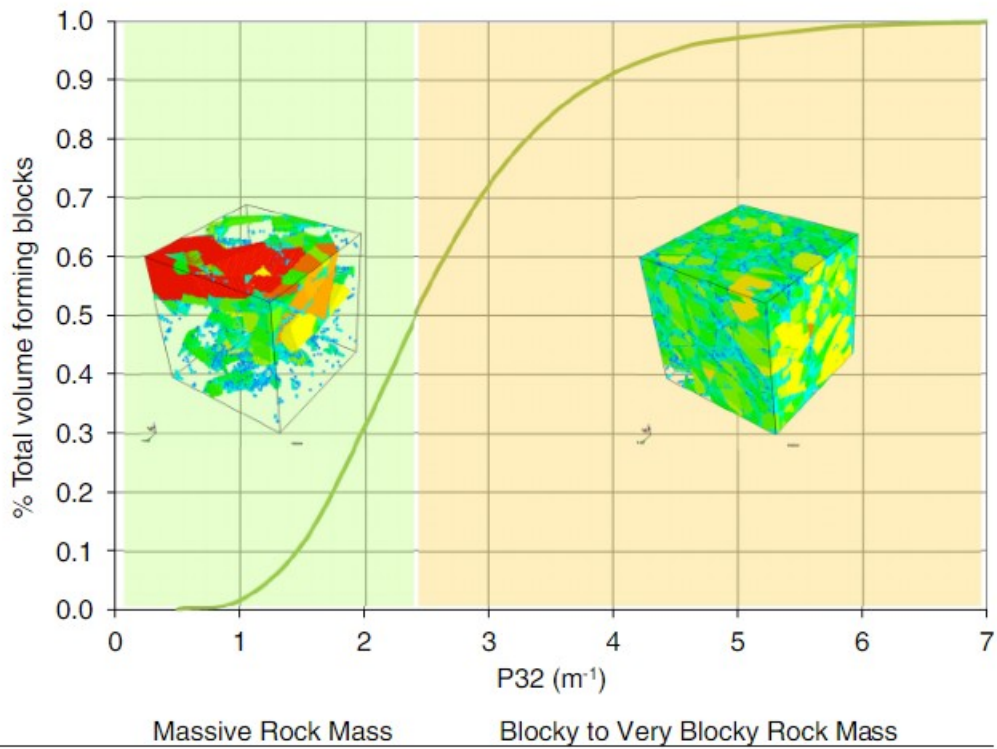
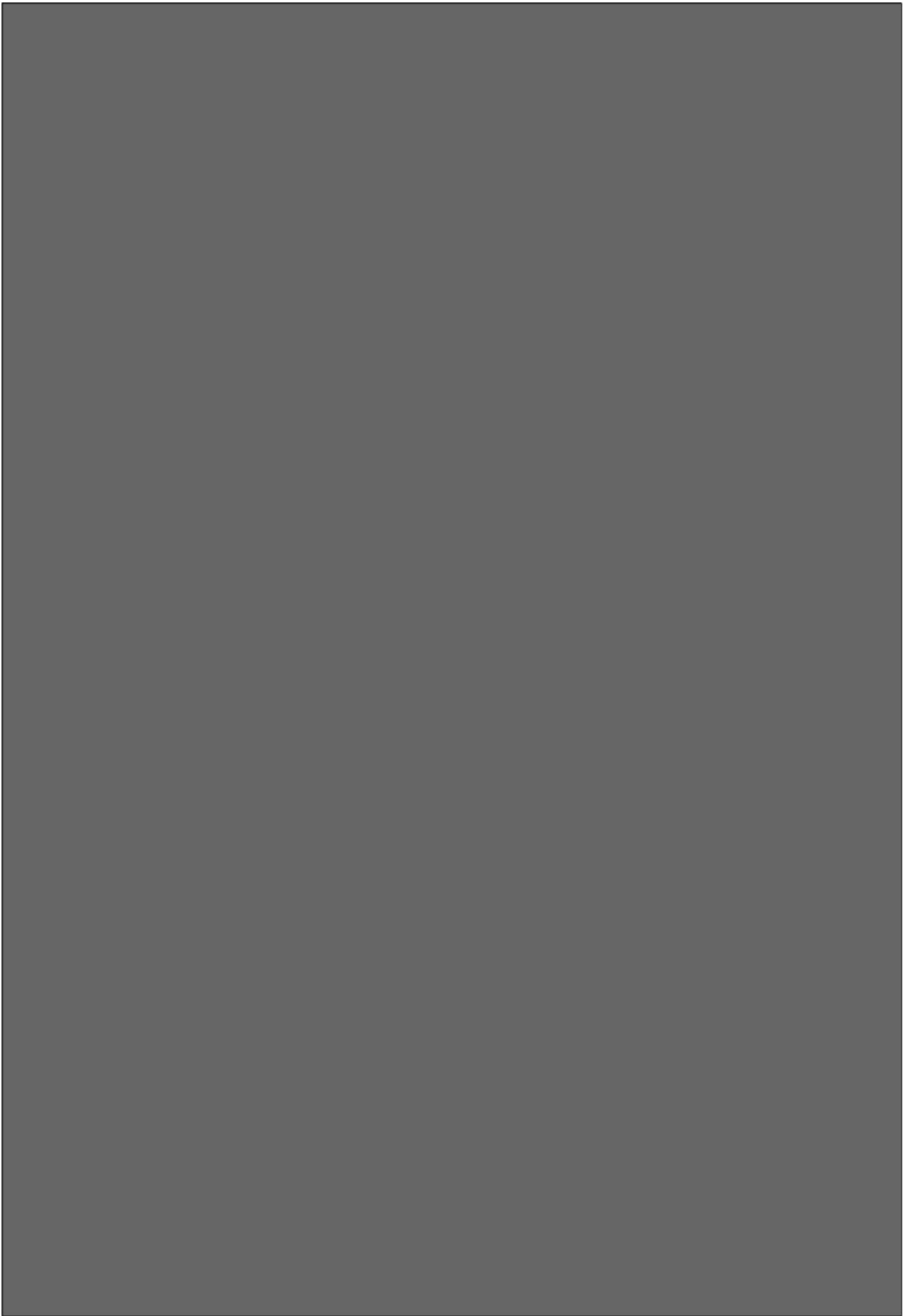


Figure 6.9: Relationship between block forming potential and P32, showing the transition between massive rock mass and blocky rock mass. Figure from Rogers et al. (2014)

Three geotechnical models displaying the block size potential of the quarry are produced assuming three scenarios for the bed thickness. The threshold determining massive and blocky rock mass correspond to a total P32 value of $2.4\text{m}^2/\text{m}^3$ for all models.



7.1 Rock mass classification

Parameters of the classification system are assigned to individual geotechnical section. The assignment of classification system parameters (RMR and Q system) to each geotechnical section relies on quantitative data for joint characteristics and UCS tests of the intact rock material (Appendix G).

The equations to estimate the RMR and Q values are provided below. The description of the ratings for each individual parameter is given in Appendix E.

$$Q = \frac{RQD}{J_n} * \frac{J_r}{J_a} * \frac{J_w}{SRF} \quad (8)$$

With:

- RQD: Rock quality design.
- J_n: Joint set number
- J_r: Joint roughness number
- J_a: Joint alteration number
- J_w: Joint water reduction factor
- SRF: Stress reduction factor

$$RMR = \sum A_i - B \quad (9)$$

With:

1. A1: Intact rock strength (Stress condition)
2. A2: RQD (Block volume)
3. A3: Discontinuity spacing (Block volume)
4. A4: JCond89 (Joint condition)
5. A5: Groundwater condition (Stress condition)
6. B: Discontinuity orientation (Stress condition)

7.1.1 Field Q values

The parameters of the Q system have only been interpreted when a photogrammetry model was available. The results for each individual geotechnical section can be found in Appendix E. Some assumptions were used to define the parameters of the Q system:

- A conservative approach to estimating the J_n was used. A J_n rating of 9 (3 joint sets) was utilized for all geotechnical sections (see section 5.1). Some geotechnical sections in formation D have no visible bedding due to dolomitization of the bedding planes. It is unclear if the dolomitized bedding planes may act as incipient joints in an underground excavation. For this reason a conservative J_n was selected.
- The RQD was estimated horizontally, utilizing the measurements of joint spacing. Moreover, the presence of dissolution features and highly weathered rock material were also considered in the RQD assessment. Sections of outcrop with a void or very weathered rock are assumed to have an RQD of 10 as per the NGI (2015).
- The joint conditions of the least favorable joint set for each geotechnical section was selected (NGI, 2015). This gives simple statistics on the J_r and J_a for the worst joint conditions inside each geotechnical section. A larger quantitative dataset for individual joint statistics is available in section 4.2.

- The NGI also uses a strength reduction factor (SRF). SRF values have been selected based on the presence of weakness zones and karstic zones. Two SRF values have been used during this study when a weakness zone was encountered (5 and 10). The SRF values used, along with a description of its use is given in table 7.1. When no weakness zone was present on a geotechnical section, an SRF value of 1 was used.

Table 7.1: SRF values used for different weak zones found in the study area.

SRF value	Corresponding weak zones
5	Single narrow weakness zones (0.5m-3m wide)
10	Multiple narrow weakness zones inside a single geotechnical section
10	Large weakness zone (weakness zone $\geq 3m$) low UCS values due to chemical weathering. Long sections with incompetent weak rock.

Example:

In table 7.2, typical Q values found in the study area are displayed. An example of three geotechnical sections analysed with the Q system is given on figure 7.1.

Table 7.2: Typical range of Q values found in the study area.

Rock condition	RQD	Jn	Jr	Ja	SRF	Q	Comment
Typical Minimum (Very poor rock)	70	9	1	8	5	0.19	Area containing a small weakness zone. Including heavily weathered joints.
Typical Poor condition	90	9	2	6	1	3.33	Joint without shear wall contact after 10 cm of shear. Spacing $>3m$ between joints. Silt infill.
Typical fair	90	9	2.5	3	1	8.33	Rough planar joint with spacing $>3m$
Typical Max (good)	100	9	3	1	1	33.33	Rough undulating joint, no alteration.
Most frequent	95	9	3	3	1	10.56	Rough undulating joint with thin sand coating.

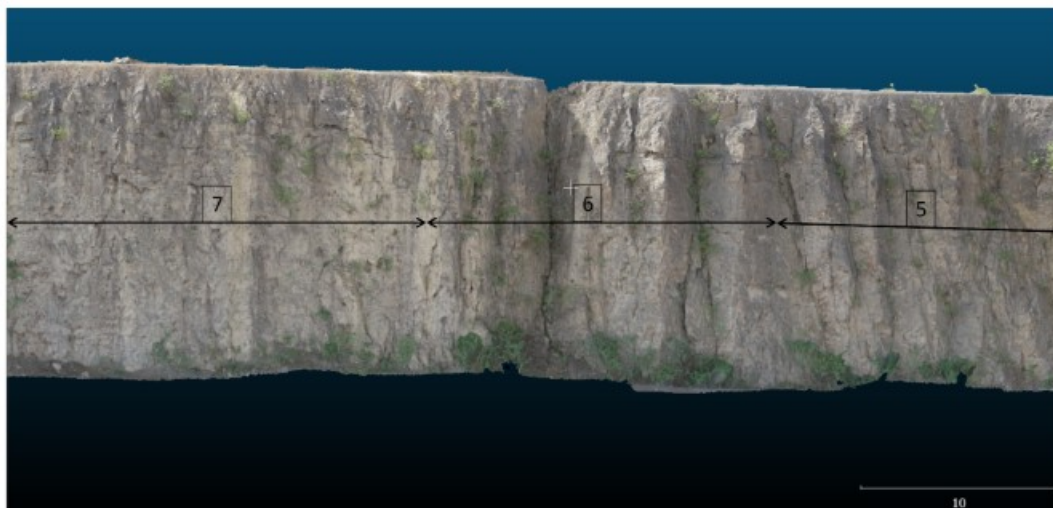


Figure 7.1: Outcrop divided into three geotechnical sections. The description and Q value for each section is provided in table 7.3.

Table 7.3: Example of Q values for three geotechnical sections observed in figure 7.1

I.D.	Width [m]	RQD [%]	Jn	Jr	Ja	SRF	Q	Description
5	15	75	9	3	3	1	8.33	Fracture corridor with altered joints. Infilling of joints is 1mm maximum and consists of dolomitic sand.
6	15	95	9	2	6	1	3.52	1 joint without wall contact after 10cm of shear but, with wide spacing between next joint Jr = 2. (NGI, 2015) Gouge as infill.
7	26	100	9	3	1	1	33.33	Massive dolomite, bedding is not visible. No joint infill.

Results

It was only possible to recover reliable results for the geotechnical domains S2a, S2b and the F domains. No photogrammetry model was available for domain S1.

Table 7.4: Percentages of rock quality in the different geotechnical domains based on 81 geotechnical sections.

Geotech domain	>Very poor	Poor	Fair	Good	Mean Weighted Q value
S2a	3%	29%	23%	45%	11.49
S2b	5%	9%	17%	72%	14.53
F-domains	43%	16%	12%	29%	4.49

The % of good rock (NGI classification) is much higher in domain S2b than in domain S2a. This is because the joint condition improves below bench 6 (outside the F domains). The F domains have, on average, much higher percentages of very poor rock conditions. This is due to the presence of many weakness zones. Domain S2b has a higher mean weighted average Q value because of improved joint conditions.

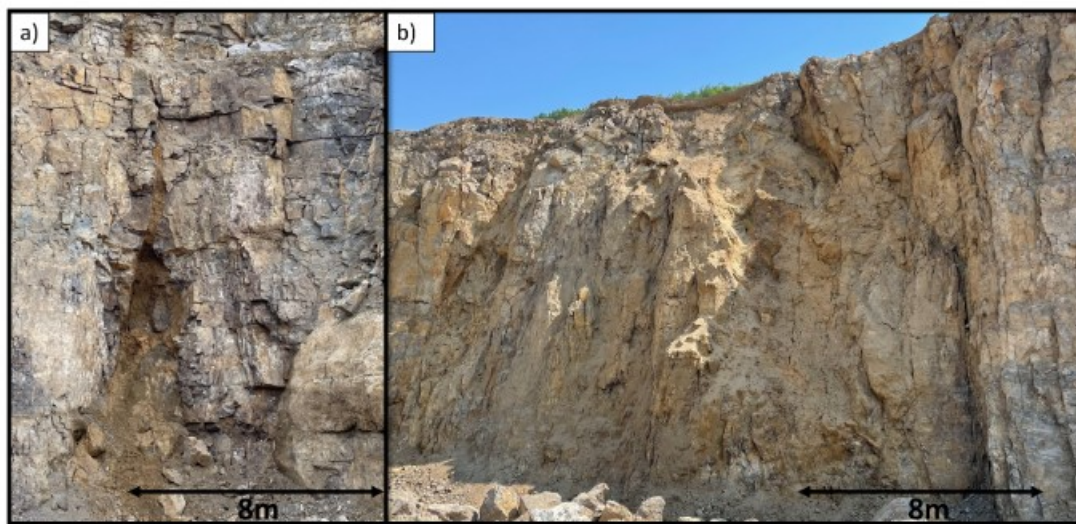


Figure 7.2: (a) Narrow weakness zone on bench 2 (Domain S0) (b) Large weakness zone in domain F3.

7.1.2 Field RMR

The field RMR was collected on the same locations as the Q values. A RMR value was only provided when a photogrammetry model was available for the purpose of third party verification. The results for the parameters of the RMR for each geotechnical section is provided in Appendix E. The parameters of the RMR have been estimated as follows:

- A1, UCS: Laboratory tests have been performed on the rock samples from the MLD quarry (Appendix G). The UCS results from the laboratory tests varied between 54-300 MPa. Heavily altered dolomite rock have not been tested because they could not be recovered from rock cores, however Schmidt Hammer tests performed on altered dolomite in the field suggest that heavily weathered rock material have UCS values between 25-50 MPa. The three ratings used for parameter A1 are given in table 7.5.

Table 7.5: Interpreted UCS values based on 27 UCS tests provided in Appendix G.

Comment/rating	UCS (Mpa)	Rating
Heavily weathered zone	25-50	4
Moderately altered dolomite (associated with fracture corridors)	50-100	7
No chemical alteration of the rock material	100-250	12

- A2, RQD: The same RQD values as estimated for the Q system have been used for the RMR rating.
- A3, joint spacing: The average true joint spacing per set measured in section 5.2.6 are used. The values range from 0.73 to 2.7m in average fracture spacing. Ranges slightly lower (0.2-0.6m) in fracture spacing will be used as parameters of the RMR for geotechnical sections inside fracture corridors. Two ratings for the joint spacing were used according to simple rules.

Table 7.6: Ratings used for the joint spacing based on quantitative datasets collection on virtual outcrops

Comment/Rating	Interpreted joint spacing	A3 Rating
Inside fracture corridor	0.2-0.6m	10
Outside fracture corridor	0.6-2m	15

- A4, joint condition: the worst joint condition will be used for each geotechnical section. Four main joint ratings will be used to rate each geotechnical sections (see table 7.7). All geotechnical section have been estimated to have joints with persistence (equal to joint height) of over 20m.

Table 7.7: Four typical joint condition found in the study area and used to estimate field RMR.

Comment/A4 subratings	A4a-Persistence	A4b-Aperture	A4c-Roughness	A4d-Infill	A4e-Weathering	A4-Total
Persistence (joint height) > 20m, aperture >5mm and silty clay infill, decomposed joint.	0	0	0	0	0	0
Persistence >20m, aperture >5mm with gouge infill and slightly rough surface.	0	0	3	2	0	5
Persistence >20m, aperture between 1-5mm with hard infill. Moderately weathered.	0	1	5	2	3	11
Persistence >20m, aperture 1mm with no infill, and slight joint weathering.	0	4	5	6	5	20

- A5, water inflow: similarly to the Q system it is assumed that the area is dry and no inflow of water is taken into account.
- B, joint orientation: a B rating of "fair" (-5) was used for every geotechnical section.

Results:

In total, the same 81 geotechnical sections as the Q system have had geotechnical descriptions, the results are displayed in table 7.8. The results show that the mean weighted RMR (mean RMR taking into account the length of each geotechnical section) value for both domain S2a and S2b can be considered as good rock quality. More than 95% of the geotechnical sections in domain S2a and S2b have a fair or good RMR rating. The F-domains have 35% interpreted poor RMR rating with an average fair RMR rating.

Table 7.8: Percentage of poor, fair and good rock mass rating for each geotechnical domain.

Geotech domain	Poor	Fair	Good	Mean Weighted RMR
S2a	1%	32%	67%	65
S2b	5%	7%	88%	73
F-domains	35%	27%	38%	51

7.1.3 Borehole Q values

The borehole Q values have been estimated using the geotechnical descriptions of the rock cores. The NGI cautions against using rock core descriptions to estimate the Q values. Some assumptions had to be made for the parameters of the Q system.

- Jn: Every geotechnical section was assumed to have 3 joint sets (Jn = 9). The same assumption was made to determine the Jn parameters for the field Q values.
- RQD: The RQD was measured for every geotechnical section using a measuring tape.
- Ja and Jr: The worst joint condition description was used for every geotechnical section.
- Jw: The water condition rating (Jw) used for every geotechnical section is 15, it is assumed that any excavation would be dry.
- SRF: All geotechnical sections were rated with SRF value of 1, the subvertical weakness zones observed in the quarry were parallel to the drilling direction and could be hard to estimate. However, the percentage of core recovery can give indications on the presence of weakness zones.

The weighted average Q values was measured by accounting for the length of each geotechnical section similarly to Golder Associates reporting methodology (Golder, 2013). The Q values in addition to the % of cores without geotechnical description and percentage of core recovery is given for all geotechnical domains.

Table 7.9: Weighted Q values from borehole core descriptions, percentage of borehole length without geotechnical description and percentage recovery by domain

Domain	Weighted average Q	Min Q	Max Q	Percentage rock core with no geotechnical descriptions	Percentage recovery.
S1- (BH176, BH180, BH181)	17.21	1.12	44.44	5%	92%
S2a- (BH176, BH180, BH181)	14.9	1.3	43.44	6%	88%
S2b- (BH176, BH180, BH181)	18.75	0.32	44.44	1%	96%
F - BH172	5.81	0.33	32.68	29%	80%
F - BH177	7.09	0.29	41.22	29%	73%

The results from the borehole Q values are higher than the field Q values. Geotechnical borehole sections usually had better joint condition. The boreholes are subparallel to the joints J1 and J2, and not all borehole sections intersected J1 or J2 joints. Subvertical joints J1 and J2 usually had adverse affects on Jr and Ja ratings for the field Q values. Additionally, no SRF value could be estimated, increasing the minimum Q values.





Figure 7.3: Single visible bedding plane (Black box) on a 30 meter wide, 15 meter high outcrop (Bench 2 location without karst).

Table 7.10: Q values with $J_n = 4$, assumption of large bed thickness without continuous bedding surfaces.

Geotech domain	>Very poor	Poor	Fair	Good	Very Good	Mean Weighted Q value
S2a	2%	3%	24%	66%	6%	25.71
S2b	5%	0%	7%	61%	27%	32.69

7.1.5 Joint condition influence on RMR and Q values



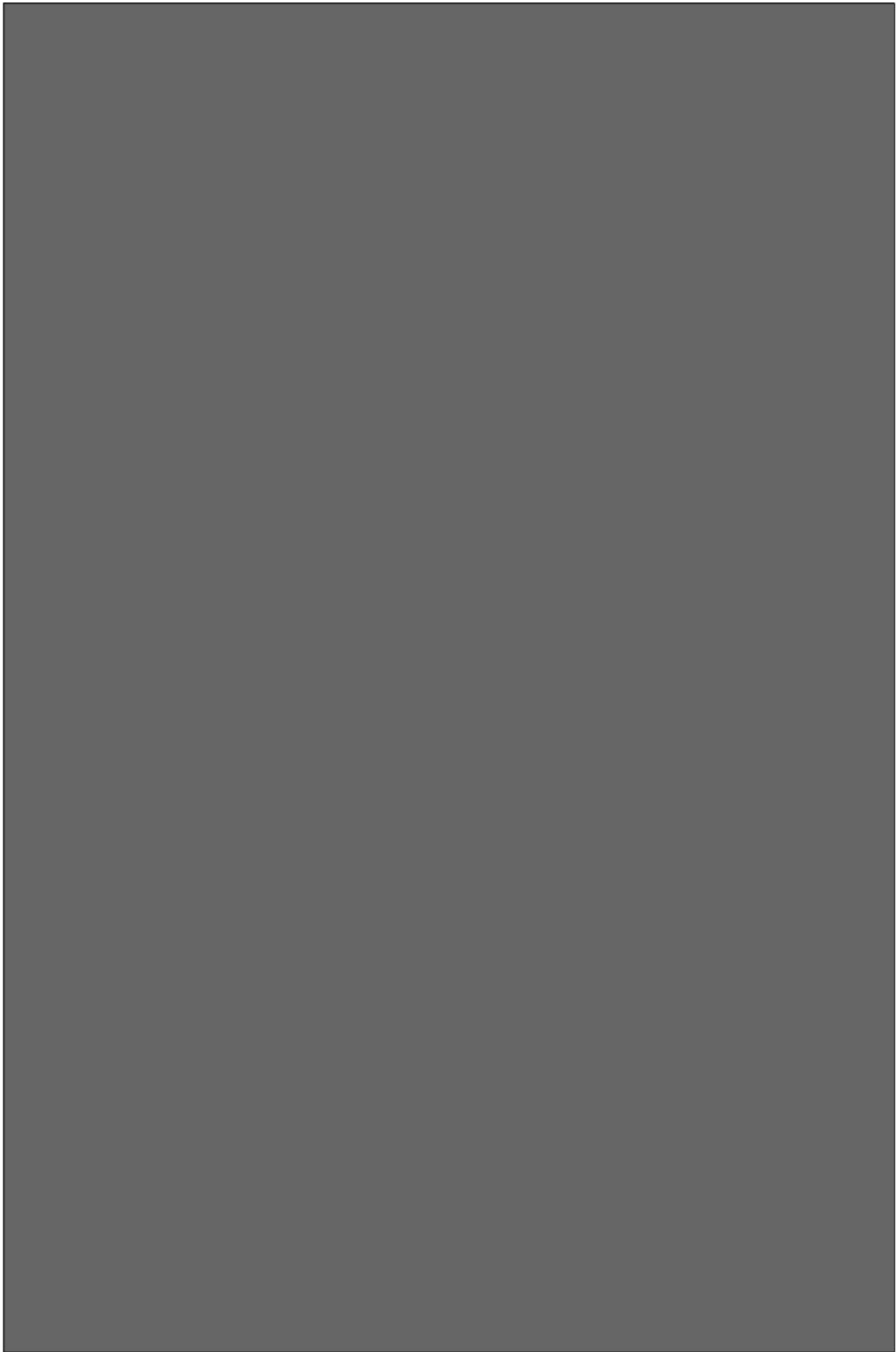
Table 7.11: Q values disregarding large dissolution joints with wide spacing between each other.

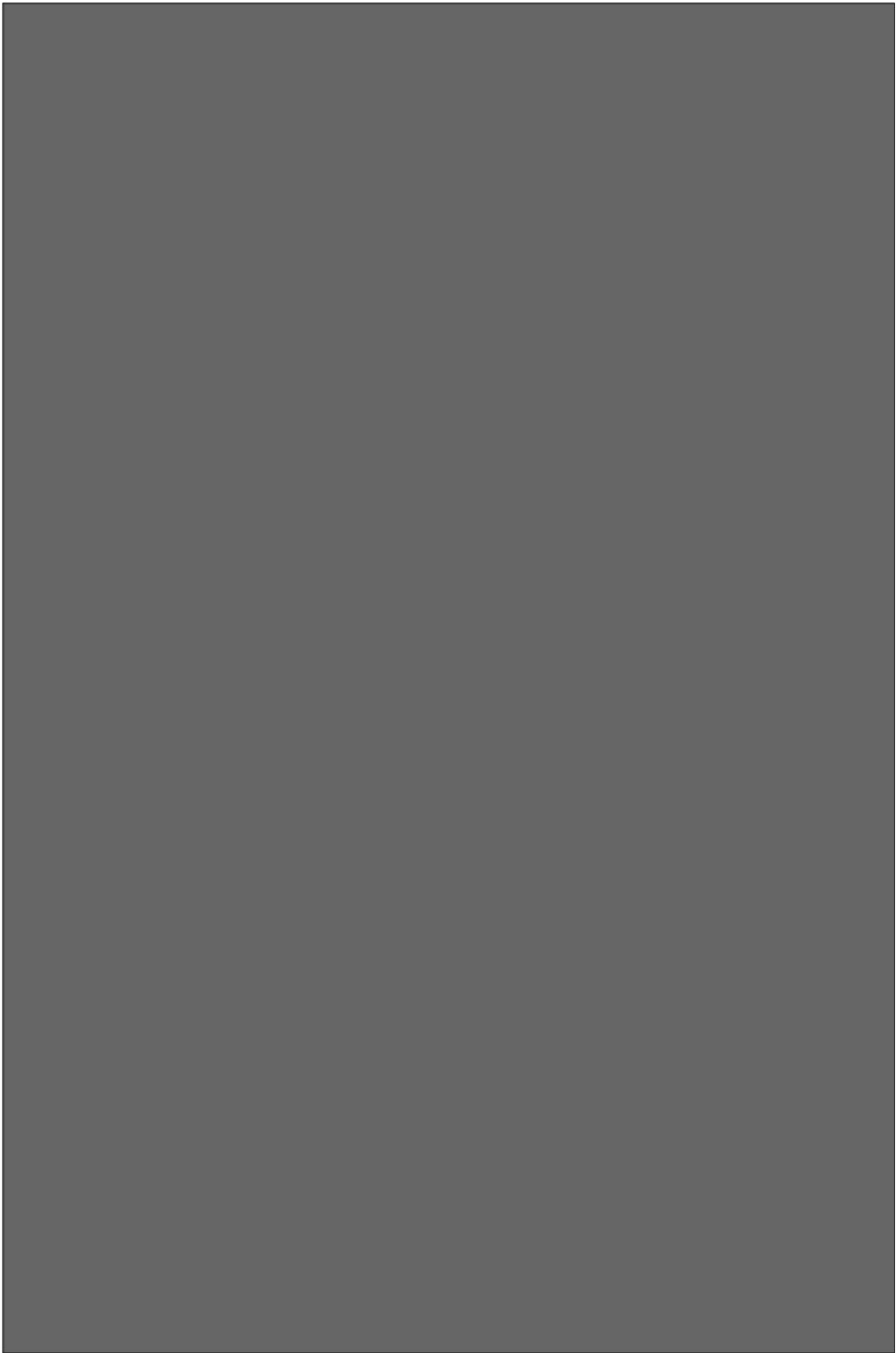
Geotech domain	>Very poor	Poor	Fair	Good	Mean Weighted Q value
S2a	3%	10%	32%	55%	13.01
S2b	5%	0%	24%	72%	14.90

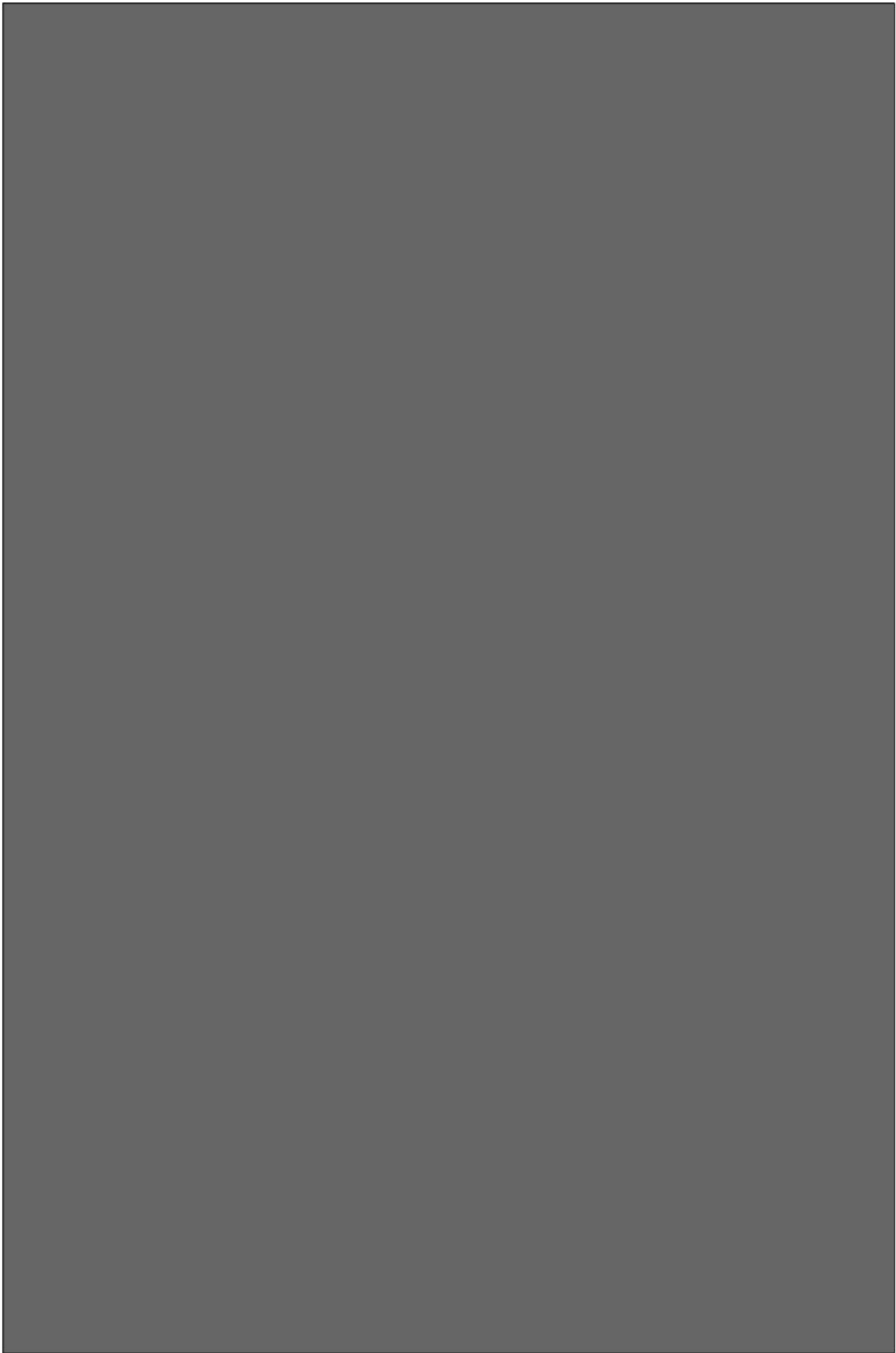
Table 7.12: RMR values disregarding large dissolution joints with wide spacing between each other.

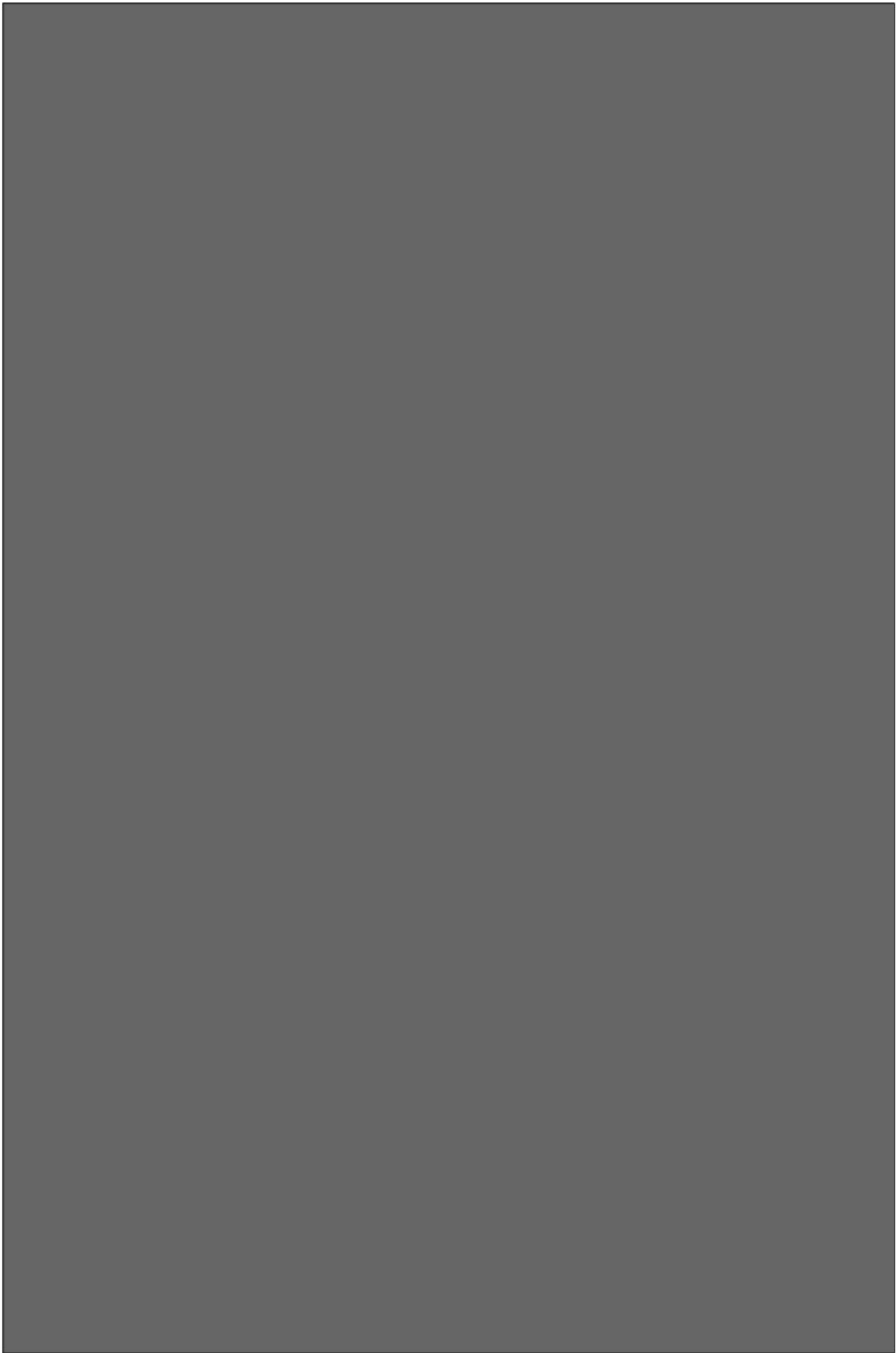
Geotech domain	Poor	Fair	Good	Mean Weighted RMR
S2a	1%	25%	74%	66
S2b	0%	7%	93%	74

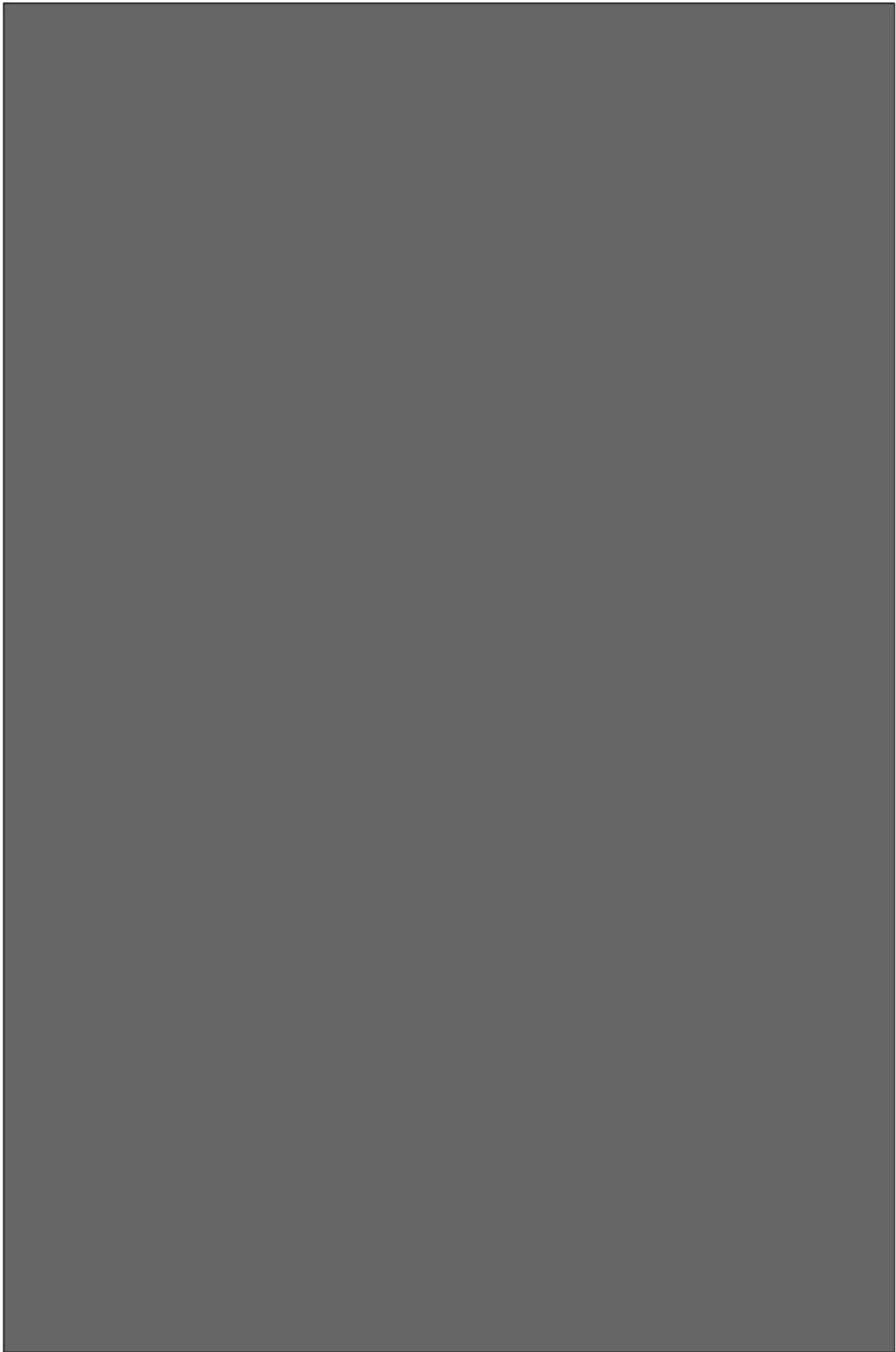


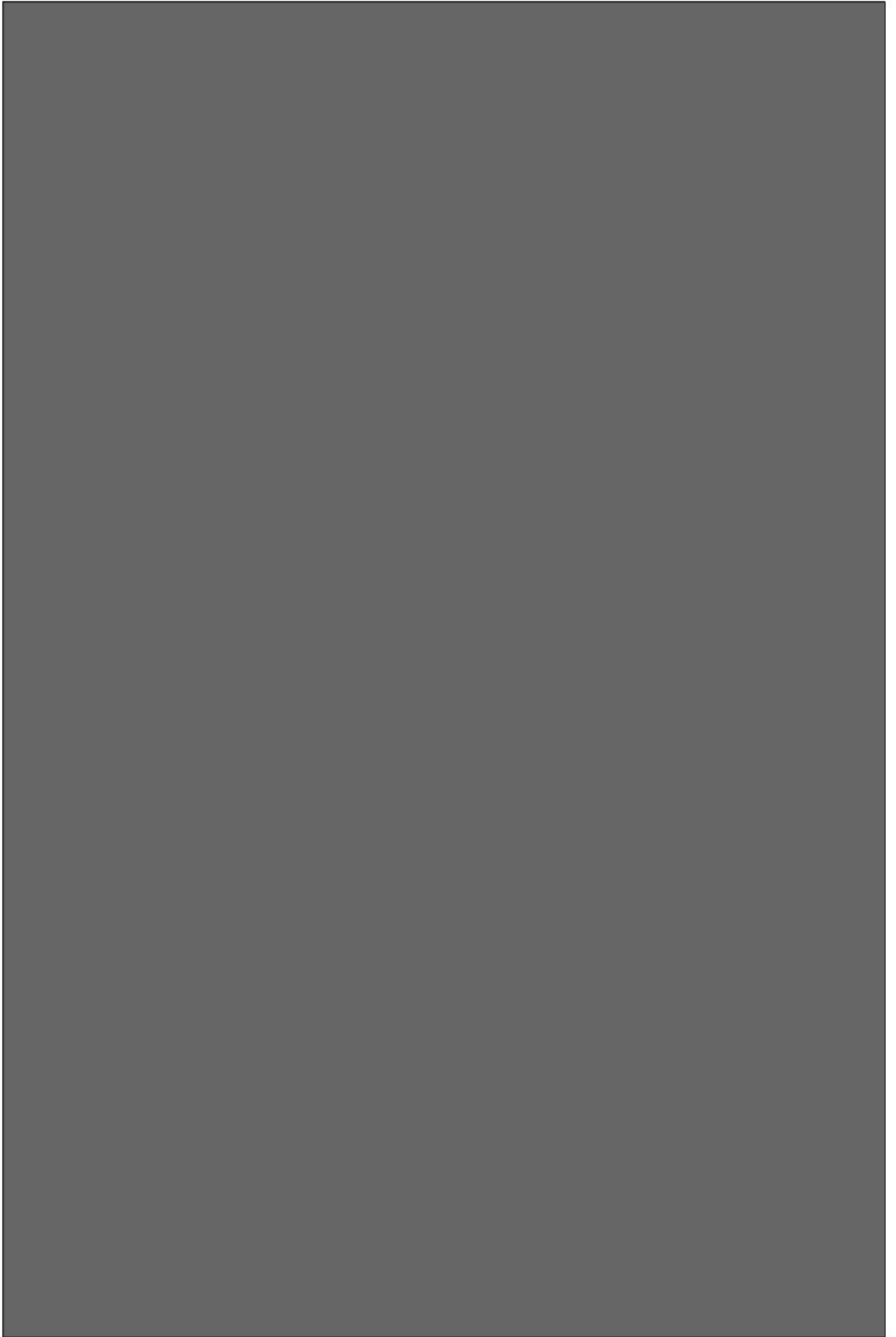


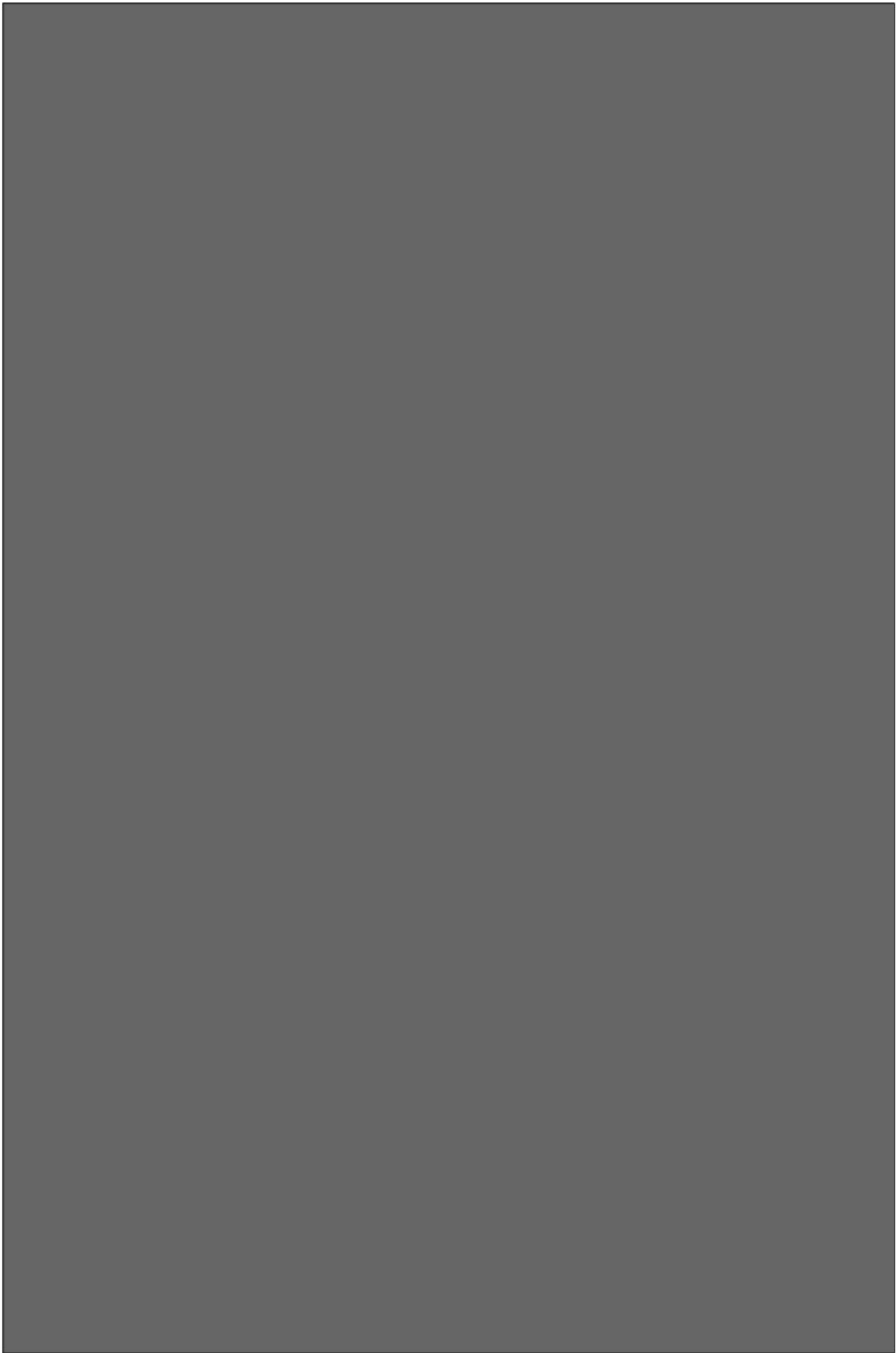


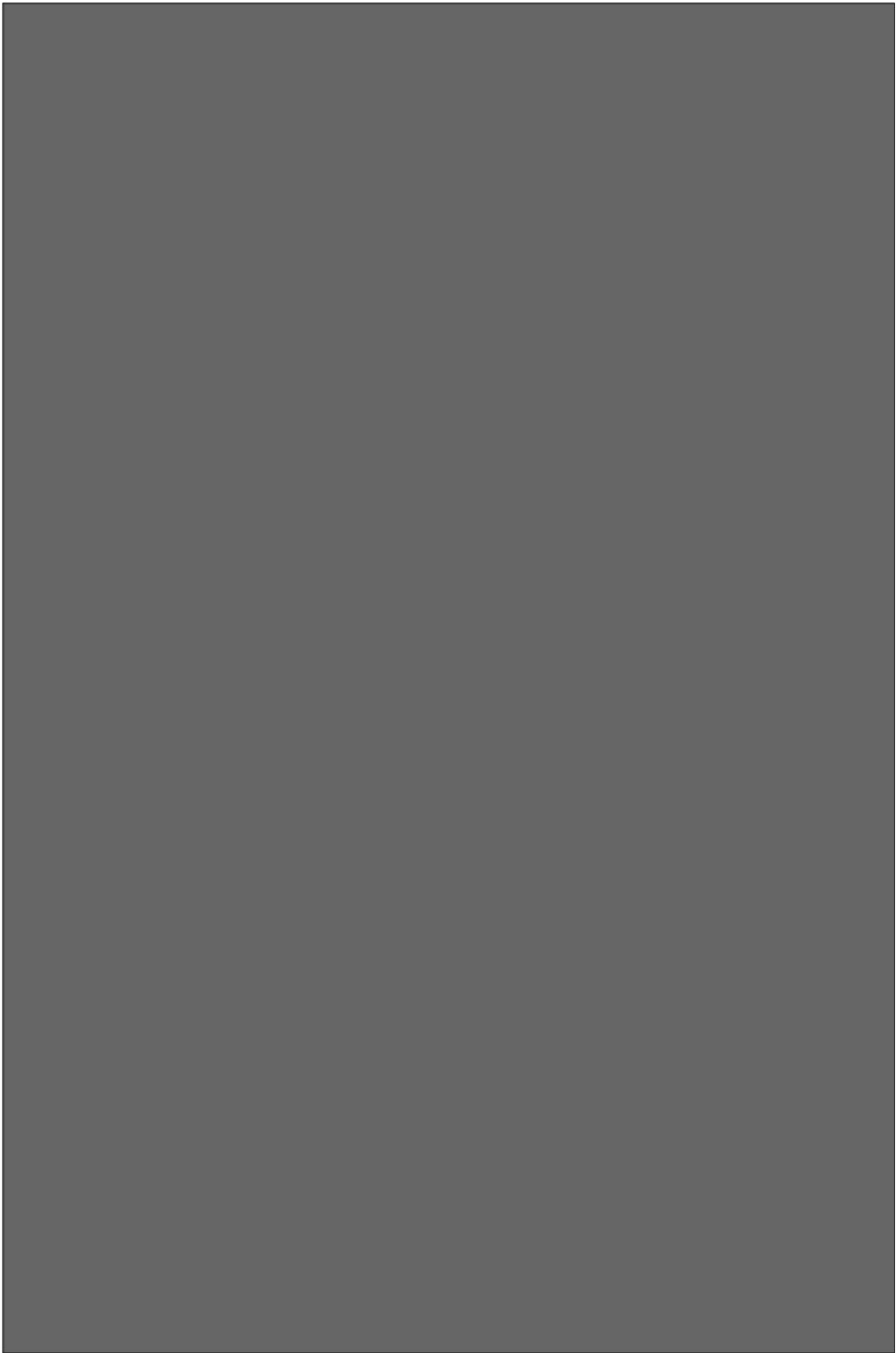


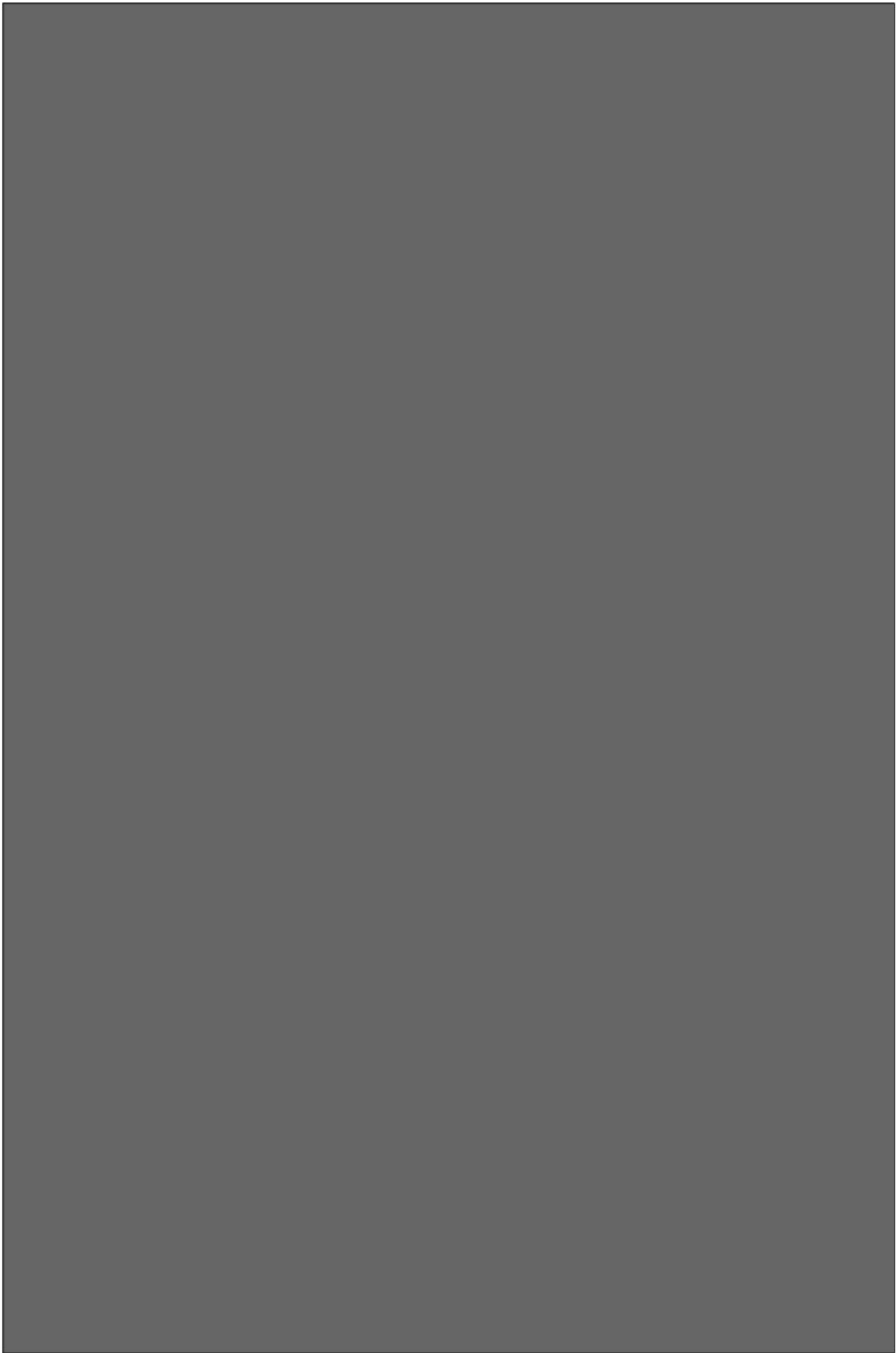


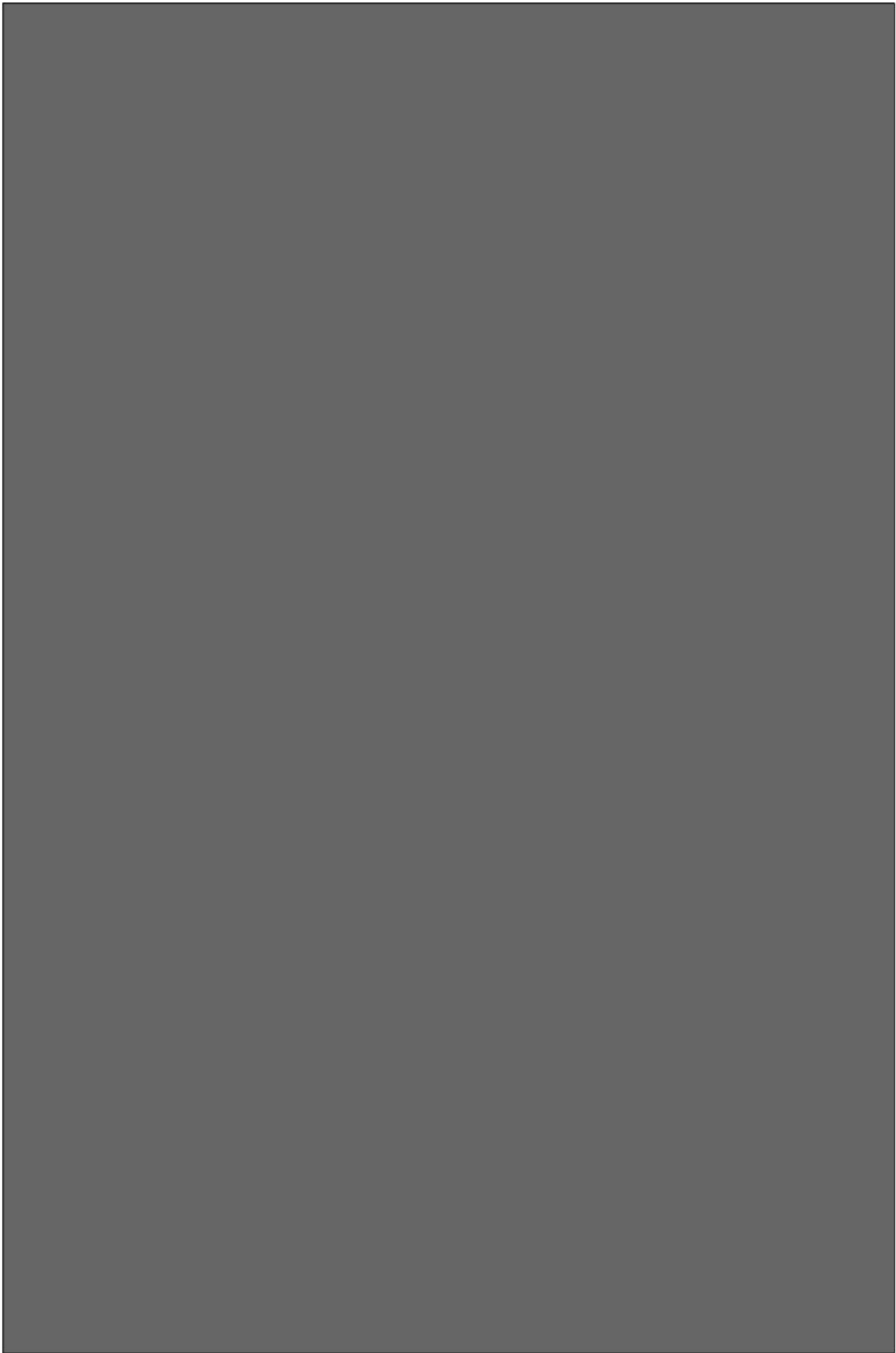












8 Discussion

8.1 Dataset validity

The dataset on joint intensities collected based on photogrammetry can be compared to Van der Voet (2022) P21 data on large orthophotos on bench 6, 7 and 8 (named SW EV in table 5.2). Human biases in joint tracing, the resolution of the model, lighting conditions in photographs, and the methodology used for data collection can all impact the P21 data (Bisdorn, 2011). The similarities in P21 results between this study and those reported in the study by Van der Voet (2022) serves to validate the data joint intensity acquisition methodology. SW6 exhibits higher P21 values compared to those reported by (Van der Voet, 2022) because the measurements were taken within a fracture corridor. Additionally, SW8 and SW7 have been traced on a different formation (E) than Van der Voet (2022) data. Those datasets have been removed from figure 8.1.

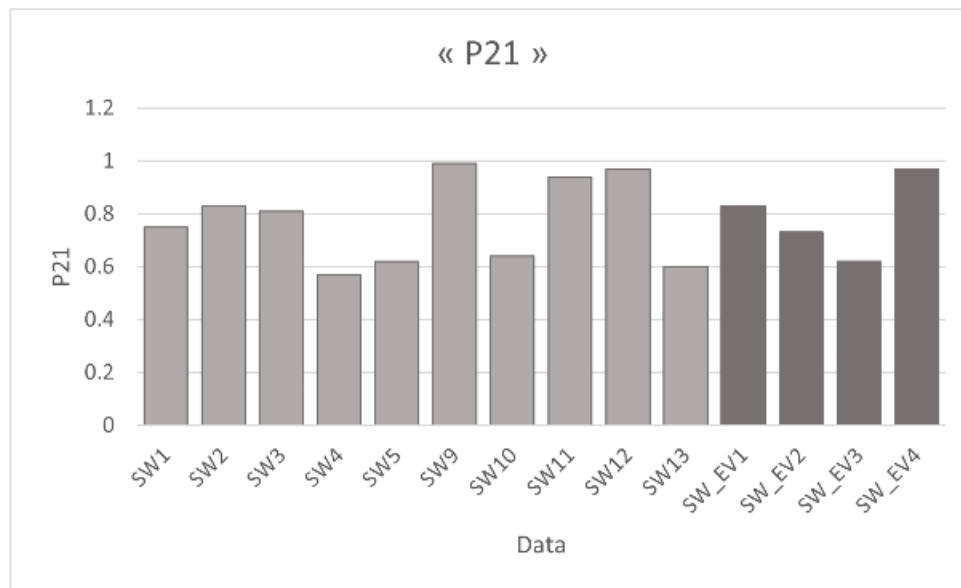


Figure 8.1: Aggregate P21 results from this study (Lightgrey) and aggregate P21 values from Van der Voet (2022) study (Darkgrey)

The joint intensities interpreted from the boreholes are more uncertain. Oriented rock cores or borehole optic scans could help to improve statistics on joint intensities collected from boreholes. Resolution issues from optic scans should also be considered and core descriptions should be done adjacent to optic scan interpretations.

The range of joint orientations collected during this study are also similar to those collected by Mathieu (1962); Van der Voet (2022). No dataset on the joint condition in the study area were available. Verification on the joint condition dataset is thus impossible. Further statistics on the joint condition should be collected. It is advised to collect joint condition data in the mine shafts as they better represent the in-situ joint condition because the joints have not been affected by weathering. The joints in the mine shafts were also excavated at a pace of 2-3 meters a day using hydraulic machinery (Pacyna & Denayer, 2010).

8.2 DFN modelling for geotechnical application

The variations in subvertical joint intensity interpolated can give insight on the joint intensity distribution across the quarry. The main finding is that the variations in subvertical joint intensity outside the F domains are generally not substantial enough to significantly affect block size. Instead, variations in bed thickness plays a more critical role in determining the block forming potential. This indicates that while the DFN and kriging interpolations provide valuable insights into subvertical joint distribution throughout the quarry, the variation in bed thickness, is a more

decisive factors influencing block volume in the study area.

In this study, the practical applications of DFN for geotechnical modeling are limited. However, the datasets collected during this study could be used for other DFN modelling applications in rock mechanics, mainly:

1. To conduct block size analysis (Rogers et al., 2014; Schlotfeldt & Carter, 2018; Takako et al., 2018).
2. To explicitly represent fractures in the rock mass for numerical modelling applications.

The MOVE software is primarily developed for reservoir engineering applications, allowing users to model reservoir properties such as permeability, construct geological models, and simulate large-scale subsidence. However, it has significant limitations for geotechnical engineering uses. For example, DFN models cannot be used for block size analysis.

Variations in fracture intensities can also shed light on the hydraulic network of the quarry. Passagez (2012) established that the subvertical joint sets J1 and J2, along with strike-slip faults dating back to the extensional domain, act as preferential networks for water flow paths. These preferential water flow paths, associated with the main joint sets, have created favorable conditions for rock mass alteration. The findings from Passagez (2012) are also evident on bench 8, which did not exist at her time (see figure 8.2 (a)). A slickensided surface, with an orientation similar to that of the J2 set serves as a preferential water flow path. Observations of water percolating or gushing from the bench walls of the quarry mainly comes from high-iron zones defined by Lhoists's chemical data. This is not surprising given the relationships between Iron sulphides- faults and karst discussed in section 3.3.8.

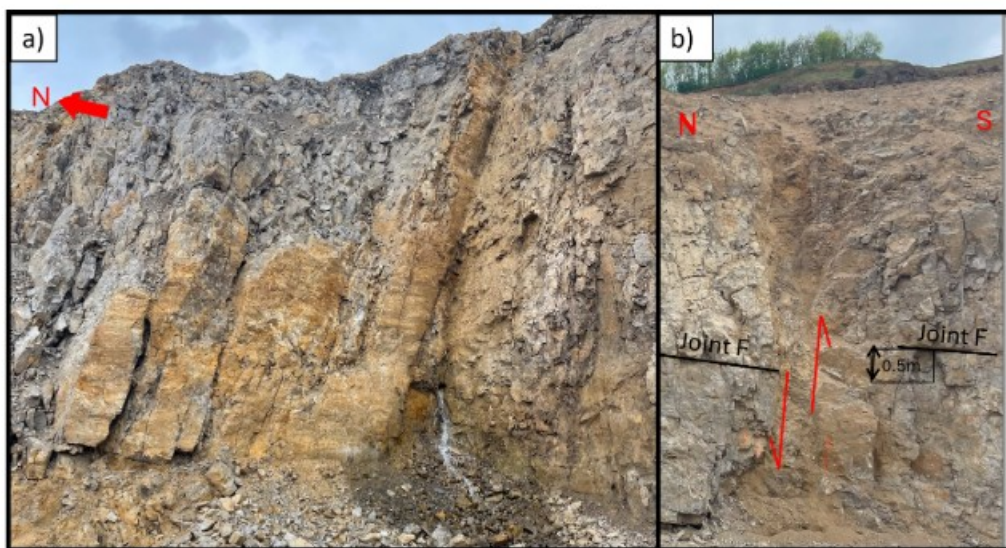
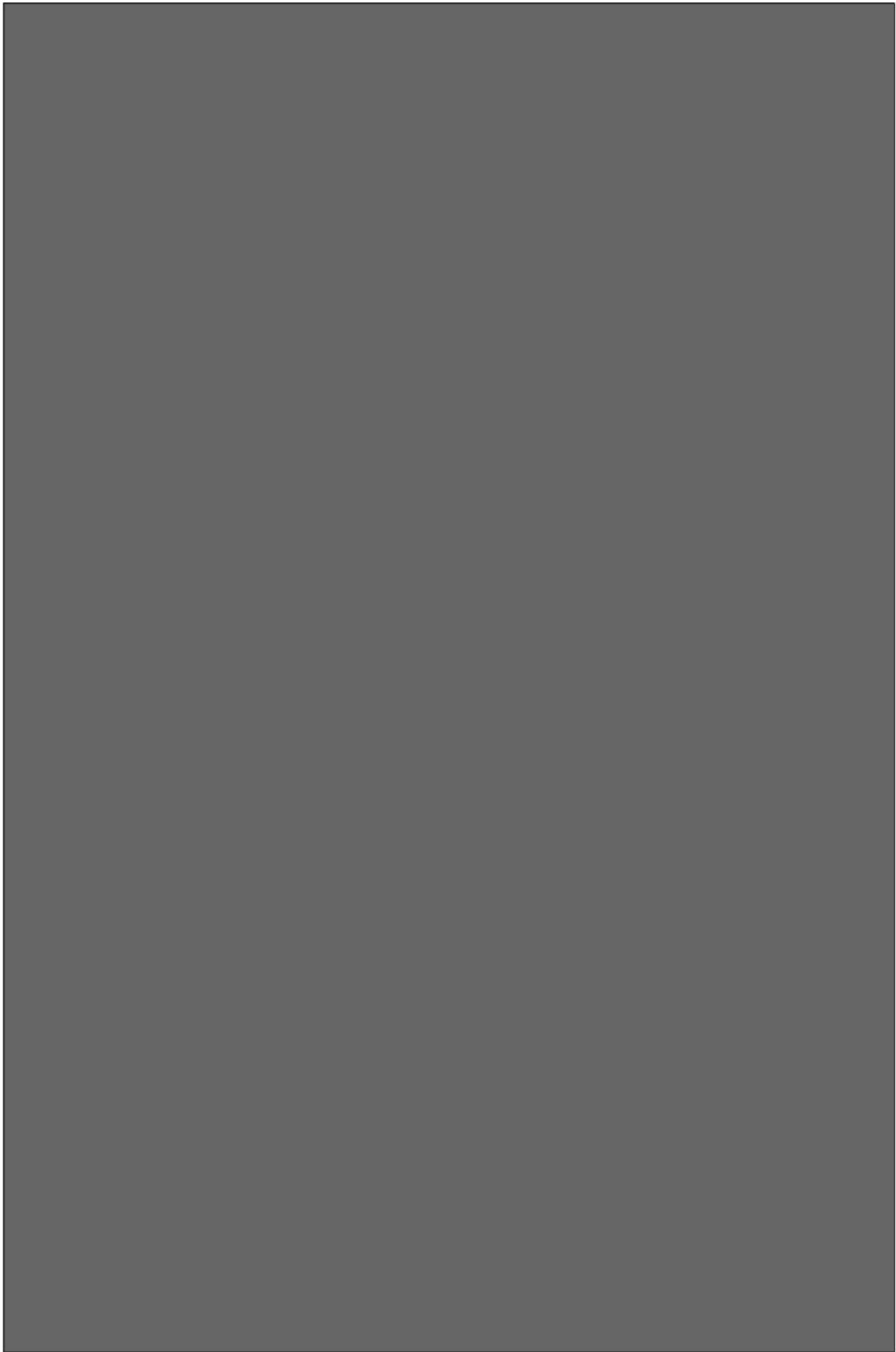


Figure 8.2: a) Slickensided surface with similar orientation as the J2 set on bench 8 acting as preferential water flow path. b) Fault on bench 7 oriented E-W probably dating to the Hercynian orogeny.

Coupled geostatistical models like those introduced by (Bruna, Guglielmi, Viseur, Lamarche, & Bildstein, 2015), which integrate fracture intensities with hydrogeological data (for example, slug well tests), could equip the study area with a structural model that enhances understanding of karstic zones. Increasing the hydrogeological dataset could also serve to build more complex numerical geohydrological models that incorporate anisotropy, unlike the models presented Passagez (2012). It is also recommended to prioritize sub-horizontal drilling to better assess the extent of the karsts inside the F domains.



9 Conclusion

The research aimed to leverage a diverse array of data sources, such as photogrammetry, field surveys, and borehole core descriptions, to gather information on joint properties within the study area. The objectives were twofold: to create a geotechnical map that delineates different geotechnical domains and to develop comprehensive Discrete Fracture Network (DFN) models for predicting in-situ joint intensities.

During this study, datasets detailing the joint properties have been collected throughout the quarry. The dataset on the joint properties bring valuable information to Lhoist. Combining the data collected in the field, literature review and corroborating field observations established that:

- Chemical contamination, high joint intensities, chemical alteration and preferential water flow path are all related. The alteration and hydrology of the area is mainly organised along the two main subvertical joint sets and minor strike-slip faults with similar orientations dating to the Jurassic-Cretaceous extensional domain.
- One of the two subvertical joint sets (J2) is more likely to be affected by dissolution phenomena.
- The amount of dissolution joints, and width of the subvertical karstic zones decreases with depth. Below bench 6 and outside the F domains, large dissolution joints should only occasionally be found.
- Dolomitization during the Visean has significantly affected the bed thickness of Tournaisian dolomite. Some locations in the stratigraphic sequence can be 5-10 meters thick without continuous bedding plane (Avin member and Lhoist formation D0 for example). Those

The characterization of the joint properties also influenced the geotechnical domain definition. The domains can probably provide a reasonable assumptions on the geotechnical conditions between the boreholes and the outcrops of the quarry. Sub-horizontal boreholes could help refine the characterization of the subvertical F domains.

One of the goals of this study was to predict in-situ joint intensities using DFN models. The methodology used during this study does not work, the DFN models in MOVE are generated from interpolated joint intensities. The application of DFN to predict in-situ joint intensities, or to assist in the design of a geotechnical model is limited in this study. The datasets collected during this study can be utilized for further DFN applications, which may prove more useful for geotechnical purposes.

Assumptions regarding the bed thickness plays a critical role in determining the block-forming potential in the study area. Further research is needed to explore the influence of dolomized bedding planes and variations in bed thickness. Variations in subvertical joint intensity have a limited impact on block size, outside of the F domains.

10 References

References

- Allmendinger, R. (2023, November). *Stereonet*. Retrieved 2023-12-22, from <https://www.rickallmendinger.net/stereonet>
- Bai, T., Pollard, D. D., & Gao, H. (2000, February). Explanation for fracture spacing in layered materials. *Nature*, 403 (6771), 753–756. Retrieved 2024-03-09, from <https://www.nature.com/articles/35001550> (Publisher: Nature Publishing Group) doi: 10.1038/35001550
- Barton, N. (1978, January). Suggested methods for the quantitative description of discontinuities in rock masses: International Society for Rock Mechanics. *Int J Rock Mech Min Sci Geomech Abstr*, 15, 319–368.
- Barton, N., Lien, R., & Lunde, J. (1974, December). Engineering Classification of Rock Masses for the Design of Tunnel Support. *Rock Mechanics Felsmechanik Mecanique des Roches*, 6, 189–236. doi: 10.1007/BF01239496
- BCG. (2022). *Dolomies de Marche-les-Dames, Recherche de phénomènes karstiques*.
- Bieniawski, Z. (1989). *Engineering Rock Mass Classifications. A Complete Manual for Engineers and Geologists in Mining, Civil and Petroleum Engineering*. A Wiley-interscience publication.
- Bisdorf, K. (2011). Modelling 3D Discrete Fracture Networks using 2D outcrop data. Retrieved 2022-11-09, from <https://repository.tudelft.nl/islandora/object/uuid%3A913c29d4-d845-4914-bde6-fdb00b52f47d>
- Bishop, R. (2020). *Applications of Close-Range Terrestrial 3D Photogrammetry to Improve Safety in Underground Stone Mines* (Doctoral dissertation). doi: 10.13140/RG.2.2.18065.04967
- Bishop, R., Monsalve, J. J., Baggett, J., Soni, A., & Ripepi, N. (2019). *A Comparison of Laser Scanning and Photogrammetry in an Underground Limestone Mine*. doi: 10.13140/RG.2.2.11354.16320
- Bonnet, E., Bour, O., Odling, N., Davy, P., Main, I., Cowie, P., & Berkowitz, B. (2001, August). Scaling of fracture systems in geological data. *Reviews of Geophysics*, 39, 347–383. doi: 10.1029/1999RG000074
- Bour, I. (2010). *Thèse de doctorat* (Doctoral dissertation, Université Paris-Sud, Orsay). Retrieved 2023-01-07, from <https://geologie-et-alpes.pagesperso-orange.fr/tfa/texte/ardenne.html>
- Brady, B., & Brown, E. (2006). *Rock Mechanics for underground mining: Third edition*. (Journal Abbreviation: Rock Mechanics for underground mining: Third edition Pages: 628 Publication Title: Rock Mechanics for underground mining: Third edition) doi: 10.1007/978-1-4020-2116-9
- Bruna, P.-O., Guglielmi, Y., Viseur, S., Lamarche, J., & Bildstein, O. (2015, October). Coupling fracture facies with in-situ permeability measurements to generate stochastic simulations of tight carbonate aquifer properties: Example from the Lower Cretaceous aquifer, Northern Provence, SE France. *Journal of Hydrology*, 529, 737–753. Retrieved 2023-01-10, from <https://www.sciencedirect.com/science/article/pii/S0022169415006691> doi: 10.1016/j.jhydrol.2015.08.054
- Cardu, M., Dipietromaria, S., & Oreste, P. (2016, May). Sub-Level Stopping in an Underground Limestone Quarry: An Analysis of the State of Stress in an Evolutionary Scenario. *Archives of Mining Sciences*, 61. doi: 10.1515/amsc-2016-0015
- Chatterjee, S., & Mukherjee, S. (2023, May). Review on drilling-induced fractures in drill cores. *Marine and Petroleum Geology*, 151, 106089. Retrieved 2024-04-15, from <https://www.sciencedirect.com/science/article/pii/S0264817222005670> doi: 10.1016/j.marpetgeo.2022.106089
- Chen, J.-h., Gu, D.-s., & Li, J.-x. (2003, September). Optimization principle of combined surface and underground mining and its applications. *Journal of Central South University Of Technology*, 10 (3), 222–225. Retrieved 2023-03-06, from <https://doi.org/10.1007/s11771-003-0013-y> doi: 10.1007/s11771-003-0013-y
- Dejonghe, L. (2010a). *Les gisements plombo-zincifères de la région d'Andenne*. Service géologique de Belgique.
- Dejonghe, L. (2010b, January). L'exploitation des gisements de fer de la région d'Andenne en minières et dans les mines concédées de Bonnine, Boloy-Grancelle, Champion, Chant d'Oiseaux, Maquelette, Marquis de Croix et Maîtres de Forge de Couthuin. *Geosciences, Terres, pierres et feu en vallée mosane*, 323–340.

- Delvaux, D. (1997). Present-day intraplate stress field in the Varican Front and Rhenish Massif: Influence of rifting and reactivation of pre-existing structures. *Belgian Symposium on Structural Geology and Tectonics*, 8, 61–64.
- Denayer, J., Pacyna, D., & Boulvain, F. (2010). *Le Minerai de fer en Wallonie. Cartographie, histoire et géologie* (Tech.Rep.). Retrieved from <https://geologie.wallonie.be/home/thematiques-sous-sol/exploitations-souterraines/minieres-et-exploit-libres/type-de-travaux.html>
- Dershowitz, W. S. (1984). *Rock joint systems* (Thesis, Massachusetts Institute of Technology). Retrieved 2023-03-09, from <https://dspace.mit.edu/handle/1721.1/27939> (Accepted: 2008-10-03T13:45:31Z)
- DMT. (2019). *Optic scan Borehole 172 MLD*.
- Elci, H., & Turk, N. (2014, February). Block Volume Estimation from the Discontinuity Spacing Measurements of Mesozoic Limestone Quarries, Karaburun Peninsula, Turkey. *The Scientific World Journal*, 2014, 363572. Retrieved 2024-04-09, from <https://www.ncbi.nlm.nih.gov/pmc/articles/PMC3947676/> doi: 10.1155/2014/363572
- Esterhuizen, G., Dolinar, D. R., Ellenberger, J. L., & Prosser, L. (2011, May). *Pillar and Roof Span Design Guidelines for Underground Stone Mines*. Department of Health and Human Services. Centers for Disease Control and Prevention.
- Firket, A. (1878). *Etude sur les gîtes métallifères de la mine de Landenne et sur la faille silurienne du Champ d'Oiseaux*. *Bulletins de l'Académie royale des Sciences, des Lettres et des Beaux-Arts de Belgique*.
- Genter, A., Castaing, C., Dezayes, C., Tenzer, H., Traineau, H., & Villemin, T. (1997). Comparative analysis of direct (core) and indirect (borehole imaging tools) collection of fracture data in the Hot Dry Rock Soultz reservoir (France). *Journal of Geophysical Research: Solid Earth*, 102 (B7), 15419–15431. Retrieved from <https://brgm.hal.science/hal-03997002/document>
- Golder, A. I. (2013, February). *GEOTECHNICAL AND HYDROGEOLOGICAL CHARACTERIZATION STUDY AND CONCEPTUAL MINE PLAN* (Personal Communication).
- Hack, R. (1998, January). *Slope stability probability classification; SSPC*. Retrieved 2024-04-23, from https://www.researchgate.net/publication/254559970_Slope_stability_probability_classification_SSPC
- Iannacchione, A., Prosser, L., Esterhuizen, G., & Bajpayee, T. (n.d.). *Assessing Roof Fall Hazards for Underground Stone Mines: A proposed methodology*. National Institute for Occupational Safety and Health (NIOSH). Retrieved from <https://www.cdc.gov/niosh/mining%5C/UserFiles/works/pdfs/arfhf.pdf>
- Ireland, G. S. (n.d.). *Enclosed depressions*. Retrieved 2024-04-22, from <https://www.gsi.ie/en-ie/programmes-and-projects/groundwater/activities/understanding-irish-karst/karst-landforms/Pages/Enclosed-depressions.aspx>
- Kim, J.-G., Ali, M. A. M., & Yang, H.-S. (2019, June). Robust Design of Pillar Arrangement for Safe Room-and-Pillar Mining Method. *Geotechnical and Geological Engineering*, 37 (3), 1931–1942. Retrieved 2024-05-02, from <https://doi.org/10.1007/s10706-018-0734-1> doi: 10.1007/s10706-018-0734-1
- Kohler, J. (2023). *8.3.1: Room and Pillar Method | GEOG 000*. Retrieved 2024-05-02, from <https://www.e-education.psu.edu/geog000/node/900>
- Kolapo, P., Oguniola, N. O., Munemo, P., Alewi, D., Komolafe, K., & Giwa-Bioku, A. (2023, March). DFN: An Emerging Tool for Stochastic Modelling and Geomechanical Design. *Eng*, 4 (1), 174–205. Retrieved 2023-03-06, from <https://www.mdpi.com/2673-4117/4/1/11> (Number: 1 Publisher: Multidisciplinary Digital Publishing Institute) doi: 10.3390/eng4010011
- Lauwers, A. (2023, May). *Questions on the history of the Marches-les-Dames quarry*.
- Mathieu, G. (1962). *Contribution à la stratigraphie des dolomies de Marches-les-Dames et Namèche, suivi des "Considérations sur le problème des dolomies"*. *Mémoire en vue de l'obtention du grade de Licencié en sciences géologiques et minéralogiques*. (Unpublished doctoral dissertation). Université Libre de Bruxelles.
- ministry of environment, B. (1998). Field methods for describing terrestrial ecosystems. In *Land management handbook no. 25*. Victoria B.C.. Retrieved from https://wiki.ubc.ca/Soil_Texture_-_Hand_Texturing_Method
- Monsalve, J. J., Soni, A., Ripepi, N., & Rodriguez-Marek, A. (2020, August). A Preliminary Investigation on Stochastic Discrete Element Modeling for Pillar Strength Determination in Underground Limestone Mines from a Probabilistic Risk Analysis Approach..
- Nahli, K., Oryzavica, V., & Radityo, D. (2017, March). PRELIMINARY STUDY OF THE NON-

- VOLCANIC GEOTHERMAL POTENTIAL AS TRANSITION FROM PETROLEUM TO GEOTHERMAL EXPLORATION AT CIPARI AREA, CENTRAL JAVA.
- Ngan-Tillard, D. (2024, April). *Friction angle/ shear strenght of joints*.
- NGI. (2015, May). *Rock mass clasification and support design*. Author. Retrieved from ww.ngi.no
- Odling, N., Gillespie, P., Bourguine, B., C, C., JP, C., N.P, C., . . . J, W. (1999, November). Variations in fracture system geometry and their implications for fluid flow in fractured hydrocarbon reservoirs. *Petroleum Geoscience*, 5 , 373–384doi: 10.1144/petgeo.5.4.373
- Olson, J. E. (2004, January). Predicting fracture swarms — the influence of subcritical crack growth and the crack-tip process zone on joint spacing in rock. *Geological Society, London, Special Publications*, 231 (1), 73–88. Retrieved 2024-03-09, from <https://www.lyellcollection.org/doi/abs/10.1144/GSL.SP.2004.231.01.05> (Publisher: The Geological Society of London) doi: 10.1144/GSL.SP.2004.231.01.05
- Pacyna, D., & Denayer, J. (2010, November). *Mines, minières et carrières souterraines en Wallonie – Risques associées et contraintes – D. PACYNA – Novembre 2010 1 Service public de Wallonie - Direction générale opérationnelle Agriculture, Ressources naturelles et Environnement Département de l'Environnement et de l'Eau - Direction des Risques industriels, géologiques et miniers Cellule Sous-sol/Géologie MINES, MINIERES ET CARRIERES SOUTERRAINES EN WALLONIE RISQUES ASSOCIEES ET CONTRAINTES*. Service public de Wallonie - Direction générale opérationnelle Agriculture, Ressources naturelles et Environnement Département de l'Environnement et de l'Eau - Direction des Risques industriels, géologiques et miniers Cellule Sous-sol/Géologie.
- Pakalnis, R., & Potvin, Y. (2015, November). *Empirical design methods in practice* (Tech. Rep.). Australian Centre for Geomechanics. Retrieved 2023-12-06, from https://papers.acg.uwa.edu.au/p/1511_0.3_Pakalnis/ (Conference Name: Design Methods 2015: International Seminar on Design Methods in Underground Mining, 2015 17-19 November, Perth) doi: 10.36487/ACG_rep/1511_0.3_Pakalnis
- Palmstrom, A. (2005, July). Measurements of and correlations between block size and rock quality designation (RQD). *Tunnelling and Underground Space Technology*, 20 (4), 362–377. Retrieved 2024-04-09, from <https://linkinghub.elsevier.com/retrieve/pii/S088677980500009X> doi: 10.1016/j.tust.2005.01.005
- Passagez, A.-E. (2012). *CARRIERE DE DOLOMIES DE MARCHE-LES-DAMES : ÉTUDE HYDROGÉOLOGIQUE ET MODÉLISATION MATHÉMATIQUE DES CONDITIONS D'EXHAURE* (Unpublished doctoral dissertation). Université Libre de Bruxelles.
- Petex. (n.d.). *Digital Field Mapping*. Retrieved 2023-12-26, from <http://www.petex.com/products/move-suite/digital-field-mapping/>
- Petex. (2022). *MOVE manual*. Petroleum expert.
- Pingot, J.-L. (2022). *Une introduction à la GÉOLOGIE de WALLONIE*. Retrieved 2023-01-07, from <http://www.geolsed.ulg.ac.be/geolwal/geolwal.htm>
- Poty, E. (n.d.). *5.5 Engihoul Formation - ENG | National Commission for Stratigraphy Belgium*. Retrieved 2024-04-10, from <https://ncs-old.naturalsciences.be/carboniferous/55-engihoul-formation-eng>
- Poty, E. (2001). *Formation de Longpré (LPR)*. Retrieved 2023-01-08, from http://geologie.wallonie.be/files/geoapps/geologie/html/48_7-8/LPR/index.html
- Read, J., & Stacey, P. (2009). *Guidelines for OPEN PIT SLOPE DESIGN* (2013rd ed.). CSIRO Publishing.
- Rocscience. (n.d.). *Shear strength of discontinuities*. Retrieved 2024-12-04, from <https://static.rocscience.cloud/assets/resources/learning/hoek/Practical-Rock-Engineering-Chapter-4-Shear-Strength-of-Discontinuities-Remediated.pdf>
- Rogers, S., Elmo, D., Webb, G., & Catalan, A. (2014, March). Volumetric Fracture Intensity Measurement for Improved Rock Mass Characterisation and Fragmentation Assessment in Block Caving Operations. *Rock Mechanics and Rock Engineering*, 48 . doi: 10.1007/s00603-014-0592-y
- Schlotfeldt, P., & Carter, T. G. (2018, October). A new and unified approach to improved scalability and volumetric fracture intensity quantification for GSI and rockmass strength and deformability estimation. *International Journal of Rock Mechanics and Mining Sciences*, 110 , 48–67. Retrieved 2023-03-08, from <https://www.sciencedirect.com/science/article/pii/S1365160917312753> doi: 10.1016/j.ijrmms.2018.06.021
- Soni, A., Monsalve, J. J., Bishop, R., Ripepi, N., & Baggett, J. (2022, April). Estimating Strength of Pillars with Karst Voids in a Room-and-Pillar Limestone Mine. *Mining Metallurgy & Exploration*. doi: 10.1007/s42461-022-00594-0
- Sonnet, P. (2004). *Un aperçu de la géologie de la Belgique*. Université catholique de Lou-

- vain. Retrieved 2022-12-15, from https://sites.uclouvain.be/sols/site_agro1100/_site_agro1100_belgique/belgique.pdf
- Takako, M., Elmo, D., & Rogers, S. (2018, October). Influence of data analysis when exploiting DFN model representation in the application of rock mass classification systems. *Journal of Rock Mechanics and Geotechnical Engineering*, 10. doi: 10.1016/j.jrmge.2018.08.003
- Thiele, S. T., Grose, L., Samsu, A., Micklethwaite, S., Vollgger, S. A., & Cruden, A. R. (2017, December). Rapid, semi-automatic fracture and contact mapping for point clouds, images and geophysical data. *Solid Earth*, 8 (6), 1241–1253. Retrieved 2023-11-16, from <https://se.copernicus.org/articles/8/1241/2017/> doi: 10.5194/se-8-1241-2017
- Todini, E., Pelligrini, F., & Mazzetti, C. (2001). Influence of parameter estimation uncertainty in Kriging: Part 2 – Test and case study applications. *Hydrology and Earth System Sciences*, 5(2), 225–232. Retrieved 2024-04-05, from <https://citeseerx.ist.psu.edu/document?repid=rep1&type=pdf&doi=6ad1223a4da45dad2e9be4892d48d5c6d90baf27>
- Van der Voet, E. (2022). *Fracture properties within a Lower Carboniferous carbonate geothermal reservoir in the Campine-Brabant Basin* (Unpublished doctoral dissertation). KU Leuven, Haarlem.
- Vandycke, S. (1997). *Post-Hercynian brittle tectonics and paleostress analysis in Carboniferous limestones*. (8th ed.).
- Wang, X., & Cai, M. (2020, March). A DFN–DEM Multi-scale Modeling Approach for Simulating Tunnel Excavation Response in Jointed Rock Masses. *Rock Mechanics and Rock Engineering*, 53. doi: 10.1007/s00603-019-01957-8
- Wang, X., & Mauldon, M. (2006, January). Proportional error of the Terzaghi correction factors. *Proceedings of the 41st U.S. Rock Mechanics Symposium - ARMA's Golden Rocks 2006 - 50 Years of Rock Mechanics*.
- WSP. (2022, March). *FracMan DFN Workflows for Simulating and Understanding of Complex Subsurface Flow*. Retrieved 2024-05-07, from <https://www.youtube.com/watch?v=QySelJ81Uh4>
- Wyllie, D., & Norrish, N. (n.d.). Rock strength properties and their measurement. Retrieved from <https://onlinepubs.trb.org/Onlinepubs/sr/sr247/sr247-014.pdf>
- Xu, C., & Dowd, P. (2012, January). The Edge Effect in Geostatistical Simulations. In (Vol. 17, pp. 115–127). doi: 10.1007/978-94-007-4153-9_10
- Zhang, Y. (2014, March). *Modelling hard rock pillars using a Synthetic Rock Mass approach*. Retrieved 2024-04-24, from <https://summit.sfu.ca/item/13996> (Publisher: Simon Fraser University)

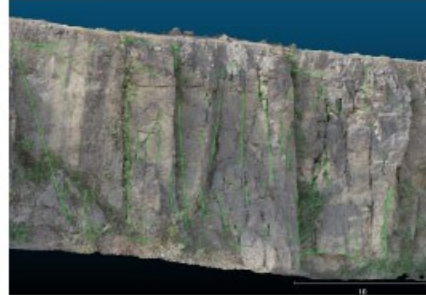
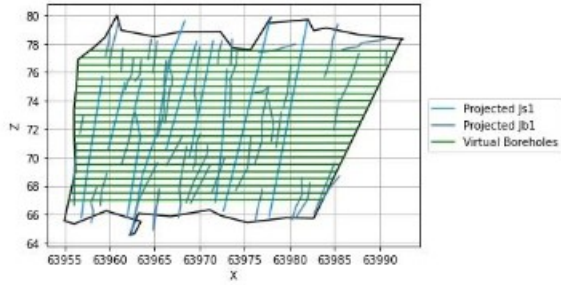
11 Appendix

A	Scan-Windows	89
B	Methodology photogrammetry model Scan-Windows	94
C	Integrated P32 dataset	105
D	Joint Condition	108
E	RMR and Q values	110

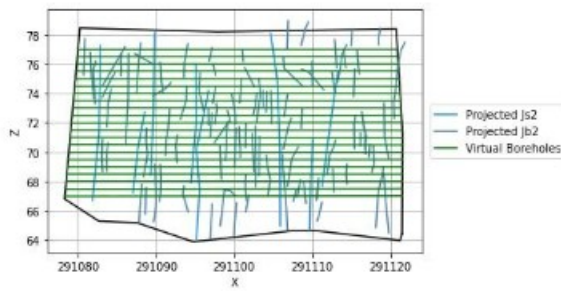


A Scan-Windows

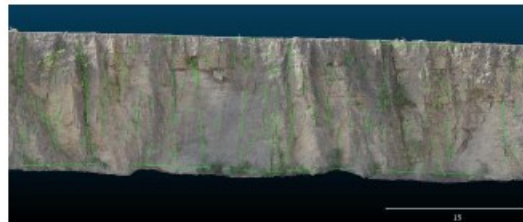
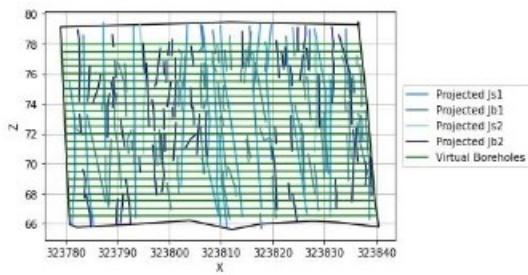
Scan-Window 1



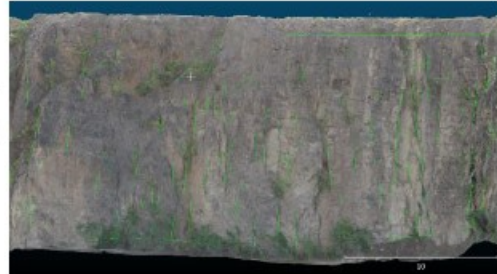
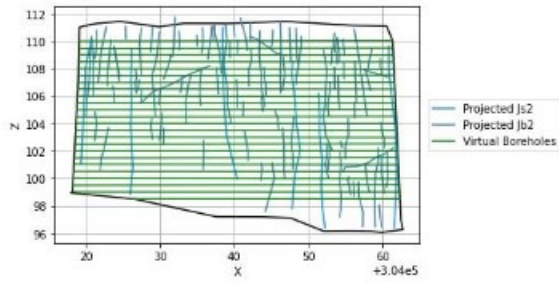
Scan-Window 2



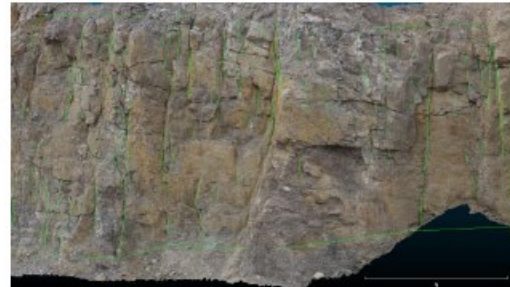
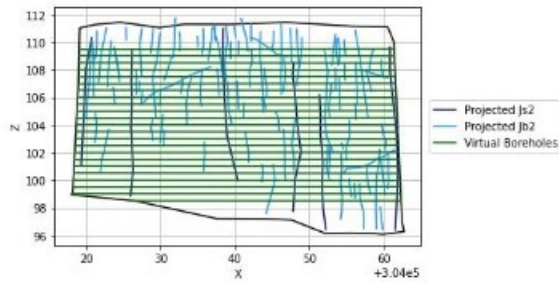
Scan-Window 3



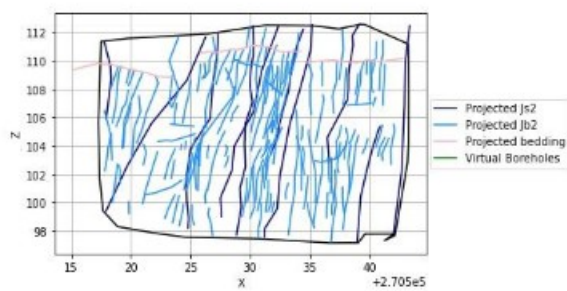
Scan-Window 4



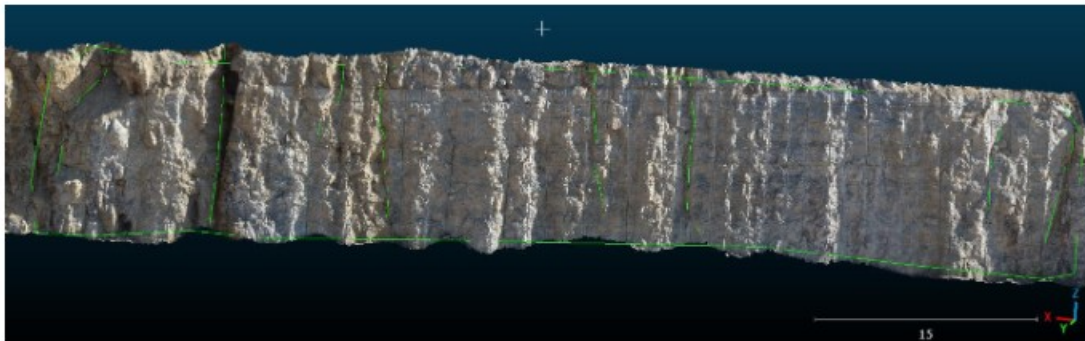
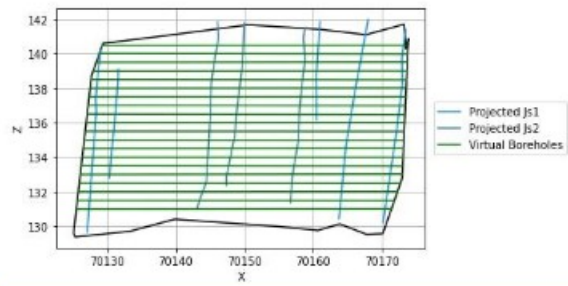
Scan-Window 5



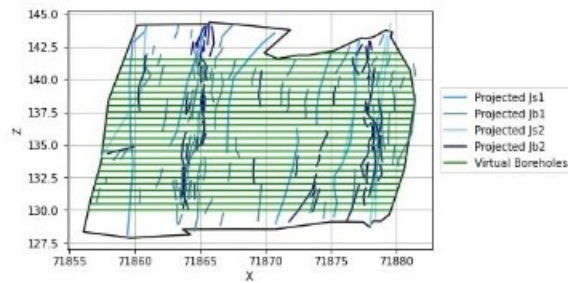
Scan-Window 6



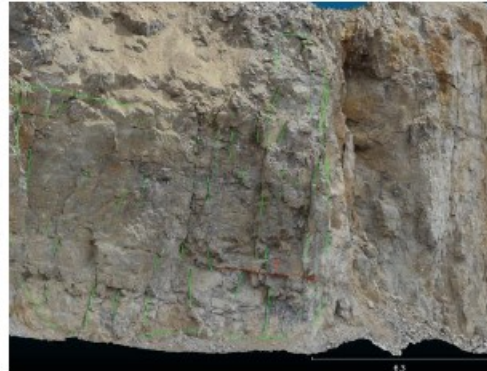
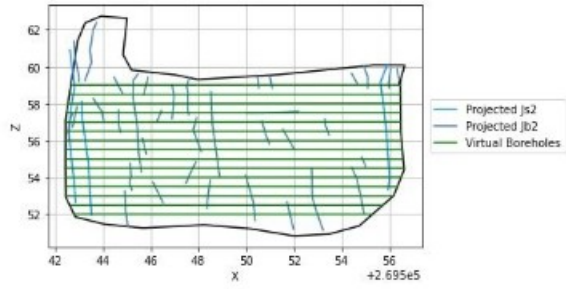
Scan-Window 7



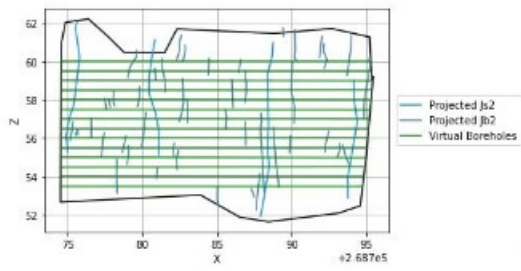
Scan-Window 8



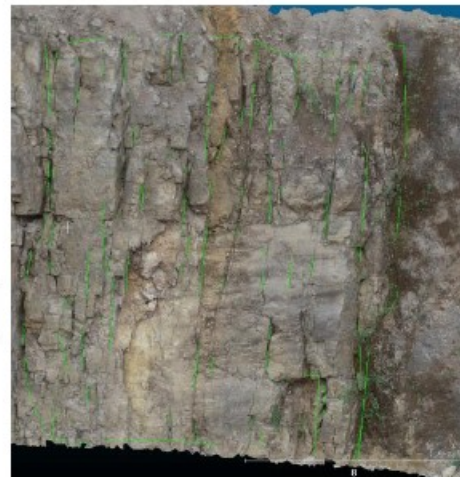
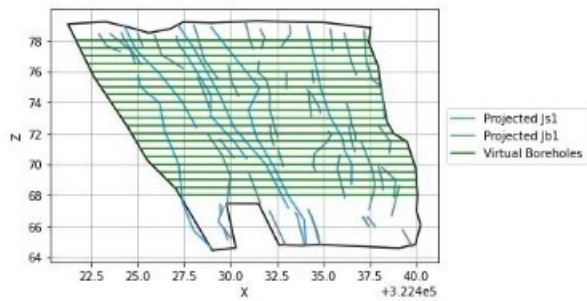
Scan-Window 9



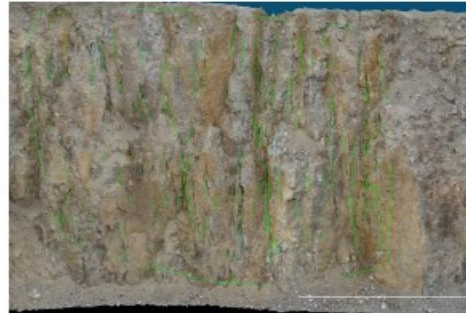
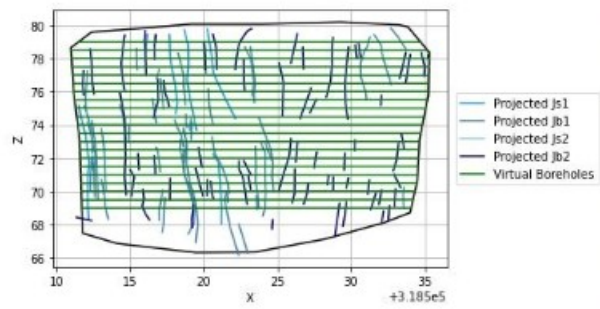
Scan-Window 10



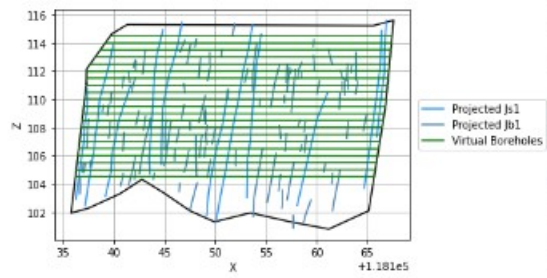
Scan-Window 11



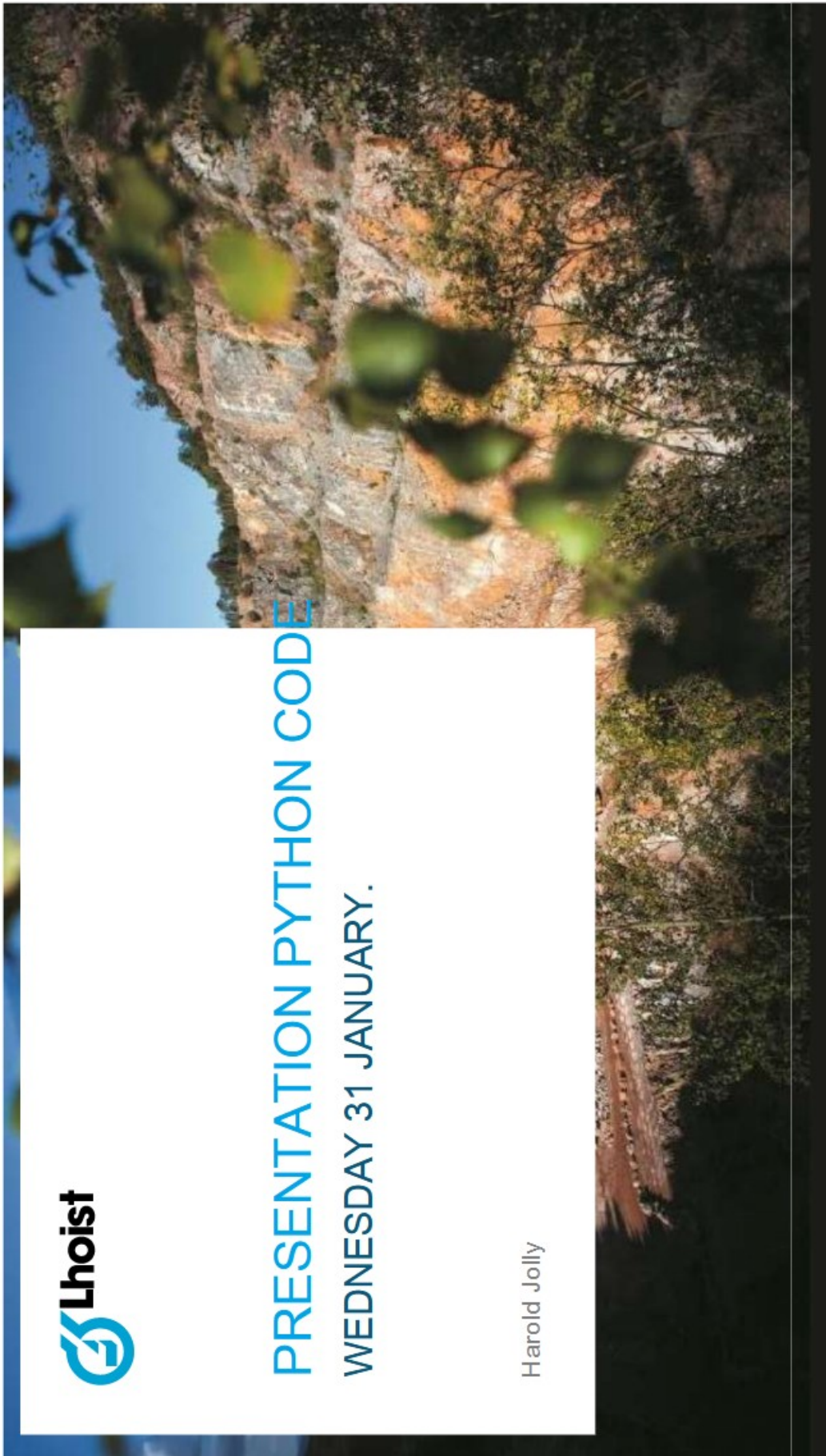
Scan-Window 12




Scan-Window 13



B Methodology photogrammetry model Scan-Windows

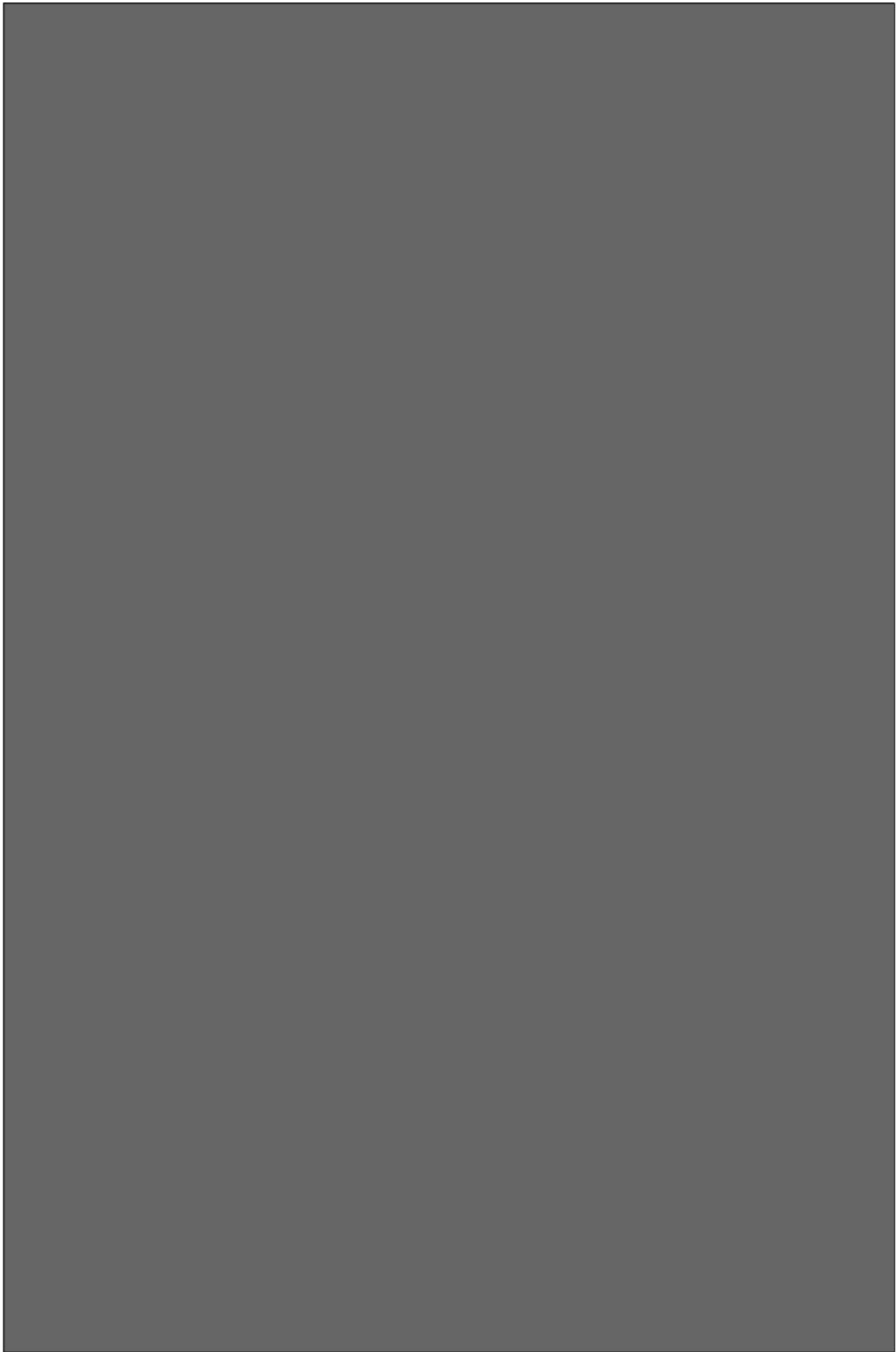


 **Lhoist**

PRESENTATION PYTHON CODE

WEDNESDAY 31 JANUARY.

Harold Jolly



THE IMPORTANCE OF ROCK MASS CLASSIFICATION SYSTEMS

- > Rock mass classification systems are empirical systems to design geotechnical structures.
- > For underground excavations the most common rock mass classification systems are:
 - > RMR (Bieniawski 1989)
 - > Q system introduced by Barton modified by the Norwegian Geological Institute (2015)
- > Q values (1) and RMR (2) can be estimated from:
 - > Rock core descriptions
 - > In-situ outcrops
 - > Outdoor outcrops

$$Q = \frac{RQD}{J_n} * \frac{J_r}{J_a} * \frac{J_w}{SRF} \quad (1)$$

With:

- RQD: Rock quality design.
- J_n: Joint set number
- J_r: Joint roughness number
- J_a: Joint alteration number
- J_w: Joint water reduction factor
- SRF: Stress reduction factor

$$\sum^{A-B} \quad (2)$$

With:

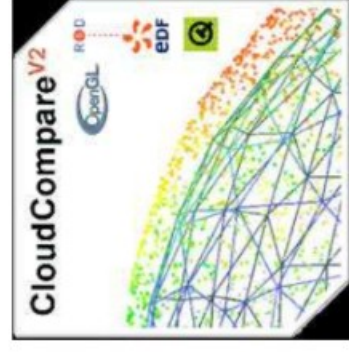
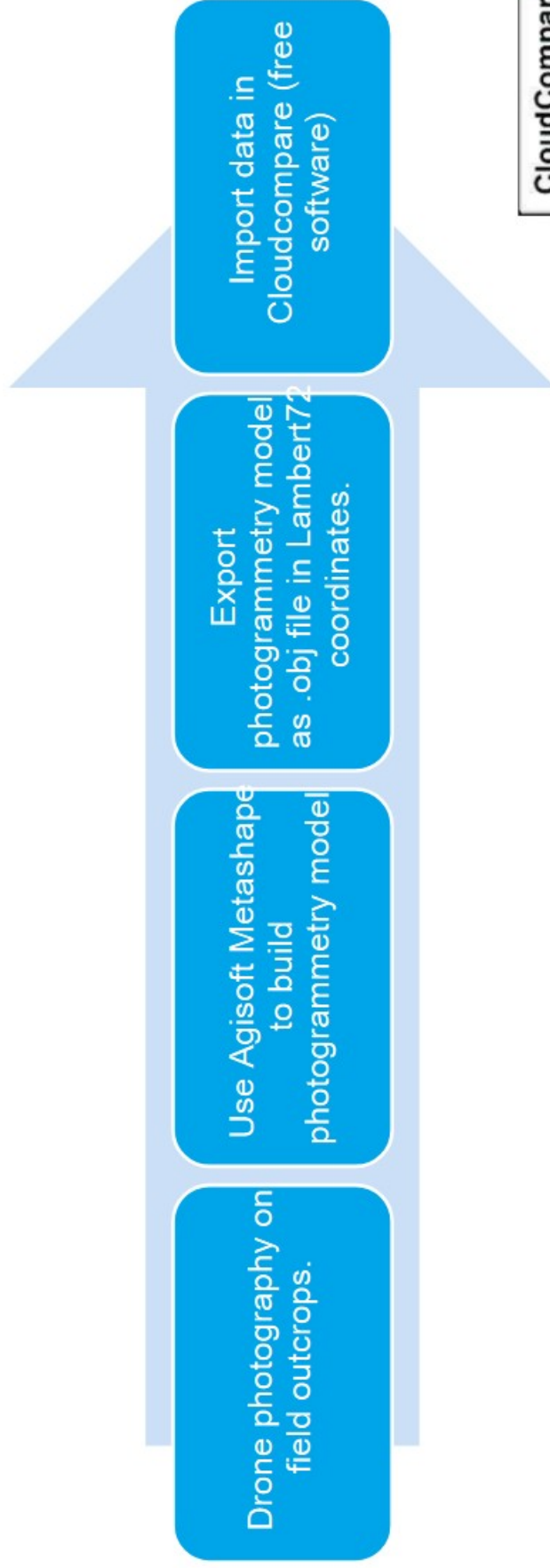
1. A1: Intact rock strength (Stress condition)
2. A2: RQD (Block volume)
3. A3: Discontinuity spacing (Block volume)
4. A4: JCond89 (Joint condition)
5. A5: Groundwater condition (Stress condition)
6. B: Discontinuity orientation (Stress condition)

WHAT DATA CAN BE QUANTITATIVELY COLLECTED

- > Two 'datasets' can be quantitatively collected using the python code and photogrammetry model:
 - > B. Joint intensity datasets (RQD and joint spacing)
 - > C. Joint Geometry datasets (Orientation and Joint size (Persistence and height))
- > Datasets must be collected using other methodologies:
 - > D. Joint condition and E. Stress level: field investigation
 - > E. Ground water: Descriptions, hydrogeologist or assumptions
 - > A. intact rock mass material: Lab tests

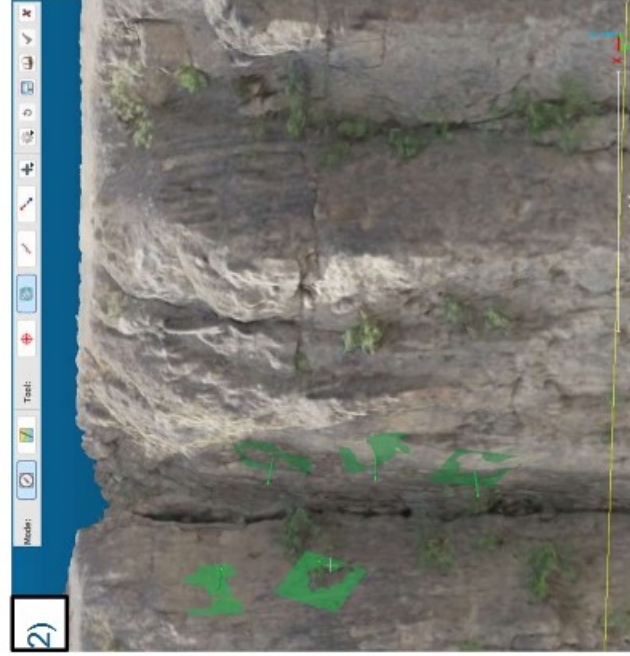
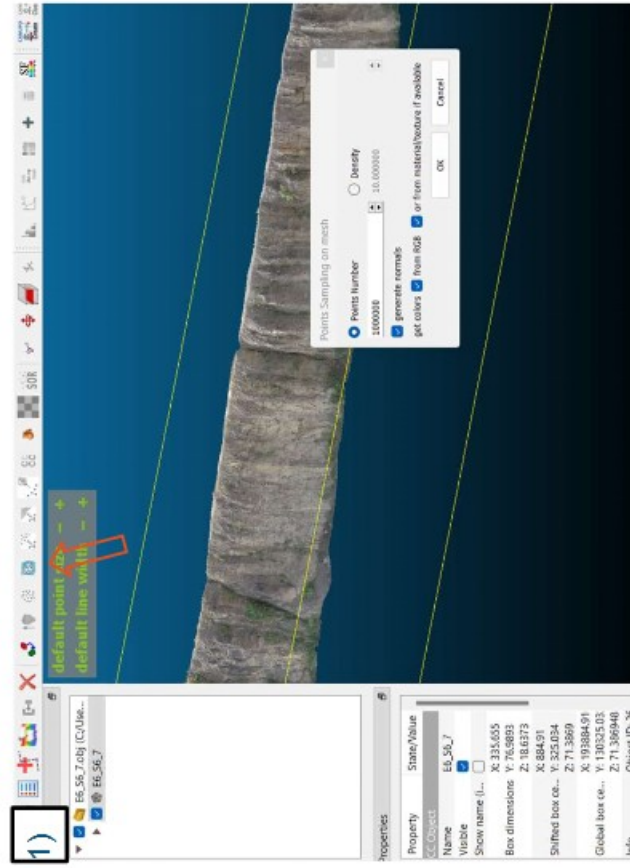
Category	Input parameters		Unit	Used in:			
	Parameter	Parameter		RMR	Q	DFN	DFN-DEM*
A. Intact rock mass material	Unconfined compressive strength		MPa	A1	-	-	Yes
	Brazilian tensile strength		MPa	-	-	-	Yes
B. Joint intensity	Joint spacing		m	A2	-	Yes	Yes
	RQD		%	A3	RQD	-	-
	P10		[joints/m]	-	-	Yes	Yes
	P21		[m/m ²]	-	-	Yes	Yes
	Joint orientation		rating	B	-	Yes	Yes
C. Joint Geometry	Number of joint sets		rating	-	-	-	-
	Joint size (Length and persistence)		rating	A4a	-	Yes	Yes
	Joint aperture		[m]	A4b	-	Yes	Yes
	Joint roughness		rating	A4c	Jr	-	Yes
D. Joint Condition	Joint alteration (infill)		rating	A4e	Ja	-	Yes
	Water inflow		rating	A5	Jw	-	-
E. Ground Water	Weakness zones		rating	-	-	-	-
	Stress level		rating	-	SRF	-	Yes

STEP 1: PHOTOGRAMMETRY MODEL AND CLOUDCOMPARE



STEP 2: ORIENTATION DATA

- > 1. Obj file => point cloud using Points sampling on mesh
- > 2. Use the plane tool inside the Compass plugin in Cloudcompare to collect orientation data along failure planes.
- > Determine different joint sets using Contour plots. (Stereonet can be used)



STEP 3: DETERMINE JOINT SETS USING CONTOUR PLOTS

- > The joint orientation collected using Cloudcompare Compass plugin is very similar to the orientation collected using other data acquisition methodologies such as optic scan orientation data or field data collected using a Compass. When no failure plane is available as surface it is not possible to measure the joint set. (variable Jn for Q system can be estimated here).

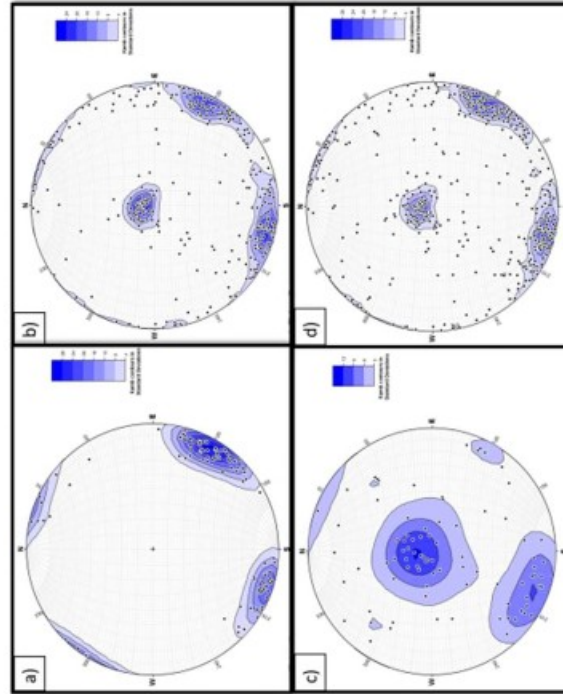


Figure 5.1: (a) Stereonet of the poles from the field dataset. (b) Stereonet of the orientation poles from the field dataset. (c) Stereonet of the poles from borehole optic scan dataset. (d) Stereonet combining all datasets.

STEP 4: FRACTURE TRACING

- > Fractures are traced by set on the photogrammetry model using cloudcompare's trace polyline tool and saved in separate folders organised by joint set (Cloudcompare, 2016).
- > Find a relatively flat outcrop and trace the fractures per set in a delimited rectangular area (named outline). Save the outline inside a folder called 'outline'.
- > Save all folders containing the fracture sets inside a single directory as .dxf files.



Figure 4.4: Example of scan-window SW13. Not all the joints appear to be traced; the polylines are sometimes hidden behind the photogrammetry surface.

STEP 5: PYTHON CODE

- > Python code consists of two codes one called 'Functions_stable1.py' the other code called 'AA_main.py'
- > Only change variable in AA_main code. The first 37 lines should be modified.
- > #1 Use the input directory consisting of the fracture DXF files and the outline. (line 14)
- > #2 Specify all the fracture sets by the name of each folder. (line 17)
- > #3 Change the height and distance between virtual boreholes. (line 24 and 25)
- > #4 If fractures were traced in 2d orthophotos change the line 28

```
13 # Define the input directory
14 input_directory = r"C:\Users\Harold.Jolly\OneDrive\Documents\Thesis\OBJ_files\DATA_scan_windows\SKI"
15
16 # Define the input folders where asc files are stored
17 input_folders = ["outline", 'Jsl', 'Jbl']
18
19 # Specify output folders (excluding 'outline' and 'bedding')
20 output_folders = [folder for folder in input_folders if folder not in ['outline']]
21
22
23 #modify this if the Virtual boreholes are not properly generated.
24 spacing_bh = 0.5
25 min_y, max_y = 67, 77
26
27 # If functions have been traced in 2D => use DataProjection2D
28 processor = DataProjection3D(input_directory, input_folders, spacing_bh, min_y, max_y, file='.dxf')
29 projected_data, virtual_boreholes, folders, three_d_data = processor.process_shapefiles()
30 processor.plot_data()
```

OUTPUT

- > Two Excel files will be generated called length_P21 and spacing_P10 respectively
- > Length_P21.xlsx: fracture length and persistence (see figure 4.6).
- > Spacing_P10.xlsx: fracture spacing and P10 for every virtual borehole.
- > QGIS folder containing the shape points of each fracture set (can be imported in QGIS) and a best fit line to measure outcrop orientation in QGIS.

A	B	C	D	E	F
Js1	Jb1	Js2	Jb2	bedding	area
9.830367	1.00285	8.847719	1.396711	5.000785	783.1847
12.94592	1.174779	7.561575	1.689768	2.266142	
6.295463	0.973356	9.490088	2.656443	0.967888	
11.71618	1.576285		1.638907	3.229966	
9.309199	1.2552		3.401668	7.628389	
10.24654	2.447446		2.318271	4.513506	
12.48546	1.517111		6.752083	13.92499	
8.399805	1.6079		1.975785	7.03181	
12.81797	0.693047		1.755621	3.261183	
10.95439	1.25272		2.550618	17.59392	
13.53337	2.513695		2.129102	1.232672	
8.712392	1.044256		1.200196	2.952354	
13.47414	1.734247		2.364109	3.875402	
12.52522	2.994678		4.295114	6.861799	

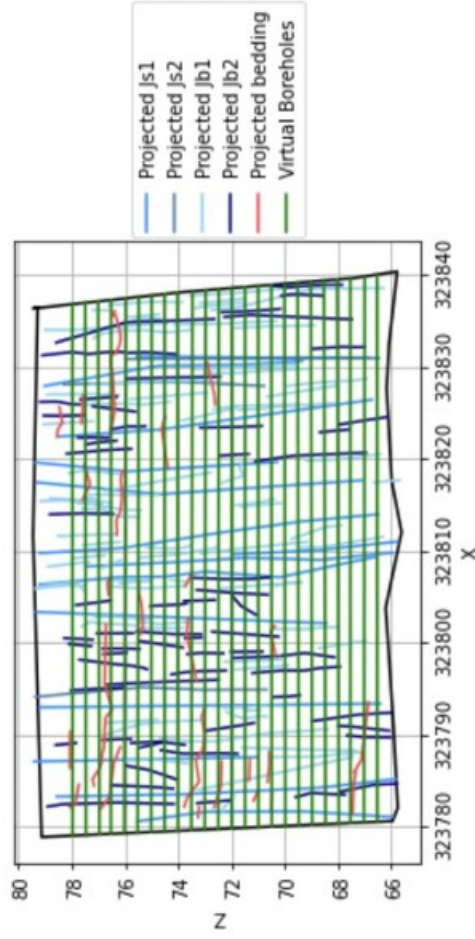


Figure 4.6: Result of the polyline lengths (in meters) by set computed using python printed in an Excel workbook. The area in m^2 of the scanwindow has also been retrieved.

P10 AND JOINT SPACING DATA- CORRECTED FOR ORIENTATION

- > Import output => QGIS= best_fit_line.shp in QGIS. and determine scanwindow trend.
- > Use Terzaghi correction
- > True spacing = spacing*C2 weight
- > True P10 = P10/C2 weight
- > C2 weight = cosinus(alpha) where alpha is the difference between the average scan window trend and average joint set dip direction.
- > Mean spacing => used for RMR
- > True P10 (fracture per meter) can determine the RQD

B	C	D	E	F	G	H
s2_spacing	Js2_P10	b2_spacing	Jb2_P10	SW trend (Qgis)	J2 average strike	C2 weight
10.81752	0.092676	0	0.370705	74	110	0.587785252
8.579199	0.116053	0.828693	0.348158			
2.143254	0.1628	0.520602	0.3256			
3.662996	0.186392	2.539247	0.326185			
7.050492	0.186727	4.234821	0.373455			

C Integrated P32 dataset

ORANGE VALUES= INTERPRETED DATA.

Location	Js1 - P32	Jb1 - P32	Js2 - P32	Jb2 - P32	P32- Total	Y	Z	Formation	Domain		
BH172	0.44	0.66	0.36	1.09	2.56	640884.272	5593864.05	57.39	D	F1	
BH172	0.74	1.11	0.62	1.85	4.32	640884.273	5593864.05	-10.2	C	F1	Nothing
BH176	0.13	0.21	0.06	0.21	0.62	640966.639	5593586.05	3.37	D	S2	
BH176	0.15	0.23	0.07	0.23	0.69	640966.64	5593586.05	-61	C	S2b	
BH177	0.45	0.67	0.37	1.11	2.61	641431.308	5593829.31	25.4	D	F1-F2	
BH177	0.47	0.71	0.39	1.17	2.75	641431.308	5593829.31	-38.3	C	F1-F2	
BH179	0.28	0.44	0.24	0.72	1.69	642009.898	5594975.42	106	C	S2a	
BH180	0.31	0.47	0.15	0.47	1.41	641149.576	5593723.24	27.52	D	S2b	
BH180	0.37	0.56	0.17	0.55	1.66	641149.576	5593723.23	-33.6	C	S2b	
BH181	0.24	0.37	0.12	0.37	1.10	641519.282	5593907.84	40.43	D	S2b	
BH181	0.2	0.3	0.09	0.3	0.89	641519.283	5593907.84	-16.1	C	S2b	
SW1	0.27	0.34			0.61	641014.44	5594115.43	72	D	S2a	
SW2	0.17	0.81			0.98	641040.22	5594115.17	72	D	S2a	
SW3	0.14	0.34	0.07	0.48	1.12	640910.731	5594100.31	72	D	S2a	
SW4			0.1	0.45	0.59	641063.89	5594125.11	72	D	S2a	
SW5			0.13	0.5	0.63	641320.16	5594150.12	97	D	S2a	
SW6			0.33	0.95	1.28	641258.59	5594116.59	97	D	F2	
SW9			0.2	0.49	0.69	641266.805	5594288.06	56	D-C	S2b	
SW10			0.13	0.41	0.54	641241.855	5594243.37	56	C	S2b	
SW11	0.54	0.66			1.21	641140.56	5594150.47	72	D	F2	
SW12	0.14	0.56	0.29	0.66	1.64	641200.672	5594161.7	72	D	F2	
SW13	0.26	0.41			0.71	641611.985	5594530.28	97	D	S2a	
SL_1	0.31	0.46	0.29	0.62	1.67	641100.06	5594140.11	72	D	S2a	
SL_2			0.25	0.58	0.83	641059.86	5594124.35	72	D	S2a	
SL_3	0.21	0.31	0.14	0.48	1.14	641022.81	5594114.52	72	D	S2a	
SL_4	0.23	0.34	0.12	0.47	1.17	641001.26	5594114.45	72	D	S2a	
SL_5	0.19	0.29	0.08	0.43	0.99	640864.53	5594090.71	72	D	S2a	
SL_6			0.15	0.50	0.65	640775.9	5594078.6	72	D	S2a	
SL_7	0.32	0.48	0.17	0.52	1.49	640679.5	5593983.1	82	D	S2a	
SL_9	0.25	0.38			0.63	641338.6	5594480.7	39	C	S2b	
SL_10	0.29	0.44	0.21	0.54	1.48	641069.29	5594081.83	97	D	S2a	
SL_11	0.21	0.32	0.13	0.48	1.14	641005.58	5594065.63	97	D	S2a	

SL_12	0.31	0.47	0.13	0.48	1.38	640878.55	5594065.25	82 D	S2a
SL_13			0.06	0.42	0.48	641271.7	5594374.01	39 C	S2b
SL_14			0.21	0.54	0.75	641217.96	5594311.44	39 C	F3
SL_15			0.05	0.41	0.46	641194.3	5594283.67	39 C	S2b
SL_16			0.09	0.45	0.54	641607.25	5594457.6	97 D	S2a
SL_17			0.11	0.46	0.58	641582.09	5594415.17	97 D	S2a
SL_18			0.20	0.54	0.73	641523	5594339.1	97 D	S2a
SL_19			0.23	0.57	0.80	641368.55	5594190.41	97 D	F3
SL_20			0.33	0.65	0.98	641348.11	5594163.54	97 D	F3

Measured data

D Joint Condition

The Joint traces for each I.D. can be found under :

#G&M LWE internship - documents/Data acquisition/Joint condition/locations

Joint set Js1

Joint_set	ID	Jr	Ja	Bench	Domains
Js1	1	3	4	6	S2a
Js1	2	1	6	6	S2a
Js1	3	3	4	6	S2a
Js1	4	3	3	6	S2a
Js1	5	1.5	2	6	S2a
Js1	6	3	4	6	S2a
Js1	7	1.5	2	6	S2a
Js1	8	1.5	3	6	S2a
Js1	9	1	6	6	S2a
Js1	10	3	4	6	S2a
Js1	11	1.5	2	6	S2a
Js1	12	1.5	2	6	S2a
Js1	13	1.5	4	6	S2a
Js1	14	1.5	3	6	S2a
Js1	15	3	4	6	S2a
Js1	16	3	3	6	S2a
Js1	17	3	4	6	S2a
Js1	18	1	6	6	S2a
Js1	19	1	8	6	S2a
Js1	20	3	3	6	S2a
Js1	21	3	2	6	S2a
Js1	22	3	2	6	S2a
Js1	23	1.5	2	6	S2a
Js1	24	3	2	6	S2a
Js1	25	1.5	2	6	S2a
Js1	26	1.5	2	6	S2a
Js1	27	1	6	6	S2a
Js1	28	1.5	2	6	S2a
Js1	29	3	3	6	S2a
Js1	30	3	3	6	S2a
Js1	31	1.5	4	6	S2a
Js1	32	1	6	6	S2a
Js1	33	3	1	6	S2a
Js1	34	1.5	1	6	S2a
Js1	35	3	2	6	S2a
Js1	36	3	1	6	S2a
Js1	37	1.5	1	6	S2a
Js1	38	3	2	6	S2a
Js1	39	1	6	6	S2a
Js1	40	3	2	4	S2a
Js1	41	3	2	4	S2a
Js1	42	1.5	2	4	S2a
Js1	43	3	3	4	S2a

Joint set Js2

Joint_set	I.D.	Jr	Ja	Bench	Domain
Js2	1	1.5	3	6	S2a
Js2	2	1	6	6	S2a
Js2	3	1	8	6	S2a
Js2	4	3	4	6	S2a
Js2	5	3	4	6	S2a
Js2	6	1	10	6	S2a
Js2	7	3	4	6	S2a
Js2	8	3	2	6	S2a
Js2	9	3	3	6	S2a
Js2	10	1.5	3	6	S2a
Js2	11	1	8	6	S2a
Js2	12	3	3	6	S2a
Js2	13	3	2	6	S2a
Js2	14	3	2	6	S2a
Js2	15	3	4	6	S2a
Js2	16	1.5	3	6	S2a
Js2	17	3	6	6	S2a
Js2	18	1	6	6	S2a
Js2	19	1	6	6	S2a
Js2	20	3	3	6	S2a
Js2	21	3	2	6	S2a
Js2	22	1	6	6	S2a
Js2	23	1.5	2	6	S2a
Js2	24	3	3	6	S2a
Js2	25	3	2	6	S2a
Js2	26	3	2	6	S2a
Js2	27	3	3	4	S2a
Js2	28	1.5	3	4	S2a
Js2	29	3	2	4	S2a
Js2	30	1	6	4	S2a
Js2	31	3	3	4	S2a
Js2	32	3	2	4	S2a
Js2	33	1	6	4	S2a
Js2	34	3	6	4	S2a
Js2	35	3	4	4	S2a
Js2	36	3	1	4	S2a
Js2	37	1.5	1	6	F
Js2	38	1	8	6	F
Js2	39	1.5	2	6	F
Js2	40	3	6	6	F
Js2	41	4	2	6	F
Js2	42	1	8	6	F
Js2	43	1	10	6	F
Js2	44	3	2	6	F
Js2	45	3	1	6	F
Js2	46	1.5	2	6	F

E RMR and Q values

Q system and RMR rating systems

Appendix C: Rock mass classification tables — RMR and Q

The following tables are provided to support the questions in Chapter 12. Note that although we have used the term 'fracture' in this book, the originators of the RMR and Q classifications used the words 'discontinuity' and 'joint', respectively. To avoid confusion with the original publications¹, we have retained these words in the tables below.

Rock mass rating system¹

$$RMR = \sum(\text{classification parameters}) + \text{discontinuity orientation adjustment}$$

(A) Classification parameters and ratings

Strength of intact rock material

Point-load strength index (MPa)	*	*	*	1-2	2-4	4-10	>10
Uniaxial compressive strength (MPa)	<1	1-5	5-25	25-50	50-100	100-250	>250
Rating:	0	1	2	4	7	12	15

* For this low range, uniaxial compressive test is preferred.

Groundwater

Inflow per 10-m tunnel length (l/min)	>125	25-125	10-25	<10	none
Ratio $\frac{\text{joint water pressure}}{\text{major principal stress}}$	>0.5	0.2-0.5	0.1-0.2	<0.1	0
General conditions	flowing	dripping	wet	damp	completely dry
Rating:	0	4	7	10	15

¹ Bieniawski Z. T. (1989) *Engineering Rock Mass Classifications*. Wiley, Chichester, 251pp.

496 Appendix C: Rock mass classification tables — RMR and Q

Drill core quality RQD (%)

	<25	25-50	50-75	75-90	90-100
Rating:	3	8	13	17	20

Spacing of discontinuities

	<60 mm	60-200 mm	200-600 mm	0.6-2 m	>2 m
Rating:	5	8	10	15	20

Condition of discontinuities

Use Table (B), or the following guidelines

	Soft gouge > 5 mm thick or separation > 5 mm, continuous	Slickensided surfaces or gouge < 5 mm thick or separation 1-5 mm, continuous	Slightly rough surfaces, separation < 1 mm, highly weathered wall rock	Slightly rough surfaces, separation < 1 mm, slightly weathered wall rock	Very rough surfaces, no separation, unweathered wall rock, not continuous
Rating:	0	10	20	25	30

(B) Guidelines for classification of discontinuities

Discontinuity length (persistence)

	<1 m	1-3 m	3-10 m	10-20 m	>20 m
Rating:	6	4	2	1	0

Separation (aperture)

	none	<0.1 mm	0.1-1.0 mm	1-5 mm	>5 mm
Rating:	6	5	4	1	0

Roughness

	very rough	rough	slightly rough	smooth	slickensides
Rating	6	5	3	1	0

Infilling (gouge)

	hard filling			soft filling	
	none	<5 mm	>5 mm	<5 mm	>5 mm
Rating:	6	4	2	2	0

Weathering

	unweathered	slightly weathered	moderately weathered	highly weathered	decomposed
Rating:	6	5	3	1	0

(C) E

Strike

drive v

dip 45

very fa

Strike

dip 20

fair

(D) R

Effect

orient

Rating

Tunn

Found

Slope

(E) R

Rating

Class

Descri

(F) In

Class

Avera

Cohes

(kPa)

Frictio

(deg)

(C) Effect of discontinuity orientations in tunnelling

Strike perpendicular to tunnel axis

drive with dip		drive against dip	
dip 45-90 very favourable	dip 20-45 favourable	dip 45-90 fair	dip 20-45 unfavourable

Strike parallel to tunnel axis

Strike parallel to tunnel axis		Irrespective of strike	
dip 20-45 fair	dip 45-90 very unfavourable	dip 0-20 fair	

(D) Rating adjustment for discontinuity orientations

Effect of discontinuity orientation (from Table C)	Very favourable	Favourable	Fair	Unfavourable	Very unfavourable
Ratings:					
Tunnels and mines	0	-2	-5	-10	-12
Foundations	0	-2	-7	-15	-25
Slopes	0	-5	-25	-50	-60

(E) Rock mass classes determined from total ratings

Rating	100-81	80-61	60-41	40-21	<20
Class no.	I	II	III	IV	V
Description	very good rock	good rock	fair rock	poor rock	very poor rock

(F) Interpretation of rock mass classes

Class no.:	I	II	III	IV	V
Average stand-up time	20 yr for 15-m span	1 yr for 10-m span	1 wk for 5-m span	10 h for 2.5-m span	30 min for 1-m span
Cohesion of rock mass (kPa)	>400	300-400	200-300	100-200	<100
Friction angle of rock mass (deg)	>45	35-45	25-35	15-25	<15

Q-system of Rock Mass Classification²

$$Q = \frac{RQD}{J_n} \times \frac{J_r}{J_a} \times \frac{J_w}{SRF}$$

Rock Quality Designation (RQD)

- 0–25 (a) Very poor
- 25–50 (b) Poor
- 50–75 (c) Fair
- 75–90 (d) Good
- 90–100 (e) Excellent

Note: Where RQD is reported or measured as 10 (including 0), a nominal value of 10 is used to evaluate Q. RQD intervals of 5, i.e. 100, 95, 90, etc., are sufficiently accurate.

Joint Set Number (J_n)

- 0.5–1.0 (a) Massive, none or few joints
- 2 (b) One joint set
- 3 (c) One joint set plus random
- 4 (d) Two joint sets
- 6 (e) Two joint sets plus random
- 9 (f) Three joint sets
- 12 (g) Three joint sets plus random
- 15 (h) Four or more joint sets, random, heavily jointed 'sugar cube', etc.
- 20 (j) Crushed rock, earth-like

Note: For intersections, use (3.0 × J_n); for portals, use (2.0 × J_n).

Joint Roughness Number (J_r)

- (i) Rock wall contact and
- (ii) Rock wall contact before 10 cm shear
 - 4 (a) Discontinuous joint
 - 3 (b) Rough or irregular, undulating
 - 2.0 (c) Smooth, undulating
 - 1.5 (d) Slickensided, undulating
 - 1.5 (e) Rough or irregular, planar
 - 1.0 (f) Smooth, planar
 - 0.5 (g) Slickensided, planar
- (iii) No rock wall contact when sheared
 - 1.0 (h) Zone containing clay minerals thick enough to prevent rock wall contact
 - 1.0 (j) Sandy, gravelly, or crushed zone thick enough to prevent rock wall contact

small-scale
 ↓
 scale increasing
 ↓
 intermediate-scale

Notes: Add 1.0 if the mean spacing of the relevant joint set is greater than 3 m.
 J_r = 0.5 can be used for planar slickensided joints having lincation, provided the lineations are favourably orientated.
 Descriptions (b) to (g) refer to small-scale features and intermediate-scale features, in that order.

² Barton, N., Lien R. and Lunde J. (1974) Engineering classification of rock masses for the design of tunnel support. *Rock Mech.*, 6, 183–236.

Joint

0.75

1.0

2.0

3.0

4.0

4.0

6.0

8.0

8.0–1

6.0, 8

or 8.0

5.0

10.0, 1

or 13.0

* Valu

prope

Joint Alteration Number (J_a)

		ϕ_r (approx.)*
	(i) <i>Rock wall contact</i>	
0.75	(a) Tightly healed, hard, non-softening, impermeable filling, i.e. quartz or epidote	
1.0	(b) Unaltered joint walls, surface staining only	25–35°
2.0	(c) Slightly altered joint walls. Non-softening mineral coatings, sandy particles, clay-free disintegrated rock, etc.	25–30°
3.0	(d) Silty or sandy clay coatings, small clay fraction (non-softening)	20–25°
4.0	(e) Softening or low-friction clay mineral coatings, i.e. kaolinite, mica. Also chlorite, talc, gypsum, and graphite, etc., and small quantities of swelling clays (discontinuous coatings, 1–2 mm or less in thickness)	8–16°
	(ii) <i>Rock wall contact before 10 cm shear</i>	
4.0	(f) Sandy particles, clay-free disintegrated rock, etc.	25–30°
6.0	(g) Strongly over-consolidated, non-softening clay mineral fillings (continuous, <5 mm in thickness)	16–24°
8.0	(h) Medium or low over-consolidation, softening, clay mineral fillings (continuous, <5 mm in thickness)	12–16°
8.0–12.0	(j) Swelling clay fillings, i.e. montmorillonite (continuous, <5 mm in thickness). Value of J_a depends on percentage of swelling clay-sized particles, and access to water, etc.	6–12°
	(iii) <i>No rock wall contact when sheared</i>	
6.0, 8.0 or 8.0–12.0	(k) Zones or bands of disintegrated or rock and clay — see (g), (h), (j) for description of clay condition	6–24°
5.0	(l) Zones or bands of silty clay, small clay fraction (non-softening)	
10.0, 13.0 or 13.0–20.0	(m) Thick, continuous zones or bands of clay — see (g), (h), (j) for description of clay condition	

* Values of ϕ_r are intended as an approximate guide to the mineralogical properties of the alteration products, if present.

Stress Reduction Factor (SRF)

<i>(i) Weakness zones intersecting excavation, which may cause loosening of rock mass when tunnel is excavated</i>			
10.0	(a)	Multiple occurrences of weakness zones containing clay or chemically disintegrated rock, very loose surrounding rock (any depth)	
5.0	(b)	Single weakness zones containing clay or chemically disintegrated rock (excavation depth <50 m)	
2.5	(c)	Single weakness zones containing clay or chemically disintegrated rock (excavation depth >50 m)	
7.5	(d)	Multiple shear zones in competent rock (clay-free), loose surrounding rock (any depth) ^a	
5.0	(e)	Single shear zones in competent rock (clay-free) (depth of excavation <50 m) ^a	
2.5	(f)	Single shear zones in competent rock (clay-free) (depth of excavation >50 m) ^a	
5.0	(g)	Loose open joints, heavily jointed or 'sugar cube', etc. (any depth) ^a	
<i>(ii) Competent rock, rock stress problems^b</i>			
2.5	(h)	Low stress, near surface	$\sigma_c/\sigma_1 > 200$ $\sigma_t/\sigma_1 > 13$
1.0	(j)	Medium stress	200–10 13–0.66
0.5–2.0	(k)	High-stress, very tight structure (usually unfavourable to stability, may be unfavourable for wall stability)	10–5 0.66–0.33
5–10	(l)	Mild rock burst (massive rock)	5–2.5 0.33–0.16
10–20	(m)	Heavy rock burst (massive rock)	<2.5 <0.16
<i>(iii) Squeezing rock; plastic flow of incompetent rock under the influence of high rock pressures</i>			
5–10	(n)	Mild squeezing rock pressure	
10–20	(p)	Heavy squeezing rock pressure	
<i>(iv) Swelling rock; chemical swelling activity depending on presence of water</i>			
5–10	(q)	Mild swelling rock pressure	
10–15	(r)	Heavy swelling rock pressure	

^a Reduce these SRF values by 25–50% if the relevant shear zones only influence, but do not intersect, the excavation.

^b Few case records available where depth of crown below surface is less than span width; suggest SRF increase from 2.5 to 5 for such cases. For strongly anisotropic stress field (if measured): $5 \leq \sigma_1/\sigma_3 \leq 10$: reduce σ_c and σ_t to $0.8\sigma_c$ and $0.8\sigma_t$; $\sigma_1/\sigma_3 > 10$: reduce σ_c and σ_t to $0.6\sigma_c$ and $0.6\sigma_t$ (σ_c = unconfined compressive strength, σ_t = tensile strength (point load), σ_1 and σ_3 are major and minor principal stresses).

Joint

1.0

0.66

0.5

0.33

0.2–0.

0.1–0.

Note:

WH
guide

(1) W

m

w

J

j

(2) T

b

st

j

w

e

(3) T

m

d

th

s

o

j

h

(4) V

'1

th

a

b

r

u

in

(5) T

Joint Water Reduction Factor (J_w)

		Approx. water pressure (kg/cm ²)
1.0	(a) Dry excavations or minor inflow, e.g. 5 l/min locally	<1
0.66	(b) Medium inflow or pressure, occasional outwash of joint fillings	1.0–2.5
0.5	(c) Large inflow or high pressure in competent rock with unfilled joints	2.5–10.0
0.33	(d) Large inflow or high pressure, considerable outwash of joint fillings	2.5–10.0
0.2–0.1	(e) Exceptionally high inflow or water pressure at blasting, decaying with time	>10.0
0.1–0.05	(f) Exceptionally high inflow or water pressure continuing without noticeable decay	>10.0

Note: Factors (c) to (f) are crude estimates. Increase J_w if drainage measures are installed. Special problems due to ice formation are not considered.

When making estimates of Q , the Rock Mass Quality, the following guidelines should be followed, in addition to the notes in the tables.

- (1) When borehole core is unavailable, for the case of clay-free rock masses RQD can be estimated from $RQD = 115 - 3.3J_v$ (approx.) where J_v = total number of joints per m³ ($RQD = 100$ for $J_v < 4.5$). J_v is evaluated as the sum of the number of joints per metre for each joint set.
- (2) The parameter J_n , representing the number of joint sets, will often be affected by foliation, schistosity, slaty cleavage or bedding, etc. If strongly developed, these features should be counted as a complete joint set: if they are poorly developed or rarely visible, then it will be more appropriate to count them as 'random joints' when evaluating J_n .
- (3) The parameters J_t and J_a (representing shear strength) should normally be relevant to the weakest significant joint set or clay-filled discontinuity in a given zone, but the value of J_t/J_a should relate to the surface most likely to allow failure to initiate. Thus, if the joint set or discontinuity with the minimum value of J_t/J_a is favourably orientated for stability, then a second, less favourably orientated joint set or discontinuity may sometimes be more significant, and its higher value of J_t/J_a should be used when evaluating Q .
- (4) When a rock mass contains clay, the factor SRF appropriate to 'loosening loads' should be evaluated. In such cases the strength of the intact rock is of little interest. However, when jointing is minimal and clay is completely absent, the strength of the intact rock may become the weakest link, and the stability will then depend on the ratio rock stress/rock strength. A strongly anisotropic stress field is unfavourable for stability and is roughly accounted for as in the note in the table for SRF evaluation.
- (5) The compressive and tensile strengths (σ_c and of σ_t) the intact rock

should be evaluated in the saturated condition if this is appropriate to present or future *in situ* conditions. A conservative estimate of strength should be made for those rocks that deteriorate when exposed to moist or saturated conditions.

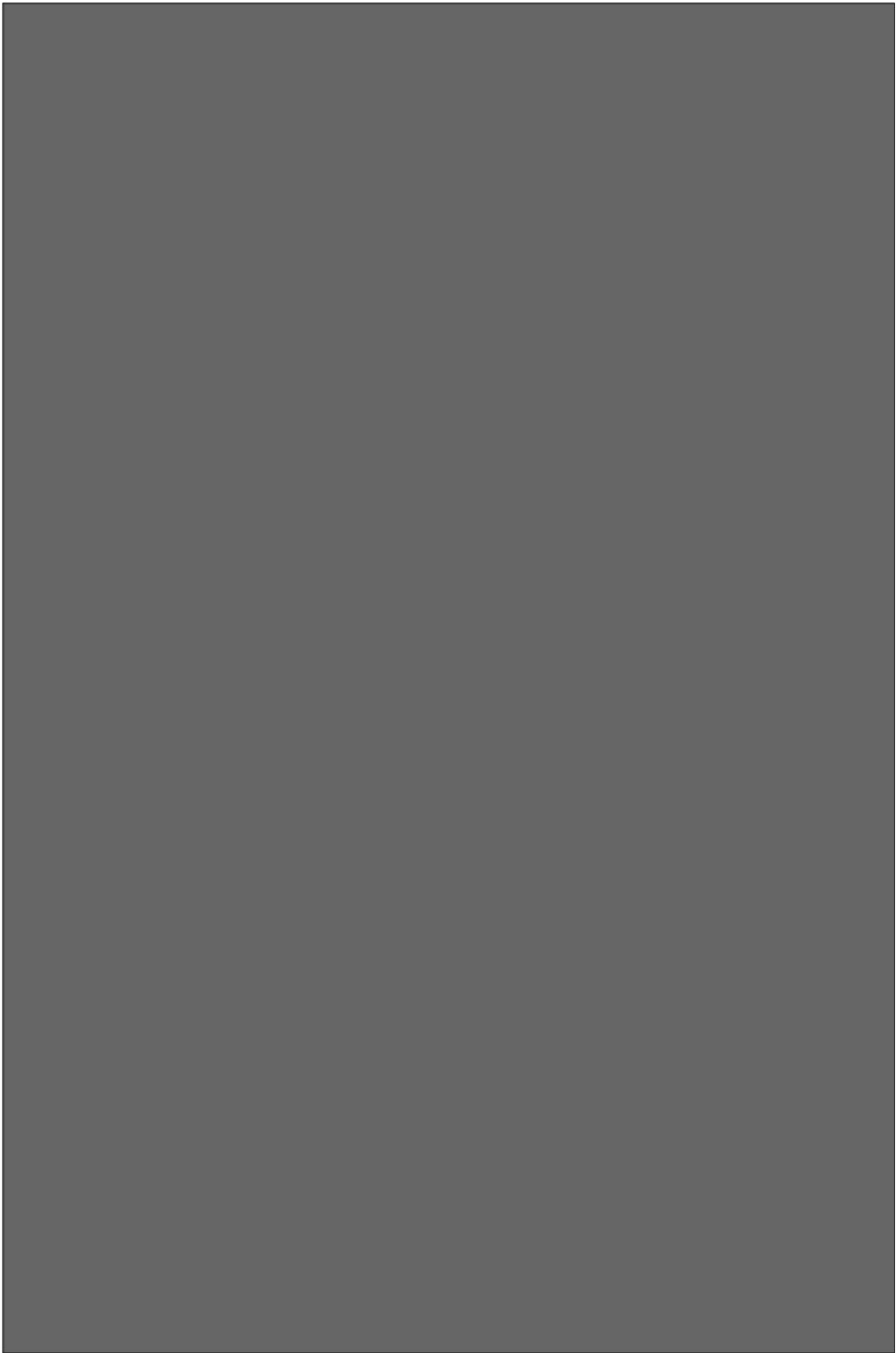
ϕ , theo
accura
adjacen
advanc
Alto Li
anisotr
que
apertu
bias 16
blastab
blastin
blocks
Buddh
cause-
cavern
bloo
und
Chann
CHILE
Chilca
coal m
comple
forc
stre
core
disk
frac
leng
creep 2
cutting
dam fo

RMR values

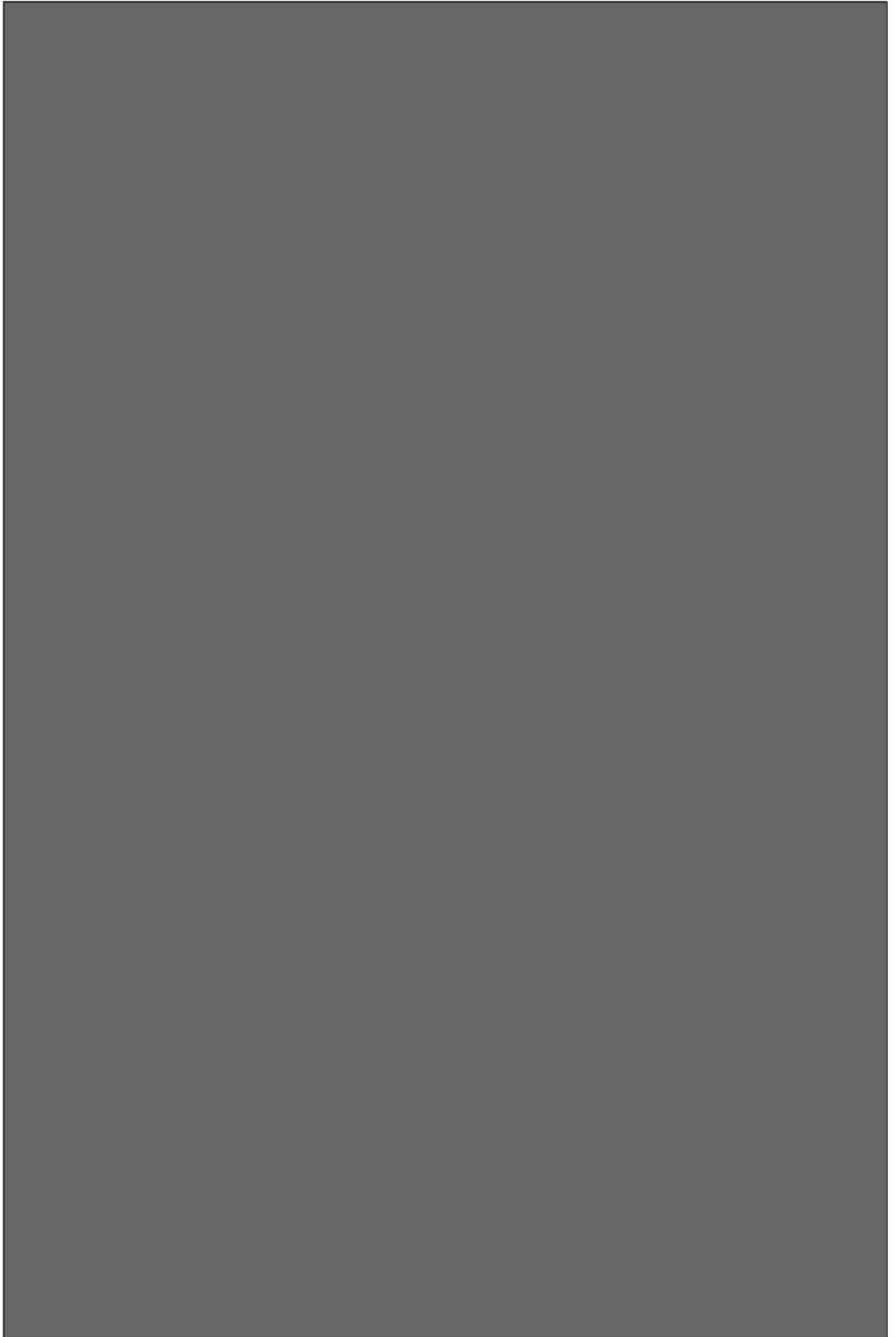
I.D	Width [m]	RQD [%]	A2	A1	A3	A4	A5	B	RMR	Domain	Class
1	23	95	20	12	15	10	15	-5	67	S2a	Good
2	31	100	20	12	15	20	15	-5	77	S2a	Good
3	18	95	20	12	15	5	15	-5	62	S2a	Good
4	50	100	20	12	15	10	15	-5	67	S2a	Good
5	15	75	13	12	15	5	15	-5	55	S2a	Fair
6	15	95	20	12	15	5	15	-5	62	S2a	Good
7	26	100	20	12	15	20	15	-5	77	S2a	Good
8	37	90	17	12	15	5	15	-5	59	S2a	Fair
9	29	75	13	7	10	5	15	-5	45	S2a	Fair
10	31	100	20	12	15	10	15	-5	67	S2a	Good
11	40	75	13	7	10	5	15	-5	45	S2a	Fair
12	20	100	20	12	15	20	15	-5	77	S2a	Good
13	42	85	17	12	15	20	15	-5	74	S2a	Good
14	29	90	17	12	15	10	15	-5	64	S2a	Good
15	18	75	13	12	10	10	15	-5	55	S2a	Fair
16	42	90	17	12	15	5	15	-5	59	S2a	Fair
17	20	75	13	12	10	10	15	-5	55	S2a	Fair
18	10	100	20	12	15	20	15	-5	77	S2a	Good
19	15	100	20	12	15	5	15	-5	62	S2a	Good
20	20	100	20	12	15	20	15	-5	77	S2a	Good
21	15	90	17	12	15	5	15	-5	59	S2a	Fair
22	16	75	13	7	15	5	15	-5	50	S2a	Fair
23	14	95	20	12	15	5	15	-5	62	S2a	Good
24	40	95	20	12	15	5	15	-5	62	S2a	Good
25	18	100	20	12	15	20	15	-5	77	S2a	Good
26	30	95	20	12	15	10	15	-5	67	S2a	Good
29	56	95	20	7	15	5	15	-5	57	S2a	Fair
30	33	95	20	12	15	20	15	-5	77	S2a	Good
31	15	50	8	7	15	0	15	-5	40	S2a	Poor
32	20	90	17	12	15	20	15	-5	74	S2a	Good
33	15	80	17	7	15	0	15	-5	49	S2a	Fair
34	27	90	17	12	15	5	15	-5	59	S2a	Fair
35	60	100	20	12	15	20	15	-5	77	S2a	Good
36	37	90	17	12	15	5	15	-5	59	S2a	Fair
37	26	95	20	12	15	10	15	-5	67	S2a	Good
38	19	90	17	12	15	10	15	-5	64	S2a	Good
39	37	90	17	12	15	10	15	-5	64	S2a	Good
40	15	80	17	12	15	5	15	-5	59	S2a	Fair
41	10	80	17	12	15	10	15	-5	64	S2a	Good
42	15	75	13	7	10	5	15	-5	45	S2a	Fair
60	22	95	20	12	15	20	15	-5	77	S2a	Good
61	22	95	20	12	15	10	15	-5	67	S2a	Good
67	29	95	20	12	15	20	15	-5	77	S2a	Good
68	19	100	20	12	15	20	15	-5	77	S2a	Good
69	13	95	20	12	15	10	15	-5	67	S2a	Good
70	11	95	20	12	15	20	15	-5	77	S2a	Good

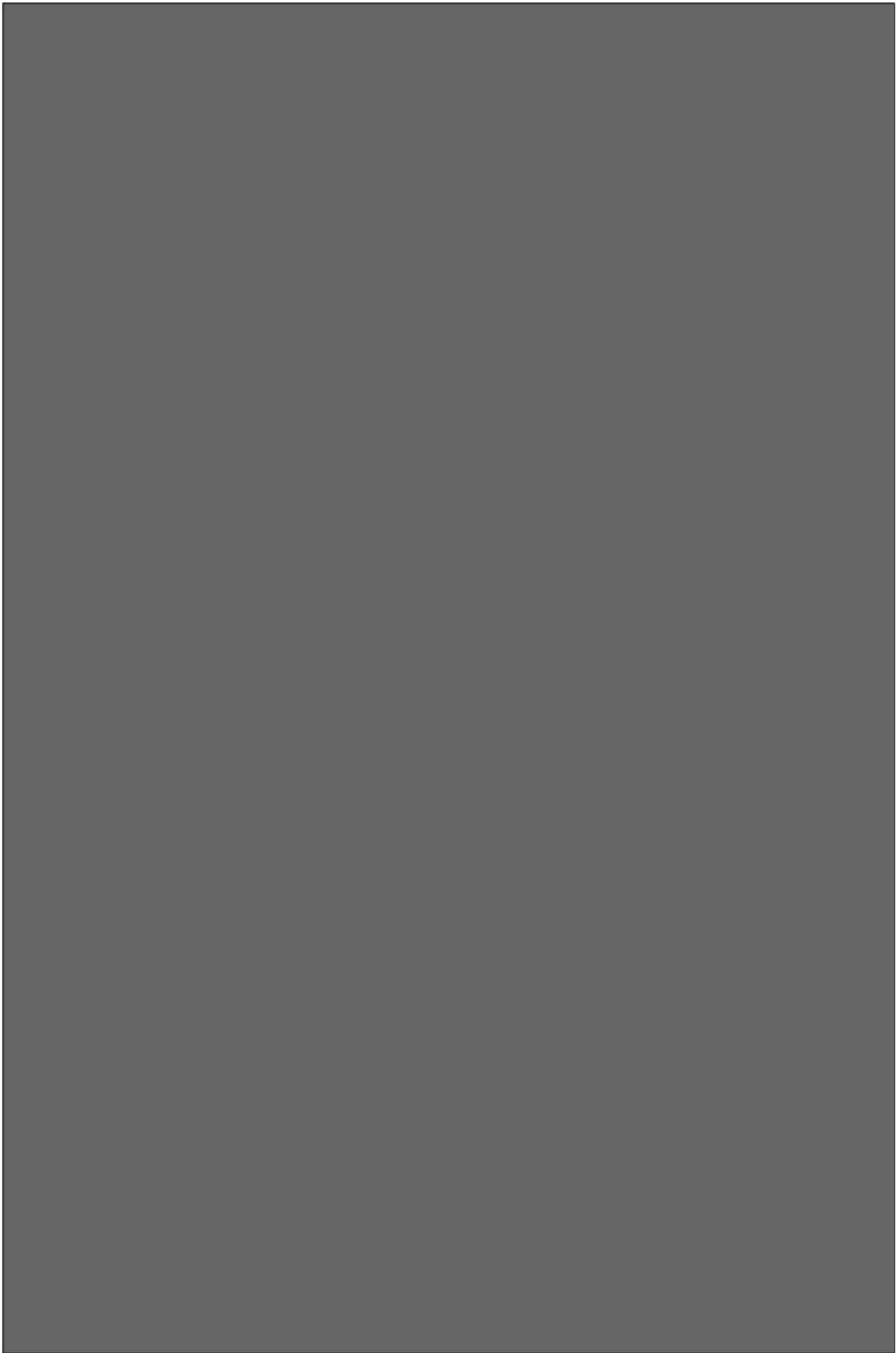
Q values

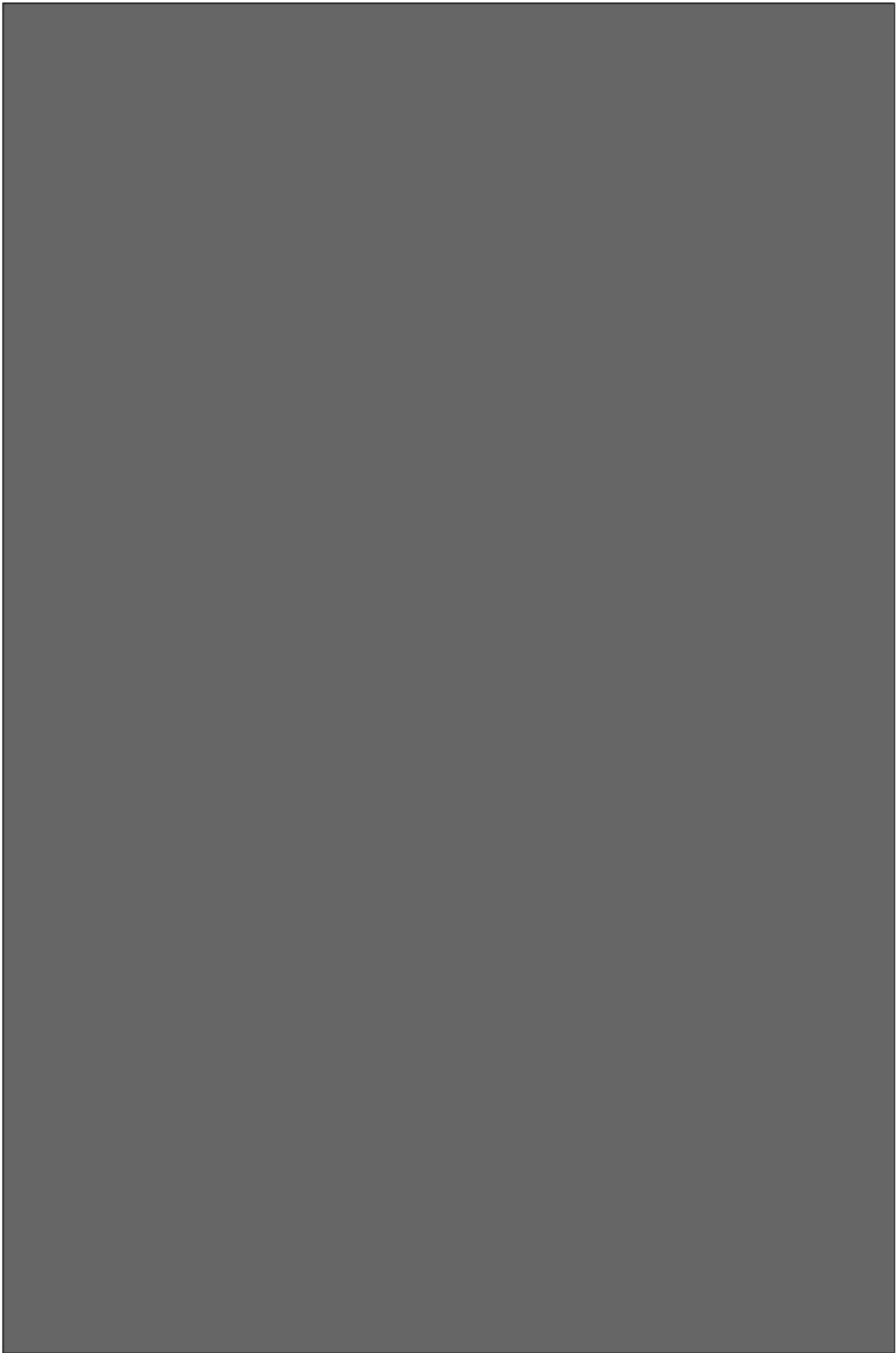
I.D. (Polyline)	Width [m]	RQD [%]	Jn	Jr	Ja	SRF	Q	Geotechnical	Category
1	23	95	9	3	4	1	7.92	S2a	Fair
2	31	100	9	3	1	1	33.33	S2a	Good
3	18	95	9	2	6	1	3.52	S2a	Poor
4	50	100	9	2.5	3	1	9.26	S2a	Fair
5	15	75	9	3	3	1	8.33	S2a	Fair
6	15	95	9	2	6	1	3.52	S2a	Poor
7	26	100	9	3	1	1	33.33	S2a	Good
8	37	90	9	2	8	1	2.50	S2a	Poor
9	29	75	9	3	3	1	8.33	S2a	Fair
10	31	100	9	3	3	1	11.11	S2a	Good
11	40	75	9	2	8	1	2.08	S2a	Poor
12	20	100	9	3	2	1	16.67	S2a	Good
13	42	85	9	3	2	1	14.17	S2a	Good
14	29	90	9	2.5	2	1	12.50	S2a	Good
15	18	75	9	2.5	3	1	6.94	S2a	Fair
16	42	90	9	3	4	1	7.50	S2a	Fair
17	20	75	9	3	4	1	6.25	S2a	Fair
18	10	100	9	3	1	1	33.33	S2a	Good
19	15	100	9	2	6	1	3.70	S2a	Poor
20	20	100	9	3	2	1	16.67	S2a	Good
21	15	90	9	2	6	1	3.33	S2a	Poor
22	16	75	9	3	6	1	4.17	S2a	Fair
23	14	95	9	1.5	3	1	5.28	S2a	Fair
24	40	95	9	3	4	1	7.92	S2a	Fair
25	18	100	9	3	1	1	33.33	S2a	Good
26	30	95	9	3	3	1	10.56	S2a	Good
29	56	95	9	3	8	1	3.96	S2a	Poor
30	33	95	9	3	2	1	15.83	S2a	Good
31	15	50	9	1	10	5	0.19	S2a	Very Poor
32	20	90	9	3	2	1	15.00	S2a	Good
33	15	80	9	1	8	5	0.22	S2a	Very Poor
34	27	90	9	4	8	1	5.00	S2a	Fair
35	60	100	9	3	1	1	33.33	S2a	Good

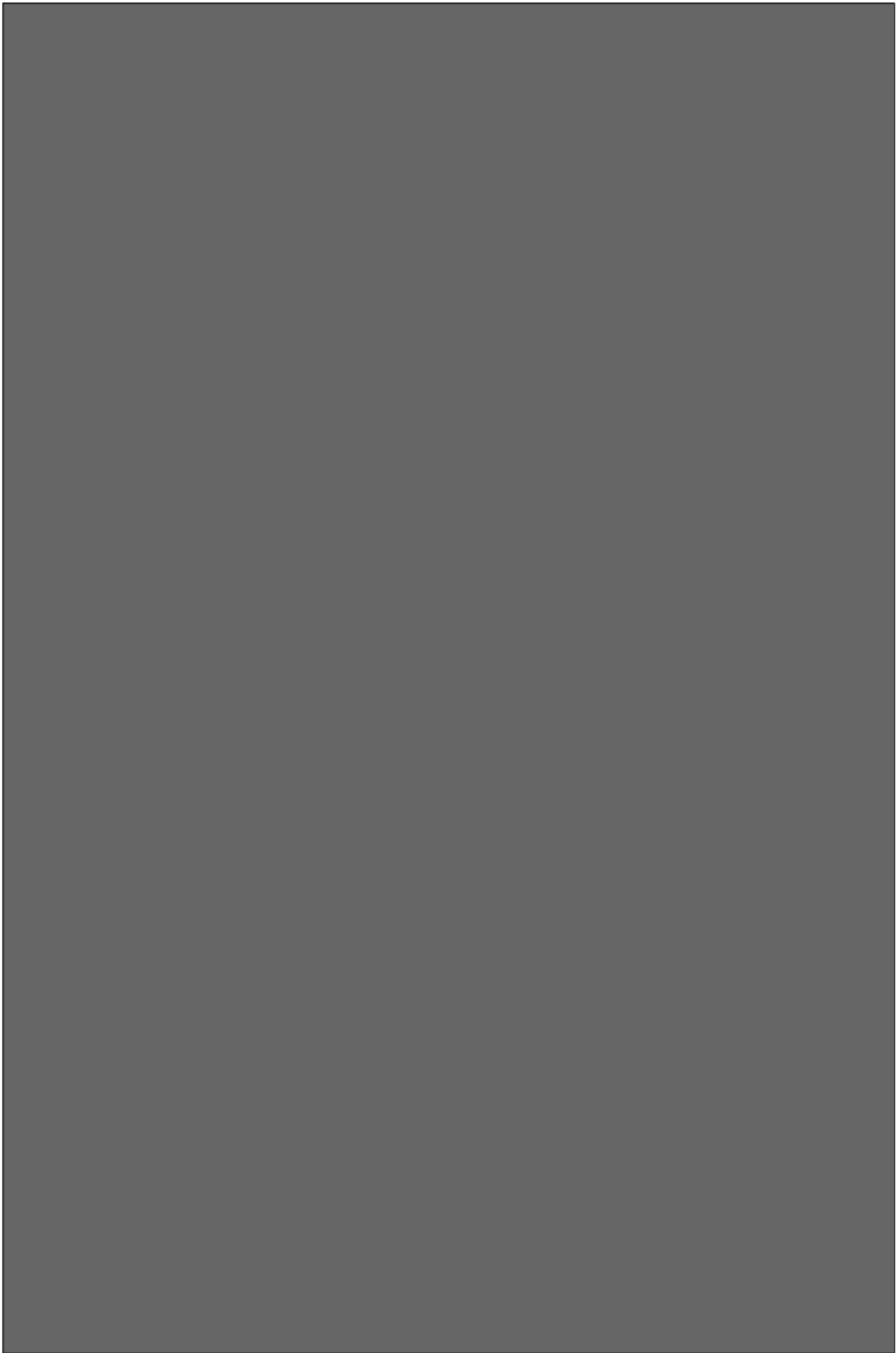


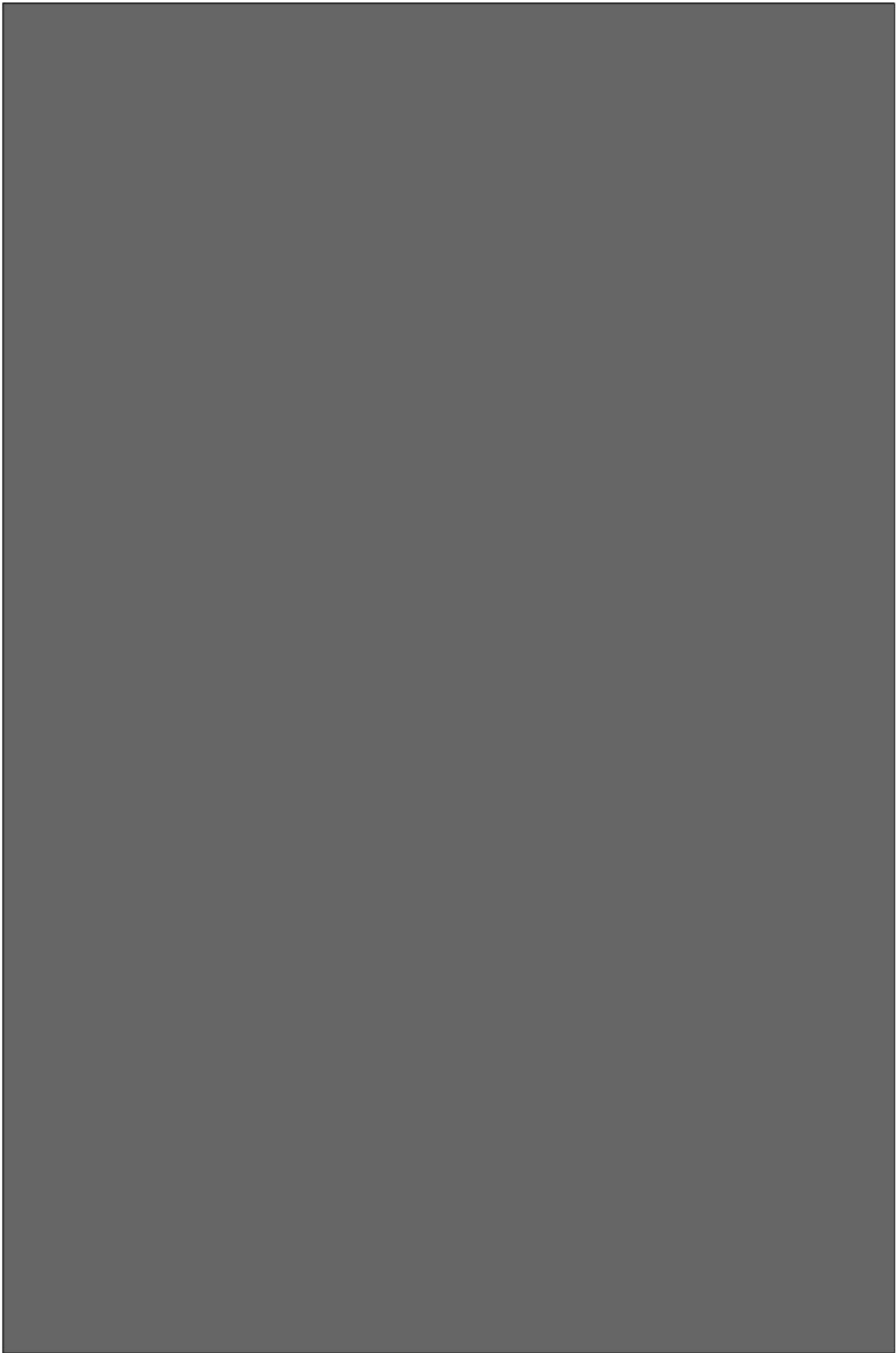
G Laboratory Report

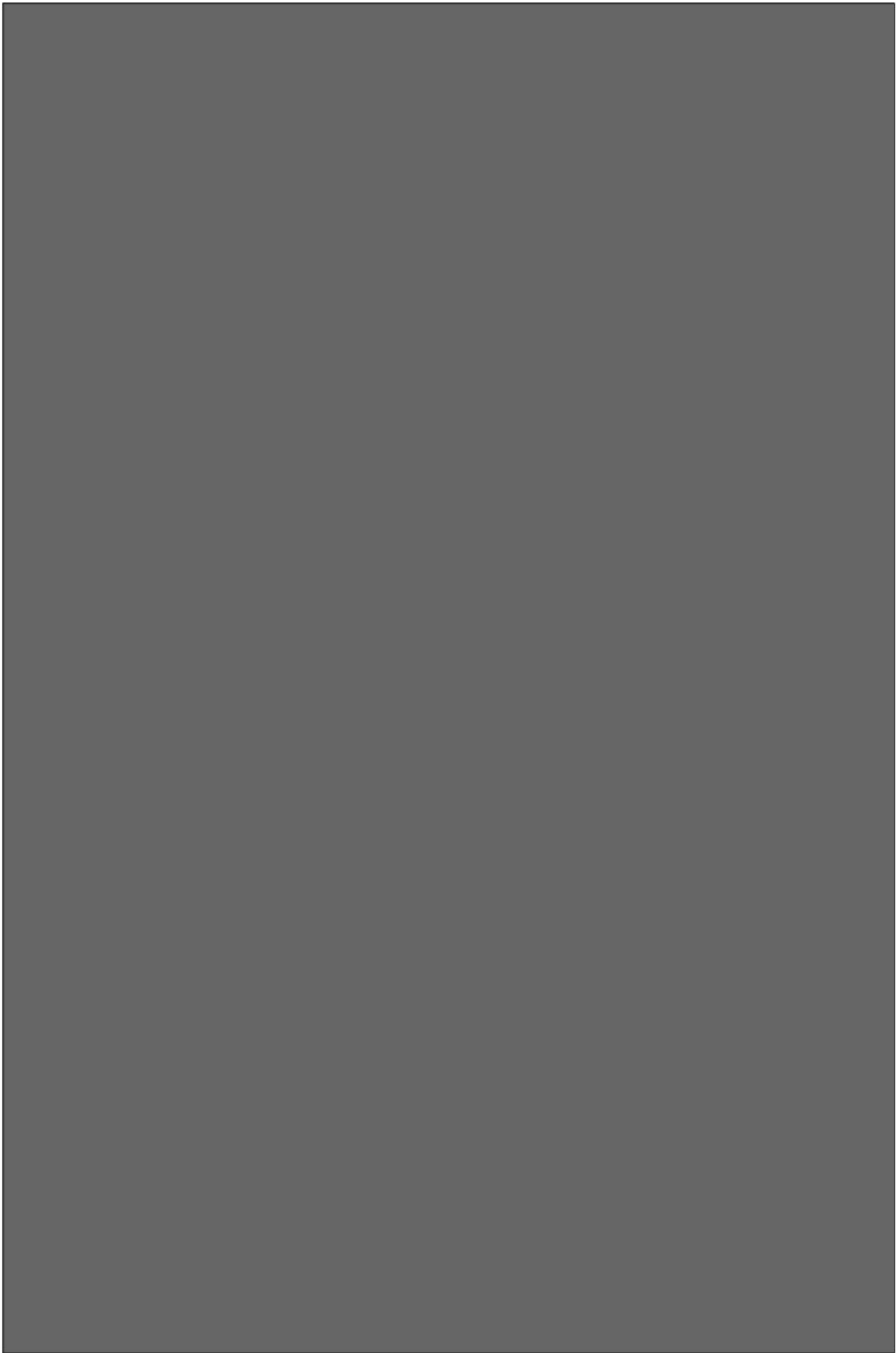


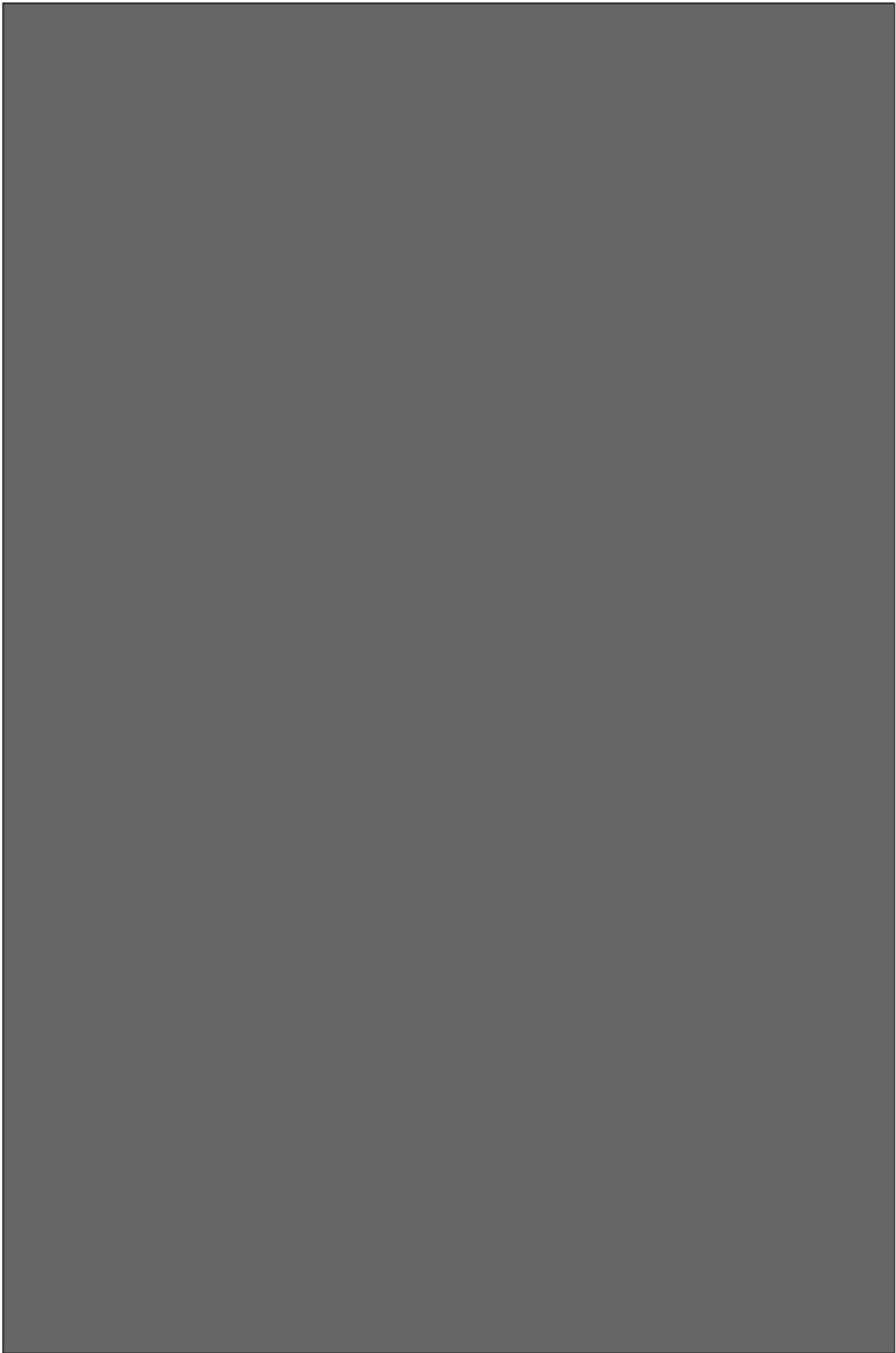


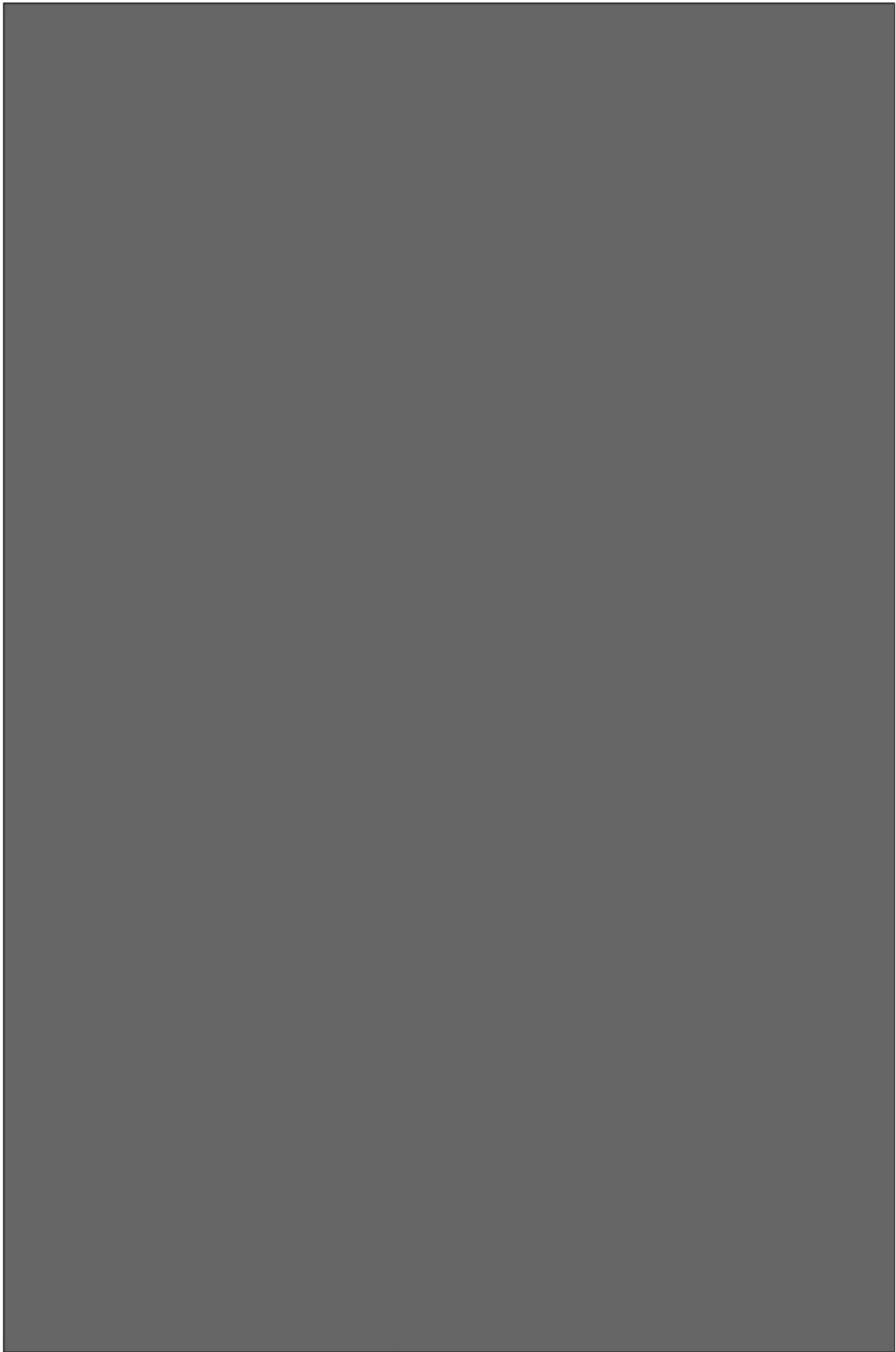


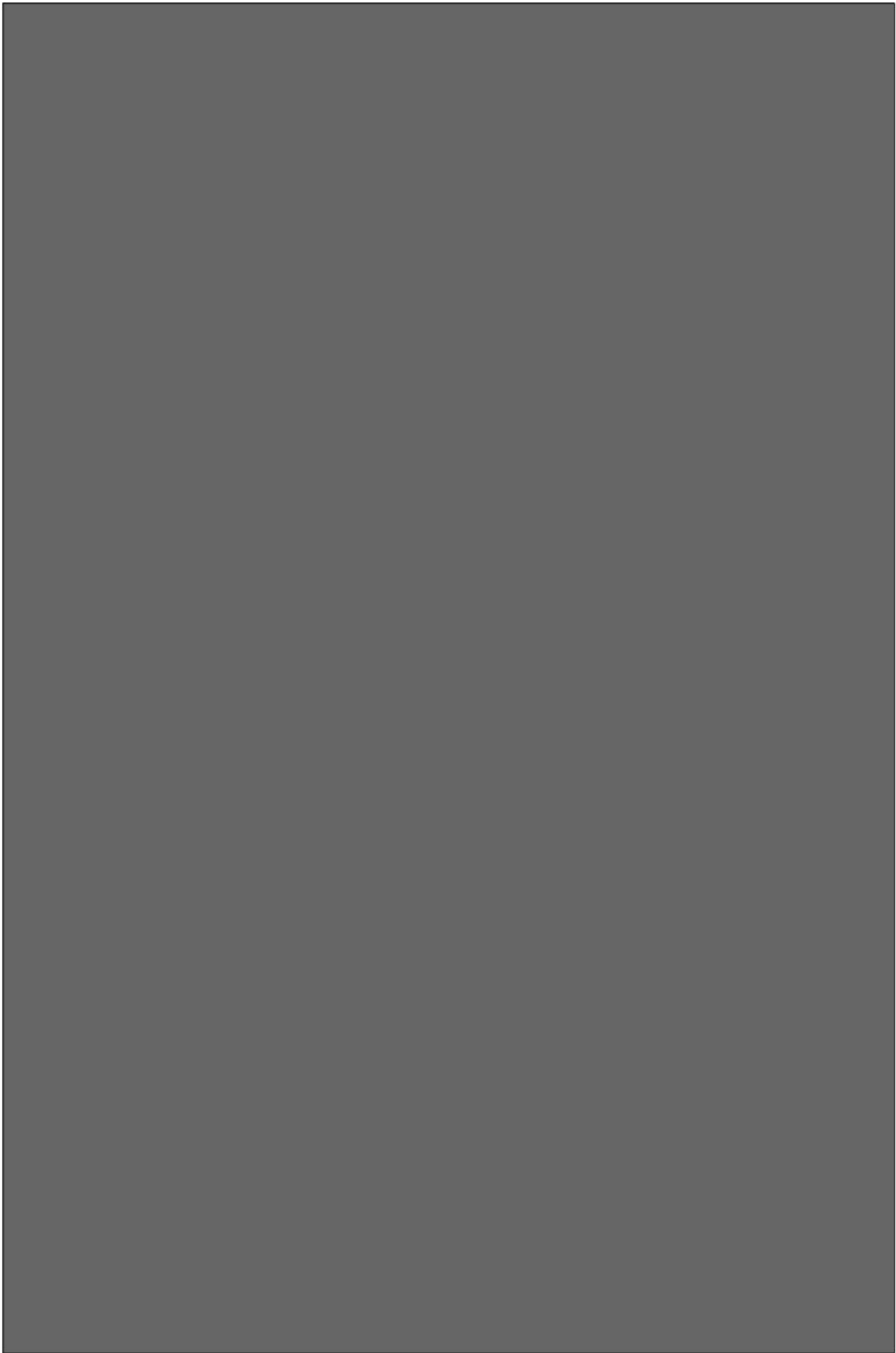


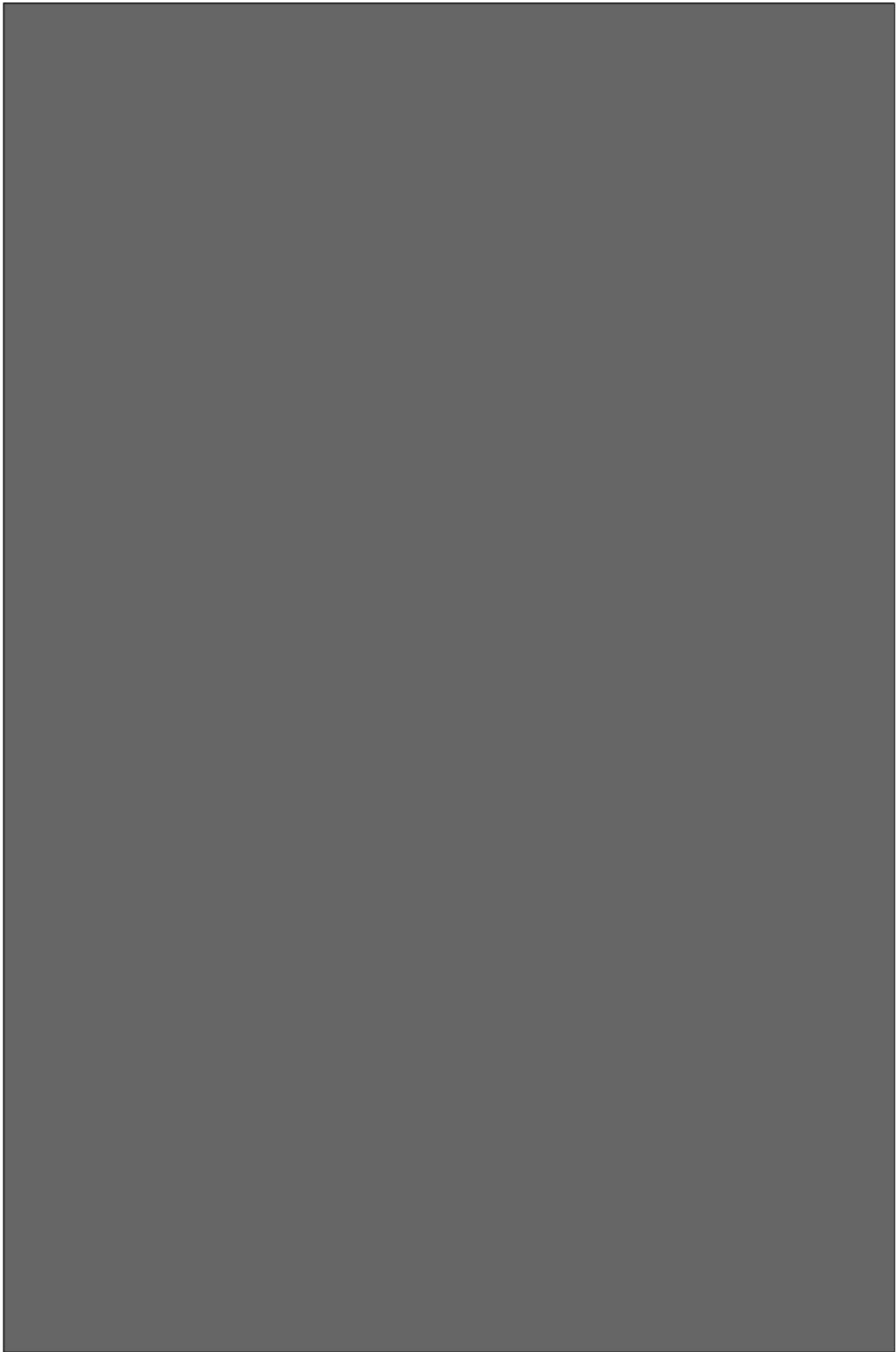


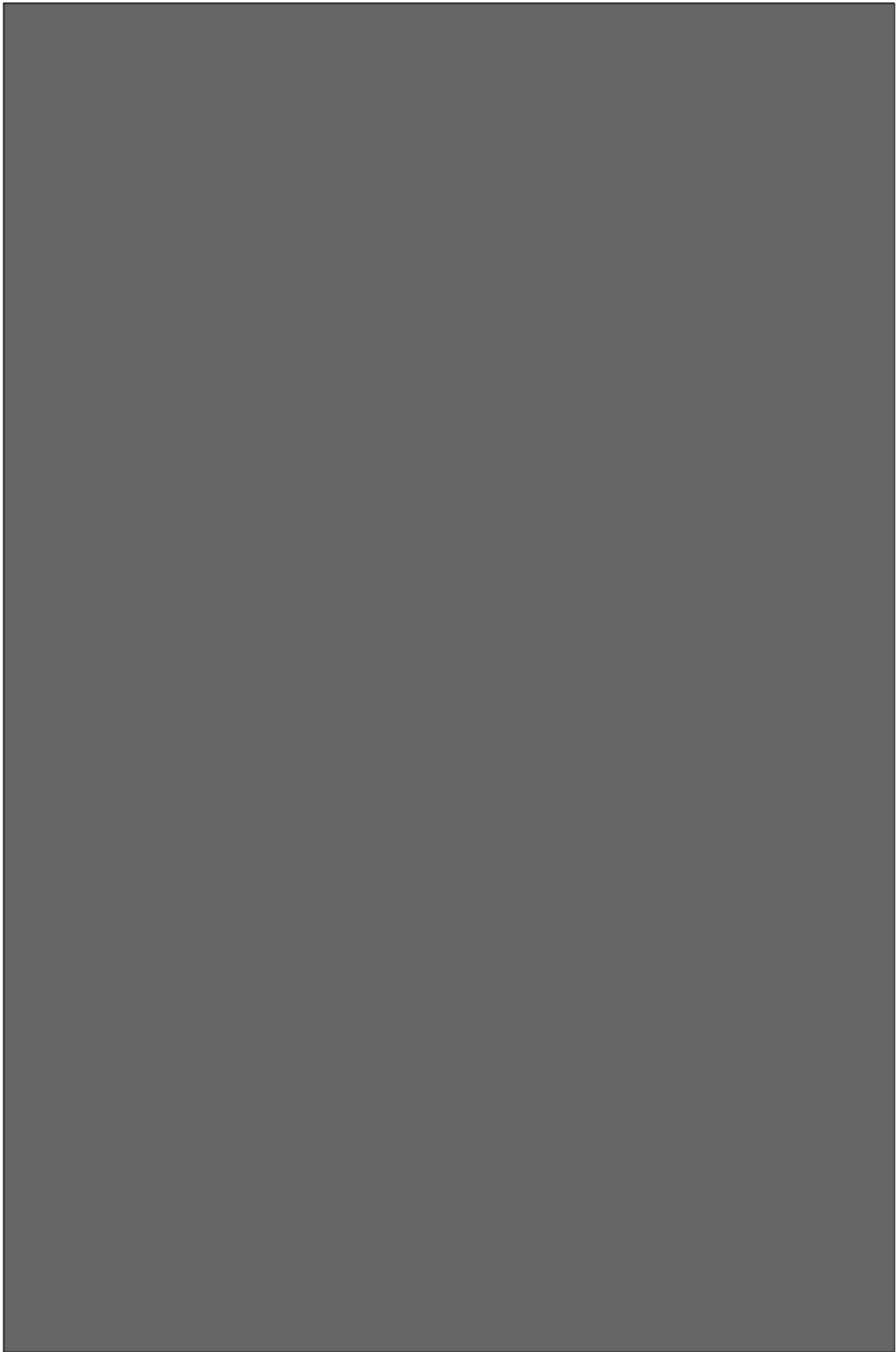


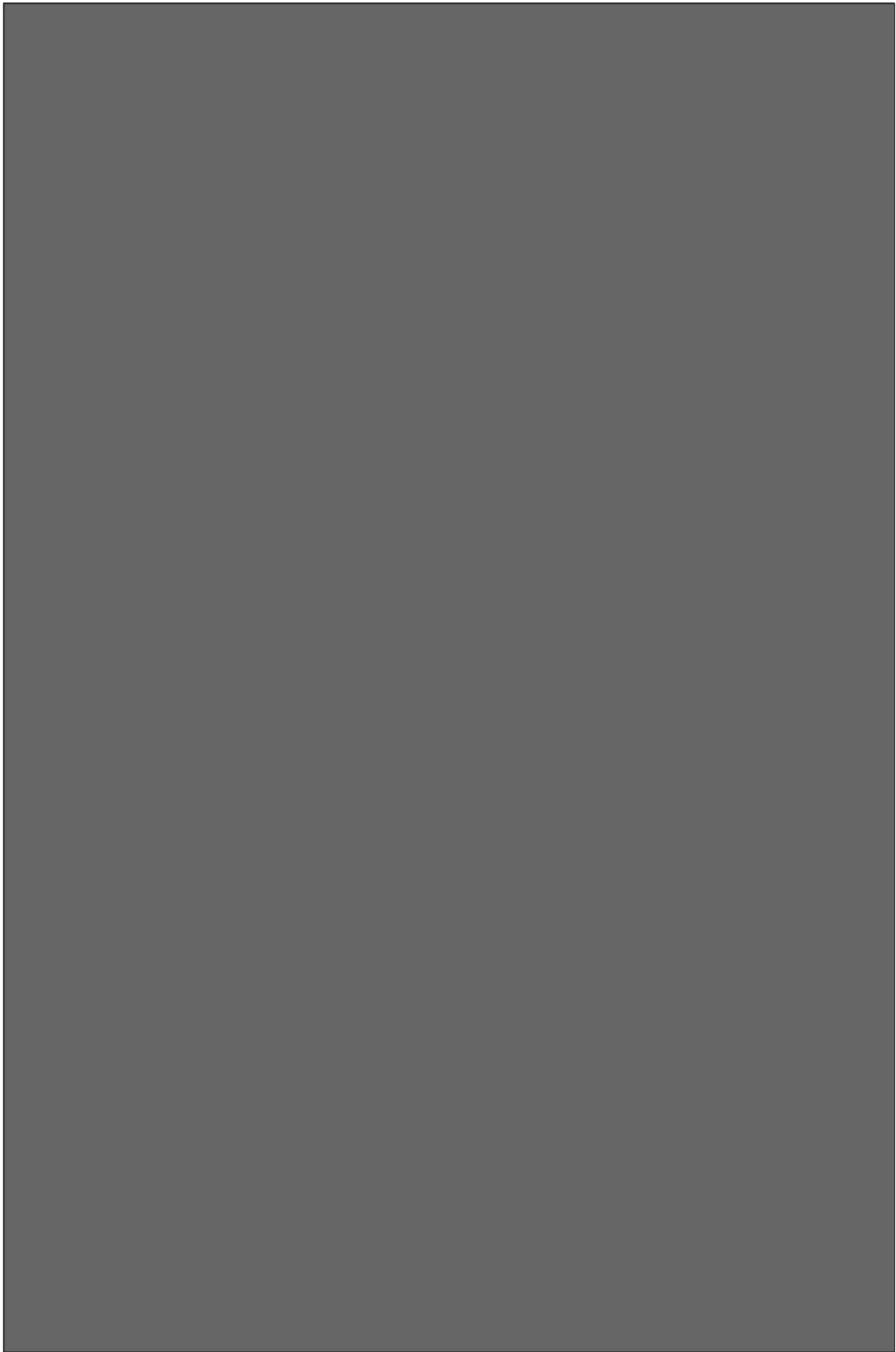


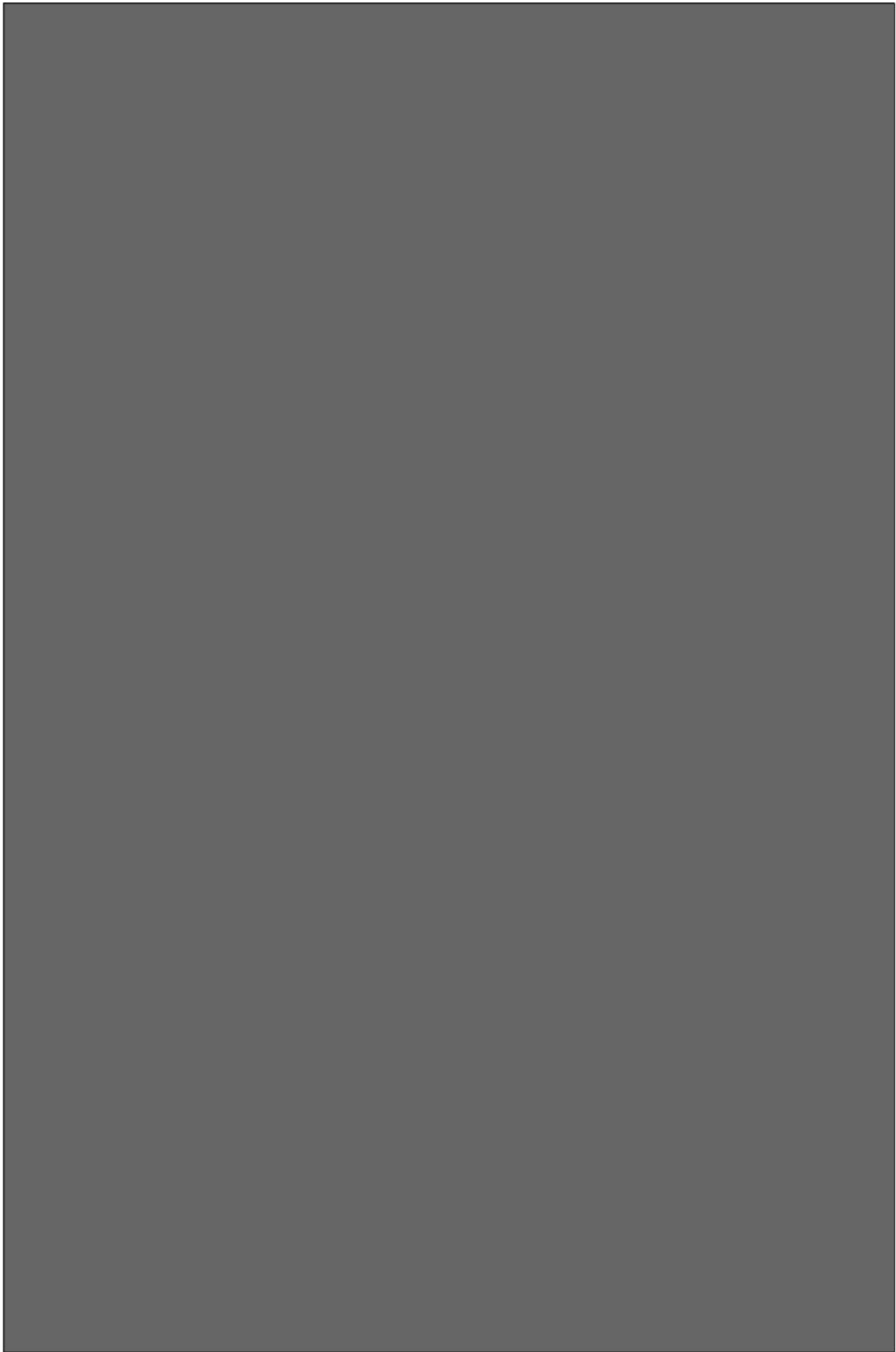


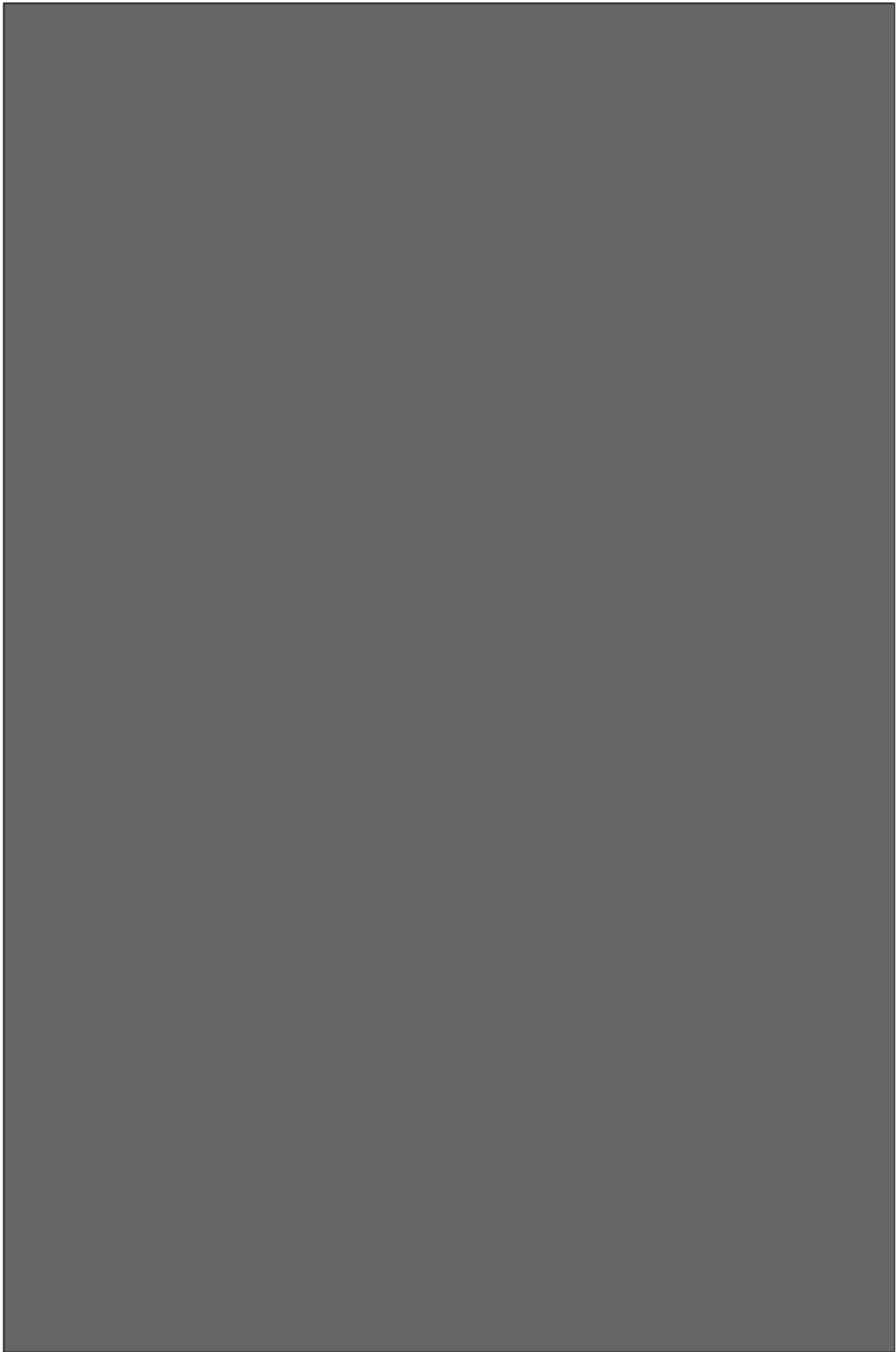


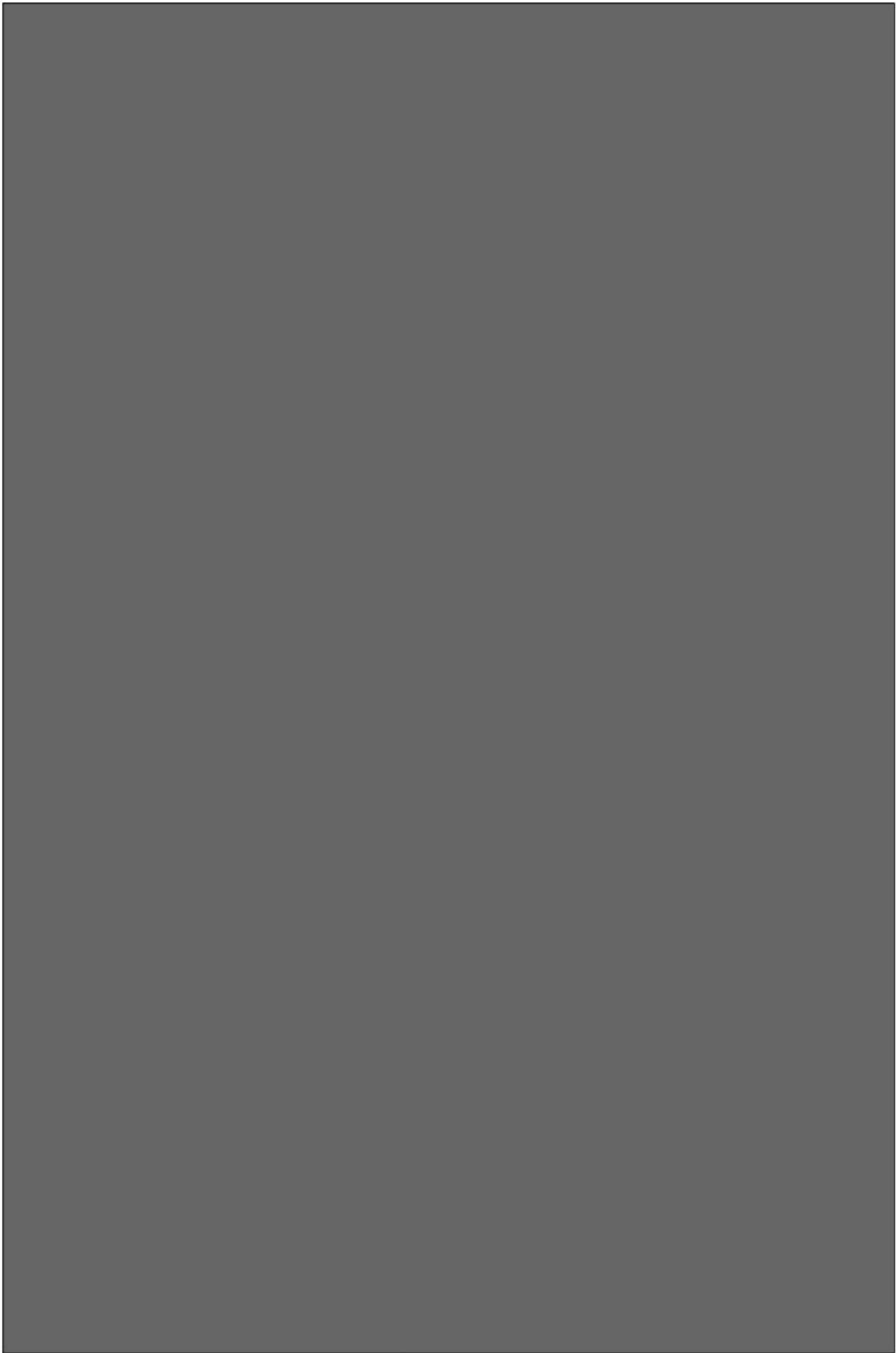


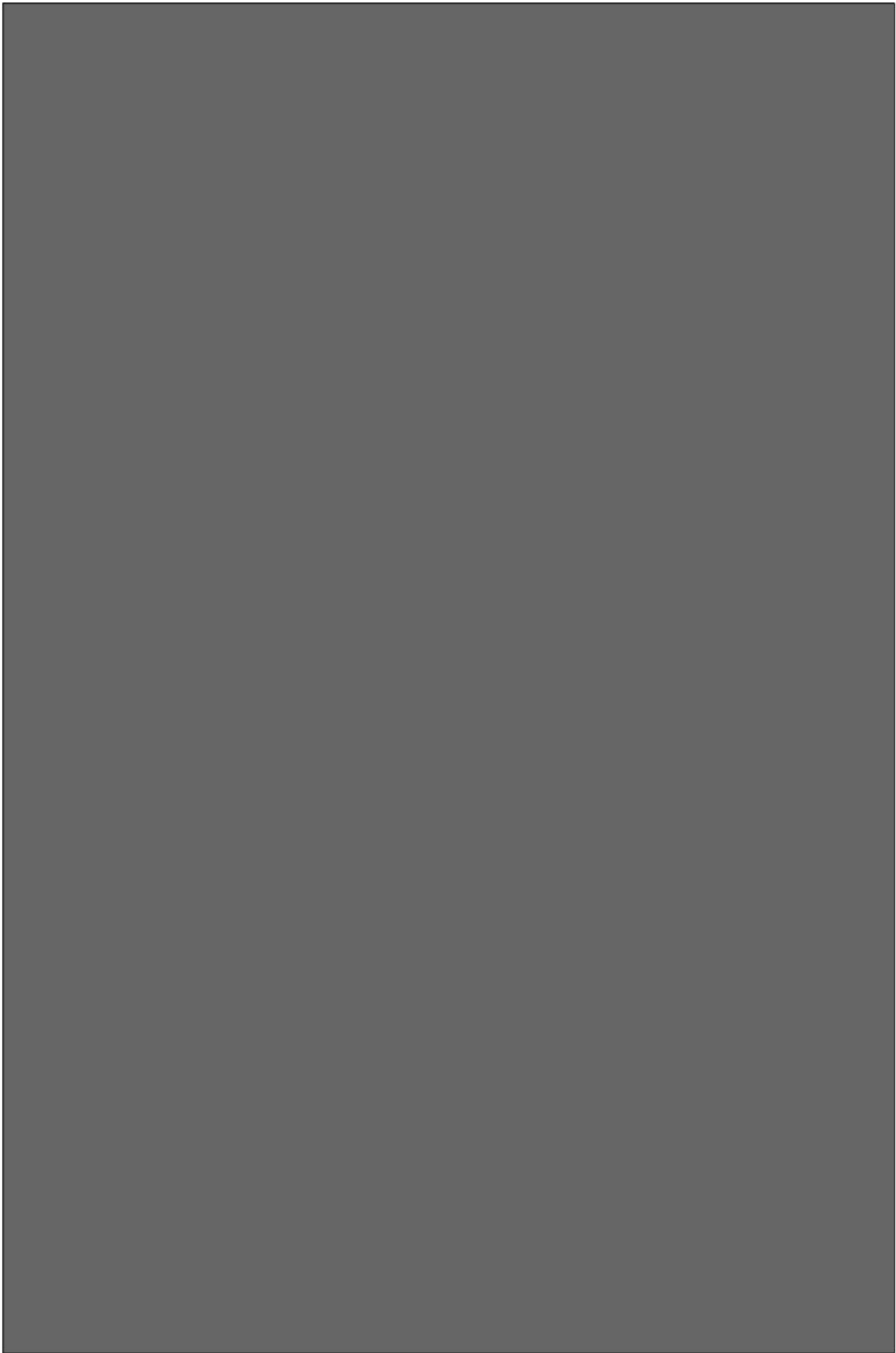


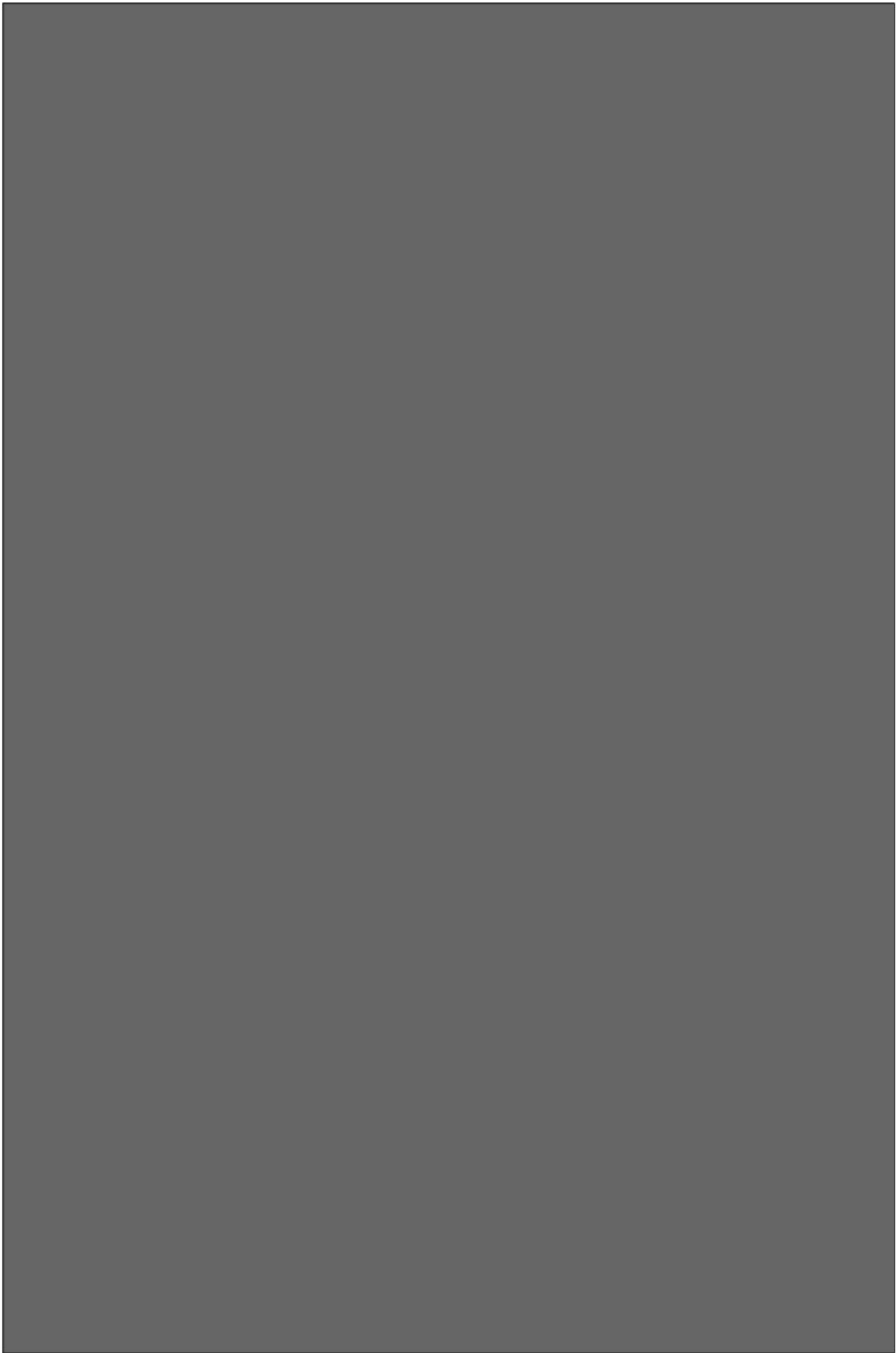


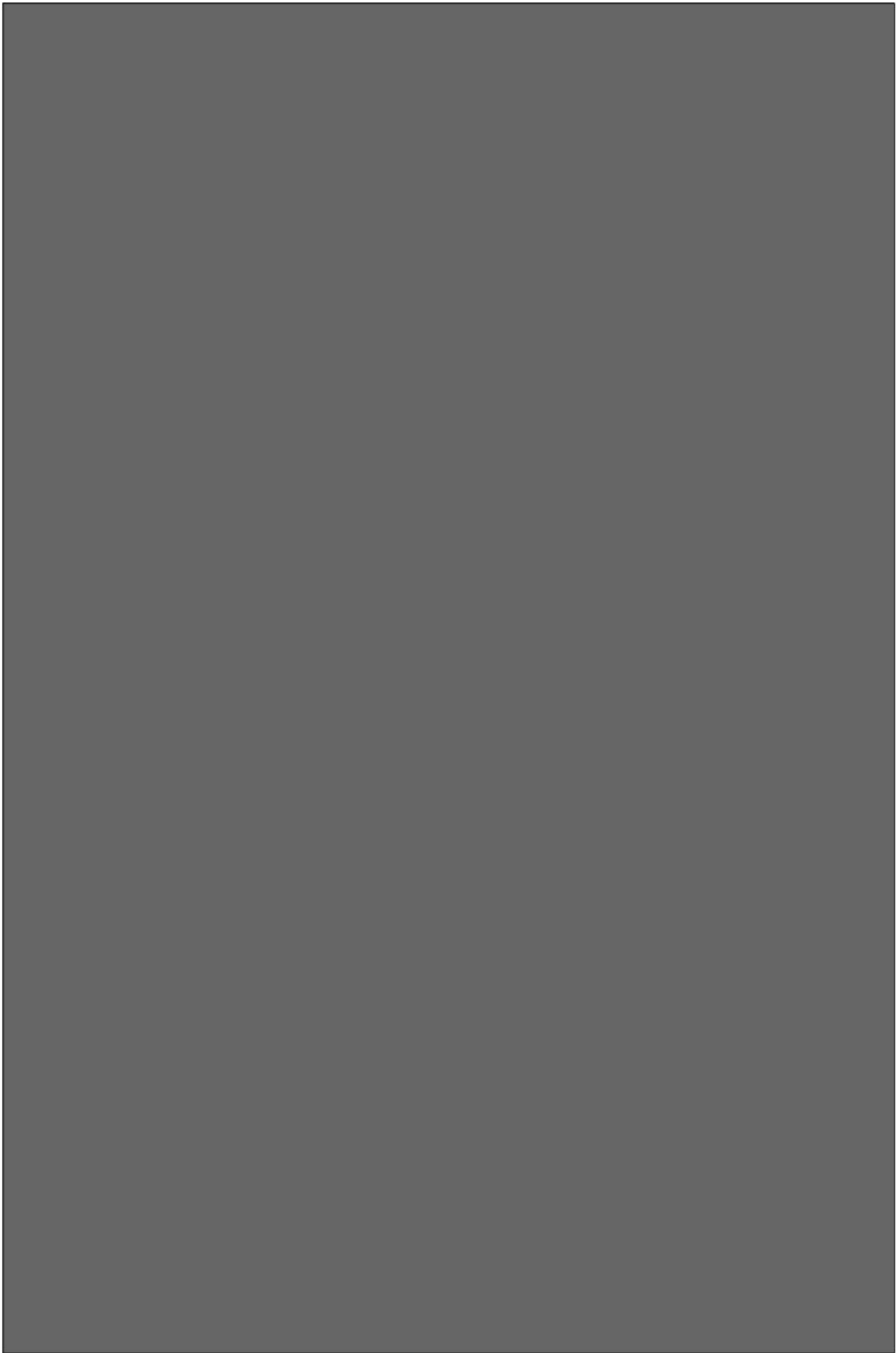


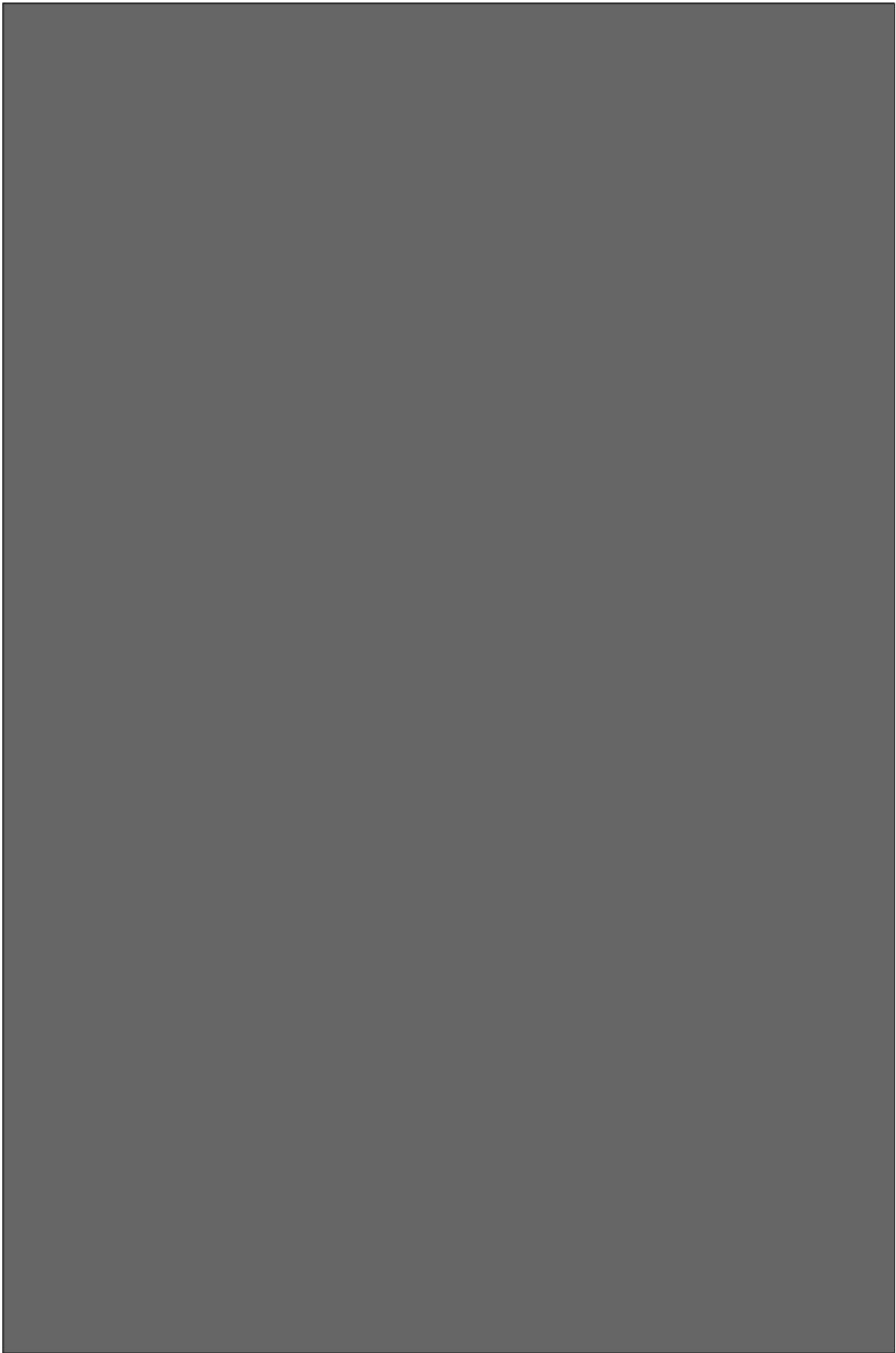


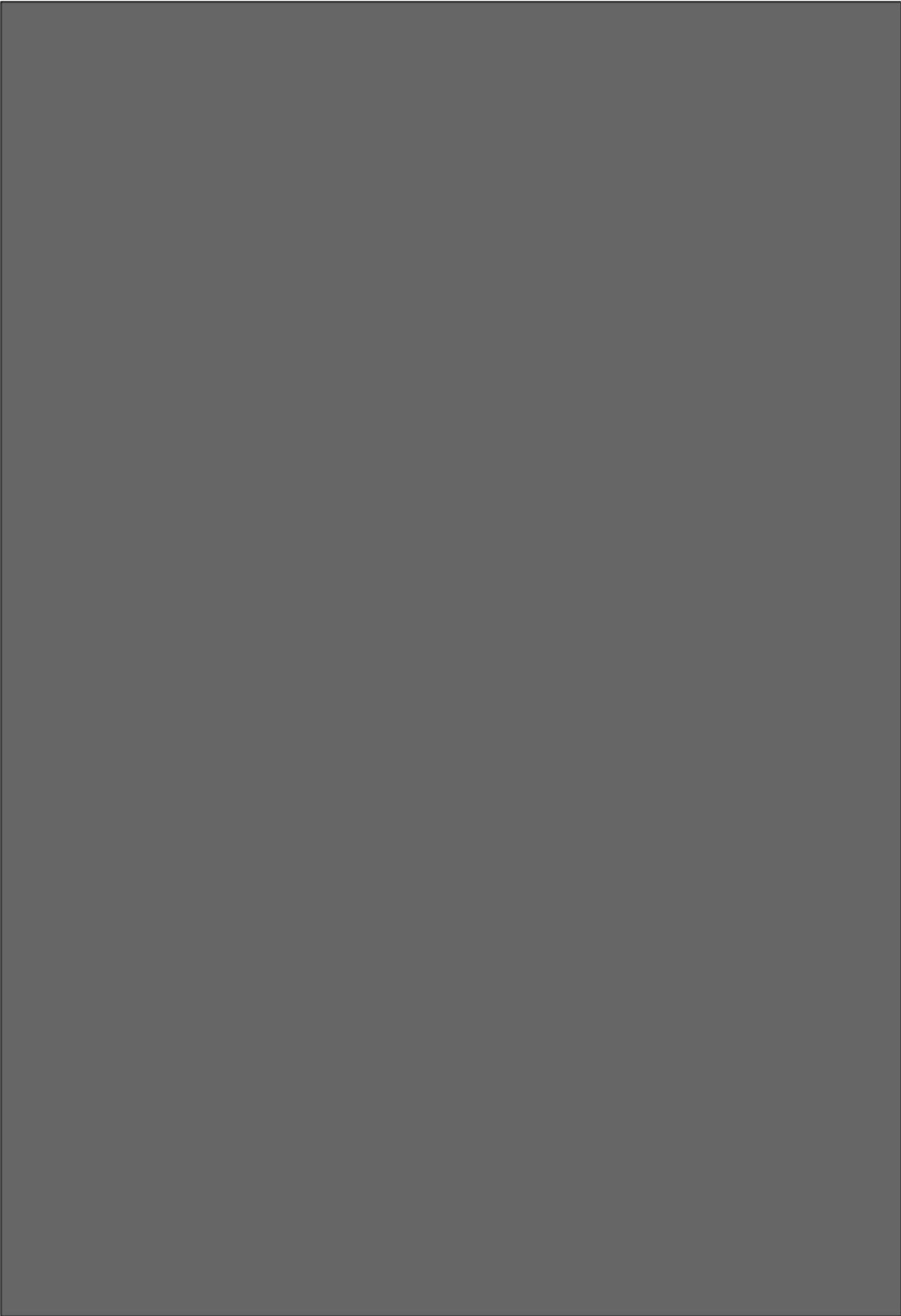




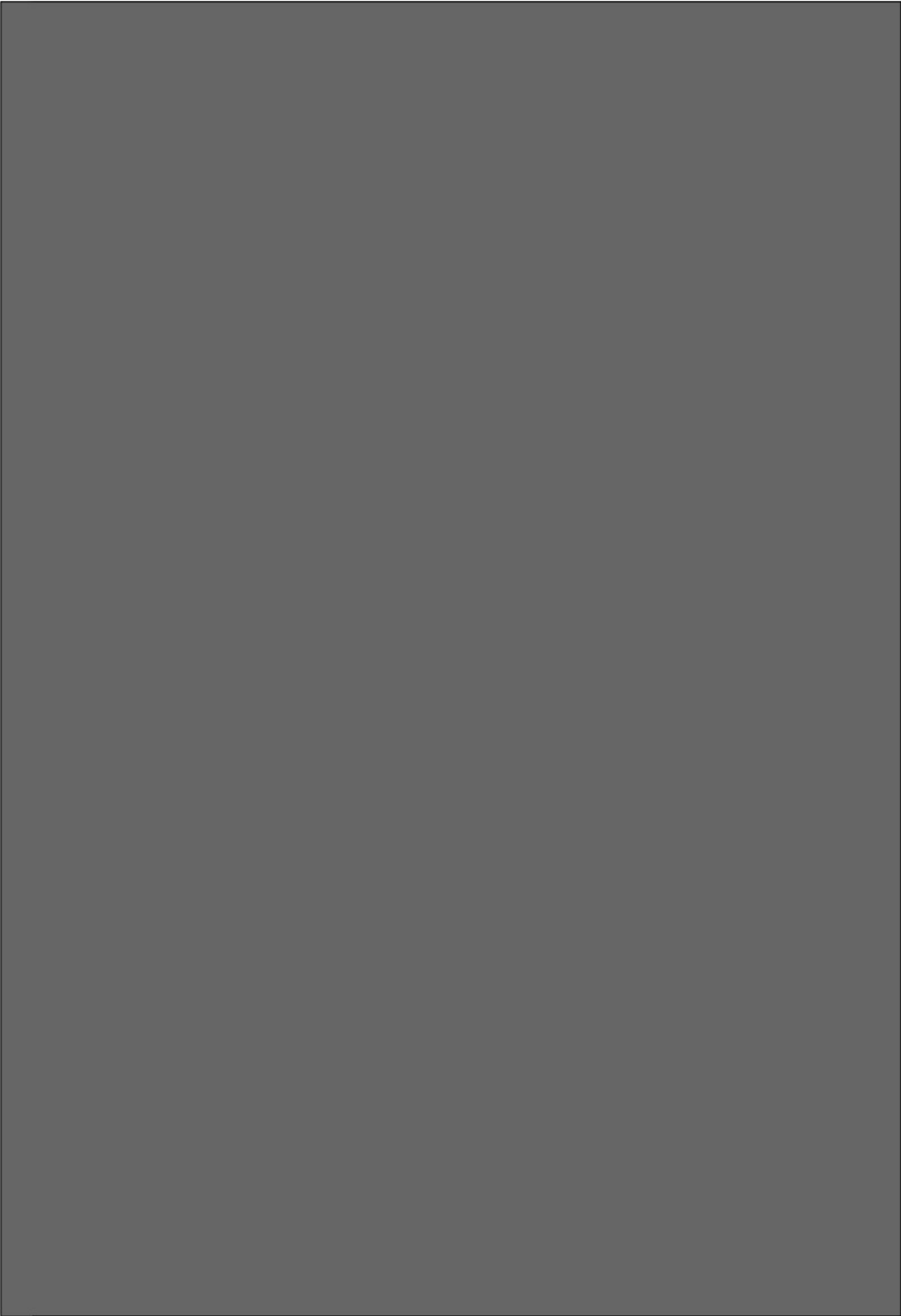


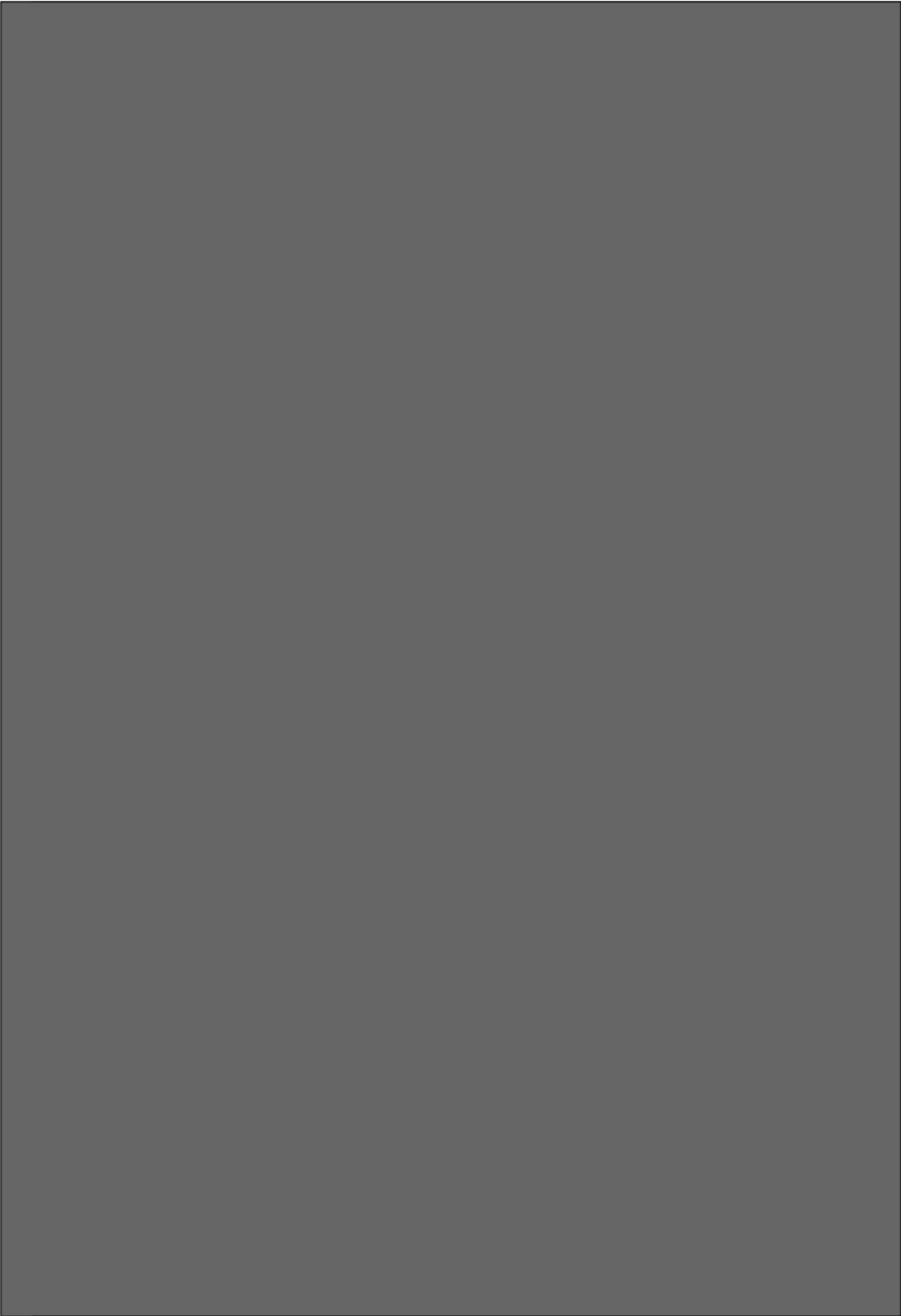


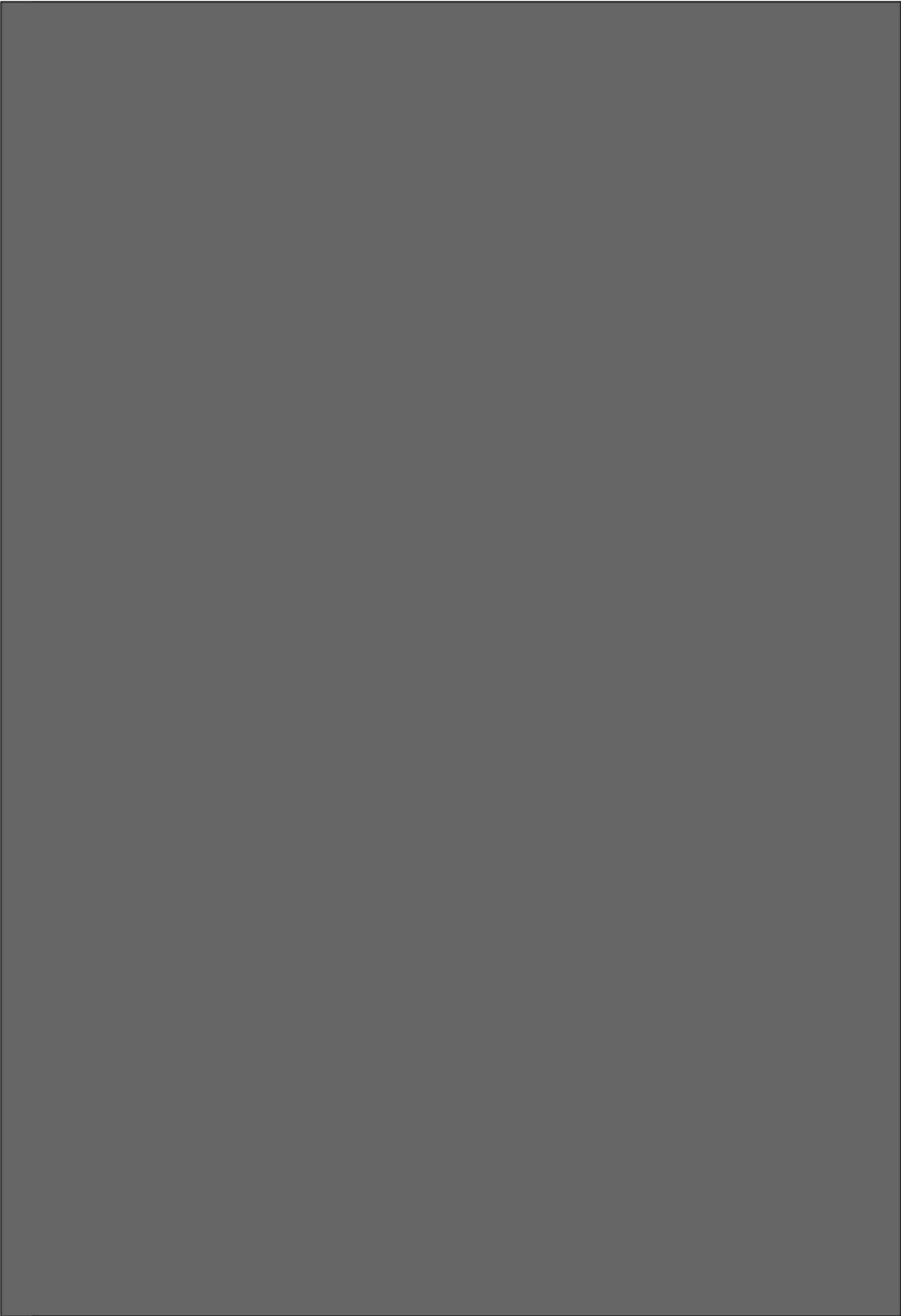


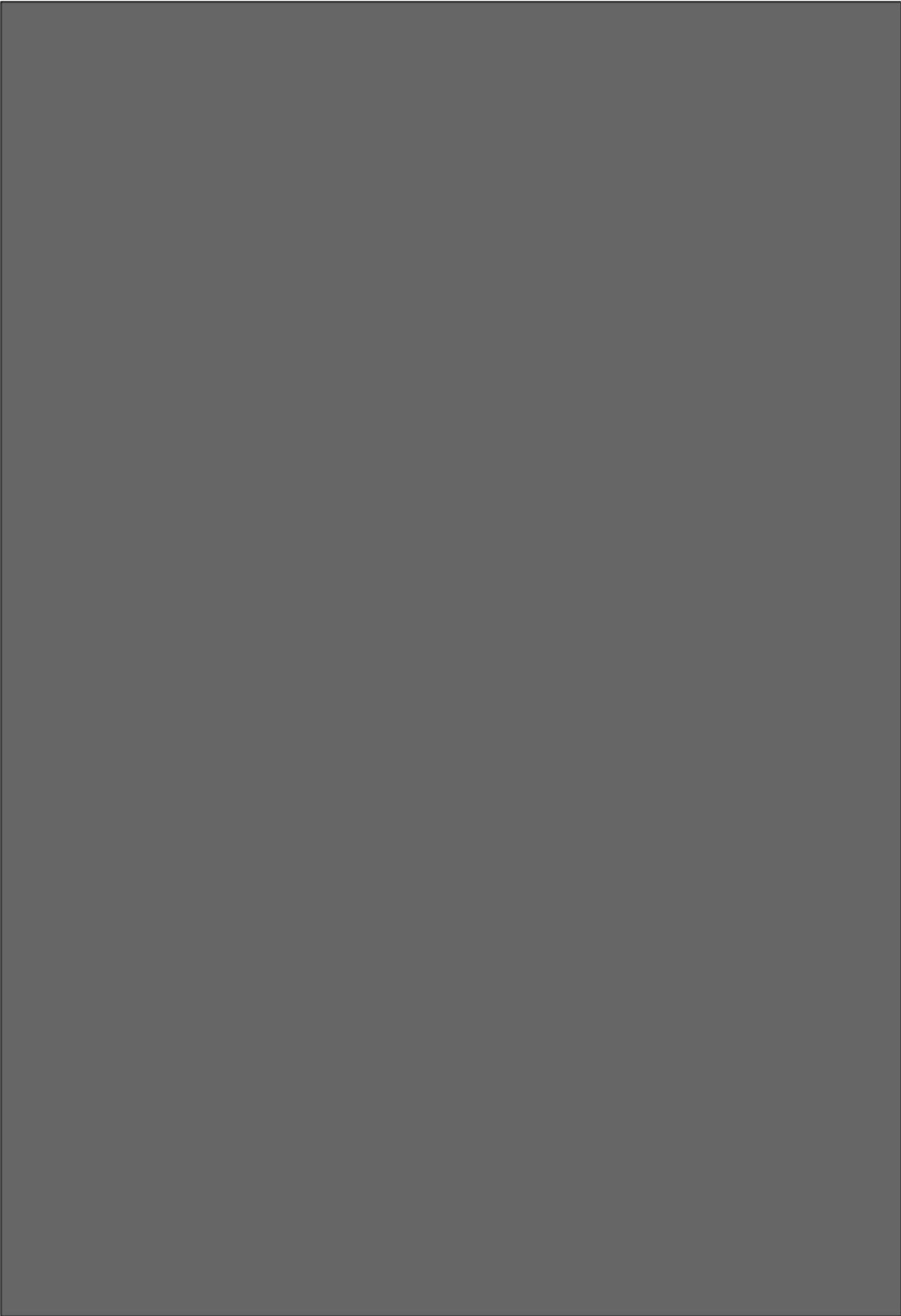




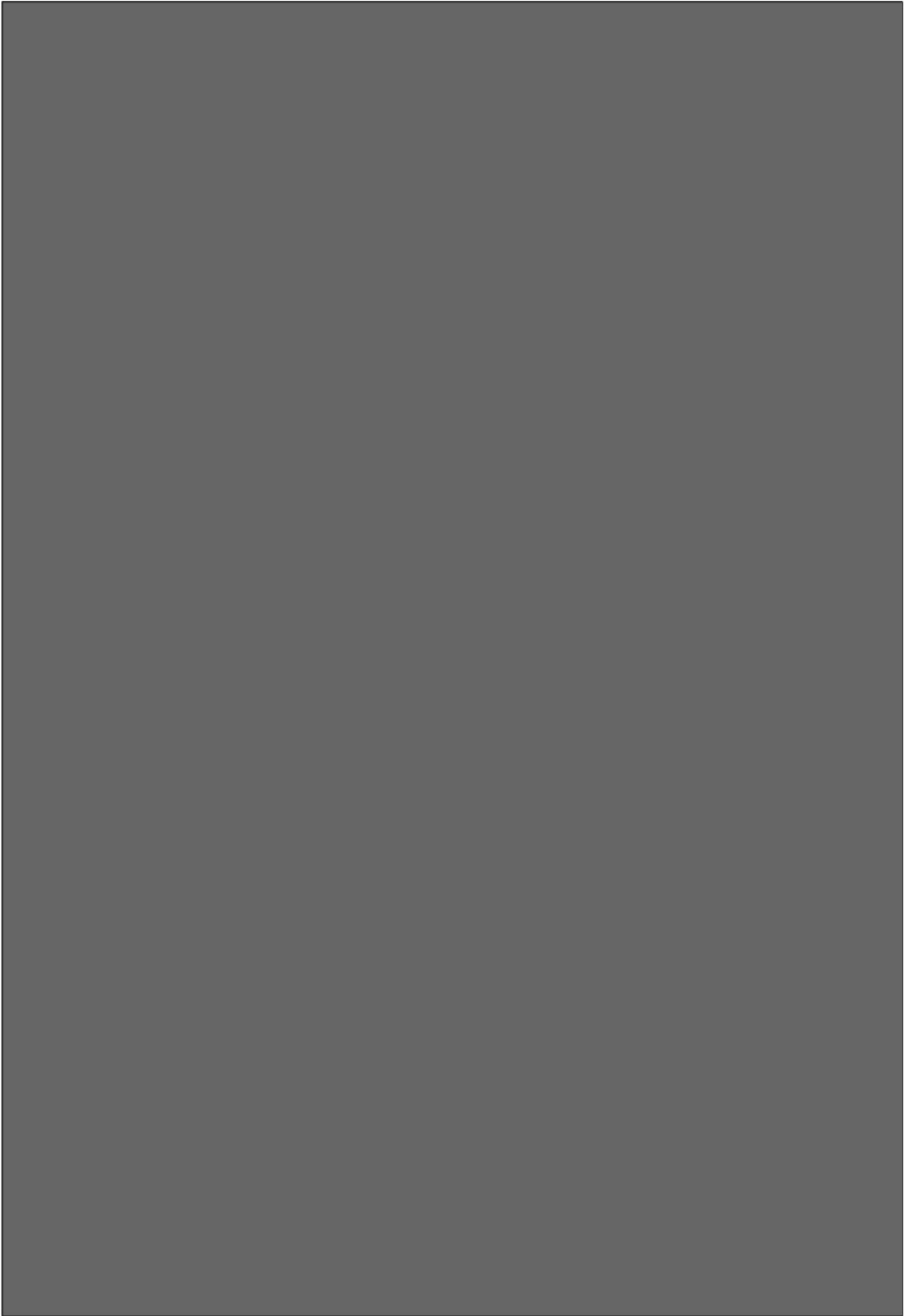


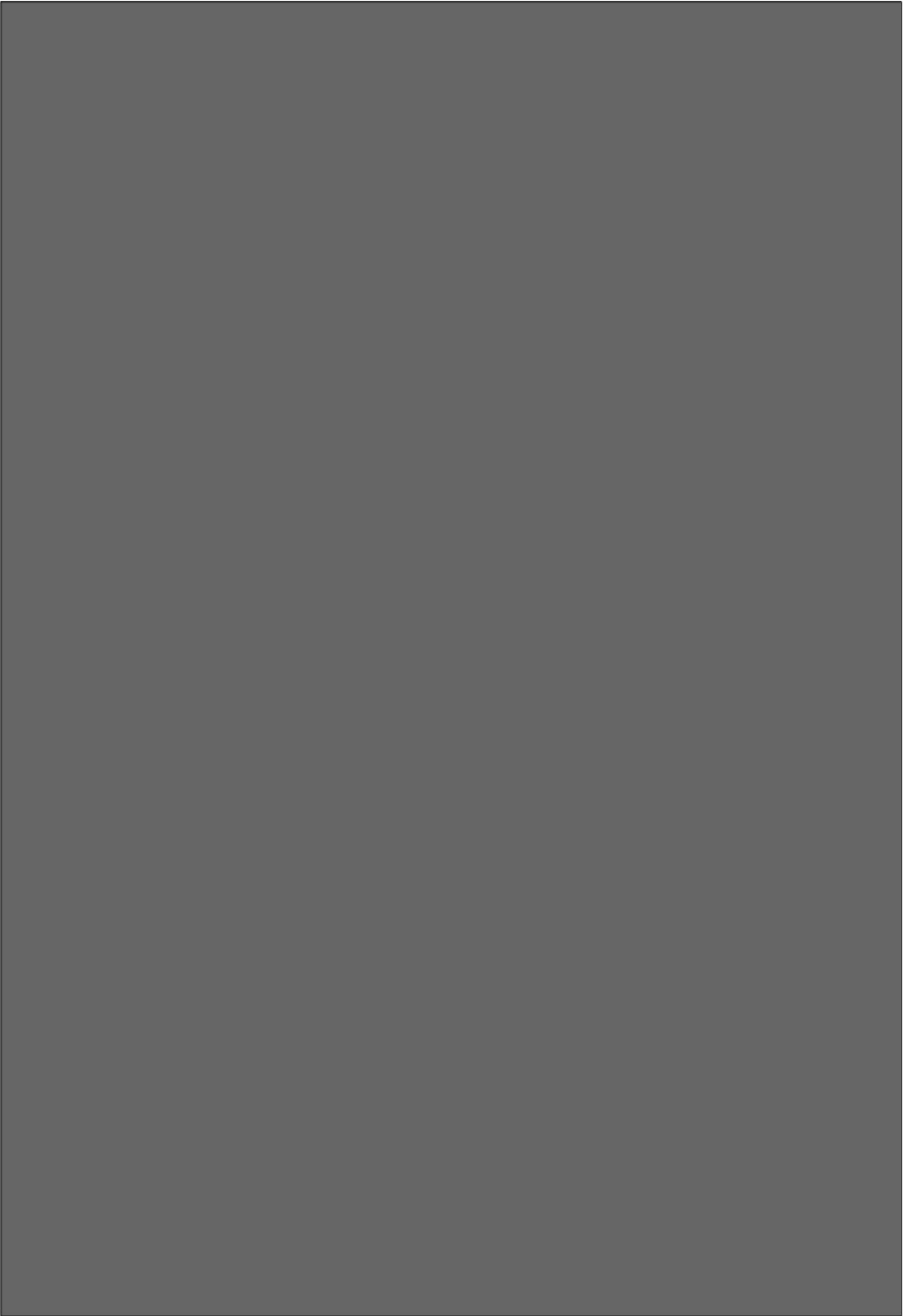


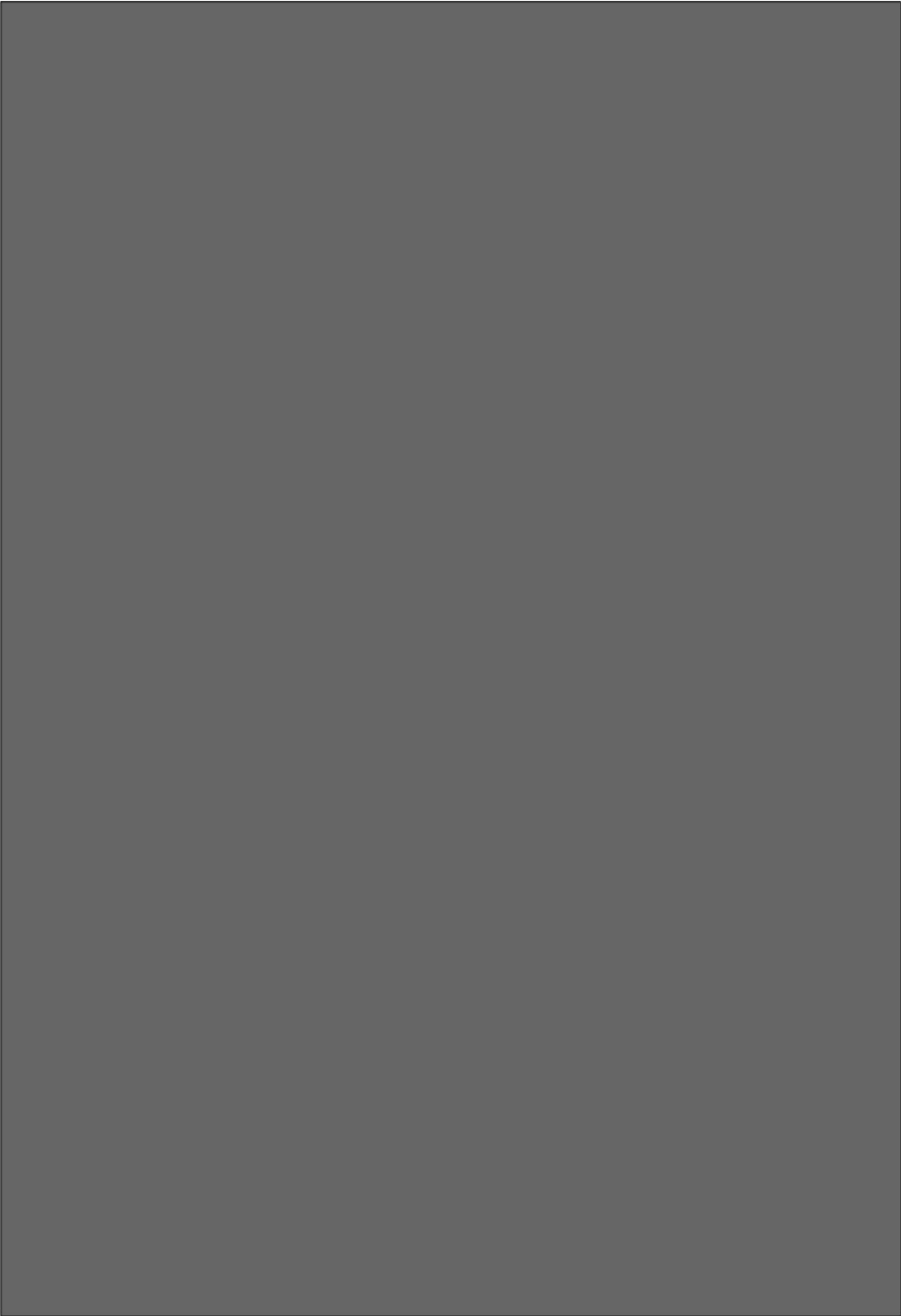


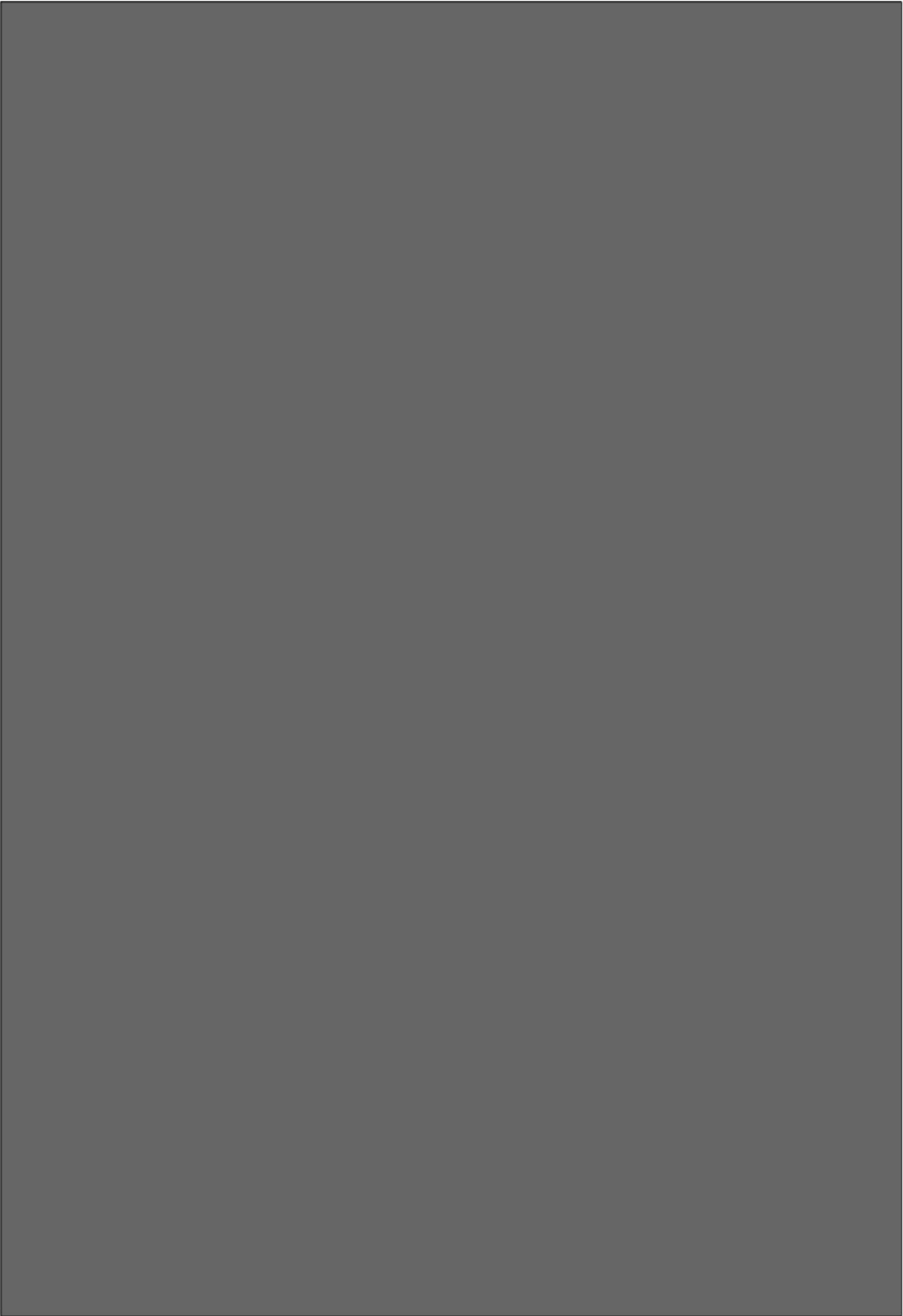




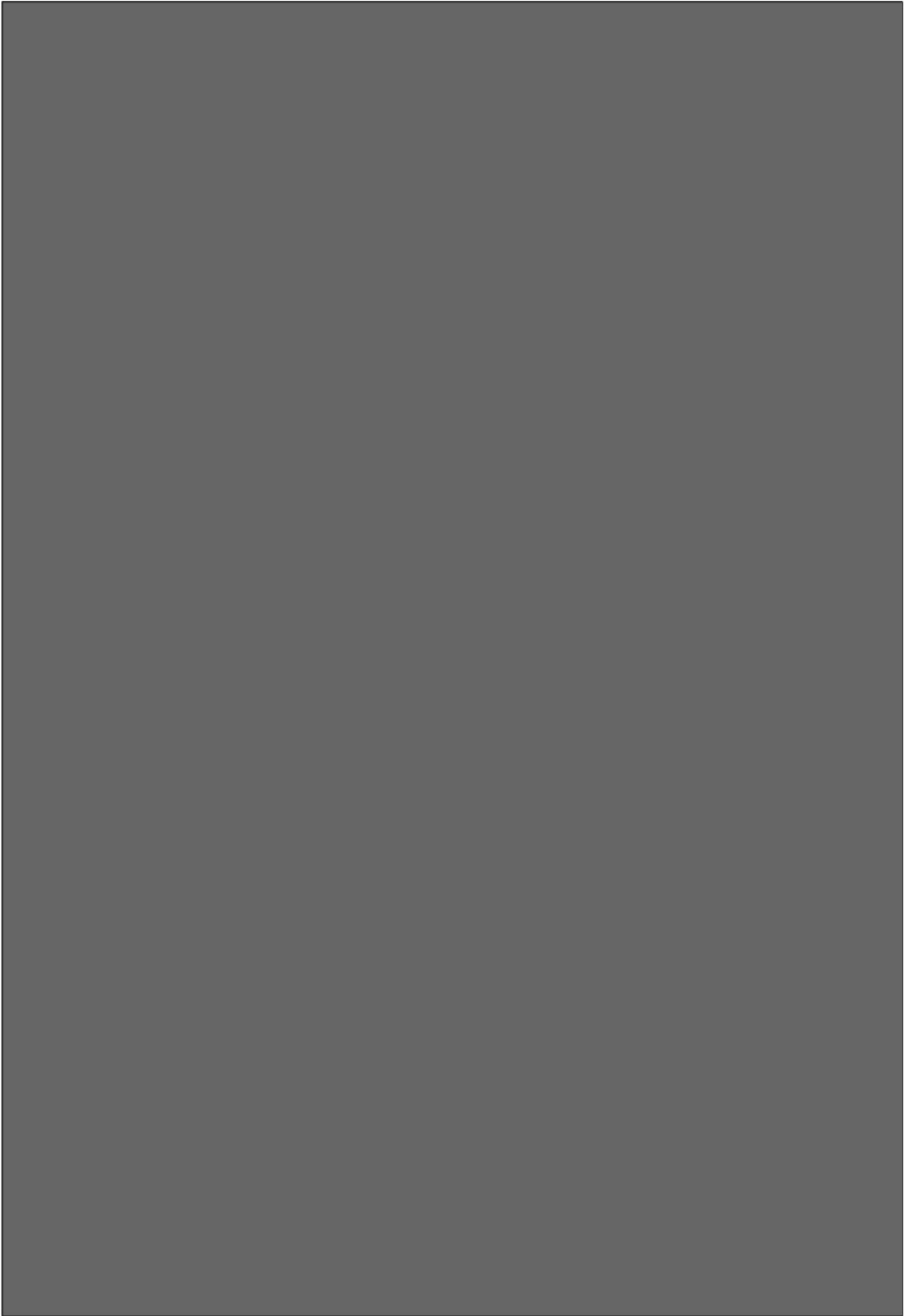


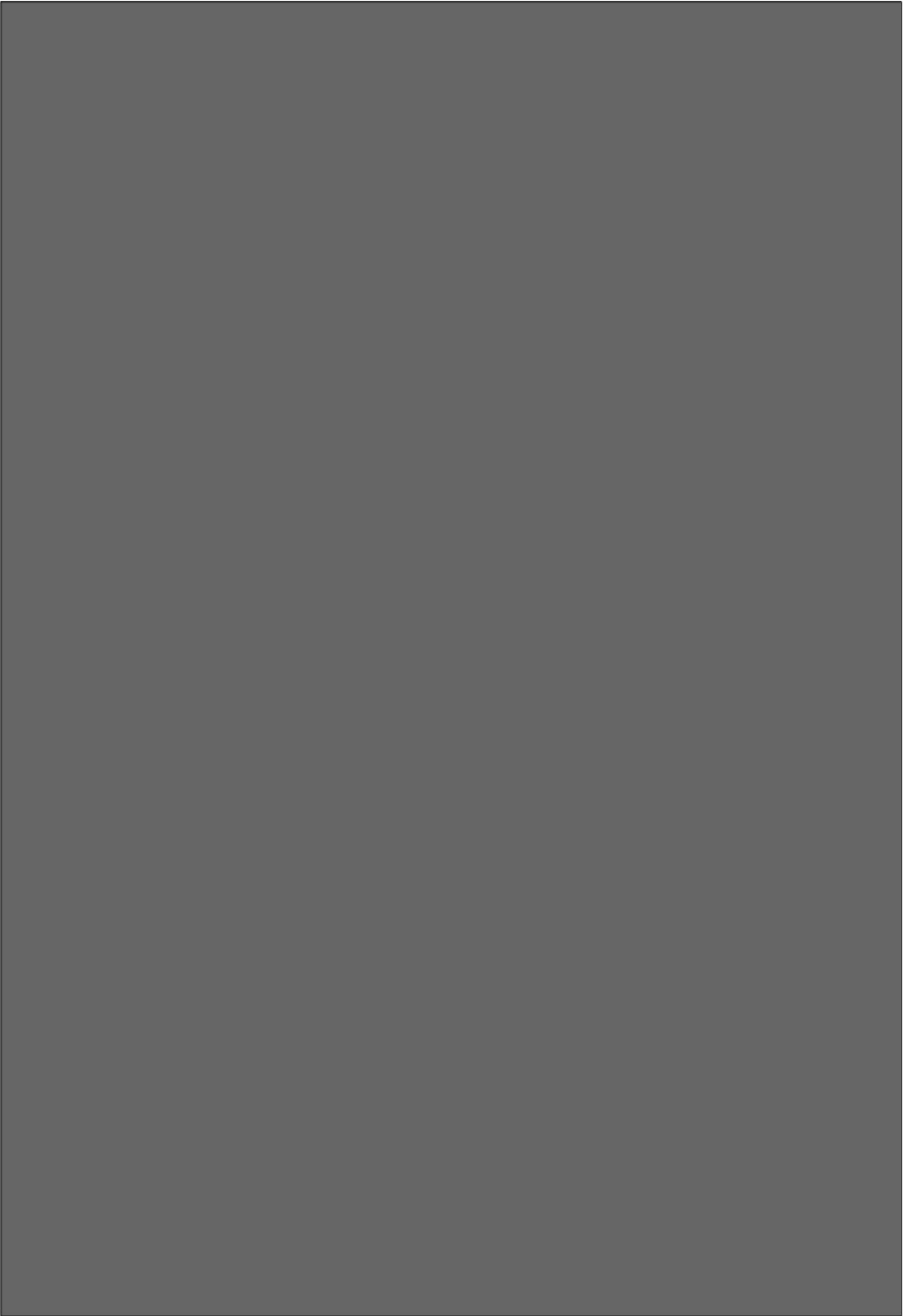


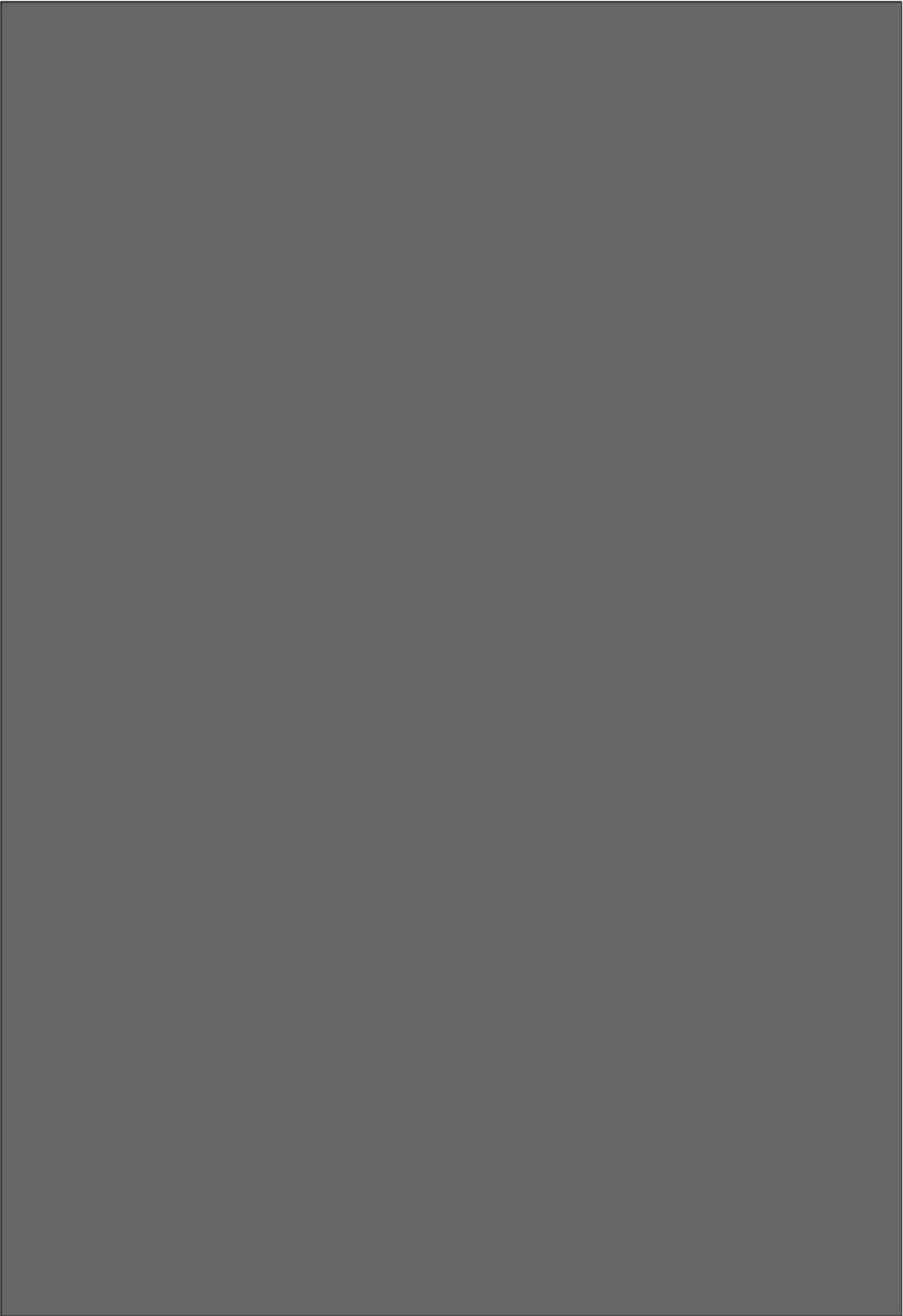


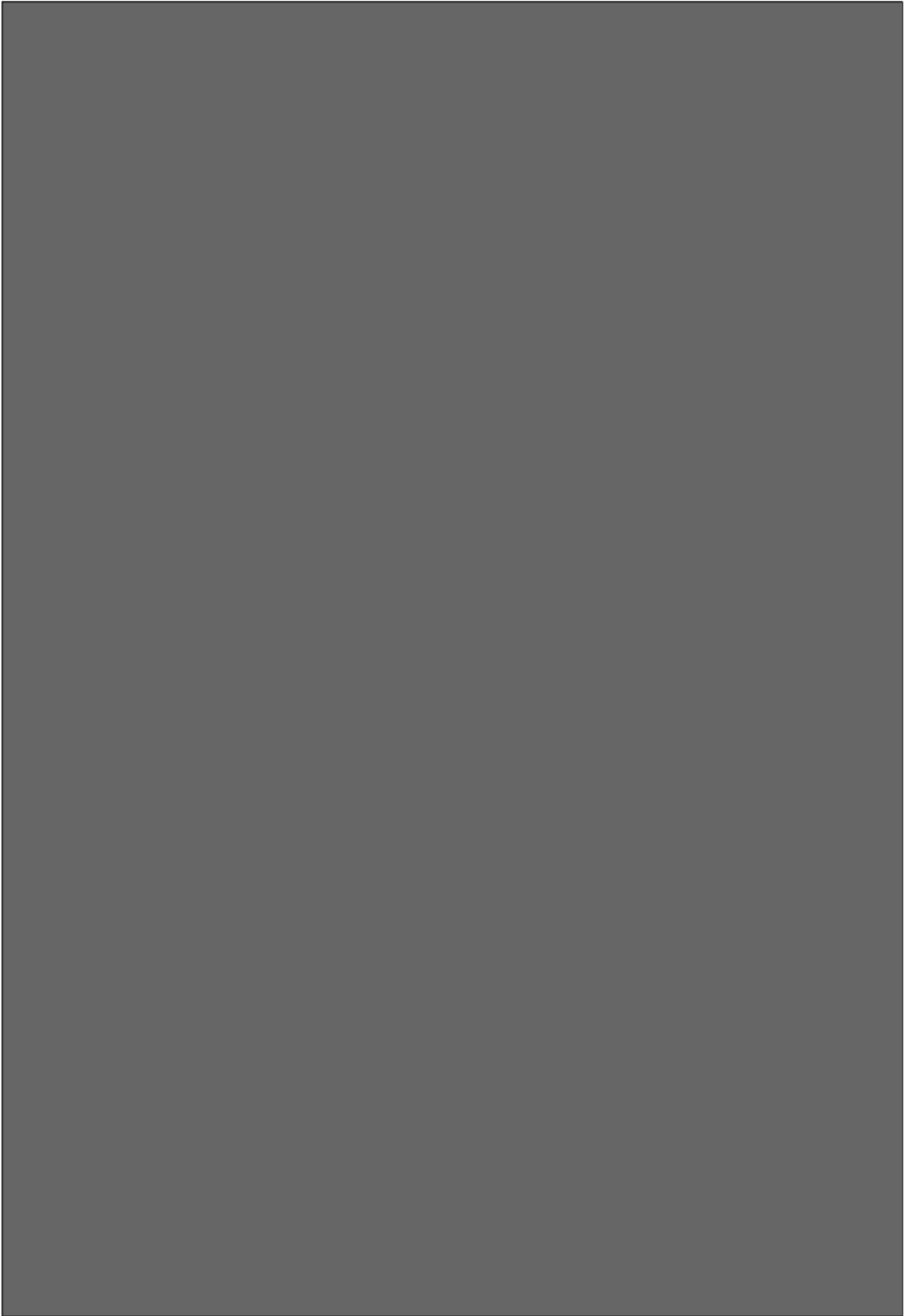


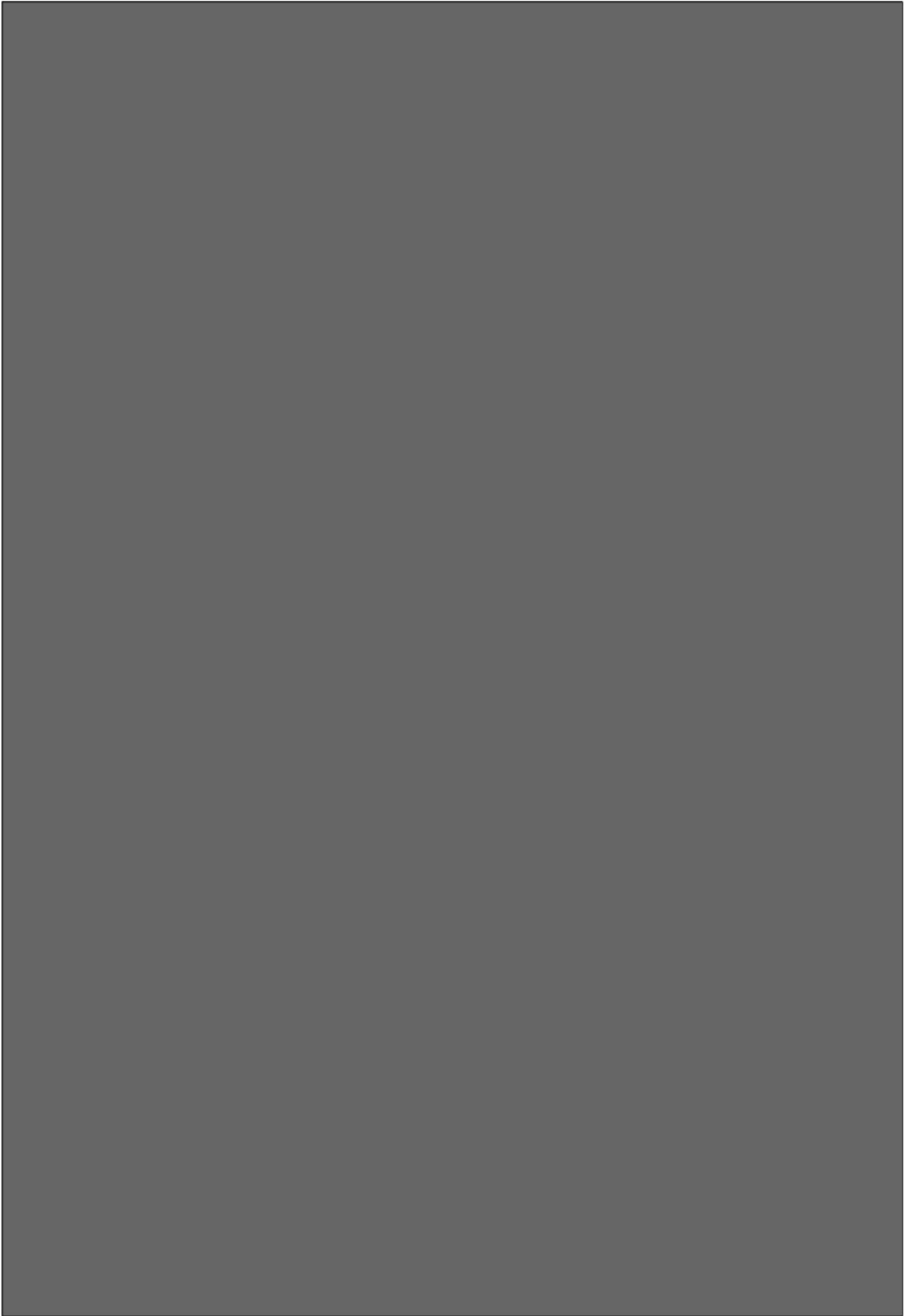


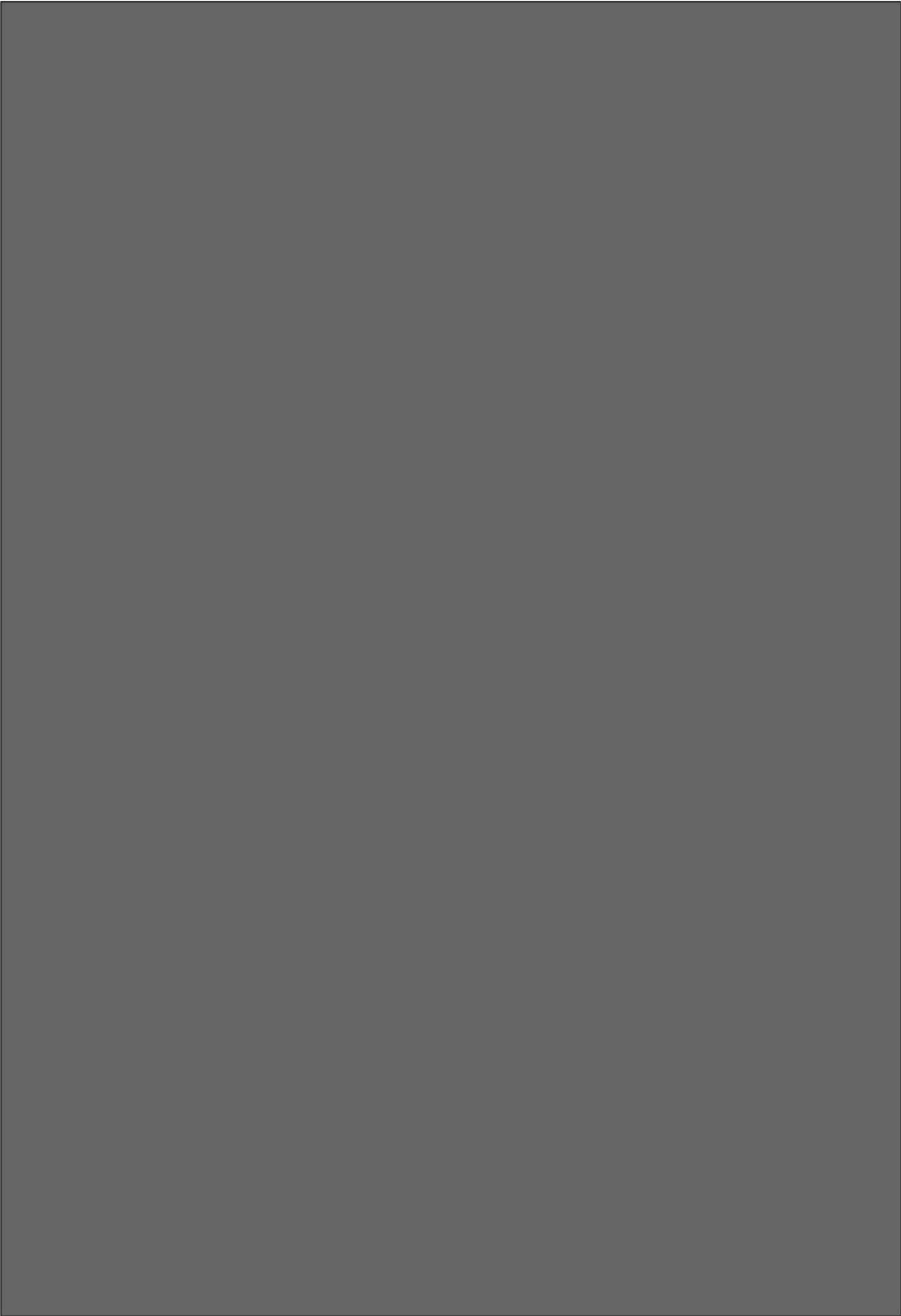




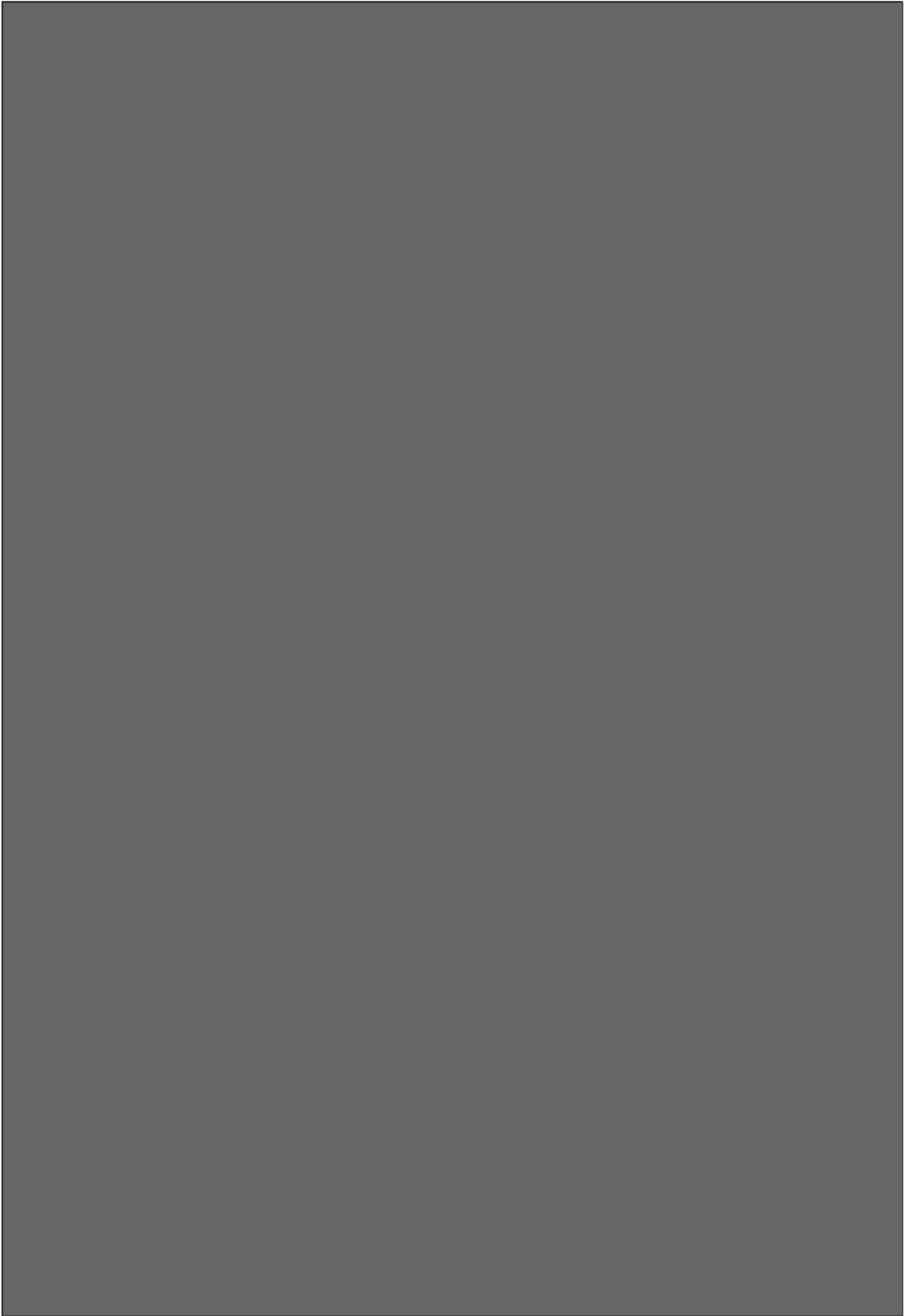


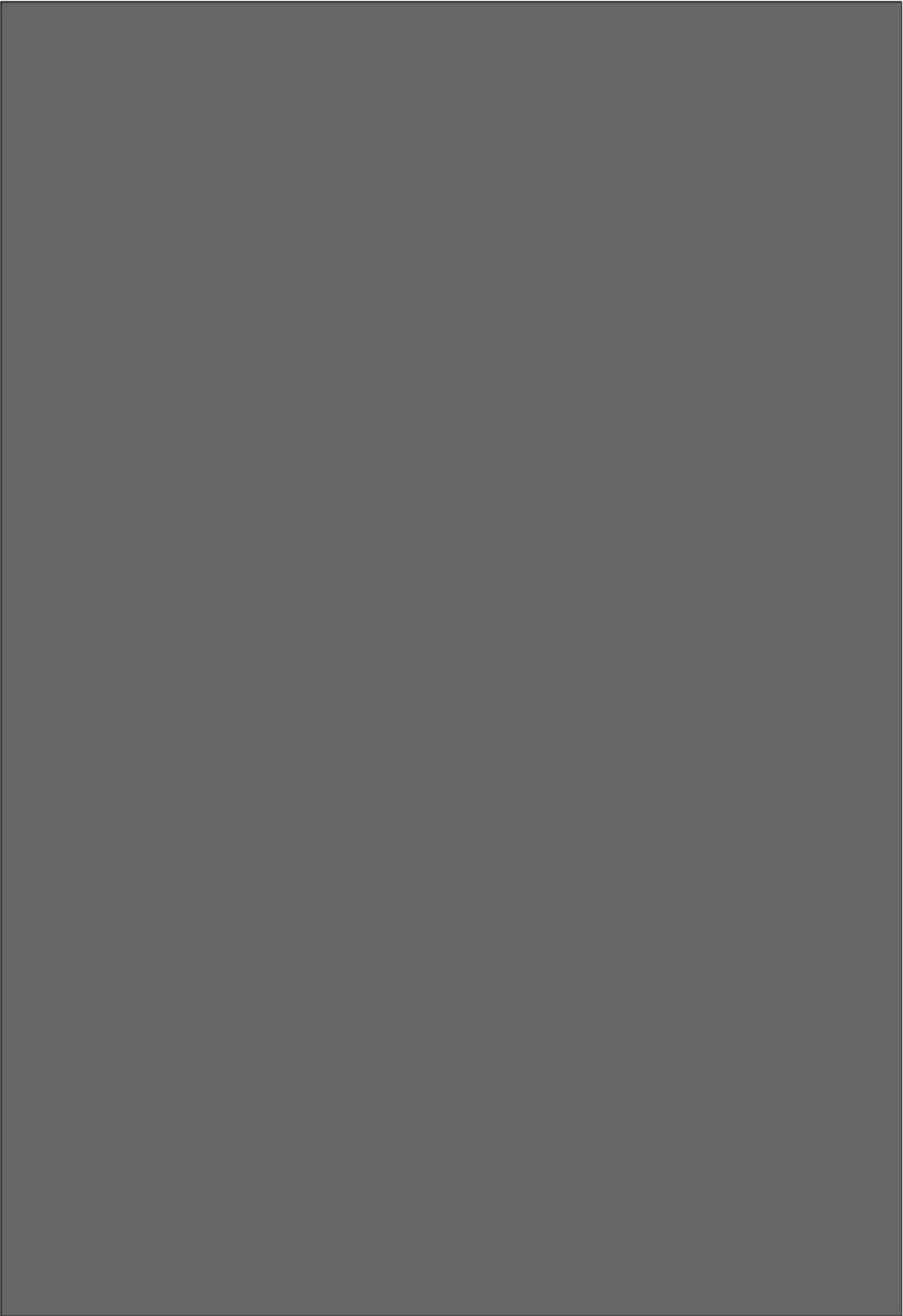


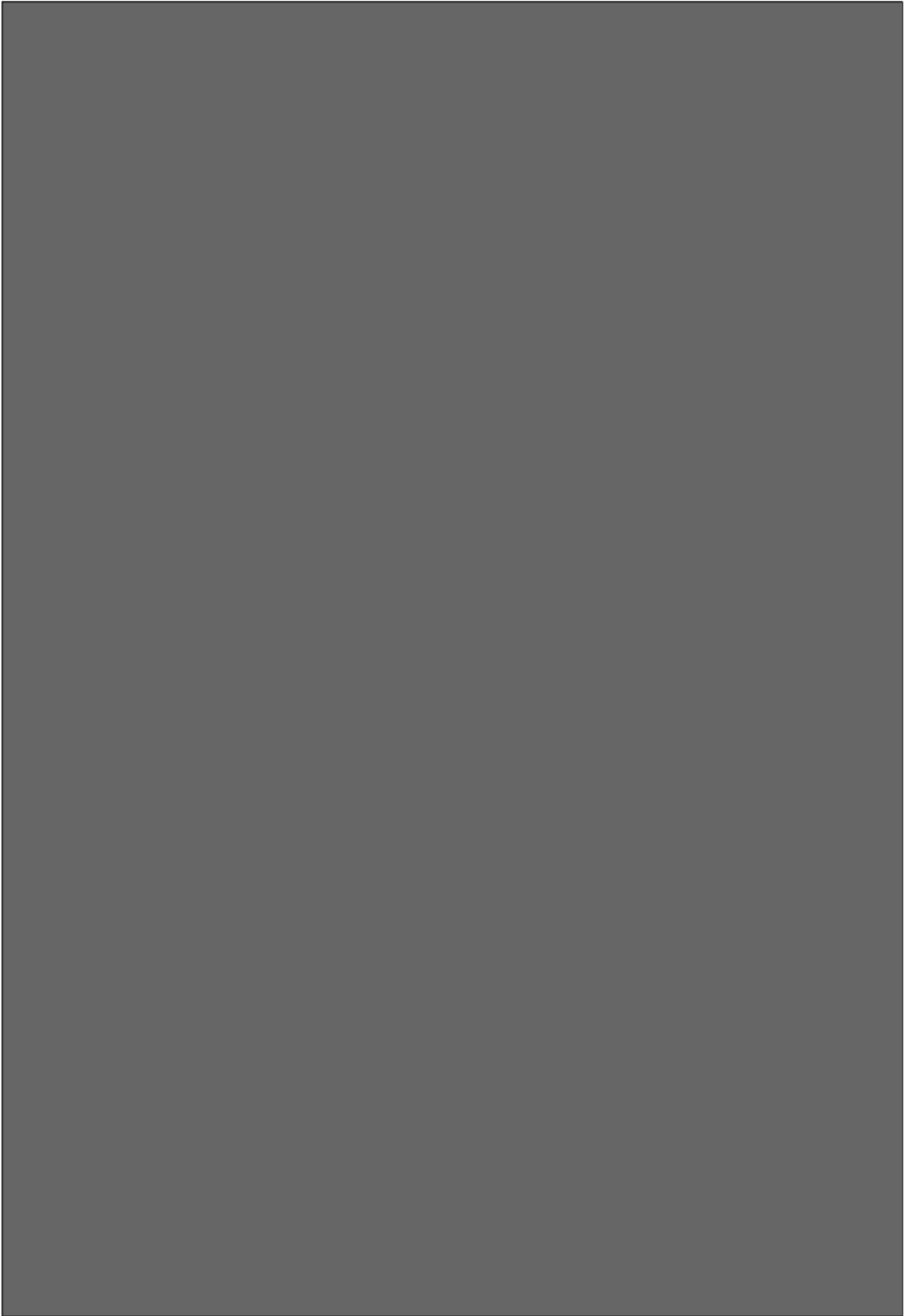




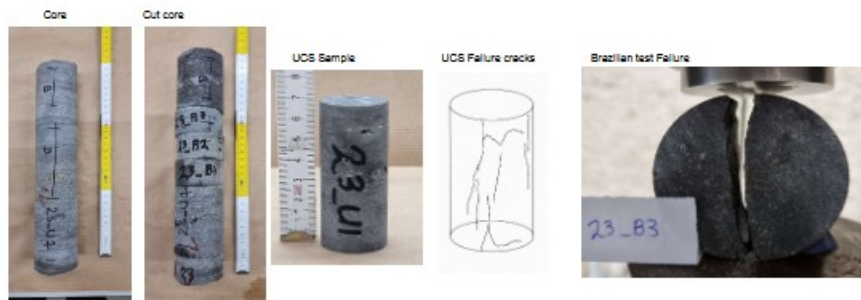








Sample	23
Sample_Lhoist	MUD161_17
Layer	5
From [m]	210.59
To [m]	210.10
Dry bulk density [g/cm3]	2.73
Wet bulk density [g/cm3]	2.76
Mineral specific gravity [-]	2.84
Porosity [%]	3.87
UCS [MPa]	165
E50 [GPa]	71.1
E uniax [GPa]	72.7
Poisson50 [-]	0.10
Poisson uniax [-]	0.19
Brazilian Tensile strength [MPa]	10.5
v _p _dry [km/s]	12.8
v _p _saturated [km/s]	10.7
mean_EH [L-Type rebound]	67
mean_ea_top_dry	661



UCS core description
 Grey with a lot of pores between 1 and 5mm, some fossils up to 4mm and very few microcracks.

Standards used for tests

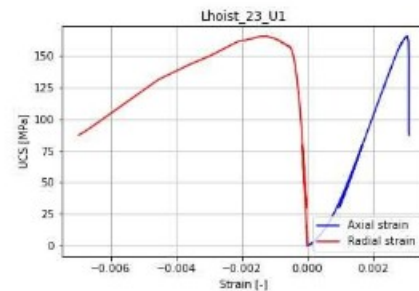
ISRM standard used for both UCS and Brazilian tests. An axial displacement of 0.001mm/sec. Unloading/reloading of some UCS samples was performed from 70% to 50% of the samples peak strength.

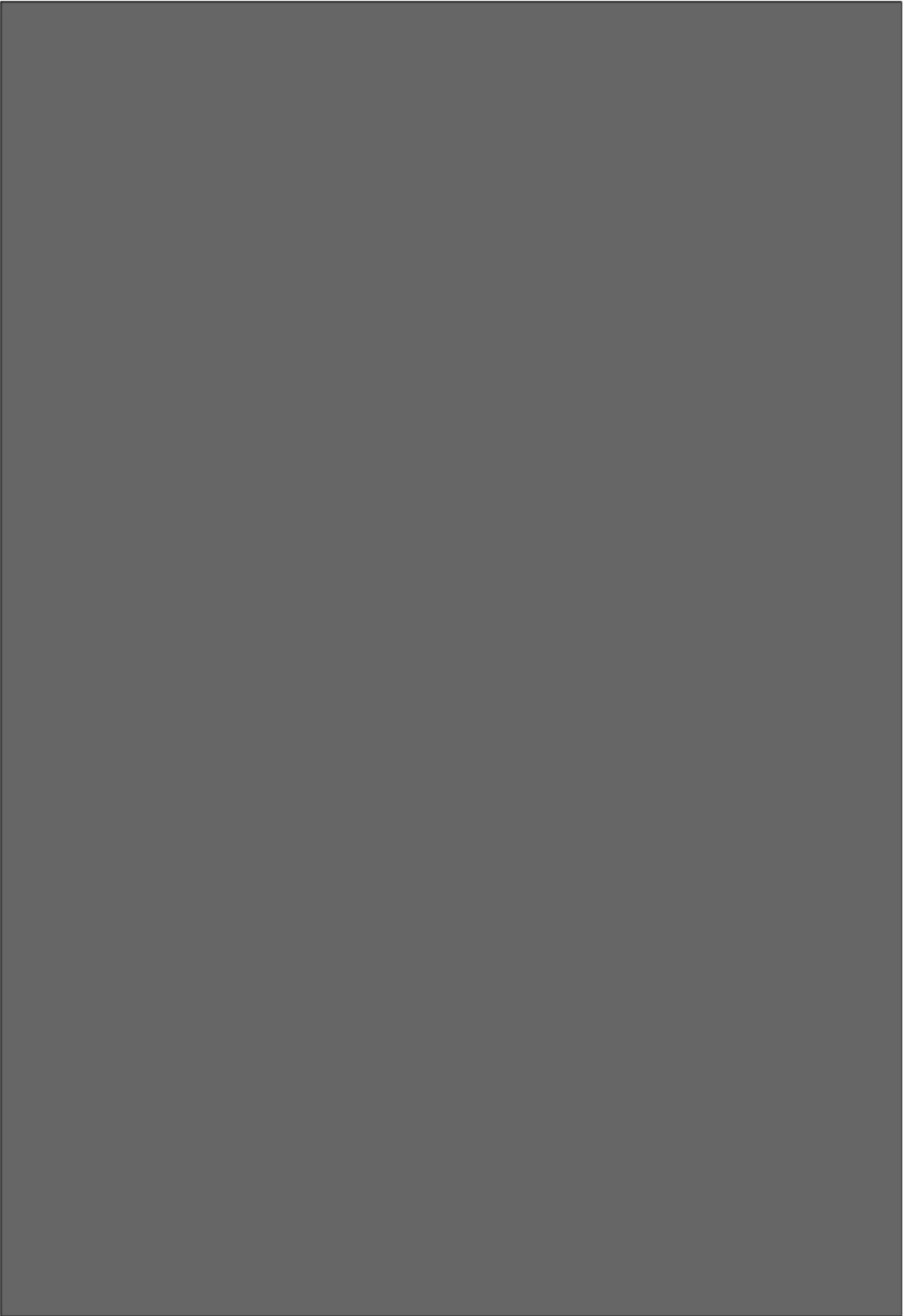
Comments

Brazilian samples

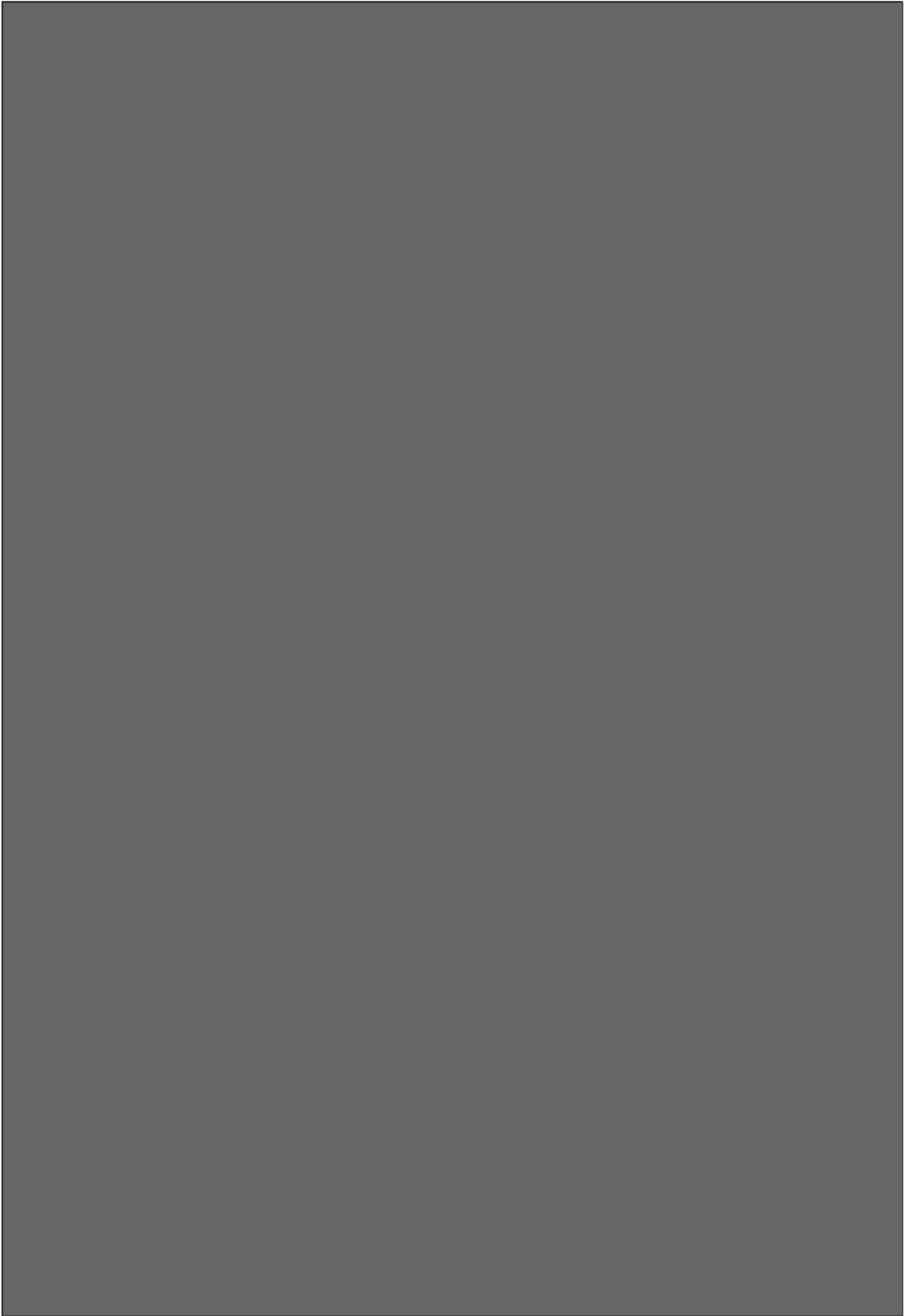


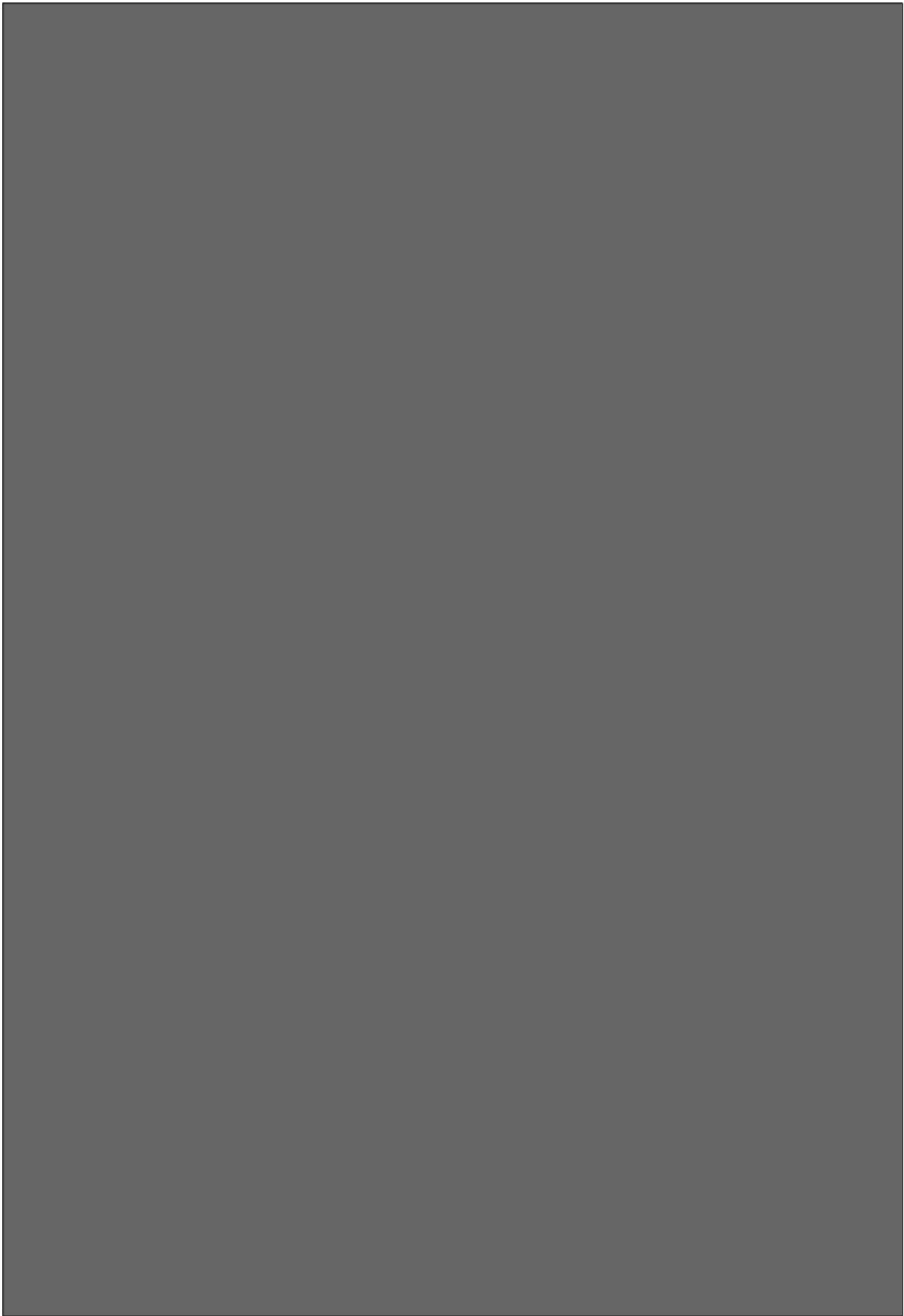
Graph for the axial and radial strain vs UCS











(21) CARRIERE DE LA S.A. DES DOLOMIES DE MARCHE-LES-DAMES.

le long de la rive gauche de la Meuse, sur la commune de Namèche, à l'Est de l'Haigneaux.

A) Côté Ouest de la carrière:

Description des bancs du sommet à la base.

- 39 31 cm. Calcaire dolomitique à grain fin, invisible à l'oeil nu.
- 39/38 Pellicule argileuse de 0,2 cm. entre deux surfaces de stratification pas très irrégulières. Ces deux surfaces sont le démoïn de l'arrêt de la sédimentation, à deux reprises.
- 38 11 cm. Calcaire dolomitique comme 39.
- 38/37 Pellicule argileuse entre deux surfaces de stratification.
- 37 9 cm. Calcaire dolomitique à grain fin, comme 39.
- 37/36 Le sommet de 36 se termine par une surface de stratification sur laquelle repose le banc 37 dont la base est légèrement argileuse sur 1 cm.
- 36 8 cm. Calcaire dolomitique formé de plages calcaires à grain fin entourées de dolomie grenue.
- 36/35 Entre deux surfaces de stratification, repose une pellicule argileuse de 0,2 cm.
- 35 8 cm. Calcaire dolomitique à grain fin.
- 35/34 1 cm. Calcaire dolomitique argileuse.
- 34 71 cm.) Bancs de calcaire dolomitique. Le grain
- 33 9 cm. (de la roche est plus fin que celui des
- 32 11 cm.) bancs inférieurs, et un peu moins fin
- 31 4 cm. (que celui des bancs supérieurs.
- 30 28 cm.) Les limites entre ces bancs sont diffi-
- 29 6 cm. (ciles à établir avec certitude. Il s'agit
- 28 52 cm.) cependant de joints argileux.



26

SECTION 21 W
... ..
... ..
... ..

21 W

NW

SE



← joints
(N.E. 100°)

28/27 Joint ouvert par la dissolution.

27 167 cm. Banc de dolomie compacte, à grain moyen. Ce banc est parcouru de 3 minces passées plus argileuses avec argile exprimée sur 0,1 cm. à 12, 16 et 32 cm. du sommet.

27/26 Le sommet du banc 26, c'est une surface de stratification marquant un temps d'arrêt dans la sédimentation.

26 133 cm. Dolomie grenue, compacte, à grain moyen, à poches de calcite réparties uniformément dans la masse de la dolomie. A 19 cm. du sommet, pellicule argileuse de 0,2 cm. avec passage vers le haut et vers le bas. A 64 et à 111 cm. du sommet, joints stylolithiques.

26/25 Mince joint argileux de 0,1 à 0,3 cm. qui repose entre deux surfaces de stratification très irrégulières.

25 135 cm. Même dolomie compacte, à grain moyen et à poches de calcite, comme 26. A 6 cm. du sommet, joint stylolithique. A 52 cm. du sommet, sur une surface érodée, repose une pellicule argileuse passant vers le haut à la dolomie.

25/24 Pellicule argileuse de 0,2 cm. reposant sur une surface de stratification assez irrégulière. Cette pellicule passe au banc supérieur rapidement.

24 Dolomie finement grenue, compacte, sans traces d'organismes, plus claire que le sommet du banc inférieur. A 63, 100, 133, 138 et 155 cm. on peut voir de très minces pellicules argileuses (0,1 cm).



26



(5) CARRIÈRE DE LA S.A. DES DOLOMITES DE Sambre ET MEUSE.

~~sur la rive gauche de la Meuse, à 1.000 mètres~~
~~au N-E. de la Meuse, sur la commune de Namèche.~~

Description des banes du sommet à la base.

- X 28 ~~25~~ cm. environ. Banc de dolomie compacte, homogène, à grain assez fin.
- 28/27 Limite se marquant par un alignement de poches de calcite.
- X 27 650 cm. environ de dolomie comme 28.
- 27/26 ?
- X 26 500 cm. environ. Dolomie très homogène, compacte
- Remarque: les bancs 26, 27 et 28 sont d'accès difficile. La nature de leurs limites n'a pas toujours été possible à déterminer.
- 26/25 Simples surfaces légèrement ondulées, sans enduit. C'est un diastème. Il y a eu un arrêt temporaire de la sédimentation sans plus. Par endroits, cette limite est soulignée par un alignement de poches de dissolution.
- X 25 168 cm. Dolomie compacte à grain assez fin, à peu d'encrasses visibles (0,5 à 0,7 cm.)
- 25/24 Diastème comme 26/25.
- I 24 438 cm. Gros ensemble de dolomie homogène, compacte, à peu d'encrasses visibles (0,5 à 0,7 cm.)
- 24/23 Alignement de poches remplies d'argile. En certains points, ces poches sont contiguës, en d'autres, il n'y a pas continuité.

- 22/23 135 cm. Gros ensemble de dolomie compacte à grain assez fin. Le long des surfaces altérées, on peut voir de nombreuses encrines dont le diamètre varie entre 0,2 et 0,9 cm., les grandes encrines étant tout aussi nombreuses que les petites. La répartition de ces encrines est assez uniforme. L'ensemble 23 peut être subdivisé en 6 plus petits bancs :
- f : 172 cm.
 f/a : mince pellicule argileuse.
 g : 100 cm.
 g/a : mince pellicule argileuse.
 d : 97 cm.
 d/c : mince pellicule argileuse discontinue.
 c : 104 cm.
 e/b : diastème.
 b : 127 cm.
 e/a : mince pellicule argileuse de 0,1 cm.
 d : 135 cm.
- 24/22. Limite se marquent bien d'un bout à l'autre de la carrière. Il s'agit d'un joint argileux d'épaisseur inférieure à 0,5 cm. avec passage de part et d'autre, aux bancs 23 et 22. Ce passage se fait sur quelques millimètres.
- 1 22 500 cm. Gros ensemble de dolomie homogène à grain assez fin, à peu d'encrines visibles (0,7 à 0,8 cm) Cet ensemble est parcouru de diastèmes semblant non continus.
- 22/21 Le sommet du banc 21 passe, sur 1 cm. à un mince joint argileux de 0,1 cm. Le sommet de ce joint est ondulé, irrégulier et bien tranché d'avec le banc 22.
- 1 21 338 cm. Ensemble de bancs de dolomie compacte, homogène, à grain assez fin. Ces bancs mesurent respectivement, depuis le sommet : 50, 83, 110 et 112 cm. environ. Leurs limites sont du même type

que celles séparant les bancs de l'ensemble 20 (Diastèmes non continus).

Comme dans 20, les encrines sont assez nombreuses, cependant, les petites (0,3 cm.) sont plus nombreuses que les grandes (0,8 cm.) contrairement au banc 22.

Quelques traces de Brachiopodes et Polypiers.

(Chonetes papilionacea)

21/20 Comme 22/21.

20 477 cm. Ensemble qui diffère du précédent (19) par sa grande richesse en encrines (des petites, 0,2 cm. et des grandes, 0,7-0,8 cm.)

Les petites encrines sont plus nombreuses que les grandes.

La dolomie est compacte à grain assez fin, elle renferme d'assez nombreuses poches de calcite et quelques poches à pseudo-brèches.

Cet ensemble peut être subdivisé en 10 plus petits bancs, tous séparés par des diastèmes non continus.

Outre les encrines, les organismes présents comportent quelques Polypiers et une colonie de *Syringopora* basculée.

Le genre Spiriferellina sp. et d'un Strophomenace.

20/19 Limite de bancs bien marquée.

II 12 399 cm. Ensemble de 8 petits bancs de dolomie compacte, à grain assez fin, à encrines peu nombreuses (0,3 cm. maximum). Ces petits bancs étaient séparés les uns des autres, probablement par de minces pellicules argileuses (cette argille a disparu presque entièrement). Sur ces joints sont alignées des poches, soit remplies, soit tapissées de calcite.

Leur couleur de ces bancs diffère quelque peu de l'un à l'autre.

19/18 Joint argileux de 0,1 à 0,2 cm. accompagné de part et d'autre, de zones mixtes, argilo-dolomitiques, pouvant atteindre 1 à 5 cm.

18 272 cm. environ. Dolomie compacte à encrines assez nombreuses et assez petites (0,3 cm.); il y a également quelques encrines moyennes (0,5 cm.) et quelques poches tapissées de calcite.

18 peut être subdivisé en 4 plus petits bancs de 75 cm. (sommet), 58 cm. et deux bancs d'environ 70 cm. chacun. Ces bancs sont séparés par de minces passées plus argileuses (0,3 cm.) accompagnées d'alignements de poches de dissolution.

18/17 surface ondulée sans joint ni enduit, dont la longueur d'onde est d'environ 16 cm. et l'amplitude 2 cm.

La direction des ondulations est grossièrement E.W.

17 674 cm. Ensemble formé d'une succession de 14 petits bancs. La stratification est peu visible, les limites des bancs sont des passées plus argileuses. La dolomie est compacte, à grain assez fin. Les bancs diffèrent les uns des autres par leur couleur.

d : 122 cm. 2 bancs..

c : 90 cm. très peu d'encrines visibles.

b : 110 cm. 4 bancs..

a : 352 cm. environ 7 bancs de dolomie assez pauvre en crinoïdes, à grain fin, chamarrée.

Remarques concernant l'ensemble 17:

Les subdivisions en a, b, c et d, sont essentiellement pratiques. Les passées plus argileuses, qui limitent les bancs de l'ensemble 17, peuvent avoir jusqu'à 3 cm. d'épaisseur. Ces limites se marquent particulièrement bien le long des parois altérées,

L'ensemble 17 est assez riche en Polypiers et Brachiopodes par endroits.

Brachythyris sp. nombreuse; *Chonetes* sp. groupe *hemisphaerica*; *Schizophoria* sp. (*Spilliferus*?)

17/138 Joint stylolithique.

IX

16

181 cm. Ensemble de 3 bancs de même nature que ceux de 17, séparés par des passées plus argileuses. Ces 3 bancs renferment des géodes de calcite, quelques encrinnes et quelques colonies de *Syringopora* basculées.

t : 48 cm. Dolomie bleu foncé, comme 15.

Q : 62 cm. Dolomie légèrement jaunâtre.

a : 71 cm. Dolomie plus claire que 15.

18/12 Joint stylolithique.

IX

12

347 cm. Dolomie compacte renfermant quelques colonies de *Syringopora* basculées, d'assez nombreuses poches à pseudo-brèches et d'assez rares encrinnes. 15 est un ensemble formé de 4 ou 5 bancs séparés par des passées plus argileuses.

16 12/14
(AYH)

Le sommet du banc 14 f est induré (à l'échelle du cm.) et irrégulier (à l'échelle du mm.)

Sur cette surface de stratification, repose un joint argilux induré, dont l'épaisseur varie entre 0,1 et 0,4 cm. et qui aplanit les irrégularités de la surface inférieure. Ce joint passe sur 0,1 cm. à une mince couche dolochisteuse de 1 à 1,5 cm. d'épaisseur. Enfin, ce dolochiste passe à la dolomie du banc 15 sur 0,2 cm. environ.

VIII

11

485 cm. Ensemble de bancs de dolomie à colonies de *Syringopora* pas très nombreuses, basculées.

f : 130 cm. Dolomie plus claire que le banc inférieur 14 e, non stratifiée, homogène, sans encrinnes visibles.

llc: Il n'y a pas de limite bien nette entre f et e. Il y a simplement une interruption de la

stratification qui caractérise le banc e.

e : 85 cm. Banc formé d'une alternance de stratifications de dolomie et de dolomie légèrement argileuse, vers le sommet, l'alternance est de plus en plus serrée. L'épaisseur des lits varie entre 0,2 et 0,6 cm. Certains présentent des épaississements lenticulaires; d'autres se recoupent (stratification entrecroisée). Cette stratification dénote une sédimentation en milieux agités,

di: entre d et e il n'y a pas de limite bien nette. La seule différence entre ces deux bancs est que l'un est stratifié et l'autre pas.

d : 72 cm. Banc de dolomie à encrines assez nombreuses (0,2 à 0,8 cm.)

d/s: Joint stylolithique.

c : 58 cm. Dolomie à encrines assez nombreuses (0,2 à 0,8 cm.). Le sommet de ce banc est stratifié.

c/b: Joint stylolithique.

b: 82 cm. Dolomie à encrines nombreuses (0,2 à 0,8 cm.). Le sommet de ce banc est stratifié.

b/a: Joint stylolithique.

a: 58 cm. Banc de dolomie à encrines très nombreuses (0,2 à 0,8 cm.) qui ressortent très bien le long des parois altérées.

H/12 Joint argileux important (2 cm. environ) ne montrant aucun passage ni vers le haut, ni vers le bas. C'est le joint principal J.P. des carrières (7) et (8). = D.I. (r Hd)

Les bancs venant sous 14/13 seront décrits assez brièvement, ces bancs se retrouvant en (7) et en (8) où ils ont été étudiés en détail.

13 83 cm. Dolomie grise, fleurie, à poches de pseudobrèches, à encrines assez nombreuses (0,3 à 0,8 cm.)

est avec quelques colonies de *Syringopora* basculées.
 Joint stylolithique.

- 12 70 cm. Comme 13.
- 11 220 cm. Banc de dolomie fleurie dont le sommet au moins, est riche en crinoïdes. Quelques colonies de *Syringopora* basculées.
- 10 150 cm. Ensemble de 5 bancs probablement séparés par des joints stylolithiques. La dolomie de cet ensemble est fleurie, elle renferme des poches à pseudo-brèches, et des colonies de *Syringopora* basculées.
- 2 95 cm. Dolomie fleurie à colonies de *Syringopora* basculées et quelques poches à pseudo-brèches.
- 8 22 cm. Dolomie grise, fleurie, à colonies de *Syringopora* basculées, à rares encrines, à quelques poches de pseudo-brèches.
- 7 25 cm. Comme 8.
- 6 80 cm. Dolomie fleurie.
- 2 52 cm. Dolomie fleurie.
- 4 30 cm. Dolomie fleurie.
- 3 32 cm. Dolomie fleurie.
- 2 25 cm. Dolomie fleurie.
- 1 Base visitée sur quelques cm. Dolomie fleurie.